Seasonal and Short-term Energy Storage Through the Integration of Solar PV/T with Thermochemical Sorption Technology for Domestic Applications

Thesis by

Kamon Thinsurat

A thesis submitted for the Degree of

Doctor of Philosophy

School of Engineering

Newcastle University

Newcastle upon Tyne, United Kingdom

November 2019

Abstract

To maximize the utilisation of solar energy and improve the solar fraction in domestic households, this PhD study explored the novel integration of solar Photovoltaic/Thermal (PV/T) collector and thermochemical sorption energy short-term & seasonal storage system for the high latitude regions, using the weather condition in the England city of Newcastle upon Tyne as a case study. Solar Photovoltaic/Thermal (PV/T) hybrid collector was used to convert solar energy into both electrical and thermal energy simultaneously, and this represents in principle one of the most efficient ways to utilize solar energy. Thermochemical sorption energy storage, as one type of thermal energy storage, exhibits its compelling advantages of much higher storage density and capacity than sensible and latent heat storages as well as feasibility for long-duration energy storage. The thermal energy output from the PV/T collector was used to provide domestic hot water and stored in the thermochemical sorption storage system for shifting seasonal load to supply the domestic hot water and space heating demands in winter. One of the key challenges in the development of such an integrated system are the operational condition match (running temperature and system capacity, etc.) between these two units and the supply and demand balance for heating within a typical household. This study looked at the sorption material and solar conversion technology selection, thermodynamic cycle development, system configuration optimization, parametric analysis and numerical modelling and simulation.

The model of the Photovoltaic cell electrical power generation was developed by using the modelling tool of Matlab Simulink and subsequently coupled with a Computational Fluid Dynamics model for the simulation of simultaneous electrical and thermal energy production of the water-cooled Photovoltaic/Thermal collectors. The combined model was validated with commercial modules and used for performance evaluation and comparison of two types of PV/T collectors, with and without air-gap. The dynamic performance of a water-jacket-type heat exchanger reactor used in the thermochemical sorption unit was numerically and parametrically investigated and integrated with the PV/T collector model for the whole system simulation. One of the key point to implement the integrated system is that the mass flow rate of the heat transfer fluid (i.e. the water loop) that extracted heat from the PV/T collectors was adjusted to deliver heat at desired temperatures, especially for thermochemical sorption energy storage due to the variation of solar irradiation during the day and the mono-variant equilibrium characteristics of the thermochemical sorption cycle.

It was found that the Photovoltaic/Thermal collector with air gap could produce 28 ~133 litre of hot water per day per m^2 collector for the output temperature range of 40~100 °C; whereas, the Photovoltaic/Thermal collector without air gap was not competent for the purpose studied in this work especially in the cold regions. The application case studies suggested that an installation of 26 m^2 air-gap Photovoltaic/Thermal collectors integrated with the thermochemical sorption energy storage (TSES) system using 6.26 m^3 of adsorbent volume with $SrCl_2$-NH_3 working pair can fully satisfy the domestic hot water (DHW) demand of an ordinary single household in the city of Newcastle upon Tyne all year round with 100% solar source, and cover at least half of the annual electricity consumption.

To contribute high solar fraction for annual heating demands, including the DHW and space heating (SPH), in a typical household in high latitude regions, the compressor-assisted thermochemical sorption energy storage (CATSES) system was introduced and investigated. The PV/T supplies electrical energy for the compressor to assist lower desorption temperatures for the TSES resulting in a considerable improvement on utilising a low-grade heat from the PV/T. The optimisation was conducted to explore the optimal temperature of the heat transfer fluid (HTF) used to carry thermal energy from the PV/T to store in the TSES. The system performance of using a variety of reactive salts such as $CaCl_2$, NaI, $BaBr_2$ and $SrCl_2$ were studied and analysed for the application in terms of, e.g., winter temperature output, storage volume, minimum compression ratio (CR) of the compressor, minimum PV/T installation area to meet the 100% solar fraction for heating demands and electricity required in the proposed system. The results suggested that $CaCl_2$ and $SrCl_2$ were the two promising reactive salts to be employed in the integrated system to provide 100% solar fraction for annual heating demands in a typical household in high latitude regions with sufficiently high winter temperature output for domestic hot water and space heating demands. The minimum CR that work with $CaCl_2$ and $SrCl_2$ were 9.44 and 11.35 respectively when 30 m^2 of PV/T was installed (averaged installable rooftop area for a household in the UK) with sufficient amount of electricity supplied by the PV/T. If the compressor has the ability to work at the CR of 16, the PV/T installation area can be reduced to 22.31 and 25.82 m^2 when $CaCl_2$ and $SrCl_2$ were used respectively with the additional amount of electricity imported from the grid. When the adsorbent density of 450 kg/m^3 was applied, storage material volume of $CaCl_2$ and $SrCl_2$ were 28.52 and 21.91m^3 respectively to be able to supply 100% thermal energy in wintertime in a typical household in Newcastle upon Tyne, UK. The future works may focus on analysing the CASTES with denser composite adsorbents to obtain a higher energy density. Moreover, other types of heat exchanger reactor, such as the fin-tube one, may be used to achieve better heat transfer

performances. The operational control of the CATSES may be studied to explore the way to physically store and release thermal energy to balance the real-time thermal energy supply (from the PV/T) and demand (from a household) to obtain the maximum efficiency.

Acknowledgements

Firstly, I would like to express my sincere gratitude to my supervisors Prof. Tony Roskilly and Dr Zhiwei Ma (Kelvin) for the continuous support and guidance of my PhD study and research. The other important person who I would like to deeply thank is Dr Huashan Bao (Vicky) for being the best supervisor I have ever had. She moved to Heriot Watt University since April 2019; however, she has always given her precious time for my thesis with her valuable advice, knowledge and useful guidance. I really appreciate her patience, motivation, and immense knowledge that she has provided to me. I also would like to thank all three supervisors for the professional environment for researching and critical thinking in the meetings. The discussions in those meetings have shaped my way of thinking about how to deliver useful researches in the future.

Besides my advisors, I would like to thank my VIVA examiners: Prof. Tadhg S. O'Donovan, and Dr Yaodong Wang, for their insightful comments, encouragement and the time spent on reading my thesis and the VIVA. Those comments are invaluable, and they widen my research from various perspectives. In addition to being the VAVA committee, I also thank Dr Yaodong Wang for his helpful advice on my PhD process from the first day, I really appreciate his help.

My sincere thanks also go to Ian Douglass and Paul for their help on the laboratory and research facilities, Jan Fairless who always help me on the administrative tasks during my PhD and John Richardson for assisting me on all of the software issues. Without their precious supports, it would not be possible to smoothly conduct this research. I also thank all of my labmates for the stimulating discussions, the sleepless nights we were working together before deadlines, and for all the fun we have had in the past four years. I will always remember those priceless moments with all of you in Sir Joseph Swan Centre for Energy Research on the second floor of the Stephenson Building, Newcastle University.

I would also like to deeply thank the Energy Policy and Planning Office under the Ministry of Energy of the Kingdom of Thailand who supported all the studying tuition and living expenses while I was studying my PhD. I am also grateful for the supports from Walailak University that allowed me to pursue the degree and also contribute some living expenses by having been being paid my salary throughout the PhD course. Without them, it would not be possible for me to come to the UK to study.

Lastly, I would like to thank my family: my parents, my brother and all of my relatives for supporting me spiritually throughout my PhD time. I feel really grateful for being one of the members of my cheerful family. I also thank teachers, lecturers and friends from Anubarn Krabi School, Ammart Panichnukul Krabi School, King Mongkut's University of North Bangkok and The University of Texas at Arlington for providing me precious pieces of knowledge and being there when in need. With their supports, I have been living in this world full of happiness. Finally, thanks for the opportunities in my life that make me able to explore the world by travelling around and working in restaurants for part-time jobs. Those lucky chances give experiences to me to meet nice people and beautiful places all around. They further encourage me to use the knowledge I have learnt from my PhD to contribute the world with renewable energy toward a sustainable solution.

List of papers

Journal articles

K. Thinsurat, H. Bao, Z. Ma, and A. P. Roskilly, "Performance study of solar photovoltaic-thermal collector for domestic hot water use and thermochemical sorption seasonal storage," *Energy Convers. Manag.*, vol. 180, pp. 1068–1084, Jan. 2019.

K. Thinsurat, H. Bao, Z. Ma, and A. P. Roskilly, "Compressor-assisted thermochemical sorption integrated with solar photovoltaic-thermal collector for solar energy seasonal storage" Manuscript submitted to *Applied Energy*, June 2019.

Conference proceeding

K. Thinsurat, H. Bao, Z. Ma, and A. P. Roskilly, "Operational optimisation of Photovoltaic-thermal collector for 100% provision of Domestic heating demands using compressor-assisted thermochemical seasonal energy storage". In: *the 5th Sustainable Thermal Energy Management International Conference, SusTEM*, May 2019.

Table of content

Table of figures

Table of tables

Nomenclature

Abbreviations

CFD	computational fluid dynamics
CATSES	compressor-assisted thermochemical sorption energy storage
CR	compression ratio
DHW	domestic hot water
EG	expanded graphite
EVA	Ethylene vinyl acetate
HTF	heat transfer fluid
PCM	Phase change material
PV	photovoltaic
PV/T	photovoltaic/thermal
PV/T-AG	photovoltaic/thermal collector with air gap
PV/T-no-AG	photovoltaic/thermal collector without air gap
SF	solar fraction
SPH	space heating
STC	standard test condition
TSES	thermochemical sorption energy storage

Symbols

A	area, contact area (m^2)
C_p	specific heat capacity (J/(kg·K))
E	activation energy (J/mol)
E_g	band-gap energy of semiconductor used in PV-cell (eV)
f	mass-fraction (kg/kg)
g	gravity (m/s^2)
G	solar irradiance (kW/m^2)
Gr	Grashof Number (-)
h	heat transfer coefficient [$W/m^2/K$]
H, h	enthalpy (J/mol)
ΔH	reaction enthalpy (J/mol (NH_3))
I	electrical current (A)

k	Boltzmann's constant (1.38×10^{-23} J/K)
k	thermal conductivity (W/(m·K))
k	turbulence kinetic energy
k_0	pre-exponential factor of Arrhenius (1/s)
K_i	PV-cell's short-circuit current temperature coefficient (A/K)
M	molar weight (kg/mol)
m	mass (kg)
m	reaction pseudo-order (-)
$\dot{m}$	mass flow rate (kg/s)
n	number of mole (mol)
n	PV-cell ideal factor (-)
N	number of the PV-cell in PV-panel (-)
Nu	Nusselt number (-)
N_e	clear sky factor [8 for clear; 0 for totally covered]
P	pressure (Pa)
P_c	operating pressure (Pa)
Pr	Prandtl number (-)
q	electron charge (1.6×10^{-19} C)
Q	heat/thermal energy (J)
R	resistance (Ω)
R	universal gas constant (8.3144598 J/mol·K)
Ra	Rayleigh number (-)
S, s	entropy (J/(mol·K)))
ΔS	reaction entropy (J/mol (NH_3)/K)
t	time (s)
T	temperature (K)
$UA, \overline{UA}$	overall heat transfer coefficient (W/K)
v	molar volume (m^3/mol)
V	voltage (V)
V	volume (m^3)
V_t	thermal voltage of a PV cell (Volt); ($V_t = kT_{pv}/q$)
X, x	global conversion (-)

Greek letters

α	absorptivity (-)
β	thermal expansion coefficient (K^{-1})
δ	thickness (m)
ε	emissivity (-)
ε(x)	porosity of the adsorbent as a function of the global conversion, *x* (-)
η	efficiency (- / %)
λ	thermal conductivity (W/m/K)
μ	dynamic viscosity (Pa·s)
ν	kinematic viscosity (m/s^2)
ρ	density (kg/m^3)
σ	Stefan Boltzmann constant (5.670367×10^{-8} $W/(m^2\cdot K^4)$)
τ	transmissivity (-)
ω	specific rate of dissipation

Subscripts

ab	absorber
ad	adsorption
ads	adsorbent
amb	ambient
comp	compression/compressor
conv	convection
con_T	constant of linear variation on temperature difference
con_G	constant of linear variation on irradiance difference
de	desorption
D	diode (current)
elec	electrical
eq	equilibrium
eva	evaporation
f	heat treansfer fluid
fw	fluid-wall
g	glass
gr	ground
heat	auxiliary heater

isen	isentropic
MPP	maximum power point
NH3	ammonia
NH3_R	reactive ammonia
NH3_t	total ammonia
oc	open-circuit
out	output from the reactor
p	parallel
pv	photovoltaic
PH	photo (current)
ray	radiation
R	reactive part, reaction
RS	reverse saturation
s	series
s, salt	reactive salt
S	saturation
SC	short circuit
SH	shunt
sum	summer
STC	standard test condition
t	thermal
v	ambient vapour
w	wall
wi	wind
wr	wall-reactant
win	winter

Chapter 1: Introduction

1.1 Introduction

Sustainability is currently the paramount concern in diverse fields of research, e.g., energy (Fuso Nerini *et al.*, 2018), agriculture (Tilman *et al.*, 2002), infrastructure development (Zhang *et al.*, 2014b), economy (Anglin, 2010) and social development and education (Bendor *et al.*, 2015). Providing sustainable energy is one of the seventeen UN's sustainable development goals to improve ongoing environmental issues such as pollutions and climate change (UN, 2017). With the unawareness of the global environmental effects from the fossil fuels, renewable energy resources had not been broadly explored until 1997 when the Kyoto Protocol was announced that the exhaust gases from burning fossil fuels are the mason of global warming effect which now become one of the most important issues preventing the sustainable global development (van Den Berg *et al.*, 2015; Ramos *et al.*, 2017). From then, renewable energy sources, e.g., solar, wind, ocean wave and tide, geothermal, biomass, biogas and nuclear fusion has been being extensively studied with the ambition to supply the world energy demands with minimal fossil fuels.

Although there are several renewable energy resources such as solar, wind, bioenergy, hydropower, etc., the most abundant one is solar energy (Parida, Iniyan & Goic, 2011). According to the world energy resources presented by World Energy Council (2013a), only 0.1% of the solar energy resource with 10% conversion efficiency alone can excessively supply four times of the world energy demand. However, in 2011, only 13% of the annual world primary energy supply was from renewable sources (World Energy Council, 2013b). Moreover, the solar energy fraction from the estimated world overall renewable energy production in 2017 is just 1.9% (Aberg *et al.*, 2018). Despite the potential of the solar energy resource, there are several difficulties to promote the solar energy source to be the main world energy supply source.

In order to get the highest efficiency of energy systems, energy resources should locate as close as possible to the demand locations to reduce losses from the transportation of carriers. In an urban area, wind is not a suitable source of energy as wind turbines obstruct the scenery of cities or communities. Moreover, according to suburb and city types of terrain, surface roughness decreases the power of the available wind that can be harvested. Biomass and biogas are neither the appropriate way to supply energy for a community in an urban area because of

its production which needs enormous area; therefore, transportation will be required to transfer bio-energy carriers into an urban area. Therefore, comparatively, the preferable energy resource which can be accessed everywhere and installed on the existing rooftop area of buildings without sight obstacle is solar energy.

Because of the lack of proper ways of utilisation, solar energy supplies only 0.6% of the world total primary energy demand which is mainly used in the form of electrical power (IEA, 2018a). According to Babu & Ponnambalam (2017), the monolayer solar PV panel could extract only up to 25% of photon energy from a solar spectrum of AM1.5G while the remaining 75% losses as thermal energy. Therefore, there is a great potential to improve the utilisation of solar energy to improve solar fraction in the energy systems. Not only the efficiency of the PV cell that is the obstacle to promote the solar energy share in the energy supply but also the intermittent properties, including the diurnal and seasonal variations, of the solar energy that introduce the disadvantage of the solar energy resource compared to other conventional energy resources (Lewis, 2016; Akinyele & Rayudu, 2014; Lindberg & Doorman, 2013; Eltawil & Zhao, 2010). Solar energy is only available during the daytime, but the energy demand continuously exists. Moreover, weather conditions also affect the solar energy supply when the sky is covered. For a long-term period, i.e., seasonal variation of the solar radiation, especially in the regions far from the equator, the mismatch between the energy demand and the solar supply becomes the significant reason of solar energy being underutilised (Akinyele & Rayudu, 2014; Herrando *et al.*, 2018; Hazami *et al.*, 2017; Lund *et al.*, 2015). In high latitude regions, solar radiation is still ample in summer when the energy demand is comparatively low. In winter when solar radiation is infinitesimal, the demand is enormous.

The residential sector may play an important role to improve the solar fraction in the overall energy demand if energy storages are integrated because the residential energy demand highly varies against the intermittent solar resource especially in the high latitude area where the solar seasonal variation is considerable. For example, in the UK in summer, 17 hours of sunshine along with comfortable ambient temperature (around 18-21 ^{o}C) may generate an extensive amount of energy for a household when the energy demand is bottommost and vice versa in winter when the energy demand is at its peak with cold ambient temperature and minimum sunshine hours. Moreover, the daily mismatch between the demand and supply is also a significant factor of increasing the solar fraction in a household. Typically, members of a household spend time at home in the morning and evening leading to two daily demand peaks during the mentioned time. During the day, a household has a small energy demand because

household members are usually out for work. In contrast, during the day, the solar intensity is at its maximum leading to the daily mismatch between the demand and supply in the residential sector. Therefore, exploring the energy storage that has the technical and economic potential to eliminate the disadvantage of the solar energy resource may contribute to the market share of solar energy supply in the future.

Energy storage technologies are acclaimed to fulfil the disparity between the demand and renewable energy supply including solar energy. However, it is arguable regarding suitable technologies for solar energy conversion and solar energy storage. It may be impractical to find one technology that solves the world complicated energy problems as mentioned before; nevertheless, it would be admirable if a number of researches may suggest or clarify the solution to enhance the solar fraction in current energy demand for specific regions which encourage other parts of the world to adopt in the way of accomplishing the sustainable global goals.

1.2 Research problems and Motivation

Considering a specific area in high latitude regions using the United Kingdom (UK) as an example, 198.97 Mtoe were consumed in 2014 in the UK for the 135.28 Mtoe of the UK final energy consumption. There was 64.9 Mtoe (32.62% of the overall final energy consumption) was loss in energy conversion and delivery as shown in Fig. 1.1. Transportation is the most energy-consuming section in the UK with 40.05% of the total energy shared mainly supplied by liquid fuel (Department of Energy and Climate Change, 2015). The domestic sector is the second largest energy-consuming section primarily supplied by natural gas. Considering the non-transport sectors, domestic, commercial and industrial combined, the main purpose of the final energy usage is for space heating with 61% of the overall energy usage as shown in Fig. 1.2. The second purpose is for water heating (Department of Energy and Climate Change, 2015); therefore, energy is used substantially for heating purpose in non-transport sectors. The information implies that thermal energy is the most important type of energy required for the non-transport sectors in the UK.

Electricity is also an essential energy supply for a wide range of applications. Although the per cent of overall final energy usage is relatively low compared to thermal energy usage in non-transport sectors, the trend of using electricity as the final energy is growing rapidly. Nejat *et al.* (2015) illustrated that electricity consumption in buildings in the domestic and commercial sectors grew 39% from 2000 to 2010. In the near future when there is more electricity demand in other applications such as electric vehicles due to its environmentally friendly, the electrical

energy system may encounter a significant negative impact on the system qualities (Muratori, 2018). There are several other applications that have changed to use electrical energy as the main source instead of the fossil fuel, e.g. electric space heating, electric water heating and heat pump integrated into the low-temperature district heating systems (Elmegaard *et al.*, 2016), which may also increase the electricity demand that is going to affect the electrical systems. Definitely, the sources of the electricity are renewable resources to promote the low carbon future world. Therefore, promoting the renewable electricity is also important other than the renewable thermal energy; however, because of the intermittent property of renewable resources such as solar and wind, it is challenging to increase the integration of renewable electricity into the current electrical grid infrastructures constrained by the limited grid capability without energy storages suitable for energy demands in different forms.

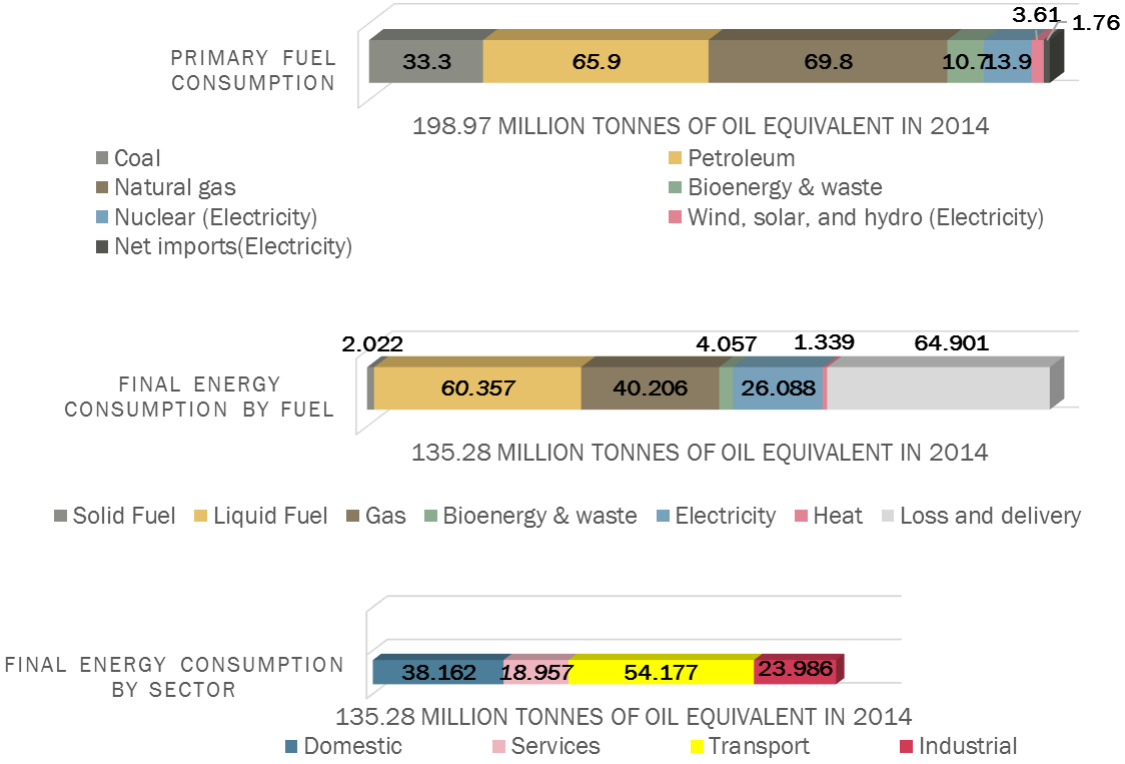

Fig. 1.1 *The UK energy consumption in 2014*

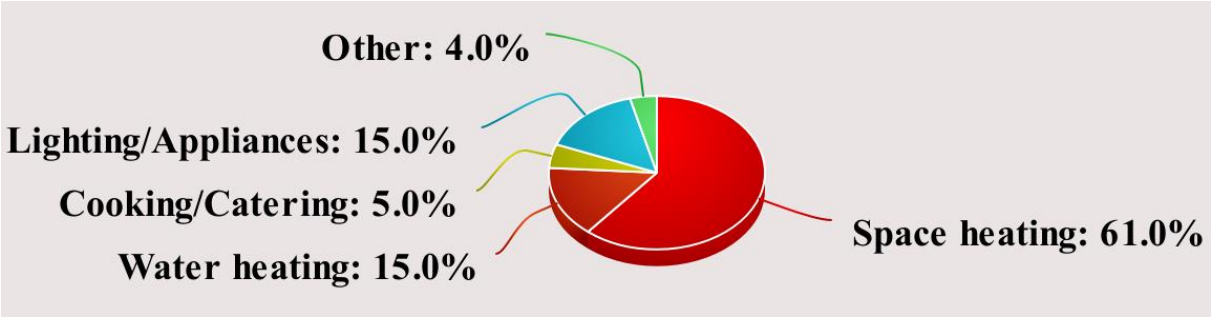

Fig. 1.2 *UK 2013 non-transport energy consumption (64.5MTOE)*

With the extremely low contribution of the renewable energy sources in the energy consumption as previously mentioned, besides the potential of the solar energy source, it is crucial to increase the solar energy fraction to the overall energy consumption. Exploring energy conversion technologies in conjunction with energy storage technologies to be able to manage the intermittency of the solar energy source has the potential to supply the energy demands, with a sustainable source. For the high latitude regions, seasonal analysis of the integrated systems between the renewable resources and energy storages becomes also essential; therefore, exploring the feasibility to seasonally store solar energy in the chemical form then release as the thermal energy is novel to reveal its potential for sustainable future.

1.3 The objectives and scope of the thesis

Residential area households in domestic sector normally located in an urban area where the installation area of solar conversion technologies, e.g., solar panels are limited. When solar panels are already installed, they may last for 25 to 30 years. Therefore, choosing the proper solar conversion technology for domestic usages is crucial to be able to transform the conventional fossil-fuel energy sources, e.g., natural gas to the sustainable source such as solar. Most policies tend to encourage households to install the photovoltaic panels (PV panels) for electricity production with the overall efficiency of approximately 10 - 15 per cent. However, the mentioned efficiency is hardly achieved because the nominal operating cell's temperature (NOCT) is usually higher than the temperature at the standard test condition (STC) leading to a lower conversion efficiency of the PV panels. NOCT varies according to the heat transfer rate between the panels and the ambient which is dependent on the ambient temperature, wind speed and the gap between the panel and the installed surface. Therefore, generally, the PV panels are designed and installed for the purpose of keeping the cell's temperature to be as low as possible.

The other famous solar conversation technology is a solar thermal collector which convert solar energy into thermal energy. Water is the common heat transfer fluid (HTF) used in the thermal collector to absorb heat for domestic hot water (DHW) applications with the conversion efficiency of approximately 30 – 70 per cent. Recently, the hybrid conversion technology named photovoltaic-thermal (PVT) collector, used to convert solar energy into electrical and thermal energy simultaneously, has been taken into attention because of two main benefits. Firstly, the thermal part can remove the undesirable heat from PV cells to keep the cell's temperature low; secondly, the removed heat can be used to contribute the DHW applications.

However, there are limited studies on how to optimally operate the PVT in order to maximise the overall utilisation of solar energy; not only for maximising the electrical efficiency.

Therefore, the first objective of this thesis is to reveal the suitable conversion technology for households to maximise the solar energy fraction in the domestic sector. The households will be focused on the cold regions where the seasonal variation of the solar energy and heating demand are relatively large. Based on the availability of the experimental facility, Newcastle upon Tyne in the UK is used as a representative of the cold region. The one-year period was studied to see the potential of using solar energy with seasonal energy storage to supply an averaged UK household.

The second objective, after reviewing pieces of literature in chapter 2, is to use the promising long-term energy storage which is the thermochemical sorption to store thermal energy storage with the identified conversion technology for the first objective. Thermochemical sorption energy storage technology is the renowned technology able to store energy in long-term period (seasonally) that can store energy in summer, when there is plenty of solar energy supply but low energy demand, and discharge energy in winter when the demand is high. The study will determine the storage size for the studied household and evaluate the performances of the storage system.

As there are limited number of research on how low carbon technologies can be intelligently integrated in a holistic approach at large scale, focusing on combining the solar energy conversion technologies with long-term energy storages, the last objective is to combine the highly efficient solar energy conversion technology with high energy density long-term energy storage, to optimise the operating conditions of each system components to maximise the useful thermal energy released in winter. To meet the requirement of heating a household heating demands in the UK, additional component may be included into the integrated system, e.g. a compressor and an auxiliary heater, to be able to obtain the highest solar fraction in a typical UK household. As solar irradiance varies depending on time of the year, examining the optimal operating conditions for different weather conditions and seasons, i.e., winter sunny/cloudy days, spring sunny/cloudy days, summer sunny/cloudy days and autumn sunny/cloudy days, would be valuable to maximise the utilisation of the solar energy resource along the year.

Performing the studies for the three mentioned objectives, this thesis demonstrates a promising solution to increase the solar fraction into the domestic household's energy supply

for cold weather regions contributing to the ambition to a more sustainable way of living. The findings of the suitable solar conversion technology, seasonal storage and optimal operating conditions in this thesis may be further applied to other weather conditions or other sectors, e.g., commercial, industrial or transportation sectors, that is going to be increasingly dependent on sustainable energy sources, especially, the solar energy which is the most abundant source of energy in the world.

1.4 Thesis overview

This thesis comprises of five chapters in addition to this chapter. In chapter 2, the literature reviews of the objectives previously mentioned are presented. This includes the three main topics which are solar energy conversion technologies, energy storage technologies and the integration of the solar energy conversion technologies with energy storage technologies for domestic long-term energy utilisation. The literature reviews in chapter 2 reveal potential technologies and viability to apply them for domestic households in cold regions. Novels of this thesis are also stated in this chapter.

Chapter 3 is dedicated to solar energy conversion technologies including working principles, mathematical models, validation and results. The performances of individual conversion technologies are examined in this chapter.

Chapter 4 integrates the conversion technology and storage technology and optimises the operational conditions for different weather conditions in Newcastle upon Tyne. The sizing of the overall system and the material selection are presented in this chapter.

Chapter 5 is appointed to the energy storage technologies containing the working principles, mathematical models, validation and results of the thermochemical sorption energy storage in energy charging and discharging stages. The dynamic performances of the compressor-assisted thermochemical sorption energy storage are determined and presented in this chapter.

Chapter 6 concludes and discusses the findings of the suitable solar energy conversion and energy storage technologies along with the optimal operating conditions of different weather condition. The potential for enhancing the solar fraction of the energy supply for the domestic sector is summarised. The discussion includes the suggestion for future works to promote the real-world implementation of the integrated technologies.

(This page intentionally left blank)

Chapter 2: Literature reviews

As the introduction chapter presented that the heating demands in the residential sector are mainly provided by fossil fuels (around 80% of the total energy consumption) emitting a large amount of the greenhouse gas, therefore, this chapter is focusing on reviewing the technical background of promising solar conversion and storage technologies suitable for using in domestic household applications expected that those technologies can reduce the use of fossil fuel. The state of the arts of each related technology will be presented with their advantages and disadvantages. With the reviewed pieces of literature, the promising solar conversion and storage technologies were chosen following by the proposed novel solution to integrate the two technologies for seasonal thermal energy storage which is feasible to increase the solar fraction in a household in the high latitude region using Newcastle upon Tyne, the UK as a case study.

2.1 Solar energy conversion technology review

Solar energy can be converted into different kinds of output energy such as electrical, thermal or chemical forms; however, the electrical form seems to be the most favourable as seen in the renewable energy share in the world final energy consumption presented by IEA (2018b). The wide range of solar spectrum can be absorbed mainly by two conversion technologies through photo-electric or photo-thermal ways. For example, a semiconductor is used as the photovoltaic that absorbed mainly the visible light to generate electrical current. High optical absorptivity materials are used to absorb all the solar spectrum in the form of heat (Mazloomi, Sulaiman & Moayedi, 2012; Escobar *et al.*, 2013; Chen *et al.*, 2015). There is a small share of solar conversion via the photochemical or photobiological ways.

By considering different types of energy output from solar conversion technologies, there are four categories; photovoltaic (PV), thermal collector, photovoltaic-thermal collector (PVT), and others such as solar fuel, etc., as illustrated in Fig. 2.1. Each group of solar energy conversion technology is reviewed in detail in the following sections.

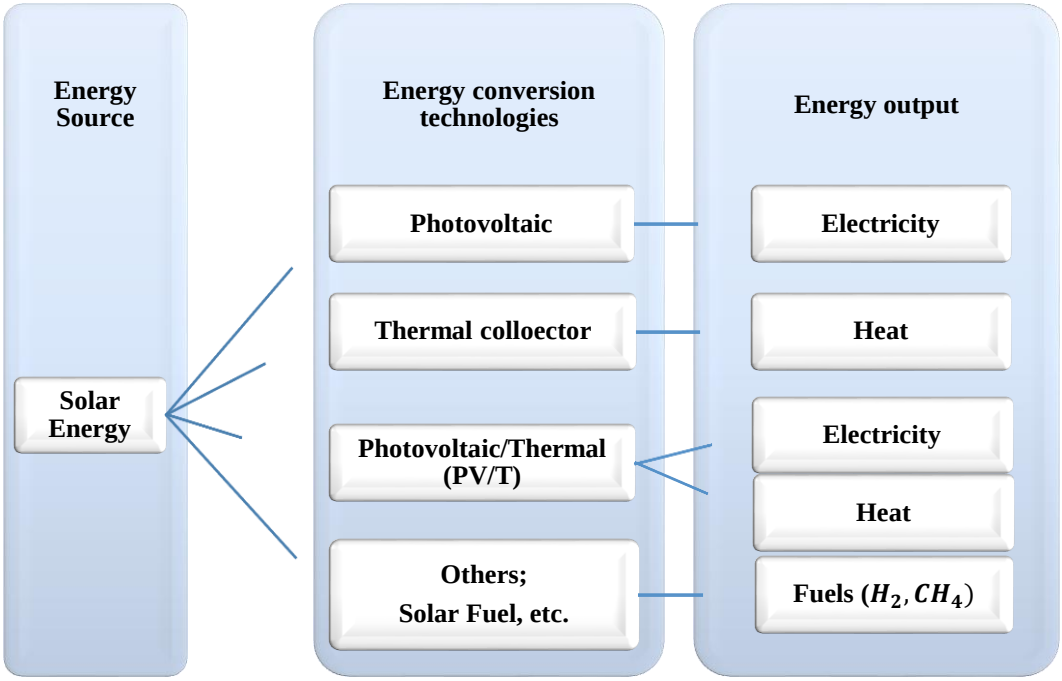

Fig. 2.1 *Solar conversion technology categories*

2.1.1 Photovoltaic (PV) cell

Photovoltaic (PV) or solar cell technology transforms solar energy in the form of the photon into electricity. PV technology first invented by Bell Telephone Lab in 1954 with only 6% efficiency (Bell Telephone, 2000) after several years of the discovery of photoelectric effect by Becquerel in 1839 (Hubbard, 1989). Photons which have different levels of energy indicated with its wavelength, or frequency, excite electrons in semiconductor materials then moved by the electrical field of the junction to the conductive layer resulting in the increasing of the electrical potential. PV efficiency varies according to the sensitivity of the semiconductor with parts of the solar spectrum. Covalence electrons of the semiconductor materials are excited by only the photons which have the exact amount of energy to make the covalence electrons change the energy level to the next orbital step and other photons are losses mainly in the form of heat. With the limitation of the absorptivity property of the single material solar cell, only approximately 15% efficiency is normally achieved for commercial panels with silicon-based material (Bahaidarah, Baloch & Gandhidasan, 2016) while the remaining energy is transformed into thermal energy and losses. Though, the world records laboratory cell of the single-crystal Gallium Arsenide (GaAs) solar cell can go up to 27.6% (Kayes *et al.*, 2011) and 26.1% for the single-crystalline silicon solar cell (Haase *et al.*, 2018) as shown in Fig. 2.2 (NREL, 2019).

Although the GaAs solar cell has several advantages over crystalline silicon solar cell (AltaDevices, 2017) such as low-temperature coefficient, good low light performance, high

efficiency, excellent radiation and moisture resistance, flexible and lightweight, the cost of the raw material is considerable and the fabrication is complicated (Connolly *et al.*, 2013); therefore, the application is mainly for space technologies. Unlike GaAs solar cell, the silicon-based solar cell is made from the abundant and cheap material, the silicon promoting the silicon-based solar cell to be the most installed technology in the world so far.

Due to the high energy consumption of the purification process and the complicated production procedure of the monocrystalline silicon solar cell (Parida, Iniyan & Goic, 2011), there are other optional solar cell technologies using less production cost and simpler production procedure in the market with compensated efficiency; for example, multi-crystalline silicon technology, thin-film technologies such as CIGS, CdTe and amorphous silicon and emerging technologies such as dye-sensitised cells, perovskite cells, organic/inorganic cells and quantum dot cells. Examples of some high efficiency of each solar cell are presented in Table 2.1.

To promote the technical feasibility of specific solar energy projects, high cell's efficiency is of priority which led to the emerging of multijunction solar cells. The concept is to use two or more semiconductors when each one absorbs different ranges of the solar spectrum. The common semiconductors used in multijunction technologies are Ge and the III-V groups such as GaInP and GaInAs (Connolly *et al.*, 2013). Therefore, with the contribution of more than one junction, the multijunction solar cells reach its world record of the conversion efficiency of 39.2% for the 1-sun condition (NREL, 2019).

Because of the high cost and complicated production of the multijunction solar cells, they are not economically suitable for the solar project on earth. However, researchers proposed the new way to reduce the overall cost of the solar project by using the concentrated sunlight to focus on a smaller area of the costly but high-efficiency solar cells. Although the concentrated sunlight induces high cell's temperature, its high efficiency with less installation area may be worthier at the end (Paquette *et al.*, 2016). If the cooling system can maintain the cell's temperature as low as the non-concentrator case, considerable higher conversion efficiency can be achieved (NREL, 2019); for example, with same multijunction solar cell, the non-concentrator case (1-sun irradiance) can produce the highest conversion efficiency of 39.2% while 47.1% conversion efficiency can be achieved when the solar irradiance is concentrated to be 143-sun (NREL, 2019). This leads to a new area of study to find the optimum PV cell area if the concentrator is integrated.

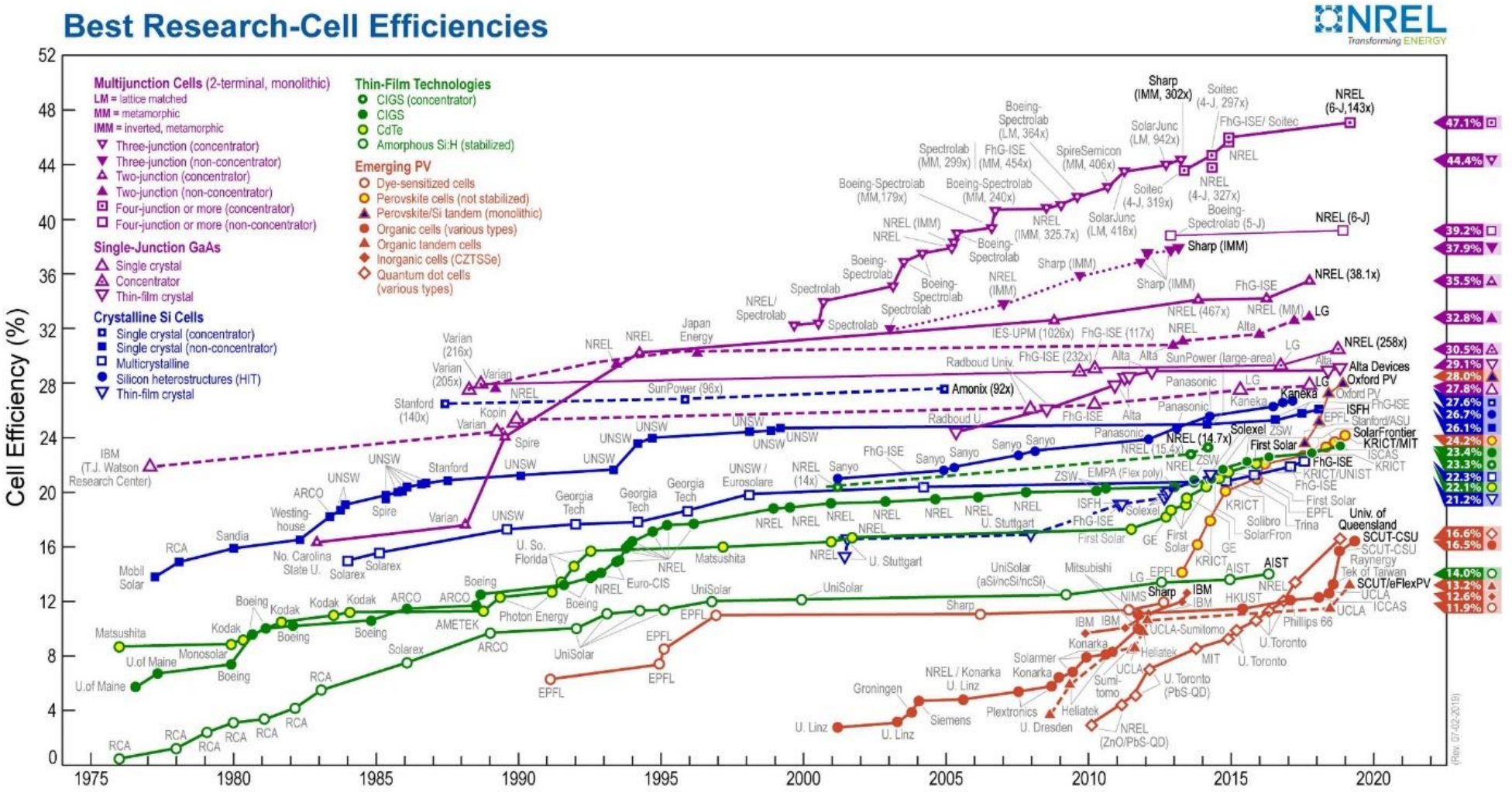

Fig. 2.2 *Timeline of PV technologies with their maximum efficiency available in research-level* (NREL, 2019)

Different types of PV cell's material have both its advantages and disadvantages which may be suitable for different applications. The amorphous silicon has lower efficiency than the crystalline silicon; however, its lower temperature coefficient makes the amorphous silicon performs well at high temperature. Pathak, Pearce & Harrison (2012) reported that 10.6% improvement could be achieved from the amorphous silicon solar cell when the 100 ^{o}C annealing is done for 1 hour every working cycle. III-V semiconductors have a very high cost which is not suitable to use in domestic rooftop application because of the economic potential. Thin-film technologies become an interesting option because of the recent increase in conversion efficiency; however, they are not widely used in the market yet. Because of the mentioned reasons, the silicon-based solar cells are still widely used currently, although perovskite solar cells may become more popular in the near future due to the promising simple production and low cost resulting in intensive researches on improving the industrial-scale production with higher conversion efficiency.

Table 2.1 *Solar Photovoltaic (PV) classification with their non-concentration efficiency (if not noted) and a rough idea of the price for each PV type*

Solar cell	Electrical Efficiency (%)	References
Crystalline silicon (c-Si)		
• The first photovoltaic cell	6.0	(Bell Telephone, 2000)
• Monocrystalline silicon (mono-Si) (US$0.22 - US$0.35 / Watt (Yangtze_Solar, 2019))	26.1	(Haase *et al.*, 2018)
• Polycrystalline silicon (poly-Si) (US$0.19 - US$0.25 / Watt (Solar_home, 2019))		
- Thin-film on a glass surface of poly-Si)	15.0	(Gall *et al.*, 2009)
- forming nanoscale pyramids on wafer surface using self-mask etching technique)	16.27	(Lin, Chen & Hong, 2013)
- forming nanoscale pyramids on a wafer surface using wet etching technique)	15.56	
• Heterojunction c-Si (US$0.48 –US$0.56 / Watt (Louwen *et al.*, 2016))	25.6	(Masuko *et al.*, 2014)
III-V Compound Semiconductors		
• Gallium Arsenide (GaAs) (US$3.89 / Watt (Bianchini *et al.*, 2016))	27.6	(Kayes *et al.*, 2011)
	26.0	(Connolly *et al.*, 2013)
• Indium Phosphide (InP)	22.0	(Connolly *et al.*, 2013)

Solar cell	Electrical Efficiency (%)	References
Thin-film technologies		
• Amorphous silicon (a-Si) (US$0.40 - US$0.80 / Watt (Bluesun, 2019))		
- MoO_3 solar cell	6.21	(Park *et al.*, 2011)
- a-Si:H solar cell	5.97	
- a-Si solar cell	14.0	(NREL, 2019)
• Perovskite Solar Cells (Expected to be as low as US$0.1 - US$0.2 / Watt (Brian Wang, 2019))	11.4	(Eperon *et al.*, 2014)
	24.2	(NREL, 2019)
• cadmium (Cd)-free CIS technology	23.35	(Yoshida, 2019)
Multijunction solar cells		
• Perovskite/Si tandem	28.0	(Sherahilo, 2018), (NREL, 2019)
• GaInP/GaInAs/Ge (240-sun)	40.7	(King *et al.*, 2007)
• GaInP2/GaAs/GeGe (US$46 - US$84 / Watt (Anon, 2019a))	30.0	(Anon, 2019b)

2.1.2 Solar thermal collector

For the solar thermal collector, the main purpose is to convert solar energy into thermal energy. Solar collector mainly consists of the high optical absorptivity material which absorbs the solar radiation and transforms to the internal energy resulting in the increasing of the material temperature. Absorbed thermal energy is then utilised by a thermal energy carrier (normally water, air, oil or nanofluid) that transfer the heat for several downstream applications such as domestic hot water use, space heating, thermal energy storage (Ma, Bao & Roskilly, 2019) or industrial preheat applications (Kumar, Hasanuzzaman & Rahim, 2019). The solar thermal collector can be categorised into two types which are stationary/non-concentrating and concentrating collectors (Kalogirou, 2004). Flat plate, compound parabolic and evacuated tube collectors are considered as stationary solar collectors and parabolic trough, Fresnel reflector, parabolic dish and heliostat field collectors are the concentrating collector.

Flat plate solar collector is the most well-known type for low to medium temperature applications such as water heating and space heating (Pandey & Chaurasiya, 2017). Ongoing researches on flat plate solar collector are related to exploring the design to improve the thermal conversion efficiency with less weight while increasing the output temperature of the collector.

One of the promising ways is by using the nanofluid as a heat transfer fluid (HTF) to improve the collector efficiency (Faizal *et al.*, 2013; Pandey & Chaurasiya, 2017). Yousefi *et al.* (2012) used 0.2 wt.% MWCNT with various pH values from 3.5 to 9.5 and found out that the lower pH nanofluid provides higher collector efficiency. Faizal *et al.* (2013) showed that the weight of water-based solar collector may be reduced about 8.6-10.2 kg per collector by using CuO, SiO_2, TiO_2, Al_2O_3 as the nanofluid because of the improved heat transfer properties of the HTF resulting in smaller collector designs at desired performances. Although nanofluid can improve the efficiency of the collector, water is still the most chosen HTF used in the solar collector because of its availability, cost, safety, no heat exchanger required, etc. (Jamar *et al.*, 2016). Thermal performance, in terms of temperature, for a flat plate thermal collector could reach a temperature of more than 200 ^{o}C for stagnation condition (Kalogirou, 2003) although the typical range of working temperature is from 30 to 80 ^{o}C (Kalogirou, 2004).

Evacuated tube collector is another type that is widely used in medium temperature ranges from 80 to 200 ^{o}C (Kalogirou, 2004) for applications such as household hot water or other industrial applications such as heat production for industrial processes, solar cooling and air conditioning, solar drying and seawater desalination because of its high efficiency (Muhammad *et al.*, 2016; Kalogirou, 2003; Jamar *et al.*, 2016) although not as common as the flat plate solar collector due to its higher initial cost (Shukla *et al.*, 2013) especially in Europe (Qiu, Ruth & Ghosh, 2015). Ayompe *et al.* (2011) performed the experimental comparison between the flat plate and evacuated tube collectors and showed that the evacuated tube collector had higher averaged annual efficiency than the flat plate collectors (evacuated tube efficiency of 60.7% compared to flat plate efficiency of 46.1%). There are two main types of evacuated tube collector which are the single-walled glass evacuated tube and Dewar tube (which has two layers of glass tube) collectors (Gao *et al.*, 2013; Sabiha *et al.*, 2015). Both types are used in several applications such as domestic hot water heating (Tang, Yang & Gao, 2011), integrated with the liquid desiccant for solar air conditioning (Mehta & Rane, 2013), sterling engine although the temperature output from the evacuated tube collector gives low efficiency (Madduri *et al.*, 2012), etc.

The other type of non-concentrating solar collector is the compound parabolic solar collector. In order to collect more solar radiation from other direction, a parabolic reflector can be installed above glazing layer to reflect indirect irradiance in addition to the direct sunlight, to the collector layers as shown by Al Imam *et al.* (2016) in Fig. 2.3. In some cases, the parabolic part can be designed to collect intense radiation which therefore the compound parabolic solar

collector can be classified as one type of concentrating solar collectors (Kaiyan, Hongfei & Tao, 2011). Generally, the geometries of the concentrating solar collector are complicated and costly which may not suitable for the domestic application which is out of scope for this thesis although they provide higher temperature output for a wider range of application especially suitable for the heat engine for a large electrical power generation (Shahin, Orhan & Uygul, 2016). To preliminarily compare the performance of different kinds of the thermal collector, the efficiency of each solar thermal collector is presented in Table 2.2.

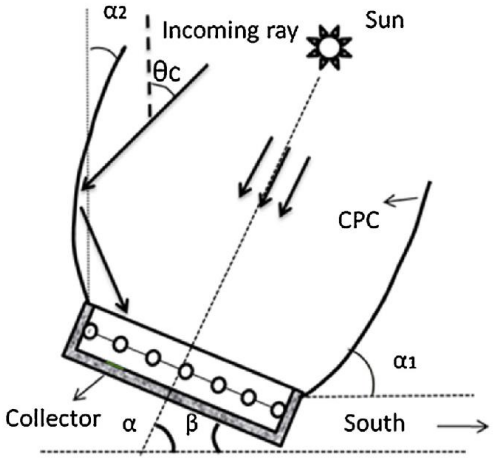

Fig. 2.3 *The compound parabolic concentrator* (Al Imam *et al.*, 2016)

Table 2.2 *Solar thermal collectors' efficiency for each type of technology*

Type	Efficiency (%)		Output temperature (ºC)	References
	Electrical	Thermal		
Non-concentrating or Stationary				
Flat plate				
	-	83.0	-	(Zondag *et al.*, 2003)
	-	20-65	36-45	(Yousefi *et al.*, 2012)
- 2 2-m^2 collectors series connected with stagnation temp. of 120ºC and 190ºC	-	46.1	<60	(Ayompe *et al.*, 2011)
Evacuated Tube Solar Collector (ETC)				
- with heat shield	-	54.7	92-130	(Zhang *et al.*, 2014c)
- without heat shield	-	23.2	91-126.6	(Zhang *et al.*, 2014c)
- Absorber surface of 3 m^2, the tubes vacuum level of 10^{-5} mbar.	-	60.7	≤60	(Ayompe *et al.*, 2011)
Compound parabolic				
- installed on the PV/T	13-15	40-50	<80	(Al Imam *et al.*, 2016)
Concentrating collector				
Parabolic trough collector				
- with 0.3kg/s, 1m long, 700W/m^2	-	62.0	100-500	(Bakos *et al.*, 2001)
	-	75.0	96-100	(Tzivanidis *et al.*, 2015)
	-	71.4	334-663	(Shahin, Orhan & Uygul, 2016)
Fresnel reflector				

Type	Efficiency (%)		Output temperature (ºC)	References
	Electrical	Thermal		
- linear Fresnel lens	-	50.0	90-200	(Zhai *et al.*, 2010)
- the concentration ratio of 9.4 with selective surface coated	-	Up to 71.2	≤60	(Ayompe *et al.*, 2011)
Parabolic dish				
- Thermoelectric (experimental)	0.94 -1.68	-	-	(Shanmugam, Veerappan & Eswaramoorthy, 2014)
- Cogen application	20.0	50.0	60-90	(Haim *et al.*, 2010)
Heliostat field collectors				
- Solar to Electricity	15.81	-	565	(Ehrhart & Gill, 2013)
	-	75.6	550	(Shahin, Orhan & Uygul, 2016)

2.1.3 Photovoltaic/thermal (PV/T) collector

Photovoltaic/thermal (PV/T) technology is the technology that combines the photovoltaic cell with the thermal collector, therefore, thermal and electrical energy are obtained from converting solar radiation simultaneously. The initial reason for combining these two technologies was to extract the generated heat from the PV cell(s), which is detrimental to electrical efficiency, and use it in certain end-user applications, leading to the improvement in solar energy conversion and utilisation efficiency (Al-Waeli *et al.*, 2017c; Babu & Ponnambalam, 2017), compared to that achieved by using two independent systems. Such integration also reduces the costs of production and installation, resulting in cheaper and more practical applications that require both electricity and heat. The thermal energy absorbed by the solar PV cell is transferred to the cooling fluid (air or liquid) through the integrated collector and used for heat applications such as space heating, domestic hot water, drying, etc. (Herrando, Markides & Hellgardt, 2014). By making use of thermal energy in addition to the electrical energy, higher total efficiency will be achieved from the technology. However, there are several concerns to this technology design in order to get the most suitable model for specific demands.

The PV/T collector has received great attention for the improved energy utilization efficiency of solar sources for the past few years leading to rapid developments in recent decades (Chow, 2010; Al-Waeli *et al.*, 2017c). To maximise the conversion and utilisation of solar energy, many research works have primarily targeted thermal energy production and applications, as the thermal energy is easier and cheaper than the electrical energy to be converted from the solar energy (Babu & Ponnambalam, 2017). Apart from the most influential external factors to energy conversion efficiencies such as geographical location and climate (including solar irradiance, ambient temperature, wind speed, etc.), the R&D efforts on the

thermal production of hybrid PV/T systems have been mainly on factors including the cooling fluid type, the design configuration and parameters of thermal collectors, in addition to operating parameters such as fluid flow rate and the type of application used, as the former two factors are the most important elements discussed in the majority of research works. Commonly used coolants are air (Tripanagnostopoulos *et al.*, 2002; Tomar, Tiwari & Bhatti, 2017) and water (Tripanagnostopoulos *et al.*, 2002; Zondag *et al.*, 2003; Ziapour, Palideh & Baygan, 2014; Hazami *et al.*, 2016), or a mix of the two (Su *et al.*, 2016; Othman *et al.*, 2016). Since water has high specific heat capacity and density compared with air, the water-based hybrid PVTs achieve higher thermal and electrical efficiency than air-based ones (Tripanagnostopoulos *et al.*, 2002; Tomar, Tiwari & Bhatti, 2017; Amori & Taqi Al-Najjar, 2012); moreover, the use of water as working fluid is more suitable for heating applications like space heating, especially domestic hot water use, or as efficient heat carrier and transfer media for other downstream applications. In recent decade, there is a strong motivation to use different nanofluids (a mixture of base fluid like water or ethylene glycol, and nanoparticles) to improve the heat transfer performance and hence both electric and thermal efficiencies of the hybrid PV/T system as nanofluids have intensified thermophysical properties, such as thermal conductivity, viscosity, and convective heat transfer coefficients compared with conventional fluids (Yazdanifard, Ameri & Ebrahimnia-Bajestan, 2017; Hassani *et al.*, 2016; Al-Waeli *et al.*, 2017a; Hosseinzadeh *et al.*, 2018). The drawbacks of using nanofluids are associated with the high cost of nanoparticles, limited time of stability, an additional device such as heat exchanger, and pressure drop in the collector. Apart from the efforts on nanofluids, incorporating PCM within the PV/T system as a heat sink is another prevailing research topic for efficiency improvement of the PV/T system in the recent decade. Works proposed to add a PCM layer beneath the absorber (Smith, Forster & Crook, 2014), or employ microencapsulated PCM slurry (Qiu *et al.*, 2015), or embed PCM in the hot water tank (Feng *et al.*, 2015), etc. Depending on the melting temperature of the PCM, although it has a limited effect on reducing the PV cell temperature with limited cooling rate compared to water cooling system, it can effectively stabilise the transferred heat and prolong the duration of the stabilised heat delivery with its high latent heat storage capacity, which could significantly improve the electric output and mitigate the thermal fatigue by limiting the peak temperature of the PV cell when the solar irradiance is the richest. Many PV/T systems with PCM also worked with the addition of air or water or nanofluid cooling to further improve the thermal energy recovery (Gaur, Ménézo & Giroux--Julien, 2017; Al-Waeli *et al.*, 2017b).

The collectors may have a typical sheet-and-tube (flat plate parallel tubes type, or serpentine tube type, etc.) configuration (Zondag *et al.*, 2003; Touafek, Khelifa & Adouane, 2014), flat-box-type (Zondag *et al.*, 2003; Chow *et al.*, 2009a; Herrando *et al.*, 2018), or heat pipe (Zhao, 2008; Hussein, 2007; Ziapour & Khalili, 2016), etc. The design of unglazed or glazed (with different numbers of glazing covers) (Zondag *et al.*, 2003; Hassani *et al.*, 2016; Tiwari & Sodha, 2006; Chow *et al.*, 2009b) and different packing factor (Ziapour & Khalili, 2016; Chow *et al.*, 2009b; Daghigh *et al.*, 2011; Herrando, Markides & Hellgardt, 2014) have significant overall effect. The box-structure collector, built from extruded aluminium alley or made of polycarbonate material, has been reported to provide higher heat transfer and achieve higher final water-temperature and higher energy efficiency even in the thermosyphon design than the sheet-and-tube collectors (Zondag *et al.*, 2003; Chow, 2007; He *et al.*, 2006). Rosa-Clot *et al.* (2016) experimented a PV/T collector called TESPI, in which a thin layer of water flowing in a polycarbonate box that was simply put on the top of the PV panel. When three collectors were series-connected, the outlet water temperature reached up to 60 °C in an open loop in some September days as the ambient temperature at around 30 °C. The total loss of electric power comparing the PV/T collector with the reference PV panel was on average 10.7%.

The heat pipe combined PV/T design is one of the effective solutions to ensure the uniform temperature of the PV/T panel without the need of water pump and to avoid freezing in cold regions. It has been studied for application of building-integrated PV/T system (BIPV/T) (Wang *et al.*, 2016), or integrated within the building envelop (BIPV) (Jouhara *et al.*, 2016), but with modest electric efficiency (less than 10%) in most cases (Al-Waeli *et al.*, 2017c). The glazed type PV/T is the better choice than the unglazed one if the target is to acquire more thermal output and higher overall energy efficiency, but the addition of glass covers results in higher optical losses, leading to electric efficiency decrease (Tripanagnostopoulos *et al.*, 2002; Zondag *et al.*, 2003; Tiwari & Sodha, 2006; Chow *et al.*, 2009b). The packing factor is an important parameter in PV/T system design, and the effect of its variation on the PV/T performance strongly depends on different PV/T configuration with different coolant types.

Many works concluded that higher packing factors were desirable in order to maximize electrical output, but not a favourable factor for the thermal production; nevertheless, in the work by Ziapour & Khalili (2016), increasing packing factor caused higher PV panel temperature, leading to higher thermal efficiency but reversely the decreased electric efficiency; in the air-cooled collector system with double glass layer design reported in (Vats, Tomar &

Tiwari, 2012), the electric efficiency decreased with the increase of the packing factor, both the annual gain of electric output and thermal output was decreased. The double glass layer design significantly contributed to the higher PV panel temperature and considerable optical loss compared to unglazed or single glass cover, however, the increment of thermal production due to the higher PV module temperature may not offset the reduced heat gain attributed to the lower packing factor within the double glass cover design. Additionally, panels connection in series favours in thermal energy efficiency, whereas it reduces when panels are connected in parallel (Bahaidarah, Baloch & Gandhidasan, 2016).

Generally, a PV/T technology contains 7 components--namely cover layer, PV layer, adhesive layer, absorber layer, heat exchanger layer, thermal insulation layer and a back closure as illustrated in Fig. 2.4. Cover and airgap layers have the purpose of reducing thermal energy loss to the environment while maintaining maximum optical energy input to the technology. The front cover is normally made of tempered glass due to its high strength (Kang *et al.*, 2012) which is coated by the antireflective film such as SiO_2 to increase the transmittance property (Nostell, Roos & Karlsson, 1999; Hammarberg & Roos, 2003; Kesmez *et al.*, 2009). An air-gap layer, acting as a thermal insulator to prevent the conduction heat transfer between the PV cell and the front glass cover, can significantly reduce heat loss and achieve higher thermal efficiency and higher HTF temperature output if thermal energy output is required at a temperature higher than 50 ^{o}C, although electrical efficiency is slightly compromised compared to the no-air-gap PVT especially in cold weather regions (Thinsurat *et al.*, 2019). Otherwise, If electrical power generation is of priority, the front cover may be directly attached to the PV layer via the encapsulator as an adhesive material to allow quick heat dissipation of the PV cell to the ambient surroundings, leading to improved electrical conversion but compromised thermal efficiency (Othman *et al.*, 2013, 2016; Saygin *et al.*, 2017). Ethylene vinyl acetate (EVA), which has high thermal conductivity and high optical transmissivity properties (Czanderna & Pern, 1996), is very suitable for the glass encapsulation layer. There is another EVA layer between PV cells and the absorber layer for the purpose of protecting PV cells from moisture, electrical leakage and scratching from neighbouring layers (Kang *et al.*, 2012; Czanderna & Pern, 1996; Lee *et al.*, 2008; Jorgensen *et al.*, 2006).

PV layer is the layer that produces electrical energy which depends on types of PV cell with their efficiency and temperature which can be classified into several types based upon cover layer types, concentrator types, photovoltaic cell types, fluid flow types and heat exchangers as described in the previous section. Crystalline silicon (c-Si), one of the first-

generation PV material, is widely used as the semiconductor material in the PV layer for PV/T technologies. The electrical efficiency in this layer made from c-Si reduces when PV cell temperature rises about -0.04% per ^{o}C (Pathak, Pearce & Harrison, 2012).

According to Zondag *et al.* (2003), by comparing the efficiency of different PV/T cover layer types, an uncovered PV/T collector provides the highest electrical efficiency than others because of the direct exposure to the sun radiation but thermal efficiency is lower than other cover layer types due to thermal loss to the environment. By adding more cover layer called double cover layer, the electrical efficiency decreases with the thermal efficiency remains the same. In terms of total efficiency, single glass cover PV/T provides the highest efficiency as shown in Table 2.3. The layout of the HTF layer also affects the efficiency of the PV/T as presented in Table 2.4 when different heat pipe layouts are studied. According to Bahaidarah *et al.* (2016), the pattern of the HTF tubes presented in Fig. 2.4 is able to keep the average PV cells' efficiency high compared to the different layout of the tubes. Therefore, the layout of the tubes as presented in Fig. 2.4 is used in this thesis.

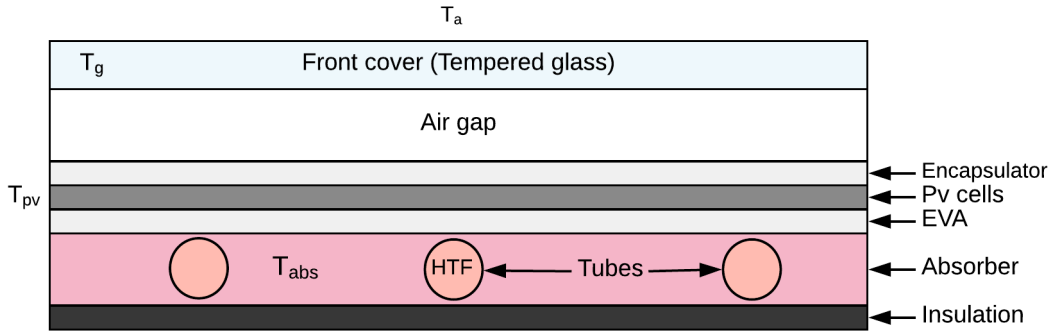

Fig. 2.4 *A classic cross-sectional flat-plate PV/T with its components* (Thinsurat *et al.*, 2019)

Table 2.3 *Efficiencies of each type of PV/T cover layer* (Zondag *et al.*, 2003)

PVT cover layer type	Electrical efficiency	Thermal efficiency	Total efficiency
PV cell	0.097	-	0.097
Uncovered PVT	0.097	0.52	0.617
Single-cover PVT	0.089	0.58	0.669
Double-cover PVT	0.081	0.58	0.661
Thermal collector	-	0.83	0.83

Table 2.4 *Solar PV/Thermal (PV/T) technologies when different heat pipe layouts are considered* (Zondag *et al.*, 2003)

Type	Efficiency (%)	
	Electrical	**Thermal**
• Channel above PV	8.4	65
• Channel underneath opaque PV	9.0	60
• Channel underneath transparent PV	9.0	63
• Free-flow PV/T collector	8.6	64
• Insulated two-absorber PV/T	8.5	66
• Non-insulated two absorber PV/T	8.4	65

Further down the line, the enhanced hybrid configuration combines an imaging or non-imaging optical concentrator with the PV/T collector as the concentrated photovoltaic thermal (CPVT) collector. A CPVT collector utilises concentrator optics to increase the intensity of the solar radiation and harvests higher-quality solar thermal energy (up to approximately 200 °C (Sharaf & Orhan, 2015; Daneshazarian *et al.*, 2018)) and more solar electrical output with a smaller area of solar PV cells compared to the most common flat-plate PV/T collectors. The high exergy contents in the extracted heat from the CPVT justifies more utilisation application, such as thermal-driven cooling [9], heat to power application like Kalina cycle (Zhang, He & Zhang, 2012), ORC cycle (Han *et al.*, 2017), thermochemical power generation system (Li & Hao, 2017), thermal-driven trigeneration through a two-stage liquid desiccant cycle (Su *et al.*, 2018), etc. However, the concentrating collectors are not suitable for the diffuse solar irradiation as a result of scattering by atmospheric particulates. For example, in the UK around 60% of annual global irradiation received on a horizontal surface is diffuse due to cloudy skies (Šúri *et al.*, 2007), for this instance, non-concentrating collectors can make use of the large proportion of diffuse sunlight and potentially convert more solar energy than the concentrating type (Freeman, Hellgardt & Markides, 2015), although with lower temperature thermal output. Additionally, the sheet-and-tube collector is the most common and a highly appropriate option for domestic application of water-based PV/T due to high efficiency (marginally lower than that of the flat-box design (Zondag *et al.*, 2003)), easiest and most affordable configuration to manufacture as it relies on well-known, readily available technology (Zondag *et al.*, 2003; Touafek, Khelifa & Adouane, 2014; Herrando, Markides & Hellgardt, 2014). In fact, by adjusting the flow rate of the cooling medium (e.g. airflow or water) with the outlet temperature feedback control, the quality of the thermal output of the PV/T collectors as well as its electrical efficiency is tuneable to meet the specific requirement of the downstream application, leading to expanding the spectrum of the application (Thinsurat *et al.*, 2019).

Depending on purposes of the downstream applications, components of the PV/T can be altered to provide the most efficient final energy outputs. If the electrical efficiency is

prioritised, thermal energy will be underperformed from its maximum potential by operating it at high HTF mass flow rate to keep the PV cells cool. One possibility to increase the total efficiency of the PV/T is to use the PV material that can maintain its efficiency at a higher temperature (low-temperature coefficient). Pathak *et al.* (2012) investigated that hydrogenated amorphous silicon (a-Si:H) can recover its full efficiency when working at a temperature higher than 50 ^{o}C although efficiency still decreases slightly about -0.01% per a degree centigrade due to the Staebler-Wronski effect (SWE) when the temperature is higher than 50 ^{o}C (Wronski *et al.*, 2004). Efficiency drops due to temperature rise is varied for these two types of PV materials according to different researches; for example, Kalogirou and Tripanagnostopoulos (2006) stated that monocrystalline and polycrystalline silicon will make the electrical efficiency decrease about 0.45% per degree centigrade and for the amorphous silicon, an electrical efficiency reduces by 0.25% per degree centigrade. If the thermal efficiency is prioritised, the PV/T should be operated to produce the HTF with sufficiently high temperatures for downstream applications to avoid additional heating systems and the output temperature should be maintain not too high as both electrical and thermal efficiencies decrease with higher temperatures (Lämmle *et al.*, 2017).

In summary, the PV/T technology can be categorised as presented in Fig. 2.5 with the detail configurations and performances shown in Table 2.5. Although extensive researches have been done on the PV/T technologies, there are still research gaps and the remaining questions or unexplored areas to be addressed further. For example, as the PV/T is a highly appropriate option for domestic applications due to the suitable temperature range that it produces, commercially availability, ease of installation on a household rooftop due to its simple configuration and the flexibility to generate both electrical and thermal energy simultaneously resulting in a high total efficiency (Nasrin, Hasanuzzaman & Rahim, 2018; Lämmle *et al.*, 2017), the majority of works on flat-plate water-based PV/T focused on low-temperature application (<60 °C), such as space heating (air heating or radiant floor heating, <40 °C) and domestic hot water use (40~60 °C) in the context of warm or hot regions with the ambient temperatures in the range of 30~37 °C, which could be problematic yet rarely explored for cold regions with lower solar irradiance and lower ambient temperature. Even for a hot climate, there is scarce information on medium temperature application (>60 °C). Considering harnessing the recovered heat for downstream applications, the quality and quantity of thermal production are both important to meet the operating requirement of the downstream applications.

For commercial PV/T products, Solar Keymark is the organisation to which widely referred for products testing, inspection and certification in Europe (Solar Keymark, 2019). The European Solar Thermal Industry Federation (ESTIF) and CEN (European Committee for Standardisation) are the first two organisations who started the Solar Keymark scheme with the help from European Commission. As the Solar Keymark is the major quality label for solar thermal products including the PV/T, it is widely used to ensure that thermal products meet the European standards and other additional requirements (Fischer & Drück, 2014; Drück, Fischer & Müller-Steinhagen, 2007). With the help of Solar Keymark, PV/T technologies may be widely used in the future as if it is recognised by well-known engineering organisations with engineering standards. To obtain the Solar Keymark Certification, a new product have to be compliance with the EN 12975 and the ISO test standards. The PV/T which its PV panel previously certified may also have to be tested with the IEC standard in addition to the thermal tests again in order to obtain the full scheme Solar Keymark certificate. With the existence of the international standard of the thermal products, the PV/T technology is becoming a promising technology for domestic applications.

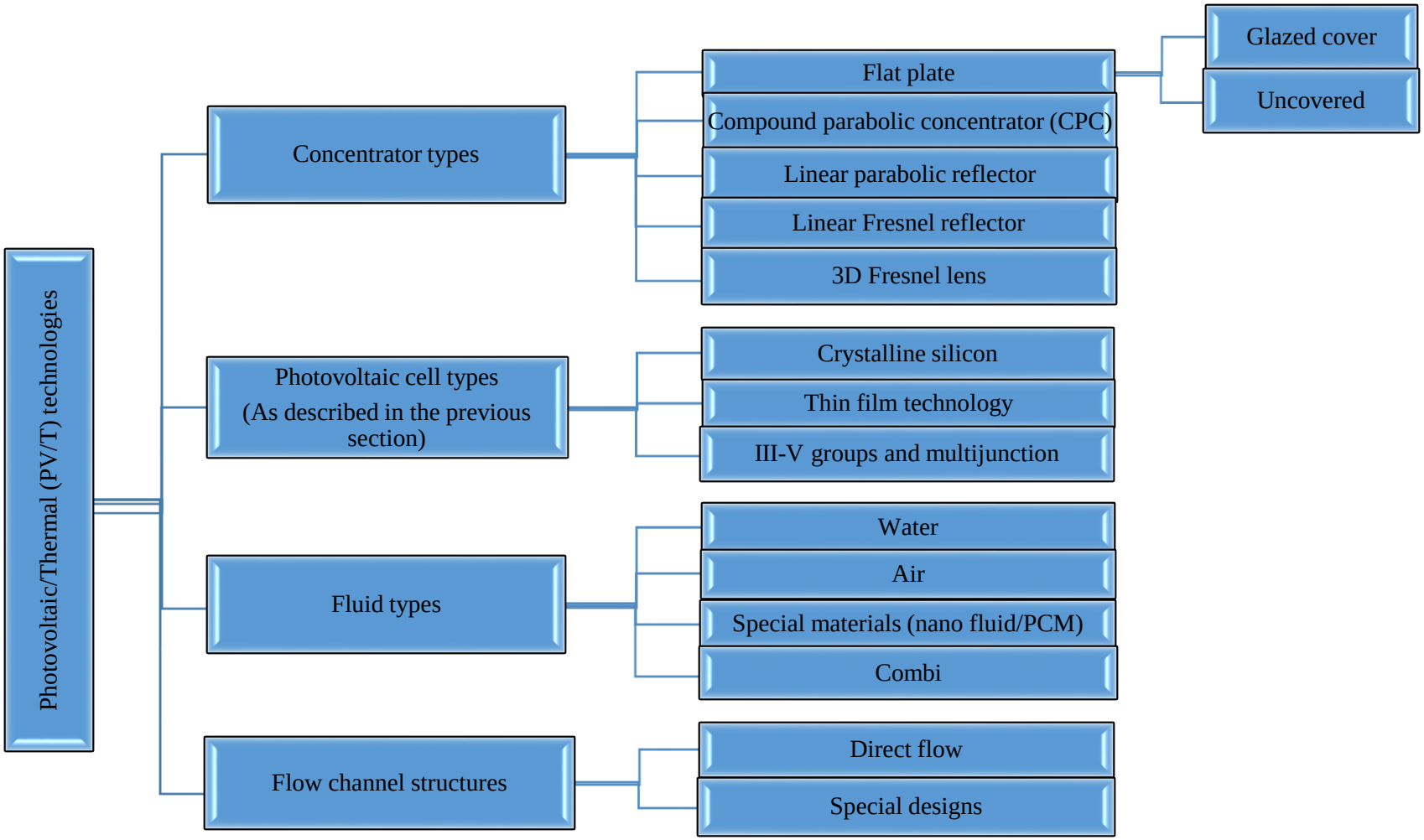

Fig. 2.5 *Photovoltaic/Thermal (PV/T) classification*

Table 2.5 *The comparison between different types of PV/T technology*

Reference	Cover layer/ concentrators	PV cell	Adhesive /absorber	Fluid type	flow structure	Efficiencies			Note
						Thermal	Electrical	Total	
Pathak et al. (2012)	-	(a-Si:H)	-	-	-	-	-	-	- 10.6% electrical energy gain from annealing process to 100 ^oC for 1 hr then use with temperature higher than 50 ^oC - Can be used in PVT to optimize thermal efficiency with high temperature
Xu and Kleinstreuer (2014)				Nano fluid (xxx)		0.59	0.11	0.7	- Additionally, cogeneration is applied
Touafek et al. (2013)	Flat plate with tempered glass	Single-crystal (UDTS50)	EVA and Tedlar/ Galvanized steel	air	Direct channel	0.48	NA	-	- Numerical simulation using Runge-Kutta 4th order method (Only time dependence) - Glass wool insulation - 0.022 kg/s airflow through 3.25cm gap - Outlet air temp can reach 60 ^oC with 35 ^oC inlet
Da Silva and Fernandes (2010)	Flat plate with glass cover and air gap	m-Si	-	Water	Direct tube	0.52-0.19	0.15-0.13	0.67-0.32	- simulation results with experimental validation - No mass flow rate, inlet and outlet temperatures provided
		p-Si				0.57-0.23	0.10-0.08	0.67-0.31	
		a-Si				0.61-0.27	0.06-0.05	0.67-0.32	
Aste et al. (2015)	Flat plate with glass cover and air gap	Multi [a-Si&µc-Si]	-/ Aluminum	Water	Direct multi-channel	0.258	0.06	0.318	- Efficiencies are from experiments data (daily average) with max irradiance of about 700 W/m^2 - Mass flow rate is set to be 0.066 kg/s

Reference	Cover layer/ concentrators	PV cell	Adhesive /absorber	Fluid type	flow structure	Efficiencies			Note
						Thermal	Electrical	Total	
									- Temp raise about 1-2 ^oC from input to output
Tripathi et al. (2016)	CPC (Partially covered)	Transparent (material is not mentioned)	Not mentioned	Water	Direct tube	xxx	0.15	xxx	- Theoretical calculation using MATLAB - Series connection of 6 PVT-CPC - Temp range from ≈ 25 (1 PV) to 95 ^oC (6 PV) - Irradiance from ≈ 200 to 850 W/m^2 - Mass flow rates are from 0.002 – 0.012 kg/s
Al Imam et al.(2016)	CPC with a glass cover and air gap	Not mentioned	Material type is not mentioned with the PCM layer and fins attached	Water	Direct tube	0.4-0.5 (clear sky) ---------- 0.4 (cloudy sky)	-	0.55-0.63 (clear sky) --------- 0.46-0.55 (cloudy sky)	- PCM properties : melting point 56 ^oC Latent heat of fusion 256 kJ/kg - Water flow rate is 0.2 kg/s - Max concentration ratio : 1.82 - heat loss : 3.5-4.5 W/m^2

a-Si = Amorphous silicon (work best in the visible solar spectrum)

a-Si:H = Hydrogenated amorphous silicon

µc-Si = Microcrystalline silicon (work best in the near-infrared spectrum)

CPC = Compound parabolic concentrator

PCM = Phase change material

2.2 Energy storage review

Energy storage has been intensively studied because of its significant role to improve the power grid qualities and energy security especially when renewable energy resources are integrated (Ould Amrouche *et al.*, 2016; Ibrahim, Ilinca & Perron, 2008; Guney & Tepe, 2017; Lund *et al.*, 2015; Soloveichik, 2014). Solar energy, the resource focused in this thesis, is one of the potential resources to promote renewable energy in the energy system which requires energy storages to fulfil the disadvantage of its intermittent property. There are several alternatives of an energy storage type to be integrated with the solar energy production which can be classified by the types of stored/released energy such as chemical, electrochemical, electrical, mechanical and thermal energy storages (Guney & Tepe, 2017) and each type has its advantages and disadvantages for specific applications (Luo *et al.*, 2015).

2.2.1 Chemical energy storage

Chemical energy storage stores energy in the form of chemical bonds between atoms or molecules. Chemical energy can be utilised through the exothermic chemical reaction from chemical fuels such as hydrogen and synthesis hydrocarbons which transformed into thermal energy or further converted into mechanical energy by heat engines then converted to electricity by the generator if demanded. Among all of the chemical fuels, hydrogen is the most researched one in the field because of its abundant substrate, environmental friendliness, ease of transportation and high energy density (Gargoom *et al.*, 2010; Escobar *et al.*, 2013; Ali, 2011; Chen *et al.*, 2015). The most common way for the hydrogen production is through the electrolysis process of water by using electrical energy and stored in the form of pressurised gas, metal hydride, cryogenic-liquid storage, etc. (Eberle, Felderhoff & Schüth, 2009). For the energy-releasing process, proton-exchange membrane fuel cell is one of the promising technologies for hydrogen power generation (Peighambardoust, Rowshanzamir & Amjadi, 2010) or combined heat and power applications (Dodds *et al.*, 2015a). Despite the potential of using hydrogen for large scales energy storage according to the mentions advantages, the high cost of each component involved in its storage system obstructs the possibility for a domestic household's applications (Dodds *et al.*, 2015b).

2.2.2 Electrochemical energy storage

Electrochemical energy storage consists mainly of two electrodes and electrolyte, store energy via electrochemical reactions in various types of battery either conventional batteries

such as Nickel-cadmium (NiCd), Lead-acid, Lithium-ion (Li-ion), sodium-sulfur (NaS) batteries, etc., or flow battery such as vanadium redox flow batteries (Doetsch & Burfeind, 2016) which provides many advantages over the conventional ones such as higher energy density, wider operational temperature, simpler design for large storage sites, long life cycle, low maintenance cost, etc. (Yang *et al.*, 2011; Ould Amrouche *et al.*, 2016). Although the electrochemical energy storage is matured and widely used in many applications due to its power density, the self-discharge rate makes it works best for short-term duration ranges from minutes to days (Luo *et al.*, 2015).

2.2.3 Electrical energy storage

Electrical energy storages normally store electricity in supercapacitors or superconducting magnetic energy storage (Luo *et al.*, 2015). Supercapacitors consist mainly of two conductive metal sheets electrically insulated and electrodes. Energy is stored by keeping electric charges (electron) in one side generating an electric field between two metal sheets. Energy can be released by simply connecting loads between the two electrodes which make supercapacitors the very high power rating storage suitable for electrical grid regulating; however, its low energy density property is the drawback of using the supercapacitors for long-term storages (Converse, 2012; González *et al.*, 2016). Because of its high power rating, the electrodes are an important part of this technology to maximise the efficiency, increase its energy density and improve its lifetime and safety (Liu *et al.*, 2010a). The most used material is the carbon-based material (Zhang & Zhao, 2009) such as graphene (Liu *et al.*, 2010b), carbon nanotubes (Avasthi & Balakrishnan, 2019), activated carbon (Jänes, Kurig & Lust, 2007), etc.

2.2.4 Mechanical energy storage

Mechanical energy can be stored in several forms. Pumped hydro energy storage (PHES) uses electrical energy to pump working fluid, normally water, to higher altitude reservoir which stored surplus electrical energy in the form of potential energy and use it to reproduce electrical energy when demanded by using the water turbine and generator. Although the PHES is a mature technology and is widely used for electrical peak power shaving in large scale power plants (Akinyele & Rayudu, 2014), it has a very low energy density property which is not suitable for domestic household energy storages nor for long-term storages (Luo *et al.*, 2015). Compressed air energy storage (CAES) is one of the mechanical energy storages which uses off-peak electricity to compress the air into reservoirs such as underground hard rock cavern, salt cavern or depleted gas field (Mahlia *et al.*, 2014). The stored mechanical energy in the form

of high-pressure air is released to the preheat burner with minimal fuel consumption, before input into the turbine connected with the generator to produce electrical power when needed. Similar to the PHES, its low energy density is the barrier to use the CAES for seasonal energy storages or domestic energy storage. Flywheels Energy storage is another mechanical storage type that stored energy in the form of rotating inertia. Despite its advantages such as low maintenance cost, long life cycle, environmentally friendly, etc., its energy loss is significant which is also not feasible for long-term energy storage (Bolund, Bernhoff & Leijon, 2007).

2.2.5 Thermal energy storage

Thermal energy storage stores energy in three different ways which are sensible heat, latent heat, and thermochemical heat storages as illustrated in Fig. 2.6. Thermal energy shares the highest amount of energy usage in non-transport sectors, including residential sector which is focused in this thesis; therefore, it is of the most interesting type of energy storages to be reviewed. Moreover, when the energy source comes from the solar conversion technologies which produce high thermal conversion efficiency, meaning that storing thermal energy is the most efficient way as conversion efficiency from the primary resource is high along with the high domestic thermal energy demand which makes the thermal energy storage the most direct way without extra conversion loss from other energy storage forms.

(a) Sensible heat storage

Sensible heat storage stores thermal energy in the form of internal energy by temperature rising; therefore, the amount of energy stored depends solely on the specific heat of chosen materials as presented in Eq. (2.1).

$$Q = mC_p\Delta T \quad (2.1)$$

where Q is thermal energy stored (J)

m is the mass of the material used to store energy (kg)

C_p is the specific heat of the material used to store energy (J/kg·K)

ΔT is temperature difference (K)

Sensible heat storages usually work in temperatures ranging from 40 to 80 ^{o}C in space heating and domestic water heating applications and materials generally used to store thermal energy are water, rock-sort materials (for example gravel, pebbles, and bricks) and soil or ground (Xu, Wang & Li, 2014). Sensible heat storage is suitable for short-term energy storages (hours to days) and water is the most used material due to its availability, high heat capacity,

and no additional heat exchanger requirement. Other than water, there are some frequently used materials for sensible heat storages shown in Fig. 2.7 (Fernandez *et al.*, 2010).

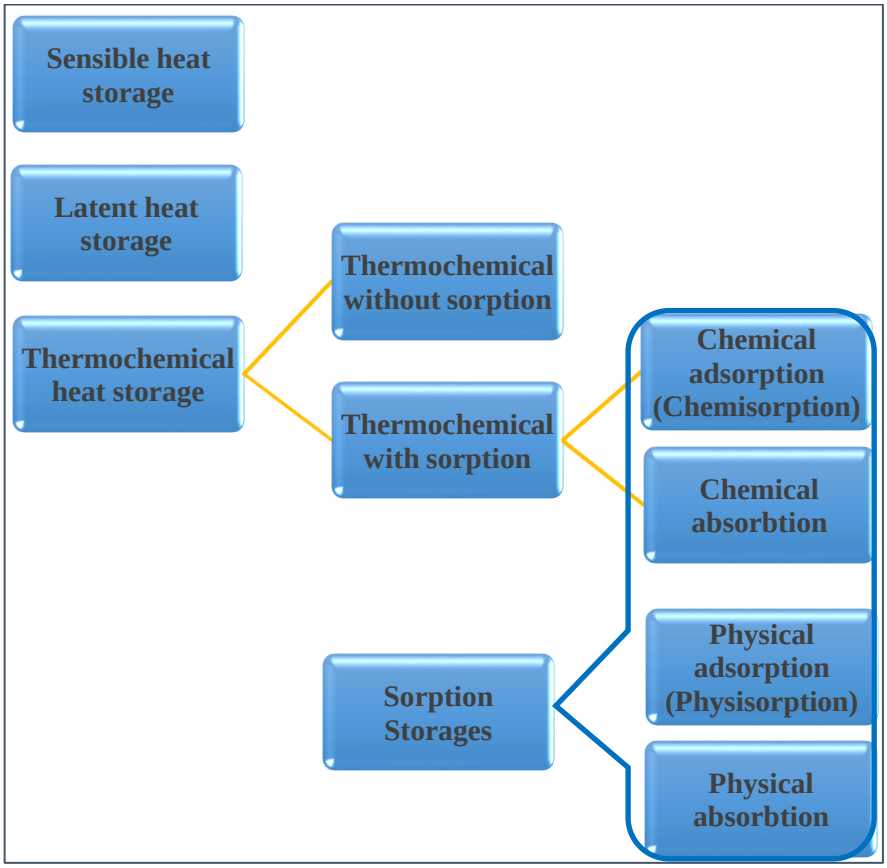

Fig. 2.6 *Thermal energy storage technology classification*

Although sensible heat storage is widely used currently, the most disadvantage of its applications is its systems' size. Sensible heat storage requires a large volume to store thermal energy compared to other types when seasonal storage is required.

(b) Latent heat storage

Latent heat storage stores thermal energy in phase change materials (PCMs) during the isothermal process of phase transition of materials which can be solid-solid (transition of crystalline structures), solid-liquid, solid-gas, and liquid-gas. Although there are four types of phase transition, solid-liquid is the most practical one due to its low volume and pressure requirements compared to liquid-gas and acceptable heat transfer rates compared to solid-solid phase transition (Mishra, Shukla & Sharma, 2015). Thermal energy stored in phase change materials as latent heat can be calculated from Eq. (2.2). There are major PCMs widely used shown in Table 2.6 with their properties.

$$Q = mL \quad (2.2)$$

where Q is the thermal energy stored (J)

m is the mass of the material used to store energy (kg)

L is the specific latent heat of fusion or vaporization (J/kg)

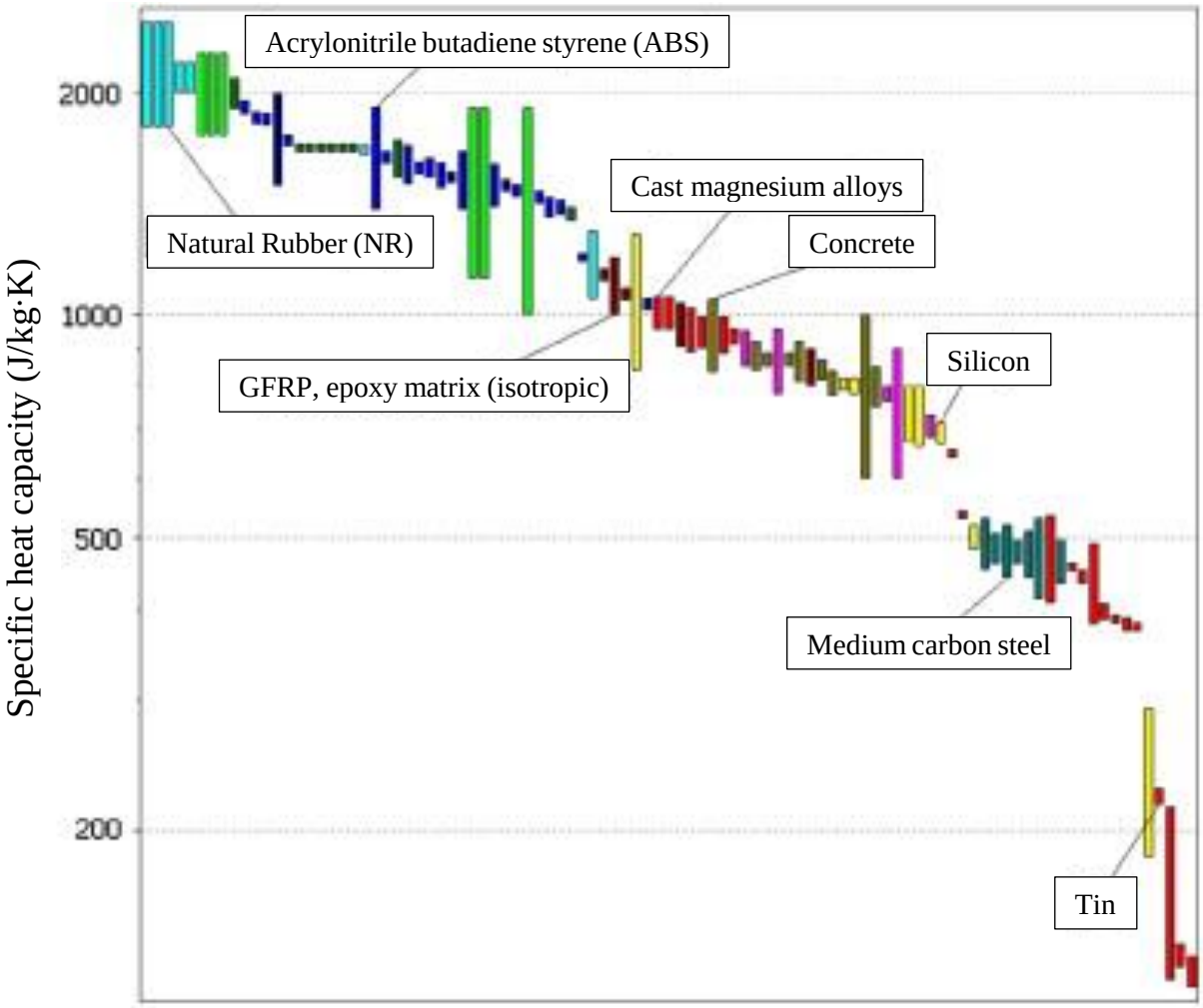

Fig. 2.7 *Frequently used material for sensible heat storage systems obtained with CES Selector* (Fernandez *et al.*, 2010)

Table 2.6 *Commercial PCMs and their properties* (Mishra, Shukla & Sharma, 2015)

Materials	**Melting Point (^{o}C)**	**Heat of Fusion (kJ/kg)**	**Specific Heat C_p for solid phase (kJ/(kg·K))**	**Conductivity, K (W/(m·K))**	**Application**
Water	0	333.6	2.05	1.6-2.2	Several types of application

Materials	Melting Point (^{o}C)	Heat of Fusion (kJ/kg)	Specific Heat C_p for solid phase (kJ/(kg·K))	Conductivity, K (W/(m·K))	Application
$CaCl_2 \cdot 6H_2O$	26-29	190.8	1.088	NA	Greenhouse
Acetamide	82	263	1.94	0.5	Solar cooker
N-octadecane	27	243.5	1.934	0.148-0.358	Building
Sodium acetate trihydrate	56.7	199	3.18	0.41-0.65	Thermotherapy
N-eicosane	36.5	247	2.46	0.1505	Cooling mobile phones, Textiles, Building
Stearic-myristic acid (80%-20%)	61-65	190.9	NA	NA	Solar water heating systems
Climsel C28 (Salt Hydrate)	28	126	NA	0.5-0.7	Cooling helmet
$0.9CH_3CONH_2 + 0.1Ca(NO_3)2.4H_2O$	27.7	141	2.51	NA	Agricultural greenhouse

(c) Thermochemical heat storage

The thermochemical energy storage may also be considered in the group of chemical energy storage because it stores energy in the form of covalence bond. However, as the thermal energy is normally the input and output of this kind of technology, it is sometimes classified as the thermal storage.

Among three different ways of storing thermal energy, thermochemical heat storage is the most favourable seasonal heat storage technology because of its high energy density leads to low storage volume and minimal heat loss for a long storing time. Thermochemical heat storage can be categorized into two types which are thermochemical without sorption or chemical reaction storage and thermochemical with sorption or chemical sorption storage (Yan *et al.*, 2015). Chemical sorption storage can be classified into chemical adsorption (chemisorption) and chemical absorption, differ from the other two types of sorption storages which are physical adsorption (physisorption such as silica gel/ H_2O and Zeolite/ H_2O) and physical absorption (such as LiBr/H_2O and H_2O /ammonia) as shown in Fig. 2.6. Sorption heat pump technology

has attracted increasing attention in recent decades because of its benign impact on the environment and its capability of effectively utilising low-grade heat, i.e. industrial waste and renewable thermal energy. It appears as one promising alternative of the mainstream, conventional technology--vapour compression heat pump system. Sorption energy storage system especially based on solid-gas thermochemical sorption process is recognised as a much preferable method of thermal storage because of its important merits: the superiority over other methods in terms of high energy density and negligible energy loss over long-term storage (Yu, Wang & Wang, 2013; Pinel *et al.*, 2011; Li *et al.*, 2016).

Chemical adsorption (chemisorption) is the action of binding one or more molecules of so-called adsorbate to the surface layer of material called adsorbent. The binding action stores energy in the form of covalent force which occurs above a certain temperature level depending on specific material pairs. Physical adsorption (physisorption) happens because of the intermolecular force called Van der Waals that bind adsorbates with adsorbents which thermal energy can be stored less than the amount from chemical adsorption storage although it does not need certain temperature levels which leads to higher adsorption rate. According to Yu *et al.* (2008), chemisorption has more advantages from physisorption, chemical absorption, and physical absorption; for example, there is no solution corrosion effect, the technology contains simple components, the material working pairs have higher energy storage density, and it can be applied to various ranges of temperature with high stability. Therefore, chemisorption or chemical adsorption technology is the most promising long-term energy storage systems among other sorption storage technologies. The chemical adsorption process can be described by Eq. (2.3).

$$A \cdot (x + y)B + Heat = A \cdot xB + yB \quad (2.3)$$

where A is the adsorbent

B is the adsorbate

x and y are the numbers of sorbate molecule

A/B can be called as an adsorption working pair

Thermochemical sorption system can be classified into several kinds according to material pair used in the storage systems as shown in Fig. 2.8; however, according to Yu *et al.* (2013), two groups are commonly used due to its environmental friendly properties which are coordination reaction of ammoniate with ammonia (number 1, 2, 3, and 4 in Fig. 2.8) and hydration reaction of salt hydrate with water (number 7 in Fig. 2.8). The properties of

coordination reaction of ammoniate working pairs which are NH_3 molecules at adsorbed/desorbed states, reaction enthalpy and entropy, molar mass, a rough value of driving temperature and energy density are shown in Table 2.7. Those properties are useful for analysing thermodynamic cycles for determining the suitable working pairs which are suit the target area with the specific weather condition and heat inputs. Most of the coordination reaction of ammoniates with ammonia have considerably higher energy density than the hydration reaction of salt hydrates with water (Yu, Wang & Wang, 2013) resulting in the coordination reaction of ammoniates with ammonia are more interesting to be used as long-term thermal energy storage.

However, in order to provide high-temperature adsorption heat as the energy discharging in chemisorption system, it usually requires comparatively higher temperature heat input for the endothermic desorption in the energy charging process, no lower than 90 °C (Ma, Bao & Roskilly, 2018, 2019) for ammonia-based chemisorption cycles. The emerging concept of hybrid thermochemical sorption cycle that combines chemisorption reactors with a compressor (or called compressor-assisted thermochemical sorption cycle) can realise the recovery of ultra-low and low grade heat, at the same time store both electric and thermal energy for later use of heating (van der Pal *et al.*, 2013; Bao, Ma & Roskilly, 2016), cooling and electrical power (Bao, Ma & Roskilly, 2016). Because the involvement of a compressor provides the thermochemical sorption system with additional degrees of freedom, enabling flexible desorption process by balancing between thermal and electric energy input. An electrical compressor can assist the pressurising process with an electrical input, that compensates for heat input at a low temperature when the desorption temperature is actually required relatively higher. This feature not just enables effective use of low-temperature heat output from the flat-plate PV/T collector but also enhances the heat pump performance in cold winter with additional electricity input when necessary.

More interestingly, as it is well known that the solar PV/T collector has trade-off between high temperature thermal and electric energy, actually either scenario of the trade-off all perfectly matches with the energy input requirement of the hybrid thermochemical sorption cycle, low temperature heat input plus more electricity input, or high temperature heat input plus less electricity input. Additionally, it also provides a better solution of disposing of the excess electricity instead of feeding into the grid, which may, in turn, lead to the grid instability issues due to the limited accommodation of the grid (Eltawil & Zhao, 2010). This is a significant capability to cope with the highly variable renewable resources, ultimately substantially

increasing the integration of renewable resources in the energy mix and contribute to decarbonisation of heat.

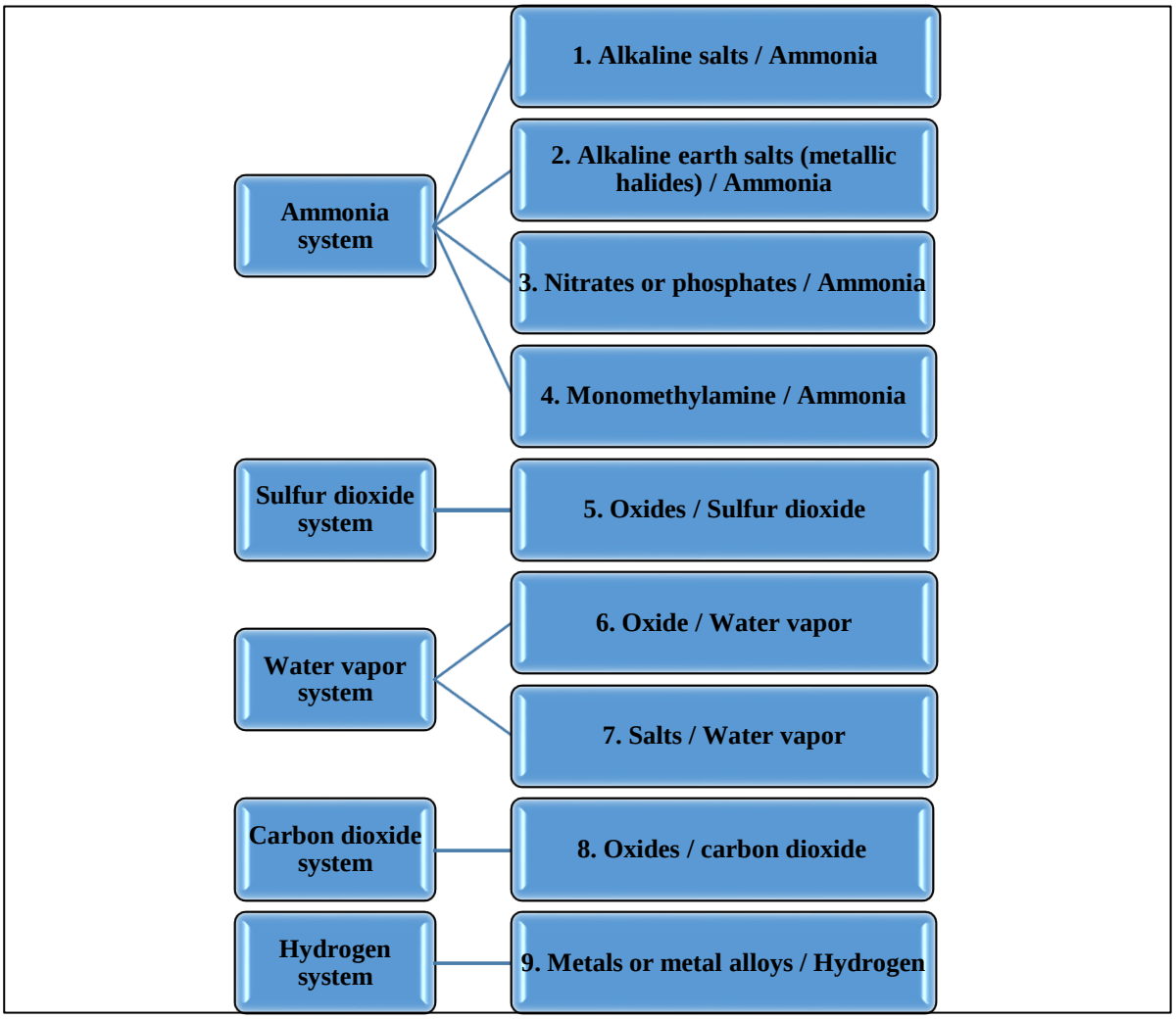

Fig. 2.8 *Classification of the thermochemical sorption heat storage*

There are rare studies so far on the hybrid vapour compression-thermochemical sorption cycle, either sorption-assisted vapour compression cycle or compressor-assisted sorption cycle. Ferrucci *et al.* (2018) studied on a hybrid air-conditioning system that mainly operated the mechanical vapour compression unit for providing continuous cooling power and a standby $BaCl_2/NH_3$ thermochemical sorption storage unit. Van der Pal *et al.* (2013) evaluated a hybrid heat pump system consisting of low-temperature sorbent reactor, high-temperature sorbent reactor (as a resorption cycle (Bao *et al.*, 2010)) and a compressor. Van der Pal *et al.*'s study proves the technical feasibility of the hybrid system effectively reducing the minimum temperature of the recoverable waste heat and also increase the upgraded heat temperature. Bao *et al.* (2016) proposed and investigated an integrated system combining compressor and expander with thermochemical resorption processes, which enables the efficient recovery and

storage of low-grade heat source from 30 °C to 100 °C and could achieve temperature lift by 10 °C to 80 °C for heat transformation depending on reactant salts used, the round-trip efficiency for electric energy storage could reach 100% and even higher when the heat source temperature was higher than 50 °C.

Table 2.7 *Properties of thermochemical sorption working pairs at various working temperatures (Li, Wang & Kiplagat, 2013)*

Reactive salt	**NH_3 molecules (adsorbed/desorbed states)**	**Reaction enthalpy ΔH (J/mol)**	**Reaction entropy ΔS $(J/mol \cdot K)$**	**Molar mass (g/mol)**	**Driving equilibrium temperature (^oC)**	**Energy density (kJ/kg)**
NH_4Cl	3/0	29,433	207.9	53.4	48	1654
$PbCl_2$	8/3.25	34,317	223.6	278	47	586
$NaBr$	5.25/0	35,363	225.2	102.9	51	1804
$BaCl_2$	8/0	38,250	232.4	208.2	56	1470
$LiCl$	4/3	36,828	224.6	42.3	67	871
$CaCl_2$	8/4	41,013	230.1	110.8	87	1481
NaI	4.5/0	39,339	224.5	149.9	90	1181
$BaBr_2$	8/4	41,850	229.8	297.1	95	563
$SrCl_2$	8/1	41,432	228.6	158.4	96	1831
$CaCl_2$	4/2	42,269	229.7	110.8	99	763
$SrBr_2$	8/2	45,617	229.3	247.4	130	1106
$MnCl_2$	6/2	47,416	227.9	125.7	152	1509
$CaBr_2$	6/2	48,965	230.4	199.8	156	980
$FeCl_2$	6/2	51,266	227.8	126.6	186	1620
$MnBr_2$	6/2	53,066	228.3	214.7	200	989
$CoCl_2$	6/2	53,987	227.9	94.3	210	2290
$MgCl_2$	6/2	55,661	230.4	95.1	214	2341
$FeBr_2$	6/2	55,828	228.1	215.6	226	1036
CaI_2	6/2	58,590	231.0	293.8	237	798
$CoBr_2$	6/2	58,590	227.5	218.7	253	1072
$NiCl_2$	6/2	59,218	227.6	129.5	259	1829
MnI_2	6/2	59,301	227.4	308.7	260	768
FeI_2	6/2	60,683	227.5	309.6	272	784
$MgBr_2$	6/2	63,612	230.2	184.1	285	1382
$NiBr_2$	6/2	64,240	227.2	218.5	306	1176
NiI_2	6/2	65,453	224.1	312.5	334	838

2.3 Integration of solar energy conversion technologies with energy storages

Because of the intermittence nature of solar irradiance along a day associated with weather conditions and also the variation of the solar intensity and sunlight hour along a year depending on the angle of incidence between the sun and a location surface causing by the orbiting nature of the earth around the sun, solar energy is not reliable to supply energy demands without additional storage technologies (Yu, Wang & Wang, 2013). Considering a typical UK class 1 domestic household in a daily basis, the average daily electricity load profile, as illustrated in Fig. 2.9, indicates that the electrical power demand is at its peak during 17:00 to 21:00 while the sun can provide the maximum irradiance around noon. Therefore, daily electricity demand and supply is mismatched. Moreover, according to the seasonal variation of the electrical demand (as shown in Fig. 2.10), the peak demands occur during winters when

solar energy is at its lowest point. In summer, when solar energy is at its highest potential, the demand is at its lowest. Thus, the daily and seasonal discrepancy between the electricity demand and the solar energy supply is the most significant complication to sustainably supply electricity by using the solar energy source.

Typically, heating systems in the UK use a single gas-central boiler to heat water and pump it to radiators and hot water taps (energysavingtrust.org.uk, 2018) and the heating demand can be represented by the gas consumption statistics which has the seasonal variation which also mismatches between the demands and solar energy supply (Anon, 2018; J.P. Zimmermann *et al.*, 2012). There is a promising solution that this thesis is going to address which is to integrate the solar PV/T which can produce both electrical and thermal energies with long-term energy storages to increase the solar fraction of domestic heating to tackle the heat stress in the UK. The feasible results of providing a high solar fraction of the heating demands in high latitude region households are expected and believed that the proposed solution will motivate people to focus on the detailed study of the integrated system to be commercialised and widely used in the future.

Dubey and Tiwari (2009) numerically studied the energy yield by 2~10 flat-plate water-based PV/T collectors (the packing factor 0.0825) connected in series under the Indian weather conditions. When the solar intensity was 600~850 W/m^2 and the ambient temperature 30~37 °C, 10 series-connected collectors produced hot water at outlet temperature max. 85 °C at a constant flow rate 0.04kg/s with the electrical efficiency of 8.7%~10.5%. In the case of coupling with a water storage tank (200 L) and the flow rate was fixed at 0.01 kg/s, the maximum temperature was achieved around 95 °C.

Huide *et al.* (2017) performed simulations on PV, PV/T and thermal collectors with experiment validations to see the annual performances of each collector integrated with daily hot water storage (120L) for residential households in four cities in China. The results showed that PV/T supplies the most useful equivalent thermal energy for all four cities. However, the authors suggested that in a rural area where the installation area is abundant, PV/T may produce oversupplied thermal energy; therefore, installing part of the area with the PV and the rest is for thermal collectors may be more suitable. Ibrahim *et al.* (2014) studied a PV panel combined with rectangular-tube spiral flow absorber to produce hot water in a storage tank up to 50 °C in the Malaysian tropical climate (ambient temperature around 35 °C). Because of the increasing temperature of inlet water in a closed water loop, thermal and electrical efficiencies were decreasing throughout the day and the average values were 48% and 10.8%, respectively.

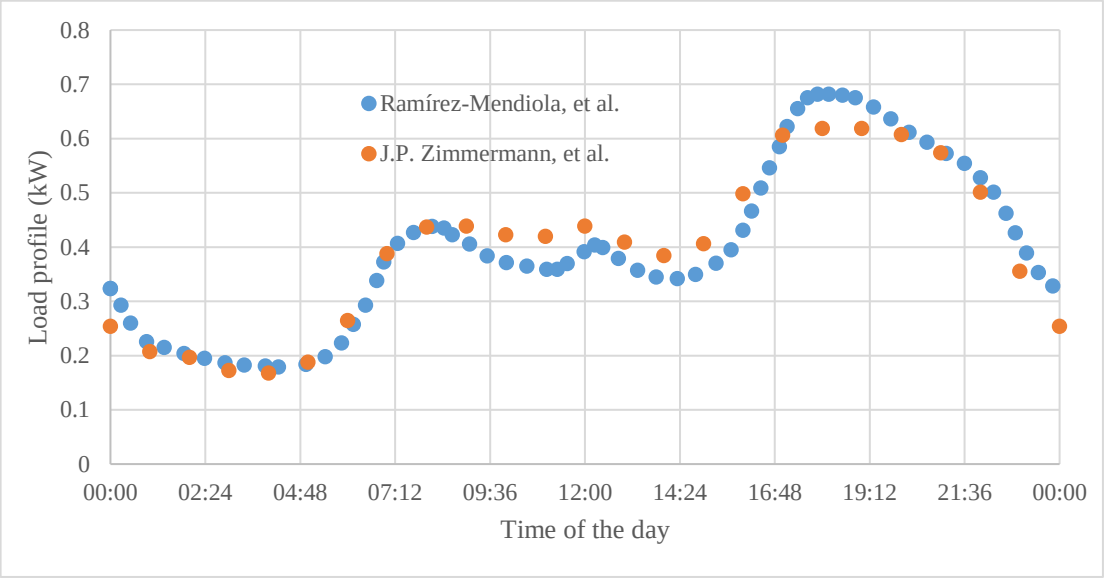

Fig. 2.9 *The average electrical load profile of class 1 (non-restricted domestic tariff) UK household* (J.P. Zimmermann *et al.*, 2012; Ramírez-Mendiola, Grünewald & Eyre, 2017)

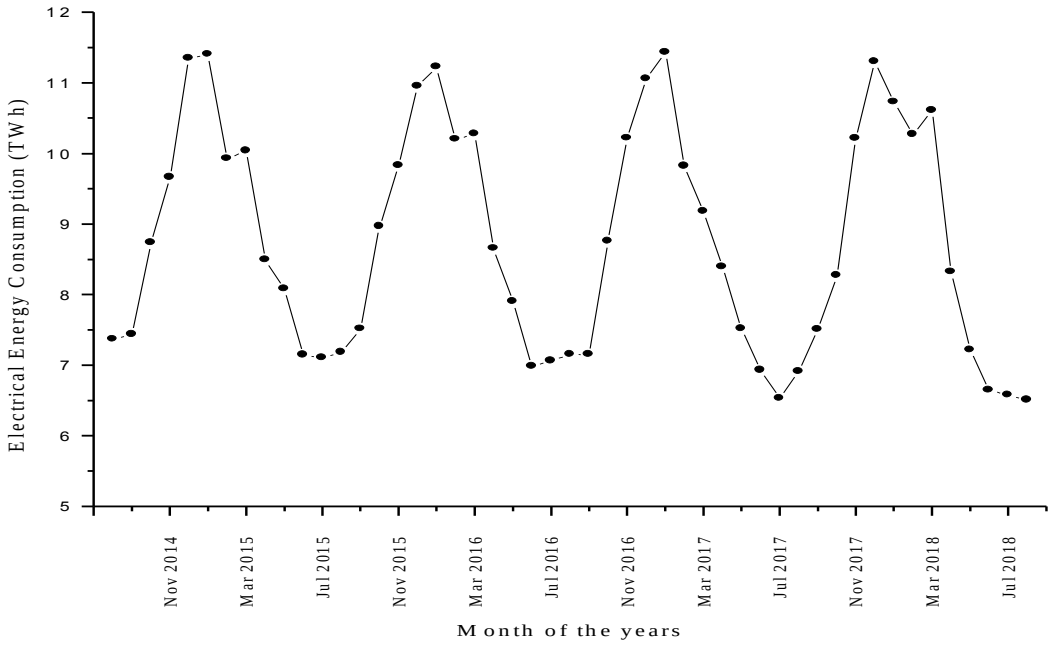

Fig. 2.10 *The seasonal electrical energy consumption in a typical UK household* (J.P. Zimmermann *et al.*, 2012)

Herrando *et al.* assessed the suitability of a single-cover sheet-and-tube PV/T system (Herrando, Markides & Hellgardt, 2014) and a polymeric flat-box PV/T system (Herrando *et al.*, 2018) for the provision of electricity and hot water for a typical house in London (low solar irradiance and low ambient temperature). The packing factor of the solar collector and the collector flow rate were specifically considered to estimate the performance of the PV/T system, and it was concluded that the coolant flow rate did not strongly influence the electrical output

but affected the hot water output, while the packing factor affected the electrical output considerably more than it did the thermal equivalent. It is worth noting that although using higher coolant flow rate increases thermal efficiency, the outlet temperature of the coolant is lower, therefore requiring greater use of an auxiliary heater to further heat it to 60 °C for the domestic hot water use. Since it is not possible to maximise both outputs at the same time, a trade-off is needed depending on the end-user needs. It was suggested a high packing factor (0.8~1) and low coolant flow rate as being appropriate in terms of adequately covering both the electrical and thermal demands.

Herrando, Markides & Hellgardt (2014) showed that a 15m^2 sheet-and-tube PV/T system, studied with a completely covered collector and a flow rate of 20L/h, can cover 51% of the total electricity demand and 36% of the total hot water demand over a year. Herrando *et al.* (2018) presented that 11 flat-box PVT collectors together with a 0.83 m^3 storage tank and a constant flow-rate of 30 L/h can cover 66% of the electrical and 29% of the thermal energy demands annually. Hazami *et al.* (2017) studied the monthly and annually performance of the SCS (Solar CombiSystem with water storage tank) with a unit module area of 1.42 m^2 for the space heating load (floor heating at around 24 °C) and domestic hot water supply (at 60 °C) and the electric energy production for a 120 m^2 building occupied by 4-5 occupants. There was a shortage of thermal energy production in cold months from November to March, during which the SCS provided from 40 to 70% of the total domestic hot water needs, whereas the SCS provided about 150% of the total energy needs in hot months. Such a system allows the preservation of about 48% of electric energy supplied by the national grid or permits the saving of about 46% of gas/gas town consumed by a gas boiler of water heating.

To further achieve a net/near-zero energy status for existing houses, beside the seasonal storage system, the district heating system was suggested to improve the quality of the energy system such as its sustainability, security, carbon abatement and costs (Pardo García *et al.*, 2017). García *et al.* (2017) showed the benefits of connecting the PV/T system with a low-temperature district heating network in three different configurations for a Central European multi-family house which could improve the overall efficiency. PVT systems provide one more solution towards low carbon and eventually zero-carbon buildings, for example, the PVT system the hybrid configuration studied produced 34% of the heat and 55% of the electricity demand of the building, which reduced its carbon footprint by roughly 50%. In terms of energy efficiency and profitability, the key was to effectively manage the excessive heat production of the PV/T system that cannot be exploited in the building, either through reliable seasonable

thermal energy storage with minimum energy loss or feeding into the district heating network. The accessibility to a low-temperature district network is currently still very low everywhere and requires the larger scale of retrofitting effort than constructing a stand-alone thermal energy storage system.

Several research papers have confirmed that there are benefits to consumers and utilities if loads management is applied. Jidong, *et al.* (2012) and Lee, *et al.* (2011) describe successful approaches for many objectives such as shaving peak demand, reducing customer electricity bills, minimizing utility operational costs, and maximizing utility profits. It is obvious that shaving peak demand will give benefits to utilities as they do not need to provide high peak power so they will use less resource to provide the same amount of energy and, in the big picture, save nature as energy will be used more efficiently; therefore, CO2 from combustion type of power plants can be reduced. However, in order to shave load profiles, the most difficult part in the future will be encouraging consumers to join demand-side management (DSM) systems. Mahmood, *et al.* (2014) states that nearly 40% of power is consumed in a building which mainly located in an urban area. Therefore, it may be beneficial to study the feasibility of integrating energy storage technologies with the PV/T technology in urban buildings that make the DSM much easier with those conversion and storage technologies being integrated.

2.4 The novelty of the thesis

The Introduction Chapter presented the potential of solar energy but have not been efficiently utilised because of its intermittent property which leads to the mismatch between the solar energy supply and household energy demands. The literature reviews from this chapter showed that several pieces of research suggest that the missing link of promoting solar energy as the main energy source on earth is appropriate energy storage technologies. Regardless of several advanced energy storage technologies available in lab scales, most technologies have not been commercialised in the market. Therefore, based on the potential of the solar energy and the energy conversion and storage technologies currently available, it may be concluded that it is not the resource and technical barriers that has prevented the solar energy to be the main energy source but the lack of assurance of how to manage the intermittent solar income to annually supply the demand. This thesis has the hypothesis that as the amount of solar energy resource is much higher than the world annual energy consumption, it must be the way to entirely supply the world from using only the solar energy resource. This thesis will present the novel way of integrating currently available solar energy conversion and storage technologies

to assure that by optimally operating the integrated system, the solar fraction of the domestic energy supply can be significantly improved.

Utilising solar energy for a domestic household requires both short-term and long-term energy storages for different time frames. Short-term energy storage may serve a household from hours to a week while the long-term energy storage is for the seasonal time frame when the excessive spring, summer and autumn solar energy is stored for the winter demand. Although the short-term solar energy storages for a household are widely available both the thermal energy storages and the electrical energy storages, studies related to the feasibility of seasonally storing solar energy for a household are limited. Moreover, most works dealt with thermal efficiency and the improved electric efficiency during the daylight only, the benefit of storing thermal energy transferred from the PV/T system for various applications after sunset has hardly been explored (Al-Waeli *et al.*, 2017c).

Although the thermochemical energy storage is extensively studied and is one of the promising technologies for seasonal storing thermal energy due to its high energy density and working temperature ranges which is viable to be integrated with the solar energy conversions suitable for households such as PV, PV/T or thermal collectors, with the knowledge of the author, there is no research that study about the optimal operational points for the conversion technologies to work with the thermochemical energy storages. Moreover, because of the fact that there are several options of the reactive working pair for the thermochemical systems, it is rare to find a research mentioned about the criteria of choosing the proper reactive working pair for any location in high latitude regions as most researches usually focus on high solar resource potential regions located close to the equator. Therefore, the feasibility study of annually supplying a household thermal energy demand solely from the solar energy resource in this thesis using Newcastle upon Tyne in the UK, the city in a high latitude region, as a case study is a novel idea that may lead to the possibility of increasing the solar fraction for the energy demand in a residential sector which may promote the bright future for a sustainable energy future.

Geographically, energy is mainly used in urban and city areas where the installation area of technologies is limited; therefore, it is important to extract the utmost amount of energy from the available area. According to the literature reviews in previous sections, the PV/T collector may be the most suitable technology for a household in the urban area; however, in order to supply the domestic hot water with the temperature required in winter, selected reactive salts may work in comparatively high temperatures which are rarely in the studied ranges of the

PV/T from most researches. This thesis is going to explore the way of controlling the mass flow rate of the HTF in the conversion technologies to optimally supply thermal energy to the thermochemical energy storage systems with adequately high temperature for the reaction rather than letting the mass flow rate fixed like other researches. The fixing mass flow rate produces uncontrollable temperature output along the day because the solar irradiance is intermittent which is not reliable for the high energy density like the thermochemical thermal storages chosen in this thesis. This method used in this thesis is, therefore, a novel study in this field.

Naturally, the chosen reactive salt that produces relatively high equilibrium temperatures in winter requires even higher desorption temperatures in summer leading to high-temperature HTF sources being desired. Without a facilitator, if the PV/T is used as an energy conversion technology, it has to work at high temperatures which may reduce its efficiency and lifecycle. Therefore, making the energy conversion technology works in a relatively medium temperature range while still able to aid the sorption process is a new idea. Using the compressure to facilitate the compressed condensation pressure and also lower the desorption pressure in the reactor is a novel idea proposed by Bao, Ma & Roskilly (2017) which has not been being studied in the integration with the PV/T technology. Therefore, it is a novel study in this thesis to explore the feasibility of using the compressor assisted thermochemical sorption energy storage with the energy input from the PV/T technology.

(This page intentionally left blank)

Chapter 3: Simulation, validation and performances of the photovoltaic, photovoltaic-thermal and thermal collectors

3.1 The working principles, modelling and simulation procedures of the PV, PV/T and thermal collectors

3.1.1 The working principles of the PV, PV/T and thermal collectors

Because of the hybrid architecture of the PV/T collector, it is firstly described in this section and the other two types of collector will be mentioned later by referring back to the PV/T working principle. The typical PV/T design, as shown in Fig. 3.1, was employed in this thesis because of its simplicity, commercial availability and high overall efficiency (Tyagi, Kaushik & Tyagi, 2012). From the top of the device to the bottom in order, the studied PV/T system is comprised of the front cover, air gap, encapsulator, PV cell, Ethylene-vinyl acetate (EVA) layer, tube-type absorber, HTF (inside the tubes) and the bottom insulation. Each layer was chosen to technical- and economical- effectively maximise the recovery of solar energy and primarily aim at the thermal product.

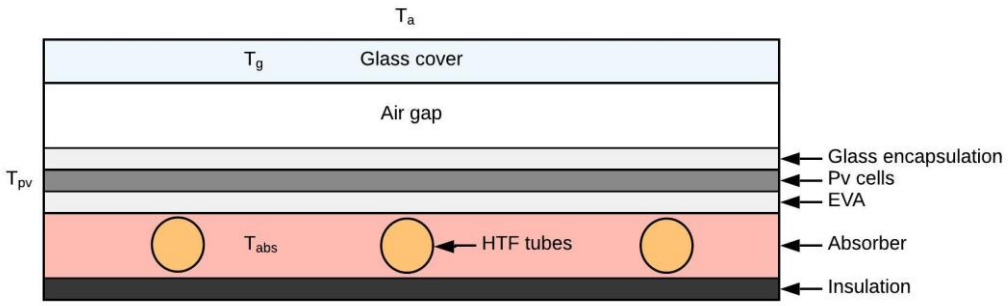

Fig. 3.1 *A typical flat-plate glass-covered water PV/T collector* (Thinsurat *et al.*, 2019)

Many developed configurations of flat-plate PV/T collectors differ from each other, like unglazed or glass-covered PV cell with or without an air gap between the glass cover and the PV cell, coupled with an air-based, or water-based or bio-fluid thermal collector. Unglazed design is more favourable if the electrical power generation is of priority, which allows quick heat dissipation of the PV cell through convection, leading to improved electrical conversion but compromised thermal efficiency. On the contrary, a glass cover generates optical loss and prevent natural ventilation, resulting in the reduction of PV cell performance, whereas, the glass cover strongly increases the thermal performance of the thermal collector, leading to a better overall thermal energy conversion (Dupeyrat *et al.*, 2011). An air gap acts as a thermal insulator

to prevent the conduction heat transfer between the PV cell and glass cover layers, it is normally used to minimize the heat loss and further enhance the thermal performance especially targeting comparatively higher output temperature. Water-based collector is studied in this work due to its greater heat transfer properties (Tyagi, Kaushik & Tyagi, 2012) compared to air-based system, and a water tank is used to collect and store the thermal output from the PV/T collector for other applications that require relatively higher temperature heat, such as domestic hot water use (>50 °C) or thermochemical storage (>70 °C).

Solar radiation passes through the front cover to the air layer before reaching the PV cells. The front cover is normally made of tempered glass due to its high strength (Kang *et al.*, 2012) and coated by the antireflective film such as SiO_2 to increase the transmittance property (Nostell, Roos & Karlsson, 1999; Hammarberg & Roos, 2003; Kesmez *et al.*, 2009). The air-gap layer acts as a thermal insulator to prevent the conduction heat transfer between the PV cell and the front glass cover. It can in turn significantly reduce heat loss and achieve higher thermal efficiency and higher heat output temperature if thermal energy output is required at a temperature higher than 50 ^{o}C, especially in cold-weather regions, although electrical efficiency is slightly compromised compared to the no-air-gap PV/T (Thinsurat *et al.*, 2019). Therefore, the air-gap layer was critical for the PV/T system studied in the present work (denoted as PV/T-AG in the context) since the PV/T thermal energy output is targeted at relatively higher temperature, i.e. for domestic hot water (DHW at 60^{o}C), and for energy charging, namely desorption of the thermochemical sorption cycle (~55 ^{o}C - 100 ^{o}C).

Solar radiation that reaches the PV cells is absorbed in two forms of energy depending on its wavelength. Depending on the type of materials used in the PV cells, the depletion region has a different band-gap value which absorbs only specific range of incoming solar spectrum (Todorov, Bishop & Lee, 2018) no higher than 23% of the overall incoming solar spectrum (Chu & Majumdar, 2012) (for one layer cells). The rest of the incident energy is absorbed in the form of heat that mainly transfers to the absorber layer. The PV cell studied in this work is the monocrystalline silicon as used in the Siemens SM46 panel, and its top is coated with an anti-reflective material to increase absorptivity property. The generated electron in each PV cell is connected in series and/or parallel to the output via a junction box.

The absorbed heat transfers to neighbouring layers: conductive heat transfer to the absorber eventually extracted by the heat transfer fluid (HTF) flowing through the tubes, natural convective heat transfer to the air gap layer and radiative heat transfer to the glass cover layer. Further radiative heat, transfers from the glass cover layer to sky and ground, is also considered

in some studies (Rejeb, Dhaou & Jemni, 2015). The impact of the glass encapsulation and the adhesive layer on the heat transfer can be neglected due to their very thin thickness, negligible thermal mass and good heat transfer properties.

EVA is very suitable for the glass encapsulation layer because it has high thermal conductivity and high optical transmissivity properties (Czanderna & Pern, 1996). There is another EVA layer between PV cells and the absorber for the purpose of protecting PV cells from moisture, electrical leakage and scratching from neighbouring layers (Kang *et al.*, 2012; Czanderna & Pern, 1996; Lee *et al.*, 2008; Jorgensen *et al.*, 2006). The absorber layer is normally made of high thermal conductivity and low-density materials such as aluminium, with circular tubes welded and insulated at the back-layer of the PV/T. Water is used as the heat transfer fluid (HTF) to carry thermal energy out of the PV/Ts and the flow rate should be controlled to achieve the desired output temperature.

Unlike majority of the reported systems coupled with a water tank, which used a closed-loop as the inlet water temperature of the PV/T collector was gradually increasing throughout the process since the water temperature in the tank was increasing, in this work it was an open loop of water circulation with a fixed inlet temperature (i.e. at the ambient temperature) and a certain temperature threshold of the outlet water in order to meet the requirement of the downstream application (e.g. 60 °C for hot water use, >70 °C for thermochemical storage). In this instance, according to the varying weather conditions, the mass flow rate of the water should be adjusted to ensure the required outlet water temperature, instead of a fixed value of the HTF flow rate. Therefore, it is important to study the influence of such operating conditions on the individual electrical and thermal efficiency and the overall energy conversion efficiency of the PV/T collector and gain insights of the potential of the PV/T collector integrated with thermochemical sorption system.

Considering the PV panel working principle, it is designed in order to generate maximum electrical energy output. The panel architecture is layered to rapidly transfer absorbed heat to the ambient to maintain low PV cell's temperature resulting in high conversion efficiency. Therefore, referring to the PV/T components in Fig. 3.1, the PV panel contains just only the glass cover, encapsulation, PV cells, EVA(another layer of encapsulation) and the back cover (or backsheet which is typically aluminium due to its high thermal conductivity) as presented in Fig. 3.2 which can be simplified for further analysis as in Fig. 3.3. The absence of the air gap and insulation layers contribute fast heat transfer between PV cells to ambient air. The working principle in the PV cells is identical to the PV cells layer used in the PV/T collector.

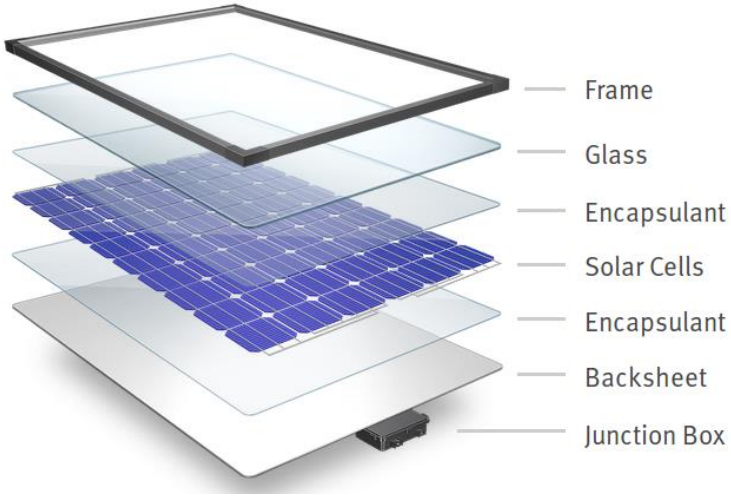

Fig. 3.2 *The components of A Photovoltaic panel* (nelsonmandelabay.gov.za, n.d.)

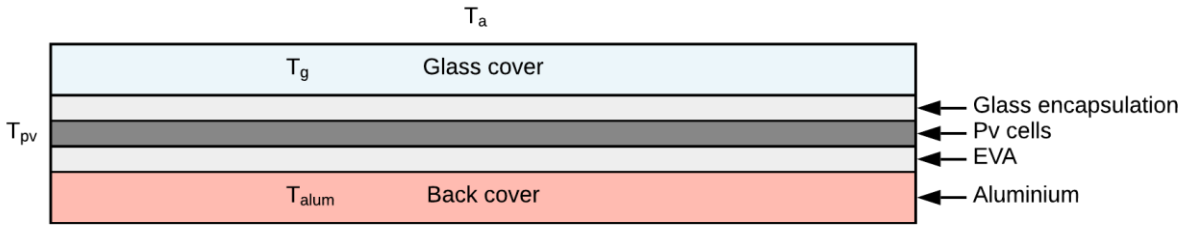

Fig. 3.3 *A typical PV panel layers*

Lastly, considering the working principle of the thermal collector, the purpose is to collect the highest possible of the thermal energy, therefore, the collector is designed to minimise the heat loss to the ambient. The double-glass cover allows the collector to have two airgap layers as the air insulator preventing heat loss to the ambient as shown in Fig. 3.4. The absorber is normally the high thermal conductivity metal such as aluminium and sometimes coated with a high absorbability material to increase the collector efficiency. The coated material layer is very thin; therefore, it is not included in Fig. 3.4.

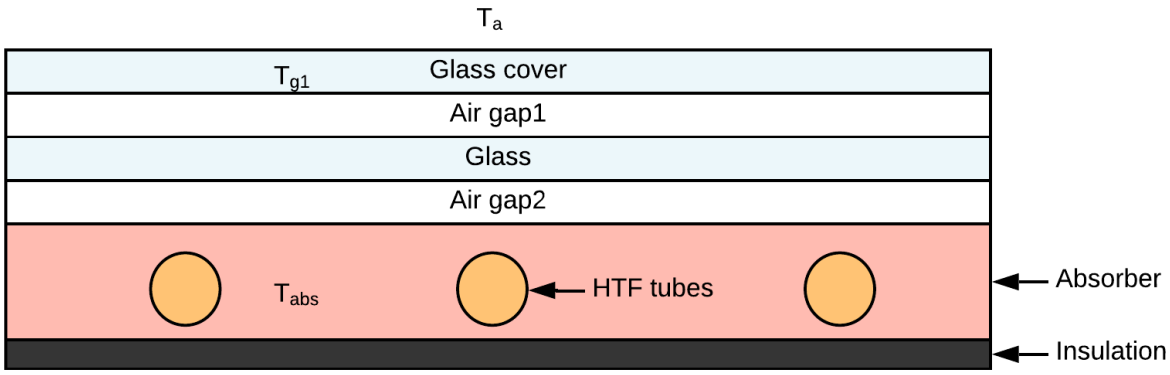

Fig. 3.4 *A typical thermal collector components*

3.1.2 Mathematical models of the PV, PV/T and thermal collectors

(a) PV cell model development and validation method

Instead of the simplified expression of electrical efficiency reported in Ref. (Evans, 1981) which was extensively used for the PV/T research works (Chin, Salam & Ishaque, 2016), the one-diode model (Tsai & Tsai, 2012) (Fig. 3.5) was used to simulate the electrical production of the PV cell with significantly improved accuracy of dynamic performance. Kirchhoff's current law is used at the circuit node of the photocurrent output (I_{PH}) in Fig. 3.5 (a) and (b), which states that the summation of currents at any circuit nodes is zero.

A PV panel consists of a number of the PV cell connected in series (N_S cells) and parallel (N_p lines) as represented by the diodes in Fig. 3.5(a). In the majority of previous research works, the ideal conditions were assumed as shown in Fig. 3.5(a) as all PV cells were perfectly manufactured and there was no internal resistance through the wiring between the PV cells. However, for a more accurate model, the wiring resistance between PV cells and the recombination loss between the P-N junctions of PV cells should be taken into account, which are represented as R_S and R_{SH} in Fig. 3.5(b), respectively. The current (I) that passes through R_S and goes to the load can be expressed in Eq. (3.1) which is the output current of the PV panel. I_{PH} is the photocurrent generated from the doped semiconductor used in the PV cells, and it varies depending on the PV cell temperature and the solar irradiance and can be calculated from Eq. (3.2). The diode currents in Fig. 3.5(a) can be combined to be I_D as shown in Fig. 3.5(b) and calculated from Eq. (3.3). I_{SH} is the shunt current obtained from Eq. (3.4). The elements in Eqs. (3.2) - (3.4) to calculate currents are the characteristics of the PV cell material, where I_{SC} is the short-circuit current of the PV cell provided by the manufacturer while the saturation current (I_S) and the reverse saturation current (I_{RS}) of the PV cell can be calculated by Eqs. (3.5) and (3.6), respectively (Carrero, Amador & Arnaltes, 2007).

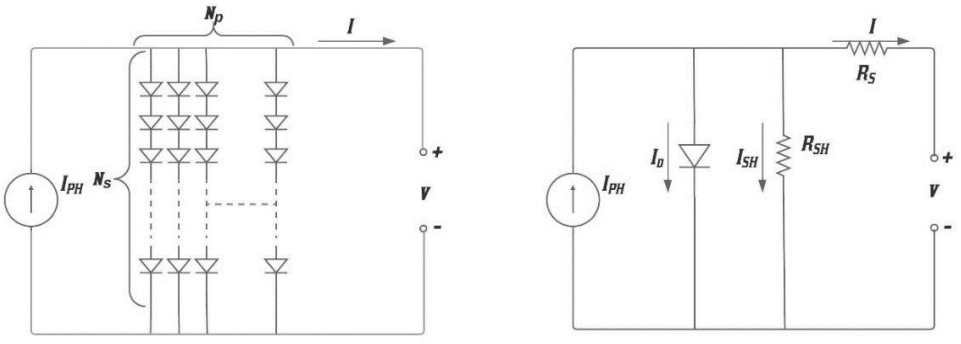

(a) (b)

Fig. 3.5 *(a) PV cell model using diodes model connected in series and parallel; (b) Photovoltaic based on the one-diode model.*

$$I = I_{PH} - I_D - I_{SH} \tag{3.1}$$

$$I_{PH} = N_p[I_{SC} + K_i(T_{pv} - T_{pv\_STC})]\frac{G}{G_{STC}} \tag{3.2}$$

$$I_D = N_p I_s \left\{ exp\left(\frac{q}{kT_{pv}n}\left(\frac{V}{N_s} + \frac{IR_s}{N_p}\right)\right) - 1 \right\} \tag{3.3}$$

$$I_{SH} = \frac{N_p V + N_S I_{RS}}{N_S R_{SH}} \tag{3.4}$$

$$I_S = I_{RS}\left(\frac{T_{pv}}{T_{pv\_STC}}\right)^3 \times exp\left(\frac{qE_g}{kn}\left(\frac{1}{T_{pv\_STC}} + \frac{1}{T_{pv}}\right)\right) \tag{3.5}$$

$$I_{RS} = \frac{I_{SC}}{exp\left(\frac{V_{oc}}{N_s n V_t}\right) - 1} \tag{3.6}$$

The characteristics and the behaviour of the PV cell (Siemens SM46 PV module and Solarex MSX-60 PV module) at the STC summarized in Table 3.1 was used to solve Eqs. (3.1) to (3.6). The series resistance (R_S) and the shunt resistance (R_{SH}) are the causes of power loss from the PV cell which alters the slope of the I-V curve and reduces the maximum power. According to Carrero, *et al.* (2007), the R_S and R_{SH} could be estimated corresponding with the value of V_{OC}/I_{SC}, but those values should be different for different PV cells; moreover, the R_S and R_{SH} should not be constant values under different conditions of irradiation and cell temperature. In this work, the initial values of R_{SH} and R_S were defined as 54 Ω and 0.54 Ω suggested by Carrero, *et al.* (2007) for Eqs. (3.7) and (3.8) respectively to start the iterative calculation; the Euclidean or the norm error (L^2) (Eq. (3.9)) was being monitored during the iteration, as this error reduced as the iteration proceeds. Therefore, the values of the R_S and R_{SH} were adjusted along with the iteration until the L^2 norm error stopped reducing, which was 0.1671 for Siemens SM46 PV model in this study.

$$R_{SH\_STC} > 10\frac{V_{oc}}{I_{SC}} \tag{3.7}$$

$$R_{S\_STC} < 0.1\frac{V_{oc}}{I_{SC}} \tag{3.8}$$

$$L^2 \text{ norm error} = \sqrt{\sum_{i=1}^{n} (u_e(i) - u_c(i))^2} \quad (3.9)$$

where the L^2 norm error represents the overall error of a dataset from a multi-point measurement, u_e(i) and u_c(i) is the measured value and the calculated value at point *i*, respectively, and *n* is the number of data points.

Table 3.1 *Characteristics of the PV cells at STC.*

Characteristics of the PV module	Siemen SM 46	Solarex MSX-60
Typical peak power (P_{MPP})	46 W	60 W
Voltage at peak power (V_{MPP})	14.6 V	17.1 V
Current at peak power (I_{MPP})	3.15 A	3.5 A
Short-circuit current (I_{sc})	3.35 A	3.8 A
Open-circuit voltage (V_{oc})	18.0 V	21.1 V
Temperature coefficient of open-circuit voltage (K_v)	-77 mV/°C	-80±10 mV/°C
Temperature coefficient of short-circuit current (K_i)	12 mA/°C	0.065±0.05 %/°C
the ideal factor of PV cell (n)	1.2	1.2
Band-gap energy of a semiconductor (E_g)	1.16 eV	1.16 eV
Number of PV cells in series	30	36
Number of PV cells in parallel	1	1

Based on the comparison between the simulated I-V and P-V curves and the measured data, the values of the series resistance (R_S) and the shunt resistance (R_{SH}) under different conditions of irradiation and cell temperature were obtained through iterative calculation. Hence, the new correlations of the R_{SH} as a function of the R_{SH_STC} and the ratio of the actual irradiation and the STC irradiation was developed and verified in this work as presented in Eq. (3.10). The R_S as a function of the R_{S_STC}, the cell temperature difference and the irradiation difference between the actual value and the reference value was proposed and verified as Eq. (3.11).

$$R_{SH} = R_{SH\_STC} \frac{G}{G_{STC}} \quad (3.10)$$

$$R_S = R_{S\_STC} + R_{s_{con_T}}\left(T_{pv} - T_{pv_{STC}}\right) - R_{s_{con_G}}(G - G_{STC}) \quad (3.11)$$

where T_{pv_STC} is 25 ^{o}C, $R_{S\_con\_T}$ is the constant for the temperature dependent term, $R_{S\_con\_G}$ is the constant for the irradiance dependent term and G_{STC} is 1,000 W/m^2.

The electrical power output of the PV cell can be obtained by multiplying its output current (I) with the connected load's voltage (V). If the connected load voltage is constant such as a 12V lead-acid battery, the connected load voltage may not be at the maximum power point that the PV cell can provide at that specific irradiance due to the variation and intermittence of the solar irradiation. Practically, a maximum power point controller (MPPC) is installed between the PV panels and loads to increase or decrease the loads voltage meanwhile the output current changes with the varying load voltage according to its I-V characteristics, irradiance and cell's temperature, in order to extract the maximum power from the PV panel at every incoming irradiance and cells' temperature. Therefore, the maximum power output (P_{max}) was considered as the electrical power output of the PV layer (E_8) in this study and can be calculated from Eq. (3.12).

$$P_{max} = E_8 = V_{P\_max} \cdot I_{P\_max} \quad (3.12)$$

where V_{p_max} is the load's voltage at the maximum-power point; I_{p_max} is the output current at the maximum-power point.

After model validation, the PV power output is simulated using the validated model expressing I-V characteristics of the PV cells for the condition of the irradiance ranging from 0 to 1,000 W/m^2 and the PV cell temperature between 0 ^{o}C and 100 ^{o}C. The simulated data of the electrical power output was then fitted for the polynomial regression of the relationship between the electrical power output and the weather conditions. In this thesis, the simulation was conducted in 30 minutes time-step as the electrical efficiency at each time-step may vary. The electrical efficiency (η_{elec}) was calculated from Eq. (3.13). If the average daily efficiency was considered, the integration interval (from t_1 to t_2) was from sunrise to sunset.

$$\eta_{elec} = \frac{\int_{t_1}^{t_2} E_8 \, dt}{\int_{t_1}^{t_2} Irr \, dt} \quad (3.13)$$

where I_{rr} is the solar irradiance as a function of time of the day (W/m^2).

(b) Theoretical analysis of heat transfer of the PV, PV/T and thermal collectors

Two types of the PV/T collectors were studied and compared with a reference PV module in this thesis, which are the PV/T collector without air gap (PV/T-no-AG) and the PV/T collector with an air gap (PV/T-AG). The cross-sectional view of these two designs modelled in ANSYS Fluent is presented in Fig. 3.6(a) and Fig. 3.6 (b) respectively. The air gap between the glass cover and the PV panel in Fig. 3.6(b) acts as an air insulation layer, which is favourable for thermal production. For the thermal collector, the double-glass layer is used as presented in Fig. 3.7. The dimensions of all models are presented in Table 3.2.

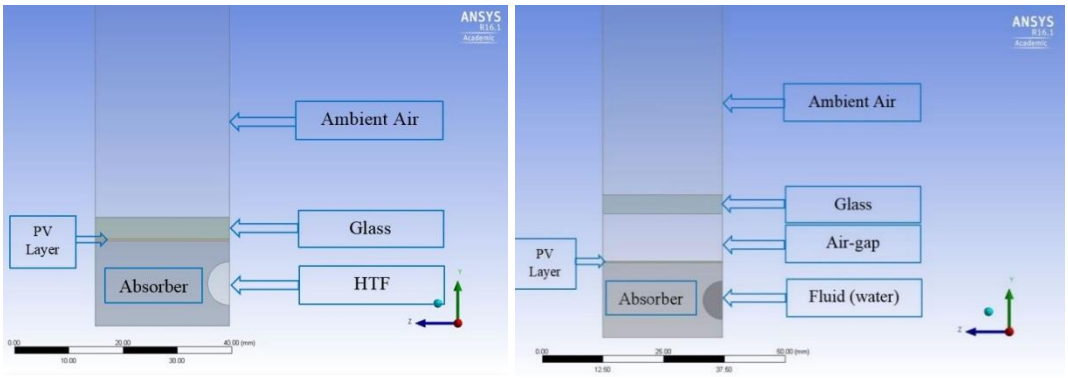

(a) (b)

Fig. 3.6 *Cross-sectional view of the PV/T collector (a) without an air gap (b) with an air gap in ANSYS Design Modeller.*

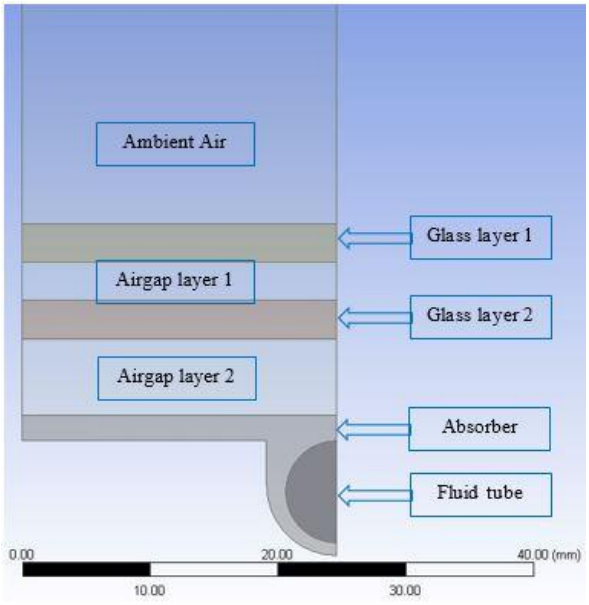

Fig. 3.7 *Cross-sectional view of the thermal collector in ANSYS Design Modeller.*

Table 3.2 *Dimension data of the PV and PV/T collectors studied.*

	PV-panel model	Thermal collector model	PV/T-no-AG model	PV/T-AG model
Ambient air thickness or Upper air thickness (Y-axis)	300 mm	300 mm	300 mm	300 mm
Lower ambient air thickness (Y-axis)	300 mm	-	-	-
Glass thickness (Y-axis)	-	3/3 mm	4 mm	4 mm
Air-gap thickness (Y-axis)	-	3/6 mm	-	10 mm
PV layer thickness (Y-axis)	0.3 mm	-	0.3 mm	0.3 mm
Absorber thickness (Y-axis)	15.7 mm	15.7 mm	15.7 mm	15.7 mm
Fluid tubes' diameter	-	8 mm	8 mm	8 mm
All components' length (X-axis)	1830 mm	1830 mm	1830 mm	1830 mm
Cut models' width (Z-axis)	24.65 mm symmetry	24.65 mm symmetry	24.65 mm symmetry	24.65 mm symmetry
Full model width (Z-axis)	986 mm	986 mm	986 mm	986 mm
Length between 2 fluid tubes	-	49.3 mm	49.3 mm	49.3 mm

The energy balance is dominated by heat conduction in the solid elements including glass cover, PV cells and absorber (including tubes), as expressed in Eq. (3.14).

$$\rho_m \delta_m C_m \frac{dT_m}{dt} = k_m \delta_m \left(\frac{\partial^2 T_m(x,y,z)}{\partial x^2} + \frac{\partial^2 T_m(x,y,z)}{\partial y^2} + \frac{\partial^2 T_m(x,y,z)}{\partial z^2} \right) + \sum Q_m \tag{3.14}$$

where the subscriber '*m*' is replaced by different symbols to represent different elements, e.g. 'g' when the glass layer is under consideration, or '*pv*' when the PV-layer is discussed, or '*ab*' for the case of the absorber layer; ΣQ is the summation of different heat sources for each layer. For all different models studied, the energy balance of the single glass cover (ΣQ_g) for example

expressed in Eq. (3.15) includes the solar radiation to the glass cover Q_1 (Eq. (3.16)), the sky radiation to the glass cover Q_2 (Eq. (3.17)), the convective heat from ambient air to the glass Q_3 (Eq. (3.18)), the radiative heat from the glass to PV cell Q_4 (Eq. (3.19)), and the radiative heat from the glass to ground Q_5 (Eq. (3.20)). For the PV/T-AG model, the convective heat between the glass and the PV cell according to natural convection in the air layer Q_{6_a} was calculated in Eq. (3.21) and replace the Q_6 in Eq.(3.15); whereas, for the PV/T-no-AG and the PV panel models, the conductive heat transfer between the glass and PV surface Q_{6_b} (Eq. (3.22)) was used to replace the Q_6 in Eq. (3.15). Note that the positive signs in Eq. (3.15) mean the heat is absorbed by the layer envisaged and minus signs represent the heat released from the layer envisaged.

$$\sum Q_g = Q_1 + Q_2 + Q_3 - Q_4 - Q_5 - Q_6 \tag{3.15}$$

$$Q_1 = \alpha_g G \tag{3.16}$$

$$Q_2 = \varepsilon_g \sigma ({T_{sky}}^4 - {T_g}^4) \tag{3.17}$$

$$Q_3 = h_{wi}(T_a - T_g) \tag{3.18}$$

$$Q_4 = h_{ray,g\to pv}(T_g - T_{pv});\ h_{ray,g\to pv} = \frac{\sigma(T_g^2 + T_{pv}^2)(T_g + T_{pv})}{\frac{1}{\varepsilon_{pv}} + \frac{1}{\varepsilon_g} - 1} \tag{3.19}$$

$$Q_5 = \varepsilon_g \sigma ({T_g}^4 - {T_{gr}}^4) \tag{3.20}$$

$$Q_{6\_a} = h_{conv,g\to pv}(T_g - T_{pv}) \tag{3.21}$$

$$Q_{6\_b} = h_{cond,g\to pv}(T_g - T_{pv}); \tag{3.22}$$

Sky temperature can be approximately calculated by using Eq. (3.23) (Adelard *et al.*, 1998) where L_0, A, B and C are obtained from Eqs. (3.24) to (3.27) respectively with the ambient vapour pressure (P_v) calculated by Eq. (3.28) (Buck, 1981). Ground temperature is approximately 2 °C lower than ambient temperature (Touafek, Haddadi & Malek, 2013).

$$T_{sky} = \left(\frac{L_0(1+0.01A) + \frac{BC(8-N_e)}{8}}{\sigma} \right)^{0.25} \tag{3.23}$$

$$L_0 = 3.6(T_a - 273.15) + 231 \quad (3.24)$$

$$A = 10.1\ln(P_v) - 12.3 \quad (3.25)$$

$$B = 1.7(T_a - 273.15) + 107 \quad (3.26)$$

$$C = -0.22\ln(P_v) + 1.25 \quad (3.27)$$

$$P_v = 611.21\exp\left\{\left(18.678 - \frac{T_a}{234.5}\right)\left(\frac{T_a}{257.14 + T_a}\right)\right\} \quad (3.28)$$

To accurately calculate Q_{6_a} in Eq. (3.21), natural convection theory is considered in the air-gap layer of the PV/T-AG and $h_{conv,\ g\rightarrow pv}$ is obtained from Eq. (3.29) where the Nusselt number (Nu_{gap}) can be calculated by Eq. (3.30), where θ is the tilt angles of the PV/T-AG which is valid from 0° to 75°, *Ra* is the Rayleigh number defined as the production of Grashof Number (*Gr)* and the Prandtl number (*Pr).*

$$h_{conv,g\rightarrow pv} = \frac{Nu_{gap}k_{gap}}{\delta_{gap}} \quad (3.29)$$

$$Nu_{gap} = 1 + 1.44\left[1 - \frac{1708}{Ra\delta_a cos\theta}\right]\left[1 - \frac{1708(sin\theta)^{1.66}}{Ra\delta_a cos\theta}\right] + \left[\frac{(Ra\delta_a sin\theta)^{0.33}}{5830} - 1\right] \quad (3.30)$$

For the pv layer of all three models, the transient energy balance can be analysed using Eq.(3.14) with PV cell material properties and ΣQ_{pv} given in Eq. (3.31). Q_7 is the heat absorbed by PV layer from the solar irradiance which can be calculated by Eq.(3.32); E_8 is the electrical power production in the PV layer which is described in the previous section and Q_9 is the conductive heat from the PV layer to the absorber layer as presented in Eq.(3.33) with its thermal contact conductance coefficient $h_{cond,pv\rightarrow abs}$ calculated from Eq. (3.34).

$$\sum Q_{pv} = Q_4 + Q_5 + Q_7 - E_8 - Q_9 \quad (3.31)$$

$$Q_7 = \alpha_{pv}\tau_g G \quad (3.32)$$

$$Q_9 = h_{cond,pv\rightarrow abs}(T_{pv} - T_{abs}); \quad (3.33)$$

$$h_{cond,pv\rightarrow abs} = \frac{1}{\frac{\delta_{pv}}{k_{pv}} + \frac{\delta_{abs}}{k_{abs}}} \quad (3.34)$$

The energy balance in the absorber layer of the PV/T-no-AG and PV/T-AG models can be expressed as shown in Eq. (3.35) where Q_{10} is the convective heat transfer from the absorber layer to the HTF (Eq. (3.36)). For the PV panel model where there is no HTF, Q_{10} represents the convective heat transfer from the absorber to the ambient air (Eq. (3.37)).

$$\sum Q_{abs} = Q_9 - Q_{10} \quad (3.35)$$

$$Q_{10\_a} = h_{abs-HTF}(T_{abs} - T_{HTF}) \quad (3.36)$$

$$Q_{10\_b} = h_{wi}(T_{abs} - T_a) \quad (3.37)$$

For the thermal collector, all the governing equations are treated in the same manner but without the PV layer. The glass layer 2 encounters the natural convection from the surrounding airgaps and the radiative heat transfer from the glass layer 2 is neglected due to its minimal temperature differences between the surrounding and this layer leading to a negligible value of radiative heat transfer compared to natural convection heat transfer. The material properties used in the models are presented in Table 3.3.

In the fluid regions including the ambient air and HTF, the continuity, energy, momentum and turbulence equations were treated using the finite volume approach to computationally solve the transport equations in Eq. (3.38) in ANSYS Fluent, where ϕ = 1 for continuity equation, $\phi = \vec{V}$ for momentum equations, and $\phi = h$ for energy equation (ANSYS Fluent, 2013). The first term on the left-hand side of Eq. (3.38) is the unsteady term, the second term is the convective term, the first term on the right-hand side is the diffusion term and the last term on the right-hand side is the generation term.

$$\frac{\partial}{\partial t}\int_V \rho \emptyset dV - \oint_A \rho \emptyset \vec{V} \cdot d\boldsymbol{A} = \oint_A \Gamma_\emptyset \nabla \emptyset \cdot d\boldsymbol{A} + \int_V S_\emptyset dV \quad (3.38)$$

Turbulent flow by using the shear stress transport k-ω (SST k-omega - 2 equations) model was chosen along with the viscous heating option to get more accurate solutions especially in

viscous heating cases such as the heat transfer between solid and fluid zones. Low-Re Corrections was selected in the cases of low Reynolds number flow. There was a big temperature gradient along the PV/T panel from the inlet side to the outlet side, so the volume-weighted average of the simulated PV temperature was used in this work. To reduce the computational time, ground and sky were treated as source terms in the unit of W/m^3.

Table 3.3 *The material properties used in the PV and PV/T collectors' models.*

Material properties	**Glass**	**PV cell**	**Absorber (Aluminium)**	**Air**	**HTF (water)**
Absorption coefficient, α (-)	0.05	0.8	-	-	-
Density, ρ (kg/m^2)	2,200	700	2719	1.225	998.2
Emissivity, ε (-)	0.88	-	-	-	-
Specific heat capacity, Cp (J/(kg·K))	670	900	871	1,006	4,182
Thermal conductivity, k (W/(m·K))	0.9	144	202.4	0.0242	0.6
Transmistivity, τ (-)	0.91	-	-	-	-
Viscosity, (kg/m·s)	-	-	-	1.79e-05	0.001003

Note: Only the relevant properties of the materials used in the models are presented in the table.

In this study, the useful thermal efficiency (η_{th}) was considered and it was calculated from Eq. (3.39). Note that if the temperature of the HTF could not reach the set temperatures, the pump would not operate and the mass flow rate would be zero, in this instance, the instantaneous thermal efficiency would be zero because it is based on useful output, even though the temperature of the HTF raised inside the PV/T, the HTF is not flowing to supply heat for the downstream application. If the overall average thermal efficiency was considered, the integration interval (from t_1 to t_2) was the time from sunrise to sunset; the integration interval was 30 minutes for the calculation of the instantaneous thermal efficiency.

$$\eta_{th} = \frac{\int_{t_1}^{t_2} \dot{m} C_{P\_HTF}(T_{out} - T_{in}) dt}{\int_{t_1}^{t_2} \text{Irr dt}} \quad (3.39)$$

where $\dot{m}$ is the mass flow rate of the HTF out from 1 m^2 PV/T collectors; C_{P_HTF} is the specific heat capacity of the HTF; T_{out} is the output temperature of the HTF from the PV/T; T_{in} is the input temperature of the HTF to the PV/T. As comparing different kinds of conversion technology with their efficiencies and energy output is not practical because the quality of the energy output is not considered. Therefore, the exergy output presented in Eq. (3.40) is introduced for the technology's comparison. As the electrical energy can be used regardless of the ambient temperature, the electrical energy output (E_8 from Eq. (3.12)) from the PV/T and the PV collectors is the 100% useful which means the electrical energy is exactly the electrical exergy. On the other hand, the quality of thermal energy depends on the ambient temperature following the second law of thermodynamics. Thermal energy can only transfer from high to low temperature leading to the limitation of the useful thermal energy. The maximum useful thermal energy, or the thermal exergy, is therefore obtained from Eq. (3.41) where the T_0 is the ambient temperature and T is the HTF input temperature of a heat cycle.

$$Ex_{total} = Ex_{th} + Ex_{elec} \quad (3.40)$$

$$Ex_{th} = Q_{th}\left(1 - \frac{T_0}{T}\right) \quad (3.41)$$

3.1.3 Simulation procedures of the PV, PV/T and thermal collectors

The overall performance of the PV/T system including electricity and thermal output depends on the solar energy input, the ambient temperature, wind speed, the operating temperature of the system components and the heat extraction conditions such as the inlet and outlet temperature and the mass flow rate of the HTF. Two different designs of the single glass-covered sheet-and-tube PV/T collectors, with and without air gap, have been analysed and compared with the reference PV module to reveal more insights. PV/T collectors without airgap are already available off-the-shelf, and measurement data is easily available for model validations in this work. Once the PV/T without airgap is validated, the PV/T with airgap model is assumed to produce acceptable results as the model's structure only added one more airgap layer to the PV/T without air gap. The ANSYS Fluent is reliable on producing results with the natural convection phenomena in the air gap layer when the gravity is activated in the software setup.

The temperature variation profile of the system components was simulated and analysed in ANSYS Fluent coupled with a detailed model of the PV cell developed in the MATLAB (Modelling of the PV, PV/T and thermal collector in ANSYS are described in detail in Appendix A). The methodology to simulate the simultaneous generation of electrical power and thermal power from the PV/T collector is illustrated in Fig. 3.8. A one-diode current-voltage (I-V) model was developed using Matlab Simulink to represent the relationship between the electrical generation performance of the PV cell and the varying solar irradiance and cell temperature when the load voltage varies from 0 to open-circuit voltages (Modelling of electrical energy production for PV panel in MATLAB Simulink is present in detail in Appendix B). The measured data of Siemens SM46 PV module and Solarex MSX60 PV module presents the current-voltage characteristics under the standard test condition (STC, i.e. the PV cell temperature at 25 °C and the irradiance of 1,000 W/m^2) was used to validate the PV cell model. To assure the generic application of the PV cell model developed in this work it was also verified against the measured data of the Solarex MSX-60 PV module at the irradiance of 1,000 W/m^2 and temperature ranges from 0 to 75 ^{o}C in addition to the STC. The datasheets of the Siemens SM46 PV module and Solarex MSX60 PV module were attached in Appendix C. Since there is little information reported for a full set of experimental data on the PV/T collectors, the thermal analysis model was also validated using the measured PV cell temperature of the same commercial PV modules.

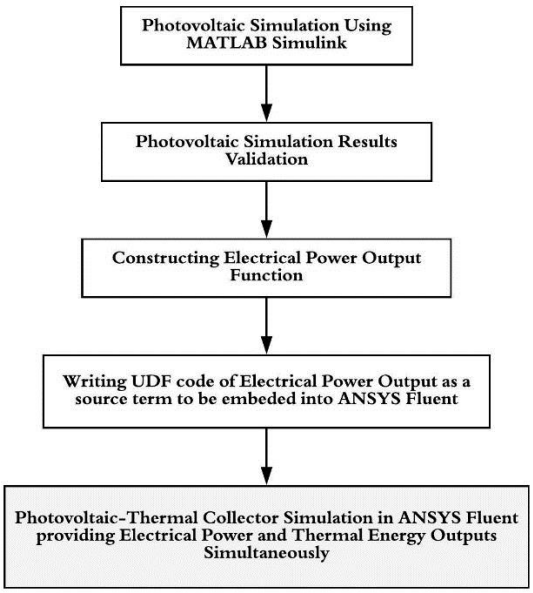

Fig. 3.8 *The methodology of simultaneous simulation of electrical and thermal energy in the photovoltaic containing panels.*

3.2 Input parameters for the simulations

The study starts from basic assessments such as characteristics of the solar resource, the seasonal and daily variations of the solar radiation including weather conditions such as temperature and wind speed of the area which affect the potential of capturing solar energy. Therefore, the input parameters will be solar irradiance (G), ambient temperatures (T), and wind speed (V). The weather data in 30-minute time step from sunrise to sunset of Newcastle-upon-Tyne, a representative high-latitude city in the UK, including atmospheric temperature, global horizontal radiation and wind speed, are available from the Meteonorm software. Meteonorm software is the weather-data database providing historical weather data analysed from more than 8,000 weather stations and five geostationary satellites from around the world to generate reliable and accurate weather parameters used in this thesis (Meteonorm, 2017). Each input parameter is described and processed as follows.

3.2.1 Solar irradiance in Newcastle upon Tyne, UK

Solar energy penetrates through the earth surface with different intensity depending on location, time of the day, and season. Moreover, it contains a wide range of wavelength with different intensity. Visible light which ranges from 400-700 nm has the highest intensity at the earth surface. It is the reason that silicon-based solar cell is the most popular material for PV panels as c-Si reacts mostly to the visible range photons. Considering location dependent of solar irradiance, because of the inclination of the earth's axis with the orbital plane and the sphere shape of the world, near equator regions experience higher intensity of solar irradiance than others and the irradiance reduces with higher latitude. Huld, Muller & Gambardella (2012) illustrate the annual solar global irradiation in Europe with their potential for electricity production in Fig. 3.9 which indicates that Newcastle upon Tyne area get approximately 900 kWh$/m^2$ per year of solar global irradiation. The solar global irradiation in Newcastle upon Tyne is considerably low compared to other southern regions in Europe such as Spain, Portugal, Italy, and Greece which their annual irradiations of more than 2,000 kWh$/m^2$.

The raw data from was processed in MATLAB to obtain the chart describing 21 years averaged daily irradiation and irradiance from 1985 to 2005 in Newcastle upon Tyne area as shown in Fig. 3.10. According to Fig. 3.10, January is the month when solar irradiance in Newcastle upon Tyne is the lowest with the averaged value of 25.6 W/m^2 leads to 614 Whr/m^2 per day of irradiation while June is the month with the highest solar irradiance of 199 W/m^2 leads to 4,770 Whr/m^2 per day of irradiation. Noting that the free version of the

weather data database does not provide the data in December due to the very low amount of irradiation in the target area; therefore, 0 W/m^2 of irradiance is set in December in this research. By accumulating the averaged solar irradiation over a year, Newcastle upon Tyne has the potential of receiving solar energy of 870 $kWhr/m^2$ per year.

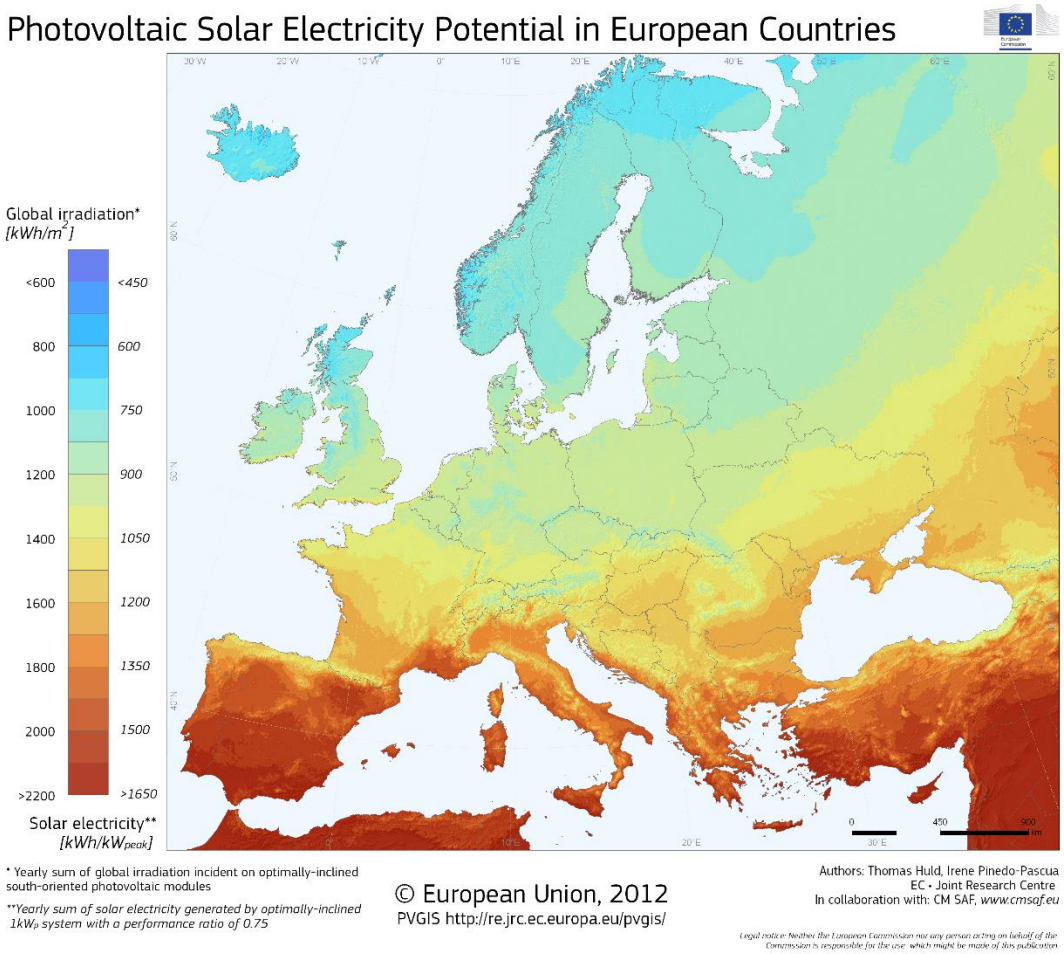

Fig. 3.9 *Europe global irradiations with electricity production potential* (Huld, Muller & Gambardella, 2012)

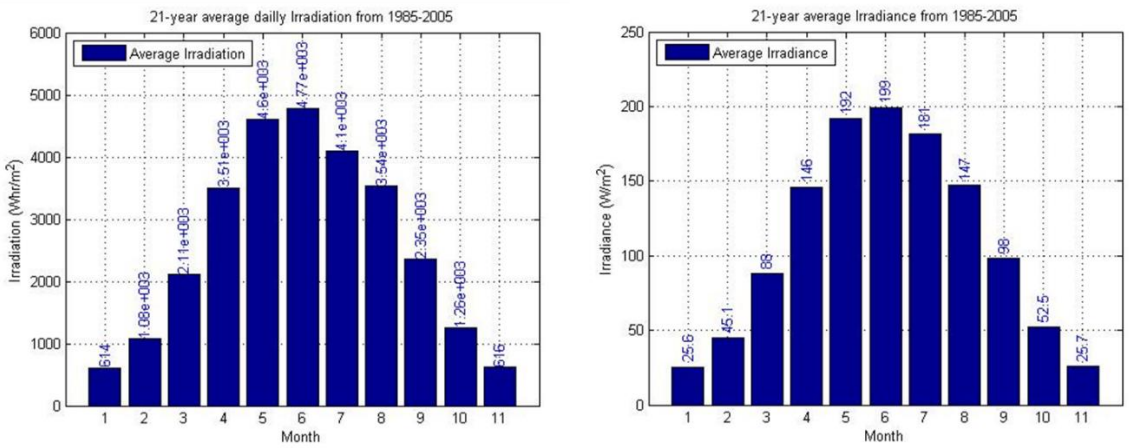

Fig. 3.10 *21-year averaged daily irradiation (left) and irradiance from 1985 to 2005(right) in Newcastle upon Tyne area*

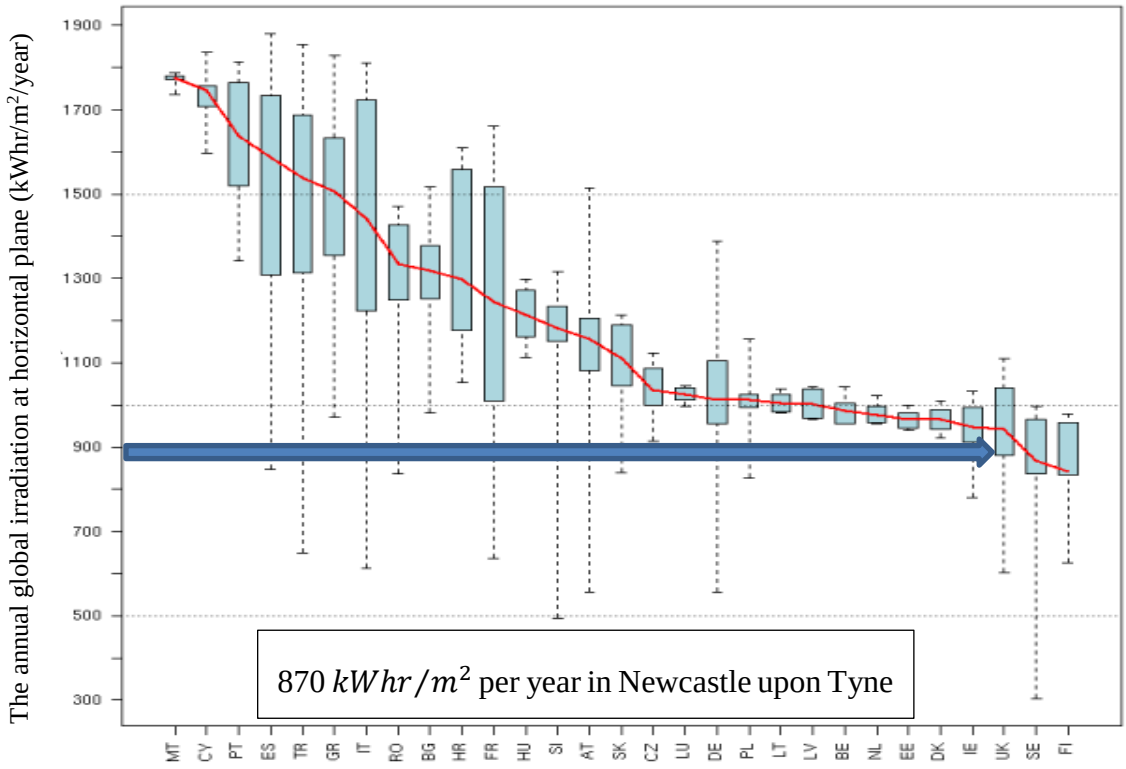

Fig. 3.11 *Annual global irradiation at a horizontal plane (Huld, Muller & Gambardella, 2012)*

Fig. 3.12 illustrates the variation of solar irradiance seasonally and hourly. Regarding the red line which is the 24 hrs of solar irradiance in 21st June 2004, the day that has the longest daylight of the year, irradiance is fluctuating as the radiance drops from its normal value of the time when there is cloud cover. In 30th November 2004, the green line in Fig. 3.12, there seemed the very clear sky and the irradiance was not fluctuating at all but the maximum value is much lower than in summer and the hour of sunshine is also much less than in summer. When considering the average temperatures in summer, which will be discussed in the following section, ambient temperatures are very close to the temperature required for indoor buildings; there is no need of using solar energy for air-conditioning but it could use a small amount of solar thermal energy for hot water heating. Therefore, most of the recovered solar energy can be stored to be used in winter when the irradiance is low as well as ambient temperatures.

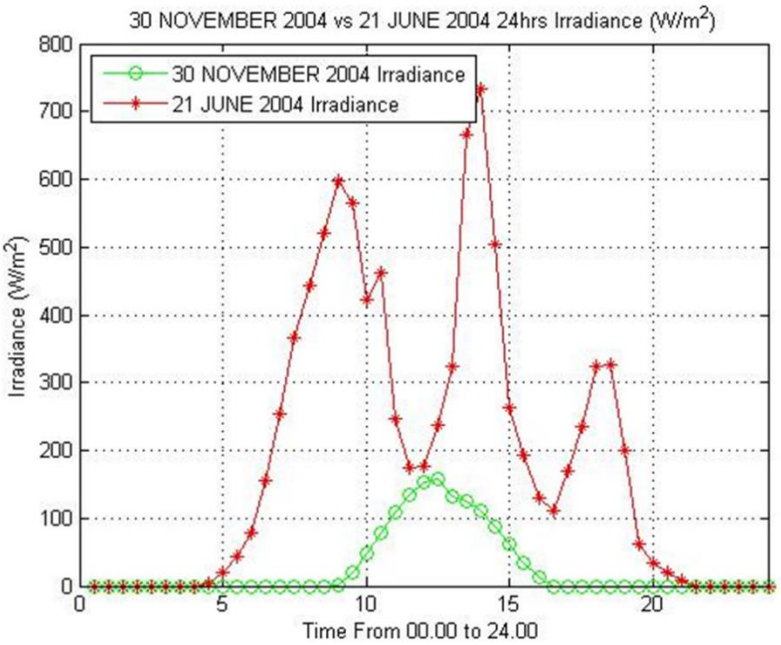

Fig. 3.12 *Hourly solar irradiance in Newcastle upon Tyne on November 30th, 2004 and June 21st, 2004*

3.2.2 Mathematical model of solar irradiance on tilted surfaces

The irradiance data is mostly available at the horizontal plane which is normally not the optimised angle to install solar conversion collectors. Therefore, the solar irradiance at a tilted angle is normally derived from the horizontal data to achieve the practical analysis of the conversion technologies. In this thesis, the mathematical model of the solar irradiance on tilted surfaces is conducted following the method reported by Duffie and Beckman (2013).

Starting from the solar constant, G_{sc}, which is the power of the sun per unit area that radiates to the earth surface outside the atmosphere perpendicular to the radiation beam direction at the average mean distance between the earth and the sun. The value of G_{sc} obtained from satellites and G_{sc} = 1367 W/m^2 is widely used, which is the value used in this thesis. However, because of the variation of the distant between the earth and the sun along a year, the emitted solar irradiance that reach the extraterrestrial surface, which is defined as extraterrestrial irradiance (G_{on}), varies depending on the time of the year with Eq.(3.42) proposed by Iqbal *et al.* (1983) with the accuracy of ±0.01%.

$$G_{on} = G_{sc}(1.000110 + 0.034221\cos(B) + 0.001280\sin(B) + 0.000719\cos(2B) + 0.000077\sin(2B)) \quad (3.42)$$

$$\textit{where}\quad B = (n-1)\frac{360}{365}\quad ; n = \textit{the day of the year; The unit of B is in degree} \quad (3.43)$$

The extraterrestrial irradiance (G_{on}) penetrate through the earth atmosphere which most of the time is not in the direction that is perpendicular to the location surface. Moreover, because of the different latitude of each location, the solar beam travel passes the atmosphere with different distance, and the distance can be taken into account by introducing the "air mass, *m*". The air mass is the proportion of the actual mass of the atmosphere that the solar beam passes through to the mass of atmosphere when the sun is overhead. Therefore, the air mass equals to 1 when the sun is exactly overhead at sea level. Normally, the PV industrial companies test the PV cells by using the solar simulator with the air mass of 1.5. For other solar angles (zenith angles, θ_z), the air mass can be calculated from Eq.(3.44) or Eq. (3.45) depending on the zenith angle.

$$m = \frac{1}{cos(\theta_z)}\ ; \textit{for } \theta_z \textit{ of up to } 60^o \quad (3.44)$$

$$m = \frac{exp(-0.001184h)}{cos(\theta_z)+0.5057(96.080-\theta_z)^{-1.634}}\ ; \quad \textit{for } \theta_z \textit{ of up to } 90^o\textit{; h is the site altitude in meter} \quad (3.45)$$

The part of the extra-terrestrial irradiance that passes through the atmosphere and directly reaches the target surface is called "beam radiation or direct solar radiation (G_b)". The other part is scattered by the atmosphere before reaching the earth surface which is called "diffuse radiation (G_d)". The combination of the beam and diffuse radiations are called "total solar radiation or global radiation (G_g). Because of the surrounding around the target surface, the reflex radiation (G_r which sometimes called Albedo radiation) may be considered to enhance accuracy. Note that the horizontal surface might receive a negligible amount of the G_r.

To calculate the incident irradiance on a tilted surface, related names and definitions of angles used in the calculation are quoted in Table 3.4 (Duffie & Beckman, 2013) to avoid the misunderstanding from the variables involved. The calculation for Newcastle upon Tyne can be done as follows;

1. Latitude, ϕ, for Newcastle upon Tyne is 54.9783° N.
2. Declination, δ, depends on the time of the year calculated from Eq. (3.46), where *B* is calculated from Eq. (3.43).
3. Surface azimuth angle, γ, is fixed to face south along the year thus $\gamma = 0^o$.
4. Slope, β, or tilted angle will be varied from 0^o to 90^o to determine the optimum angle in Newcastle upon Tyne.
5. Hour angle, ω, varies along the studied day
6. The angle of incidence, θ, can be calculated from Eq.(3.47) or in the other form of Eq.(3.48).

$$\delta = \frac{180}{\pi}(0.006918 - 0.399912cosB + 0.070257sinB - 0.006758cos2B + 0.000907sin2B - 0.002697cos3B + 0.00148sin3B) \quad (3.46)$$

$$\cos\theta = \sin\delta\sin\phi\cos\beta - \sin\delta\cos\phi\sin\beta\cos\gamma + \cos\delta\cos\phi\cos\beta\cos\omega + \cos\delta\sin\phi\sin\beta\cos\gamma\cos\omega + \cos\delta\sin\beta\sin\gamma\sin\omega \quad (3.47)$$

$$\cos\theta = \cos\theta_z cos\beta + sin\theta_z sin\beta\cos(\gamma_s - \gamma) \quad (3.48)$$

Using the above equations for calculating involved angles, the extraterrestrial irradiance that reaches the horizontal surface in the direction that perpendicular to the horizontal surface can be calculated from Eq. (3.49). When $G_{on\text{-}H}$ is known at the specific time of studying, the measured horizontal irradiance obtained from sensors (I_H) at a studied site can be compared to get the sky clearness index, k_T, calculated from Eq.(3.50). After obtaining the sky clearness index (k_T), the diffuse irradiance ($I_{d\text{-}H}$) which is a fraction of the total horizontal irradiance (I_H) can be calculated from Eq. (3.51).

Therefore, the beam irradiance on a horizontal plane can be obtained from Eq.(3.52). After knowing the components of solar irradiance on a horizontal surface, the components on a tilted surface can be traced back by analysing the incident angles of the tilted surface corresponding to the horizontal plane. On a tilted surface, the reflective irradiance from the surrounding can be included to get better accuracy, thus the total solar irradiance on a tilted surface can be obtained from Eq. (3.53) where the last term on the right-hand side is the reflective irradiance. Note that during sunrise and sunset time, the θ_z may approach 90^o which will make the R_b closer to enormous number leading to an overestimation of the beam radiation; therefore, in this thesis, the R_b is limited to the maximum of 10 at the time of sunrise and sunset.

Table 3.4 *The symbols, names and definitions of the angles involved in the calculation of solar irradiance on a tilted surface* (Duffie & Beckman, 2013)

Variable symbol	Variable name	Variable definition
ϕ	Latitude	the angular location north or south of the equator, north positive; $-90^o \leq \phi \leq 90^o$
δ	Declination	the angular position of the sun at solar noon (i.e., when the sun is on the local meridian) with respect to the plane of the equator, north positive; $-23.45^o \leq \delta \leq 23.45^o$
γ	Surface azimuth angle	the deviation of the projection on a horizontal plane of the normal to the surface from the local meridian, with zero due south, east negative, and west positive; $-180^\circ \leq \gamma \leq 180^\circ$.
β	Slope	the angle between the plane of the surface in question and the horizontal; $0^o \leq \beta \leq 180^o$. ($\beta > 90^o$ means that the surface has a downward-facing component)
ω	Hour angle	The angular displacement of the sun east or west of the local meridian due to the rotation of the earth on its axis at 15° per hour; morning negative, afternoon positive
θ	Angle of incidence	The angle between the beam radiation on a surface and the normal line of that surface
Θ_z	Zenith angle	The angle between the vertical and the line to the sun, that is, the angle of incidence of beam radiation on a horizontal surface
α_s	Solar altitude angle	The angle between the horizontal and the line to the sun, that is, the complement of the zenith angle
γ_s	Solar azimuth angle	The angular displacement from south of the projection of beam radiation on the horizontal plane. Displacements east of south are negative and west of south are positive

$$G_{on-H} = G_{on}\cos\theta_z \tag{3.49}$$

$$k_T = \frac{I_H}{G_{on-H}} \tag{3.50}$$

$$\frac{I_{d-H}}{I_H} = \begin{cases} 1.0 - 0.09k_T : (a) \\ 0.9511 - 0.1604k_T + 4.388k_T^2 - 16.638k_T^3 + 12.336k_T^4 : (b) \\ 0.165 : (c) \end{cases} \tag{3.51}$$

$$(a): for\ k_T \leq 0.22$$
$$(b): for\ 0.22 < k_T \leq 0.80$$
$$(c): for\ k_T > 0.8$$

$$I_{b-H} = I_H - I_{d-H} \quad (3.52)$$

$$I_T = I_{b-H}R_b + I_{d-H}\left(\frac{1+\cos\beta}{2}\right) + I_H\rho_g\left(\frac{1-\cos\beta}{2}\right) \quad (3.53)$$

$$where\ R_b = \frac{G_{bT}}{G_{bH}} = \frac{\cos\theta}{\cos\theta_z}$$

$$\rho_g\ is\ the\ reflectance\ of\ the\ surrounding\ surface$$

3.3 PV, PV/T and thermal collectors models' validations

3.3.1 PV cell 's model validation

Considering the Siemens SM46 PV module, the load voltage was varied from 0 Volt to the open-circuit voltage to obtain the I-V and P-V characteristics of the module. Shunt and series resistances are iterated until the I-V characteristic approaches the datasheet. Euclidean or L^2 norm error is used to monitor the simulated I-V to the datasheet as shown in Fig. 3.13.

According to Fig. 3.13, the first iteration starts with the first guess of shunt resistance of 54 Ω and series resistance of 0.54 Ω according to Eqs. (3.7) and (3.8) respectively. Series resistance will be fixed and shunt resistance is increased until the L^2 norm error is the lowest possible which happens at shunt resistance equals to infinity in this case (at 4th iteration in Fig. 3.13). Series resistance then changed to the ideal condition which is 0Ω (at 5th iteration in Fig. 3.13) then slightly increased until the L^2 norm error does not furtherly reduce (at 9th iteration in Fig. 3.13).

Using the developed correlations of R_{SH} and R_S in Eqs. (3.10) and (3.11), the calculated I-V characteristic under different conditions satisfactorily agree with the datasheets of the Siemens SM46 PV module and the Solarex MSX-60 PV module as shown in Fig. 3.14 and Fig. 3.15 respectively.

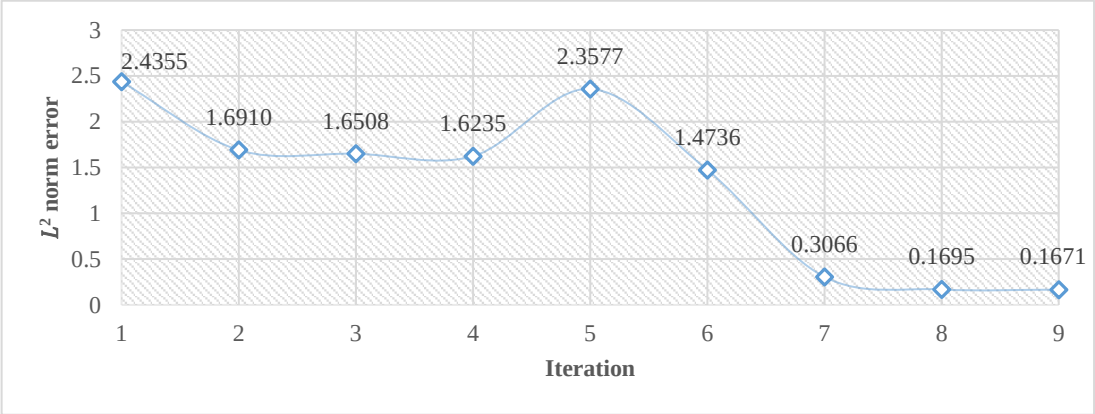

Fig. 3.13 *L^2 norm error of simulated PV current compared with the datasheet of Siemens SM46 PV on STC from iterations of different shunt and series resistances*

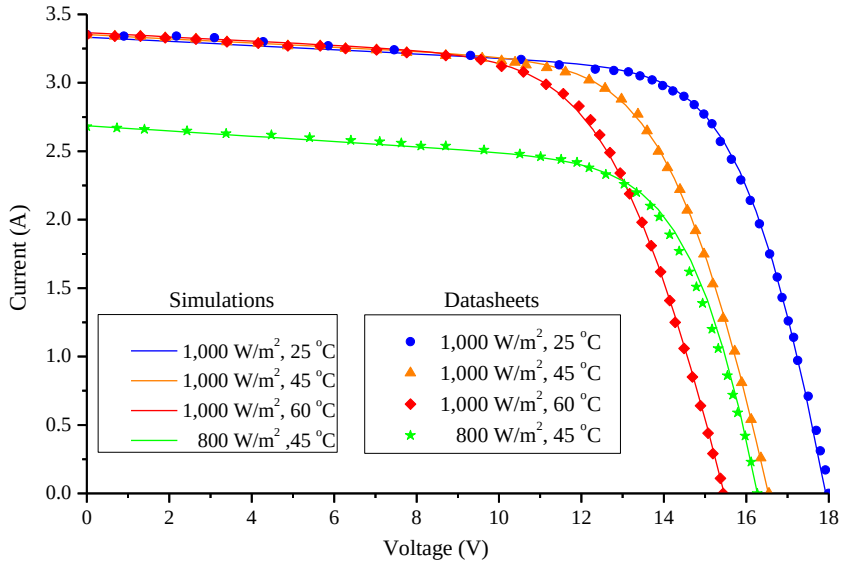

Fig. 3.14 *Verification of simulation results with the datasheet of I-V characteristics in different conditions for Siemens SM46 PV module.*

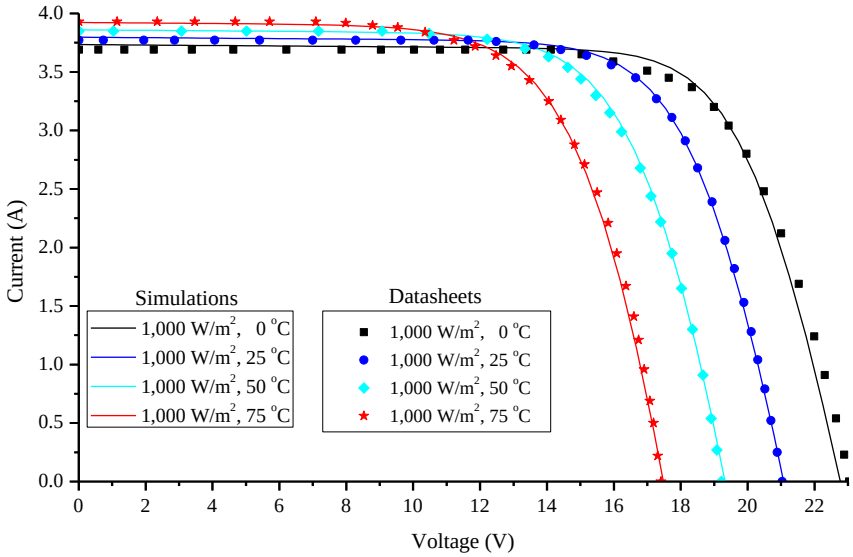

Fig. 3.15 *Verification of simulation results with the datasheet of I-V characteristics in different conditions for Solarex MSX-60 PV module.*

Compared to using the R_S and R_{SH} value from the calculation of V_{OC}/I_{SC}, using these modified equations of R_S and R_{SH} made the average error of electrical power output at MPP reduce from 1.59% to 0.52% for Siemens SM46 PV module, from 1.50% to 1.04% for Solarex MSX-60 PV module. The reduction of the average error over the low PV cell temperature range studied are insignificant, the errors at medium to high PV cell temperatures are substantially decreased. For example, the error of the PV power outputs operating at 60 °C at MPP reduces from 3.57% to 0.85% for Siemens SM46 PV module. Therefore, when the PV cell is used at medium to high temperatures, the modified correlations in Eqs. (3.10) and (3.11) are worth applying for better accuracy.

The other validation is done by using the experimental data from (Jazayeri, Uysal & Jazayeri, 2013) with the short-circuit current (I_{sc}) of 2.57 A, the open-circuit voltage (V_{oc}) of 21.6 V, the ideal factor of 1.3, and the temperature coefficient of short-circuit current (K_i) of 2 mA/ ^oC with 1,000 W/m^2 and the PV cell temperature was measured to be 32 ^oC. The PV module simulation result of the I-V curve is in a good match of the experimental data from (Jazayeri, Uysal & Jazayeri, 2013) as illustrated in Fig. 3.16.

Note that shunt and series resistances are modified to make the simulated data matches to the experimental data as when the experiments performed, added circuit lines from PV panel to the maximum power point controller and loads will increase the series resistance of the system, leads to the change of I-V characteristic of the PV module. Additional losses also happen, and they are represented as a shunt resistance in the simulation model. In Fig. 3.16, shunt resistance is adjusted to 135 Ω and series resistance is verified to be 0.9 Ω at the lowest L^2 norm error. After the PV's electrical characteristics are validated, it is assured that the mathematical model of the PV cell is accurate and is appropriate to be used in a wide range of cell's temperature up to 100 ^oC.

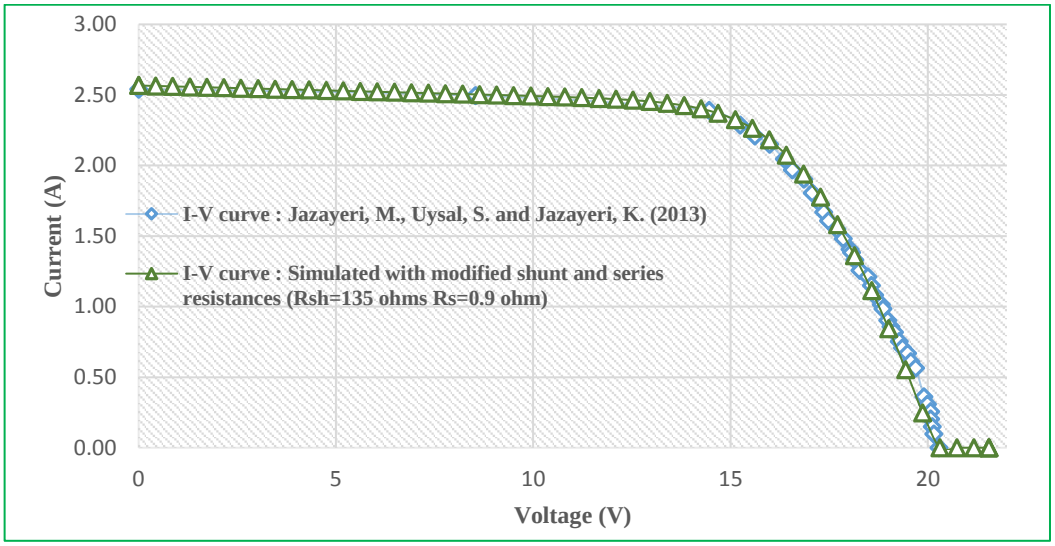

Fig. 3.16 *Simulated P-V characteristic of Siemen SM 46 on 1,000 W/m^2 and 32 degree Celsius of PV temperature with R_s=0.9Ω and R_{sh}=135Ω compared with the data from* (Jazayeri, Uysal & Jazayeri, 2013)

3.3.2 PV collector validation

Firstly, because the mathematical model of the PV is complicated which is not suitable to input as a using the user-defined function (UDF) into ANSYS Fluent; the correlation of the maximum power as the function of irradiance and PV-temperature conditions were developed by using the surface fitting in MATLAB as shown in Fig. 3.17 with the equation presented in Eq.(3.54). Eq. (3.54) will be attached as a negative energy source (sink) in ANSYS Fluent to represent a fraction of energy that the PV layer absorbs and transforms to electricity instead of heat by UDF to interpret the heat source (sink) in the PV layer.

$$\begin{aligned} P_{pv}(T_{pv}, G) = {} & p_{00} + p_{10}T_{pv} + p_{01}G + p_{20}T_{pv}^2 + p_{11}T_{pv}G + p_{02}G^2 + p_{30}T_{pv}^3 \\ & + p_{21}T_{pv}^2G + p_{12}T_{pv}G^2 + p_{03}G^3 + p_{40}T_{pv}^4 + p_{31}T_{pv}^3G + p_{22}T_{pv}^2G^2 \\ & + p_{13}T_{pv}G^3 + p_{04}G^4 + p_{50}T_{pv}^5 + p_{41}T_{pv}^4G + p_{32}T_{pv}^3G^2 + p_{23}T_{pv}^2G^3 \\ & + p_{14}T_{pv}G^4 + p_{05}G^5 \end{aligned} \tag{3.54}$$

where T_{pv} is the PV cell temperature (K)

G is the irradiance (W/m^2)

All coefficients with 95% confidence bounds are

p_{00} = 661.3000 (-1.119e+04, 1.251e+04)

p_{10} = -10.8000 (-195.8, 174.2)

p_{01} = 0.5843 (-2.398, 3.566)

p_{20} = 0.06982 (-1.083, 1.222)

p_{11} = -0.00456 (-0.04116, 0.03204)

p_{02} = 0.0003155 (-0.0006787, 0.00131)

p_{30} = -0.0002245 (-0.003806, 0.003357)

p_{21} = 1.871e-05 (-0.00015, 0.0001875)

p_{12} = 2.593e-07 (-8.493e-06, 9.011e-06)

p_{03} = -6.927e-07 (-1.049e-06, -3.364e-07)

p_{40} = 3.597e-07 (-5.194e-06, 5.913e-06)

p_{31} = -3.874e-08 (-3.852e-07, 3.077e-07)

p_{22} = -2.331e-09 (-2.854e-08, 2.388e-08)

p_{13} = 5.745e-10 (-1.327e-09, 2.476e-09)

p_{04} = 5.717e-10 (4.396e-10, 7.037e-10)

p_{50} = -2.299e-10 (-3.666e-09, 3.206e-09)

p_{41} = 2.927e-11 (-2.38e-10, 2.965e-10)

p_{32} = 2.442e-12 (-2.424e-11, 2.913e-11)

p_{23} = 9.227e-14 (-2.703e-12, 2.887e-12)

p_{14} = -3.113e-13 (-6.086e-13, -1.414e-14)

p_{05} = -1.719e-13 (-2.083e-13, -1.355e-13)

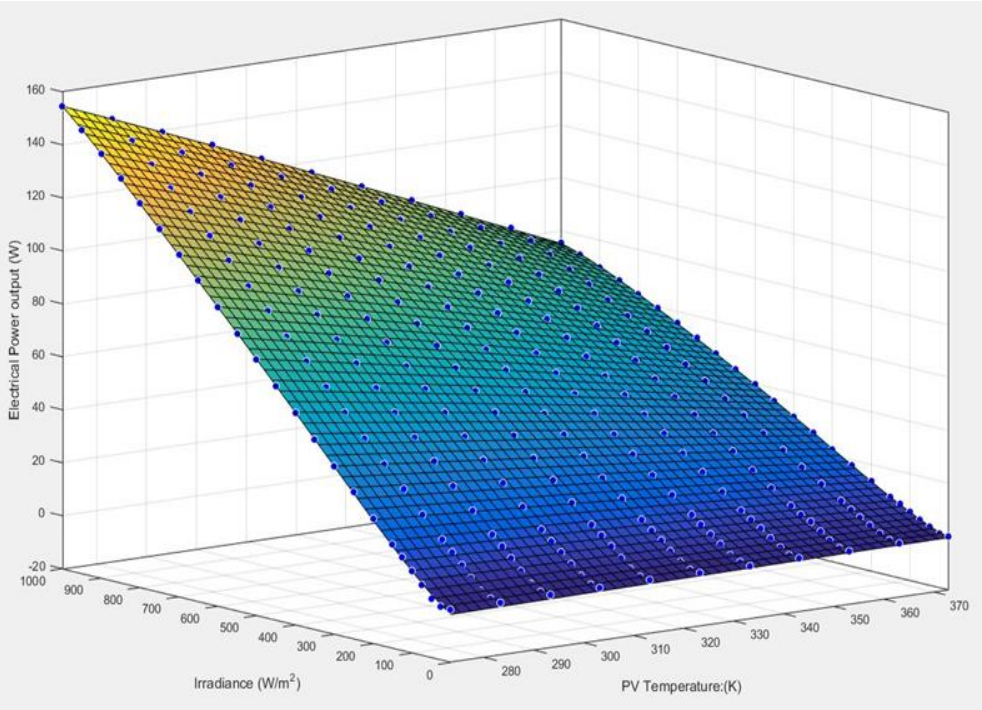

Fig. 3.17 *The fitting result of electrical power output (W) as a function of Irradiance and PV cell temperature*

After obtaining the power output function of the PV cell's layer, the developed PV model that uses the modified equations of R_S and R_{SH} was then validated by using one-day real weather data and the real PV panel's experimental data of electrical power output from Tsai *et al.* (2012). The experiment from Tsai *et al.*(2012) contains six main components which are the SM46 PV module, the SunSaver10 MPPT controller, battery storage, electric load (fan), two multimeters, a wind monitor (Young model 05013 V), temperature sensors (TES-1314) and an irradiance sensor (Fronius Mono-Crystalline Si-Sensor). The experiment was performed at Da-Yeh University in Taiwan with the tilted angle of the PV module of 23.5^o with south-facing direction. The experimental data was collected and visualised using the LABVIEW software with 5-minute time-step size from 08:00 AM to 04:00 PM on a summer day in 2011.

Fig. 3.18 shows the great agreement between the simulated PV electrical power output at MPP and the measured data reported in (Tsai & Tsai, 2012), the average error is 2.55% with 0.66 W average absolute difference. To validate the thermal analysis model, the simulation results of the PV cell temperatures was compared with the measured data provided by (Tsai & Tsai, 2012) (in Fig. 3.19), there was an average relative error of 4.57% with an average absolute difference of 2.03 K, that implies that the PV model coupled with the CFD model developed in this work is reasonably reliable.

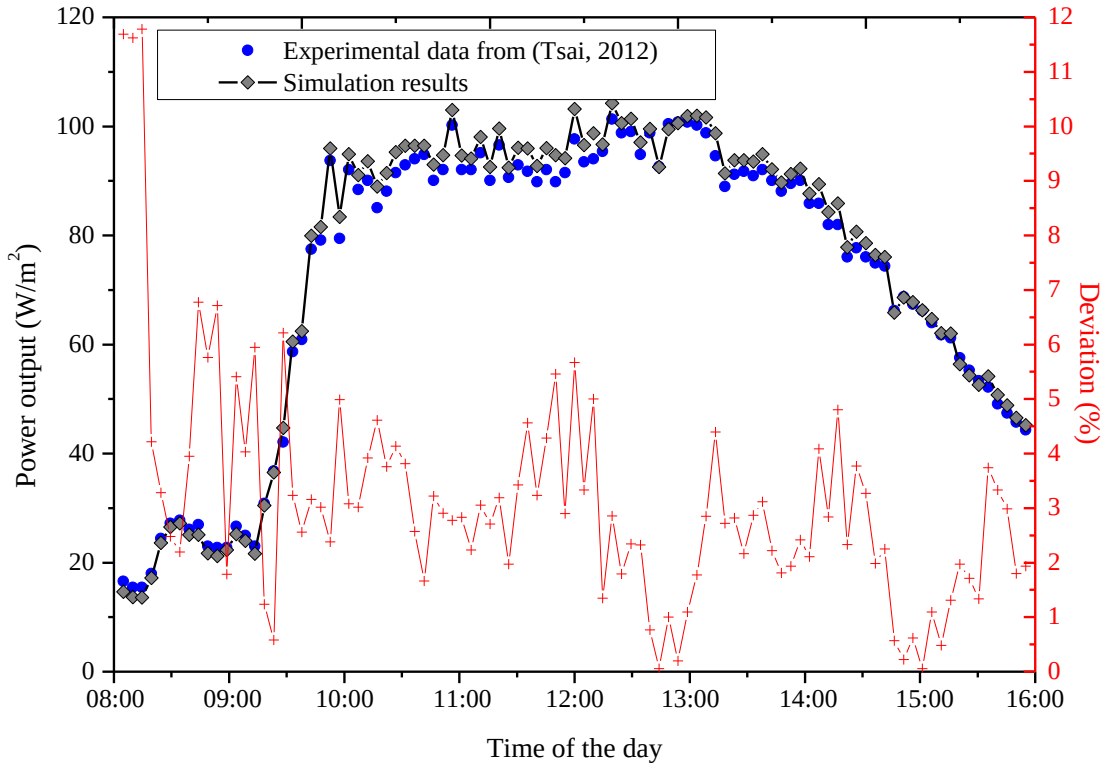

Fig. 3.18 *PV Electrical power output between the measured data from* (Tsai & Tsai, 2012) *of and the simulation results.*

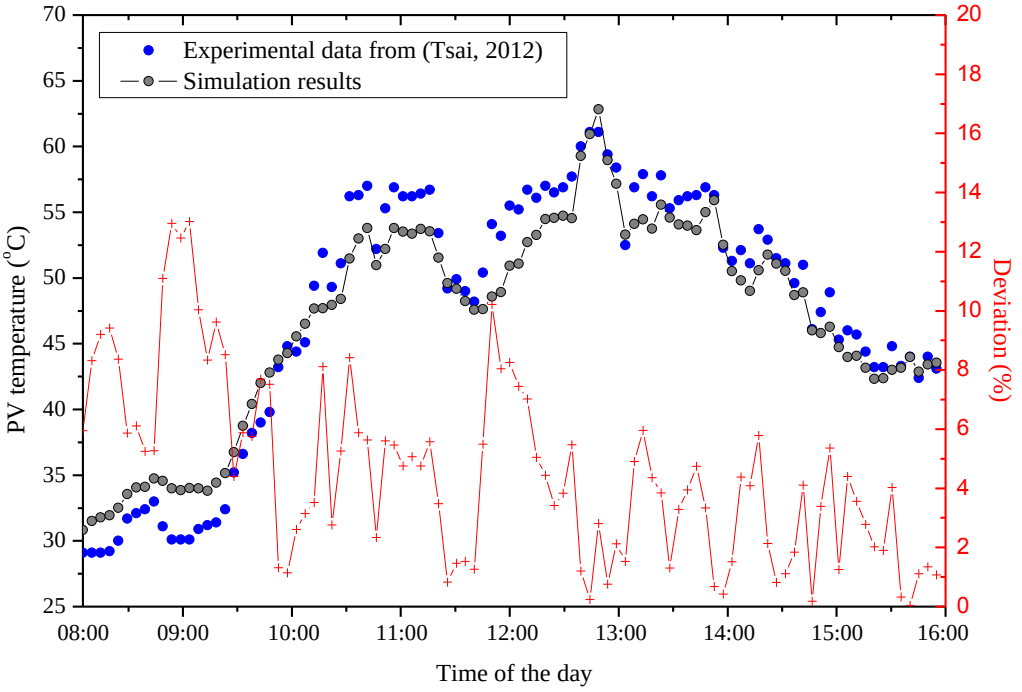

Fig. 3.19 *PV temperatures between the measured data from* (Tsai & Tsai, 2012) *and the simulated volume-weighted average temperature.*

3.4 The production of electrical power and heat of the PV, PV/T and thermal collector in Newcastle upon Tyne, UK

The weather data of sunny and cloudy days in spring, summer, autumn and in Newcastle Upon Tyne are used as a case study to explore the potential hot water production by the studied solar energy conversion technologies. In case of the PV/Ts and thermal collector, the water outlet temperature was preset at 10 targeted points but only 40 °C, 60 °C, 80 °C and 100 °C target points are mostly presented because of the readability in figures. The target temperatures were achieved by varying the water flow velocity so that to cope with the desorption heat requirement of the thermochemical sorption storage unit. The weather data in 2005 was chosen because of the completeness and free availability of the data. The sunny and cloudy days in each season were manually selected corresponding to the irradiance profiles and the chosen days are shown in Table 3.5. All simulation cases were considered with the 30-minute time-step size. Those chosen days present the best profiles for the studied weather conditions and they were close to the middle of each season to represent the best conditions for each season. More accuracy may be easily obtained by calculating all days of the year; however, because of the limited time of the PhD, it is not feasible to do the time-consuming computational tasks for all 365 days with several setting conditions.

Table 3.5 *The chosen days of the year for the studies*

Season	Weather condition	Day of the year	Chosen day
Spring	Sunny	100	10th April 2005
	Cloudy	104	14th April 2005
Summer	Sunny	179	28th June 2005
	Cloudy	180	29th June 2005
Autumn	Sunny	247	4th September 2005
	Cloudy	250	7th September 2005
Winter	Sunny	341	7th December 2005
	Cloudy	343	9th December 2005

3.4.1 PV panel energy production in Newcastle upon Tyne

According to the weather data in Newcastle upon Tyne, the solar irradiance at the tilted angle of 40^{o} (annual optimum tilted angle for Newcastle upon Tyne) in each season is presented in Fig. 3.20(a) for sunny days and Fig. 3.20(b) for cloudy days. The ambient temperature is also shown in Fig. 3.21(a) for sunny days and Fig. 3.21(b) for cloudy days. Because the optimum tilted angle was applied and fixed, the solar irradiance in spring and autumn is slightly lower than the irradiance in summer on sunny days. In cloudy days, solar irradiance in spring, summer and autumn is similar because only diffuse radiation reaches the panel which is fairly the same in those 3 seasons. In terms of ambient temperature, the daily variation is comparatively stable regardless of the sunny days and cloudy days in all season.

Applying the PV model mentioned in chapter 3, the electrical power production was achieved as shown in Fig. 3.22. In sunny days (Fig. 3.22(a)), the electrical power production of the PV panel in spring is comparable to the production in summer during 11 AM ~ 4 PM. One of the reasons is because of the lower ambient temperature in spring approximately 7 ^{o}C than in summer, leading to lower PV cells' temperature as presented in Fig. 3.23(a), resulting in higher conversion efficiency as shown in Fig. 3.24(a). The conversion efficiency of the PV cells also depends on the level of solar irradiance. When the solar irradiance is low, during early morning and late afternoon, the conversion efficiency is also low as illustrated in Fig. 3.24

regardless of the positive effect of lower cell's temperature. The flatten conversion efficiency drop during midday in sunny days is because of the high PV cell temperature from absorbing more solar irradiation. The conversion efficiency in sunny winter days is impressively high compared to other seasons due to the very low ambient temperature; however, because of the low irradiance input, the electrical power production in winter is comparatively low.

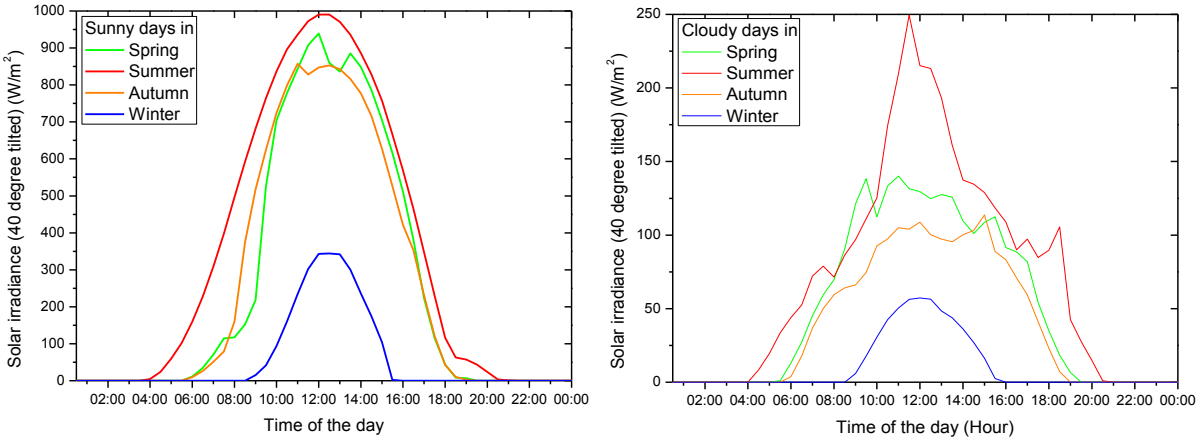

(a) (b)

Fig. 3.20 *Solar irradiance at 40^o tilted angle in Newcastle upon Tyne for all seasons in (a) sunny days and (b) cloudy days*

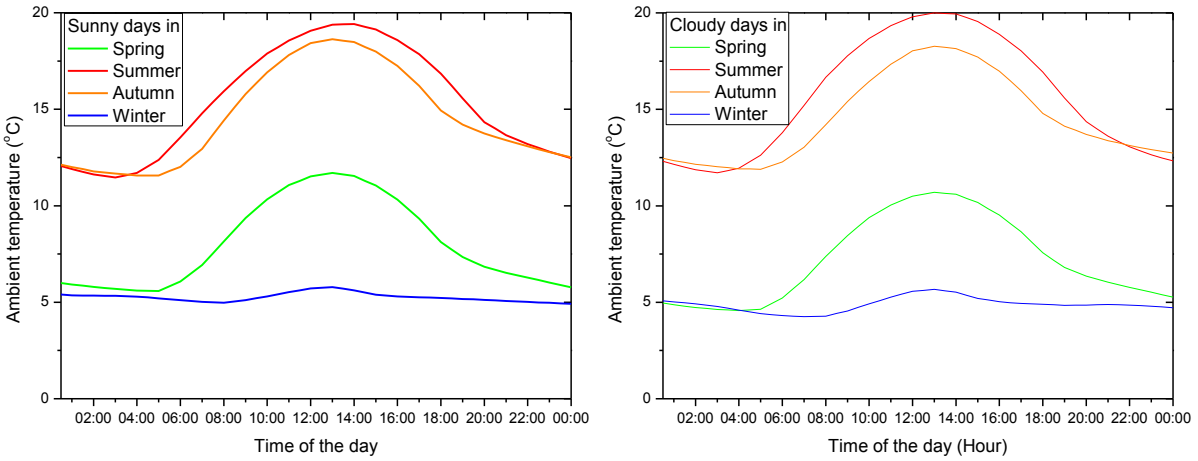

(a) (b)

Fig. 3.21 *Ambient temperature in Newcastle upon Tyne for all seasons in (a) sunny days and (b) cloudy days*

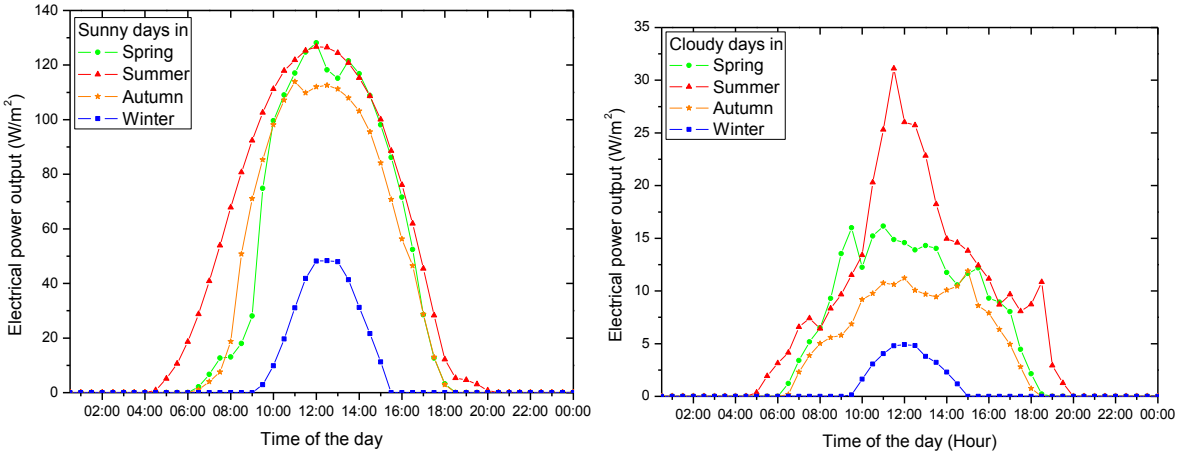

(a) (b)

Fig. 3.22 *The electrical power production from the PV module in each season: (a) in sunny days, (b) in cloudy days*

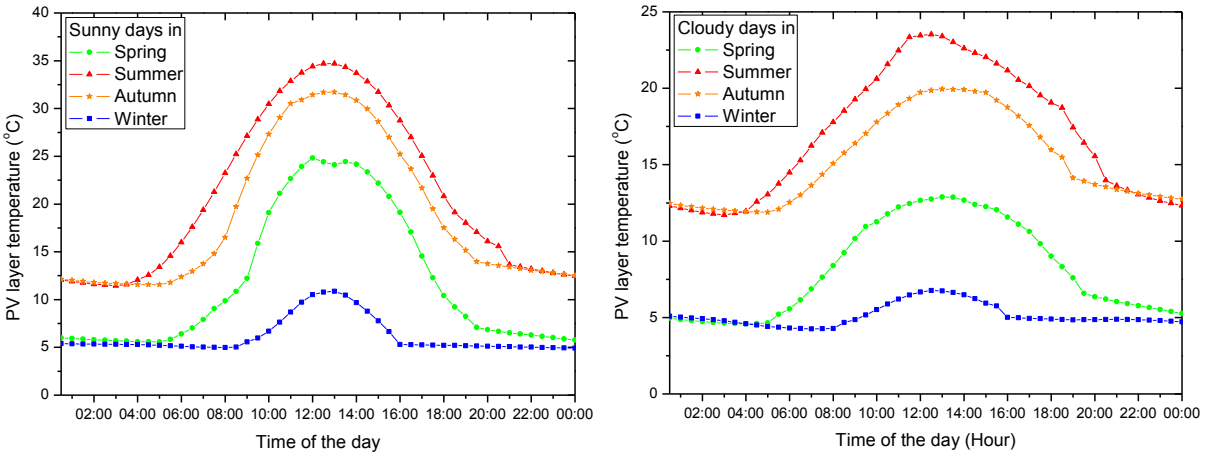

(a) (b)

Fig. 3.23 *The PV layer temperature of the PV module in each season: (a) in sunny days, (b) in cloudy days*

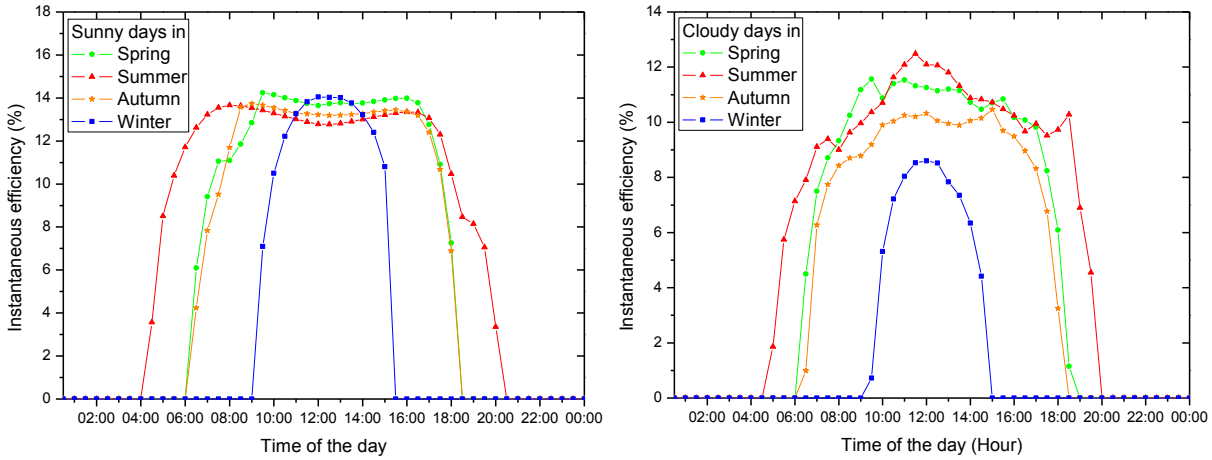

(a) (b)

Fig. 3.24 *The instantaneous conversion efficiency of the PV module in each season: (a) in sunny days, (b) in cloudy days*

3.4.2 PV/T energy production in Newcastle upon Tyne

The half-hourly variation profile of the hot water output temperature at different preset points and the corresponding solar irradiation in 3 different seasons are shown in Fig. 3.25 for the PV/T with the air gap (PV/T-AG). The calculation started when solar radiation was firstly available on the chosen days. The inlet water temperature was assumed to be the same temperature as the ambient temperature of the first time-step of each considered day. Solar irradiance was increasing in the morning, but it was not intense enough to heat up the water in the absorber tube to the targeted temperature levels until 07:00 ~10:00 am in summer, 10:00 am ~12:00 pm in spring and 09:30 ~11:00 am in autumn depending on different targets. Before that, it was assumed a stagnation condition of the water loop, i.e. no fluid flowing in the collector, until the stationary water was heated up to the targeted temperature resulting in the uniform increasing temperature over the PV/T panel area. Since then, the water circulation started and the flow rate was afterwards adjusted according to the varying irradiation in each season as shown in Fig. 3.26.

The lower targeted output temperature, the higher water mass flow rate allowed (Fig. 3.26) and the higher average thermal efficiency obtained as well as electrical efficiency (Fig. 3.27), i.e. higher overall energy efficiency of the PV/T collector, because the lower PV/T temperature means lower heat loss and it is beneficial for electrical power generation. The instantaneous efficiency was used in this thesis not only for indicating the performance of the conversion technologies along the day but also for monitoring the initial time of the day that the conversion technologies generate the output HTF temperature at a specifically targeted temperature level.

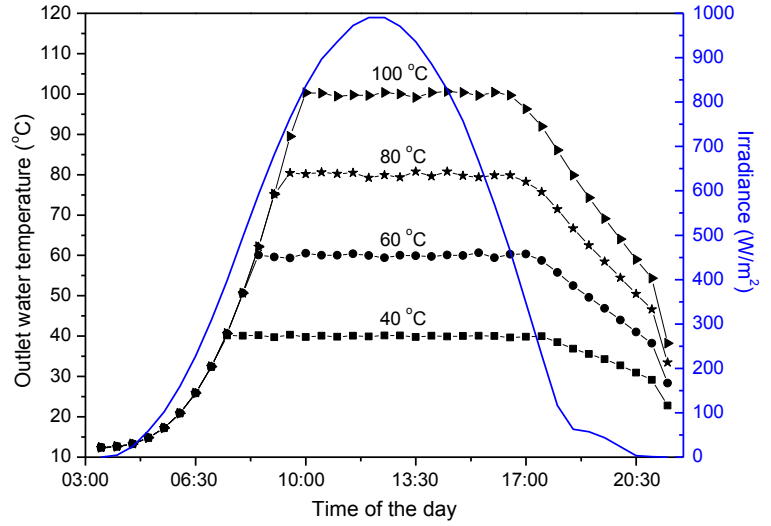

(a)

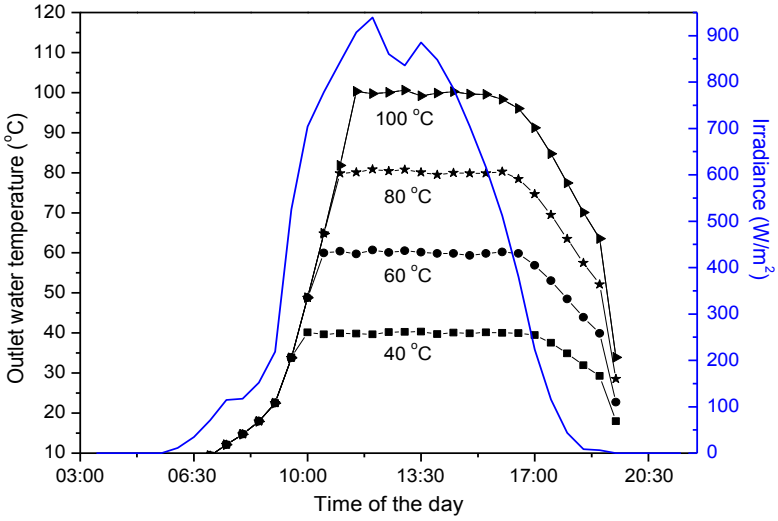

(b)

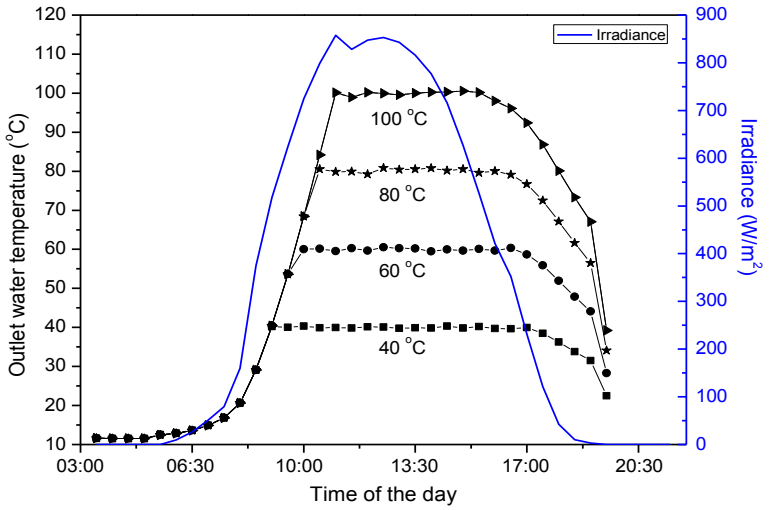

(c)

Fig. 3.25 *The water output temperature at different targeted levels from the PV/T with airgap collector in Newcastle upon Tyne, UK; (a) on a sunny summer day, (b) on a sunny spring day and (c) on a sunny autumn day.*

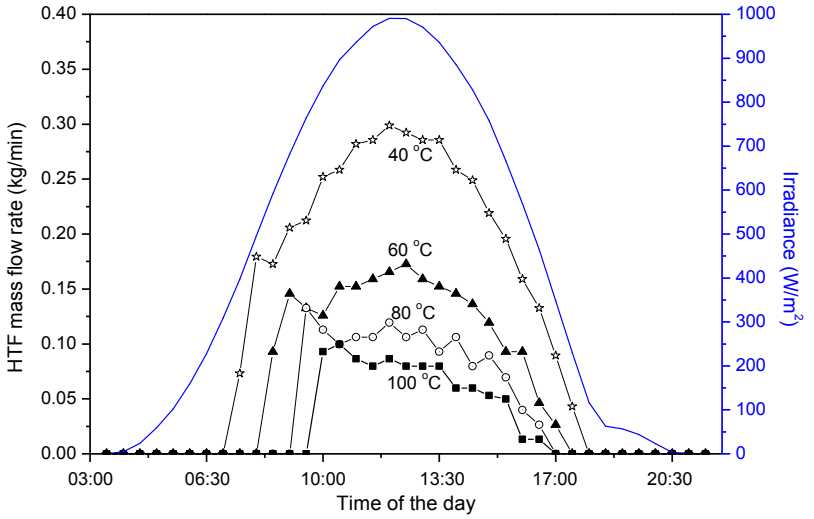

(a)

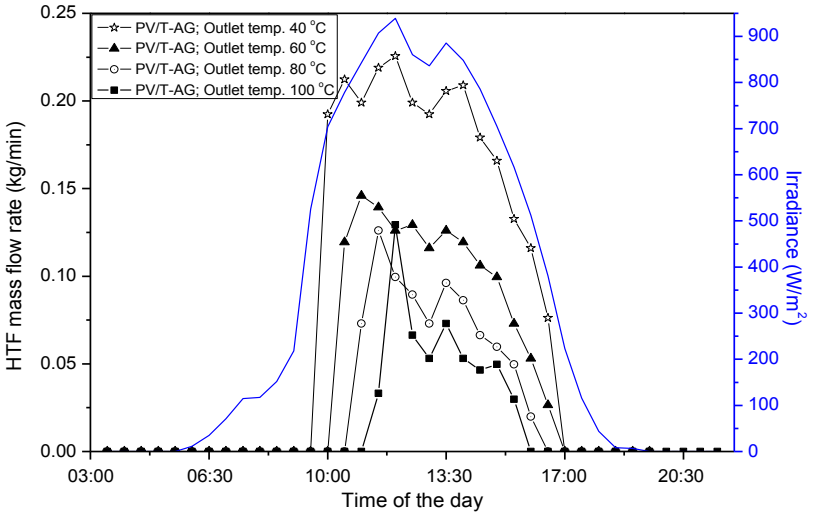

(b)

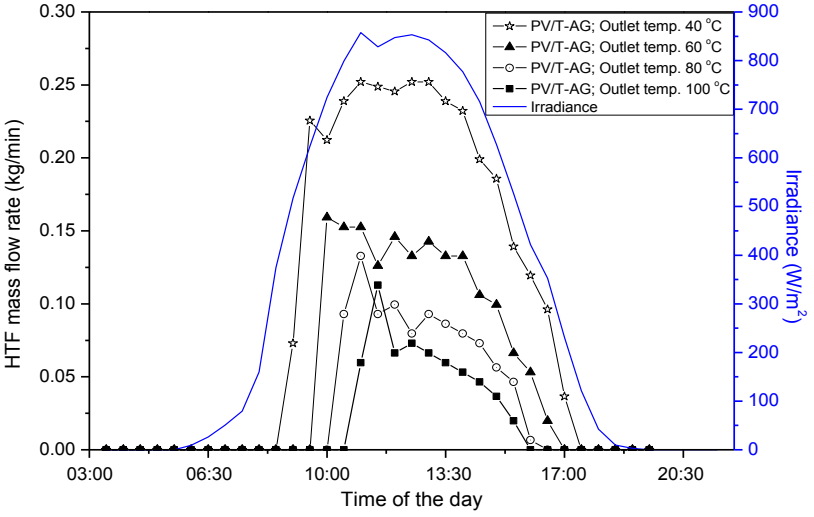

(c)

Fig. 3.26 *The mass flow rate of the output fluid at different targeted temperature from the PV/T with air gap models in Newcastle upon Tyne, UK; (a) on a sunny summer day, (b) on a sunny spring day and (c) on a sunny autumn day.*

It is noted that, when there was a stagnation situation of the water loop with the water temperature inside the PV/T increasing while it was absorbing energy from the sun, the useful thermal efficiency was considered to be zero because there was no thermal energy carried out of the PV/T panel. The higher the set output temperature, the longer time it waited before the water pump started working. The moment when the water pump started, the average water temperature in the PV/T collector as a whole reached the targeted level as there was a nearly uniform temperature all over the collector in a stagnation condition. That led to the highest instantaneous useful thermal efficiency and a drop of instantaneous electrical efficiency, and this phenomenon is more obvious for the cases requiring higher temperature water output, e.g. 80 °C and 100 °C curves in Fig. 3.27. Once the water flowed and the freshwater at ambient temperature came into the absorber tubes, the average water temperature inside the PV/T collector dropped and the water flow rate in the next time step had to be adjusted lower accordingly to be able to deliver the targeted high-temperature water output. Afterwards, the water flow rate increased again in the 40 °C and 60 °C curves as the increasing irradiance was intense enough to produce qualified water with relatively flat profile of thermal efficiency during the daytime; otherwise, for the 80 °C and 100 °C curves, the flow rate and the thermal efficiency decreased in a zig-zag pattern as the time went on.

The half-hourly variation profile of the water output temperature at different preset points on a sunny summer day for the PV/T collector without air gap (PV/T-no-AG) is shown in Fig. 3.28. It is not surprising to learn that under the given climatic condition the water temperature of the PV/T-no-AG type cannot be heated higher than about 43 °C even in a stagnation condition all day long. The wind speed and ambient temperature can have considerable influence on the effective heat delivered, especially in the cold region even though in the sunny days the heat loss to the ambient could be much more compared to the PV/T-AG type. Therefore, it can be concluded that the addition of air insulation layer is significant to enhance the thermal energy output of the PV/T collector especially for the weather conditions similar to that in Newcastle upon Tyne.

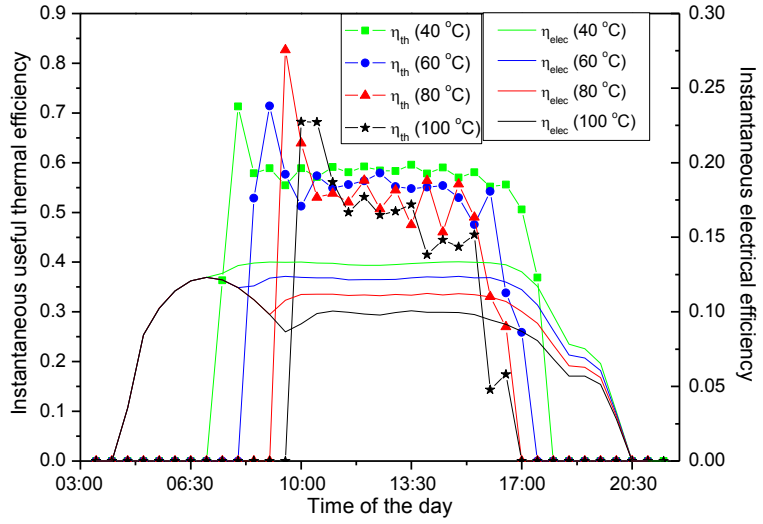

(a)

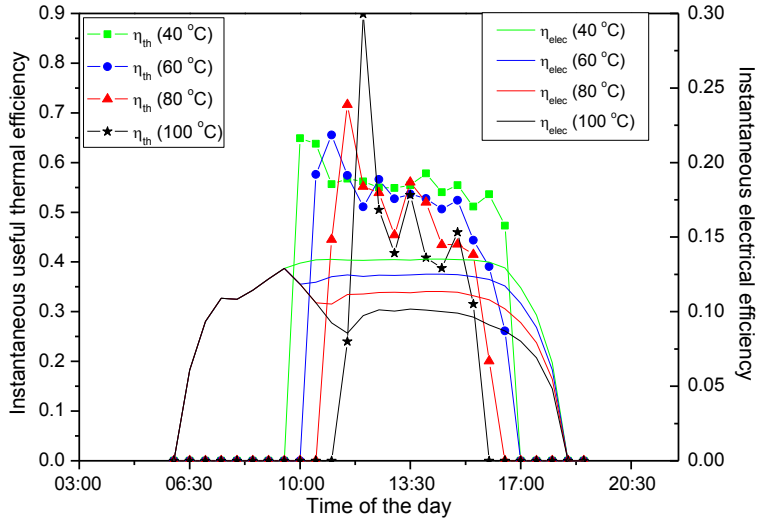

(b)

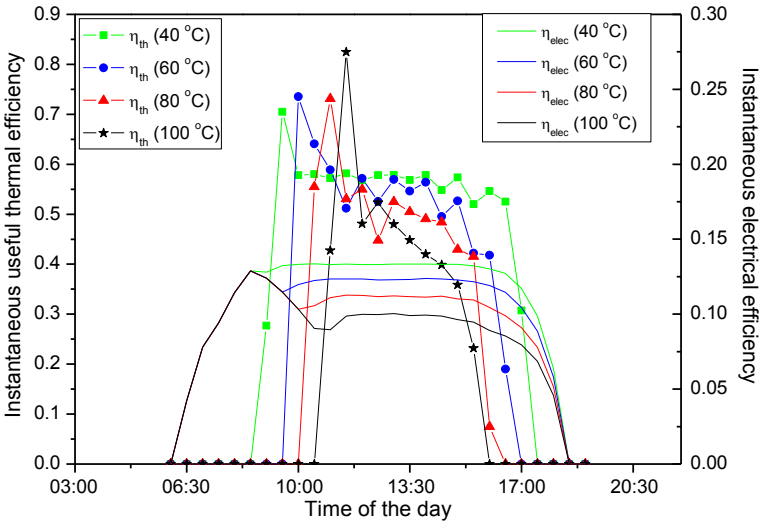

(c)

Fig. 3.27 *Instantaneous thermal efficiency and electrical efficiency of the PV/T collector with the air gap in Newcastle upon Tyne, UK; (a) on a sunny summer day, (b) on a sunny spring day and (c) on a sunny autumn day.*

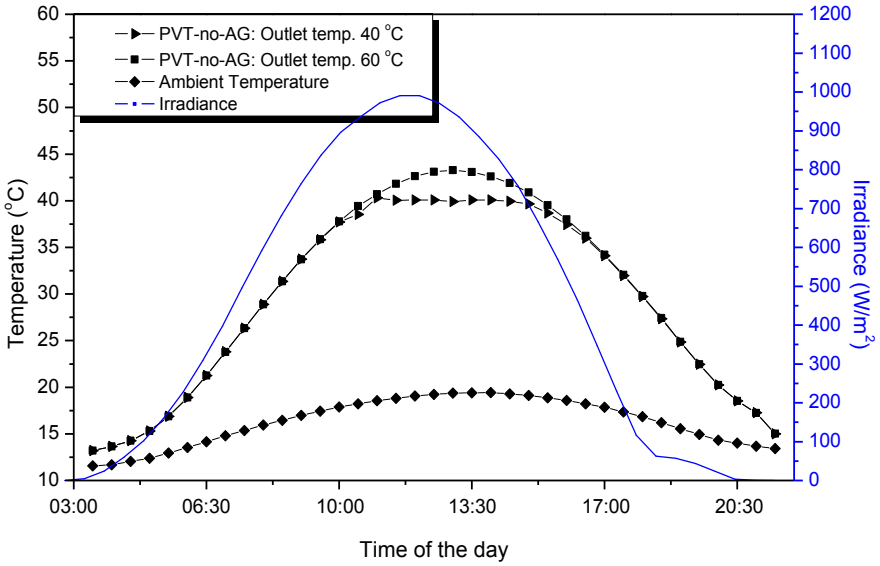

Fig. 3.28 *The water output temperature at different targeted levels from the PV/T without airgap collectors on a sunny summer day in Newcastle upon Tyne, UK.*

Electrical power production from the PV/T-AG collector and PV/T-no-AG collector on a sunny summer day are shown in Fig. 3.29(a) and Fig. 3.30 respectively in comparison with the production from the PV panel. The 40 °C curve of the PV/T-AG collector is closer to the reference PV curve, and has a slightly higher maximum power output during the mid-day than that of the reference PV curve; whereas, the electrical power gradually reduces with the increasing water output temperature, as the maximum power output on the 100 °C curve is about 23% lower than that of the reference PV curve. In general, the normal PV/T collector even without air gap design would be expected to produce more electrical power than the PV-only panel. However, in this work, the PV/T-no-AG collector operated under a stagnation condition of the water loop most of the time, which in fact to some extent hampered the heat dissipation and increased the PV cell temperature, as shown in Fig. 3.28. Because higher PV cell temperature has a detrimental effect on electrical power generation, and the average PV cell temperature of the PV/T-no-AG collector is always higher than the reference PV panel, which explains the less production from the PV/T-no-AG collector than that of the reference PV panel. With the same reason, the power output curve of the reference PV panel is in between the 40 °C and 60 °C curves for the PV/T-AG collector, it is echoed by the comparison between the PV cell temperature curves in Fig. 3.31. It also implies that if the electrical generation from the PV/T-AG is of primary, the outlet temperature should be kept lower than 40 °C to have tangible improvement in electrical efficiency.

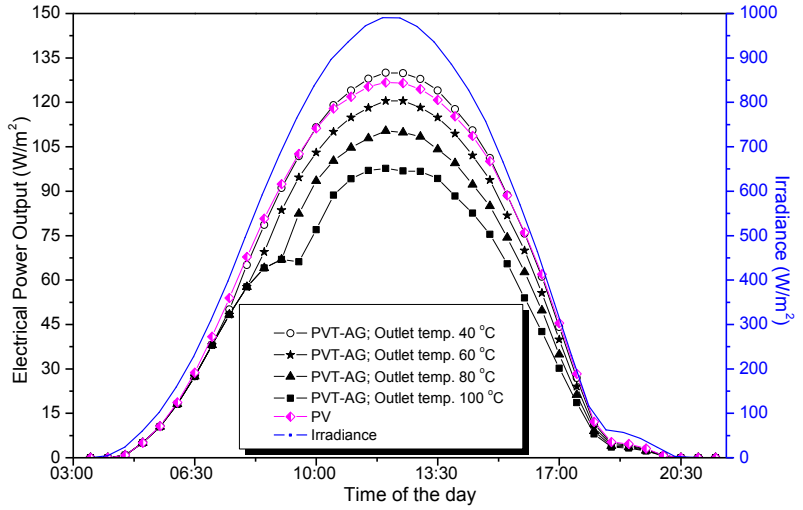

(a)

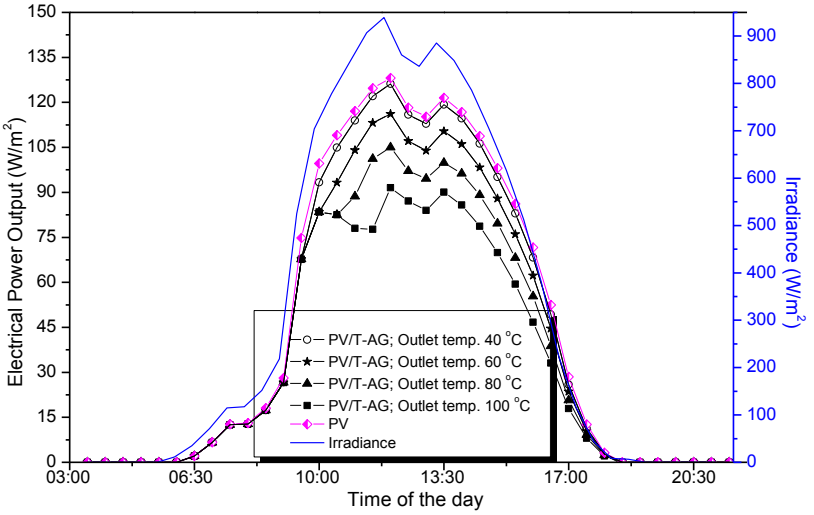

(b)

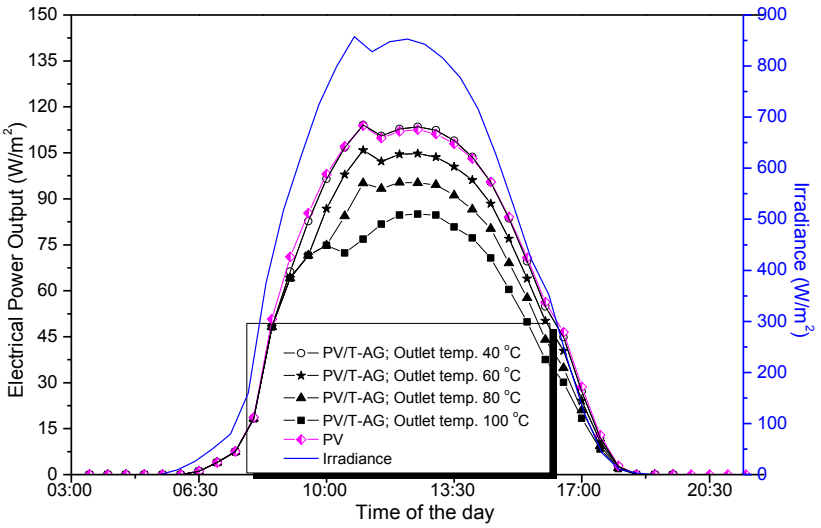

(c)

Fig. 3.29 *The electrical power output from the PV/T with airgap models in Newcastle upon Tyne, UK; (a) on a sunny summer day , (b) on a sunny spring day and (c) on a sunny autumn day.*

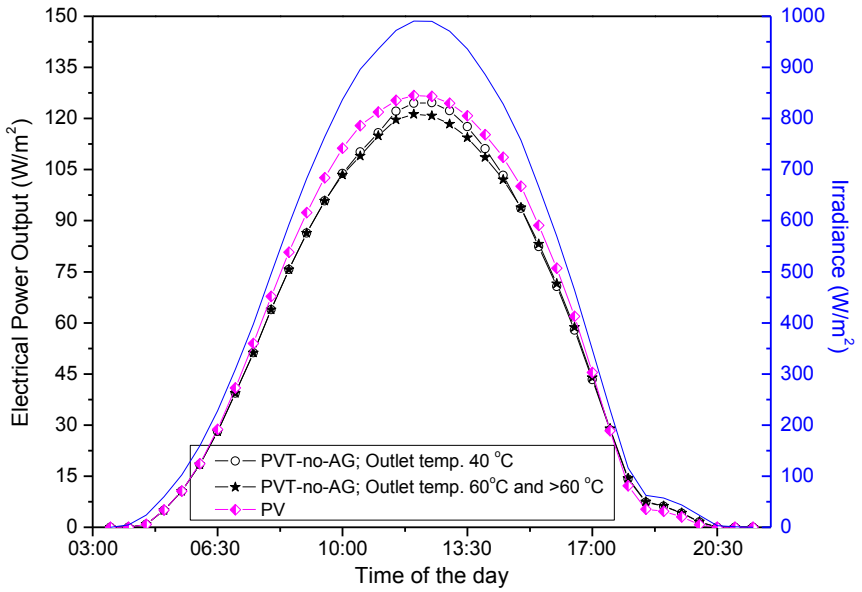

Fig. 3.30 *The electrical power output from the PV/T without airgap models on a sunny summer day in Newcastle upon Tyne, UK.*

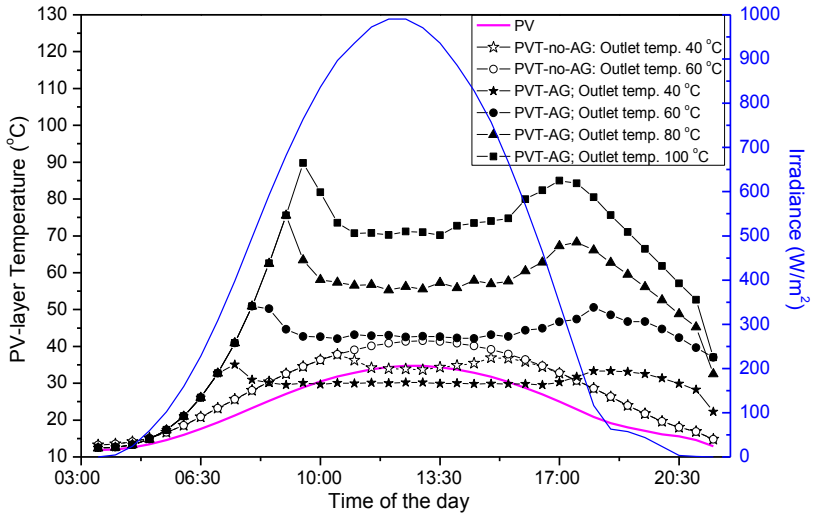

(a)

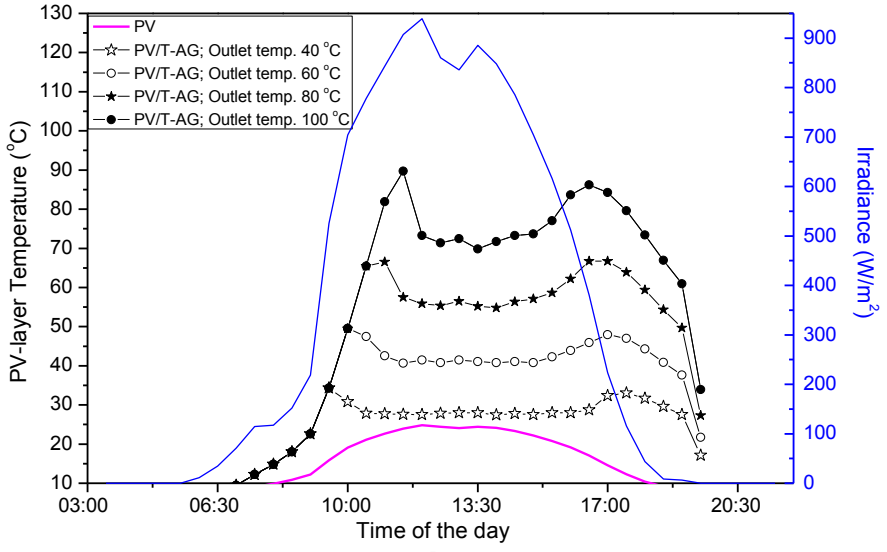

(b)

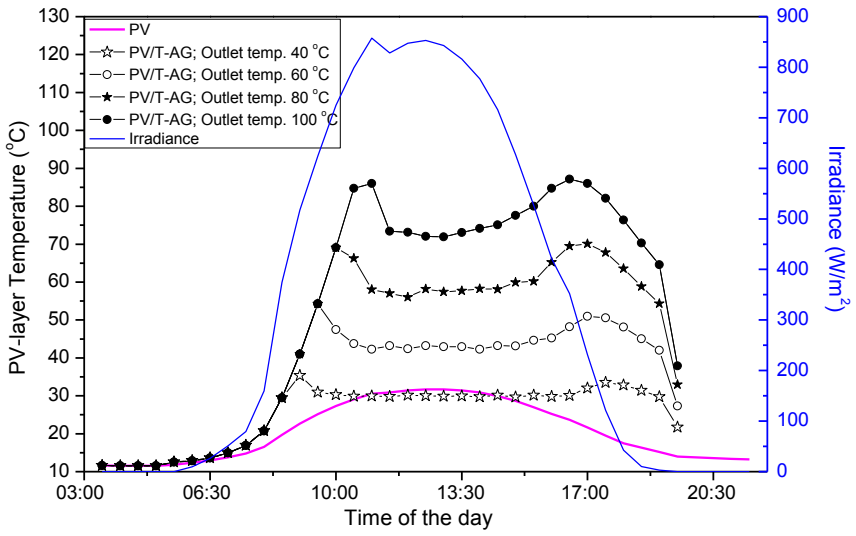

(c)

Fig. 3.31 *The PV-cell temperature of the PV/T collectors in Newcastle upon Tyne, UK; (a) on a sunny summer day, (b) on a sunny spring day and (c) on a sunny autumn day.*

3.4.3 Thermal collector energy production in Newcastle upon Tyne

Following the typical design of the thermal collector which contains double-glass cover (T-AG) to maximise thermal efficiency as described in previous sections, the results supportably show that the heat loss in the T-AG is lower than the PV/T-AG; therefore, the outlet HTF temperature of the T-AG (as shown in Fig. 3.32) increases faster than the PV/T-AG (in Fig. 3.25) leading to the earlier starting time of operation. Using the sunny summer day as an example, the outlet water temperature from the T-AG reaches 40 ^{o}C at around 6:30am while it is at 7am in the PV/T-AG technology.

The other reason of higher thermal efficiency in the T-AG than the PV/T_AG is that the T-AG does not have the PV cells that convert part of the incoming energy into electricity; therefore, all the absorbed energy is totally transformed into thermal energy. For example, under the same weather condition on a sunny summer day, the average thermal efficiency of the T-AG is 73.84% compared to 53.22% of the PV/T-AG. Those reasons contribute the T-AG to produce more hot water output as presented in Fig. 3.33.

Considering the water output temperatures of the T-AG in each season (in Fig. 3.32), when the output temperature is low, e.g. 40 ^{o}C, the output temperature could be stably controlled at the targeted value with minimal oscillations. However, when the targeted output temperature is getting higher, the controlled output temperatures oscillate with higher amplitude correspondingly. The reason of these phenomena might be because of the numerical error due to the sweep-step of the mass flow rate in the coding. For example, at each time-step, this thesis

set the sweep-step of the mass flow rate (MFR) of 0.0001 kg/s to numerically find the closest MFR that provide the target temperature output. ANSYS Fluent will adjust the initial MFR of the flow field according to the HTF outlet temperature. If the HTF outlet temperature is higher than the target temperature, the initial MFR at the inlet will incrementally increase by 1 sweep-step until the HTF outlet temperature reduces to the target temperature. However, if the sweep-step is too big, ANSYS Fluent may not be able to get the solution as the initial MFR will be skipped the solution MFR back and forth. If the sweep-step is too small, the initial MFR may not reach the solution as the ANSYS Fluent cannot increase the initial MFR fast enough before other residuals reach the thresholds. To get the solution, solution's residuals may be set to very low which is also contribute the more accuracy solution; however, it leads to an extremely high computational expense which is not practical for this thesis timescale. The sweep-step in this thesis was carefully chosen to provide acceptable deviations as presented in the validation section and also maintain the solutions' accuracy in a numerical aspect. The oscillations also happened with the mass flow rate as shown in Fig. 3.33.

Considering the thermal efficiency in the T-AG, at the starting of the HTF flow as shown in Fig. 3.34, the spikes can be described as already mentioned in the PV/T-AG cases as following. Before the water pump started, the HTF in the T-AG absorbed energy and its temperature was increasing steadily from its initial temperature for the overall collector area because of the stagnation condition. After the average water temperature in the T-AG as a whole reached the targeted level, as there was a nearly uniform temperature all over the collector, the HTF that already carried part of the energy absorbed from the previous time-steps which considered to be zero efficiency as it had not produced output HTF from the T-AG yet, therefore, provided the high spike of instantaneous useful thermal efficiency at the first time of the flow. Later on, the temperature profile from the inlet to the outlet of the T-AG is not uniform and the mass flow rate reduced corresponding to the solar energy input from the present time-step leading to a drop of instantaneous electrical efficiency. This phenomenon is more obvious for the cases requiring higher temperature water output

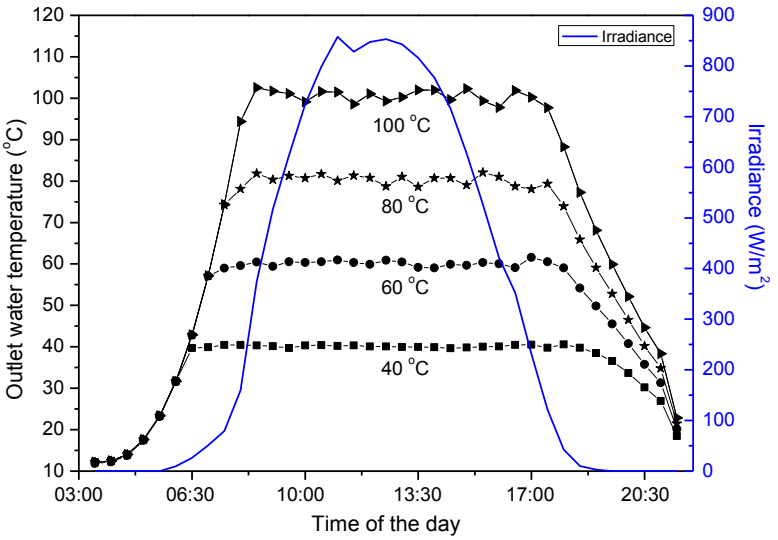

(a)

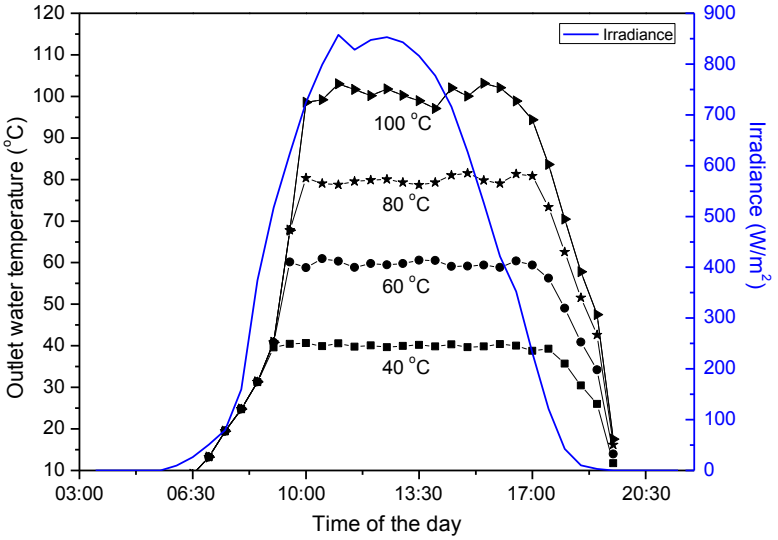

(b)

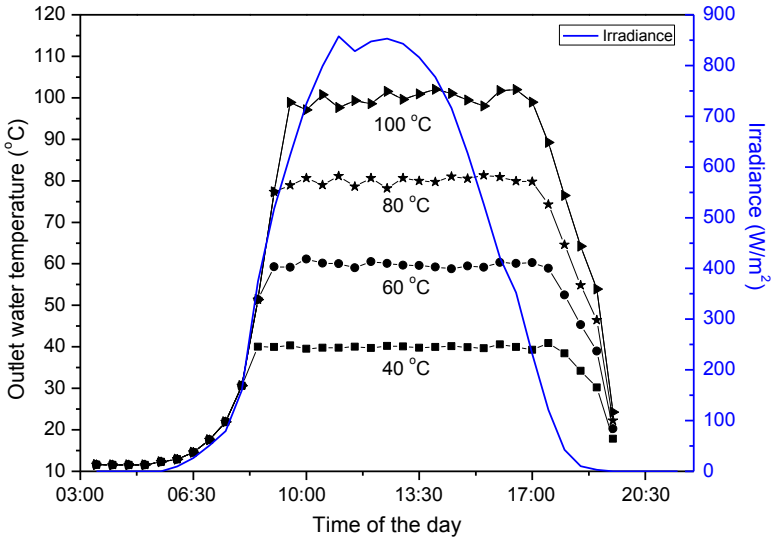

(c)

Fig. 3.32 *The water output temperature at different targeted levels from the thermal collector in Newcastle upon Tyne, UK; (a) on a sunny summer day, (b) on a sunny spring day and (c) on a sunny autumn day.*

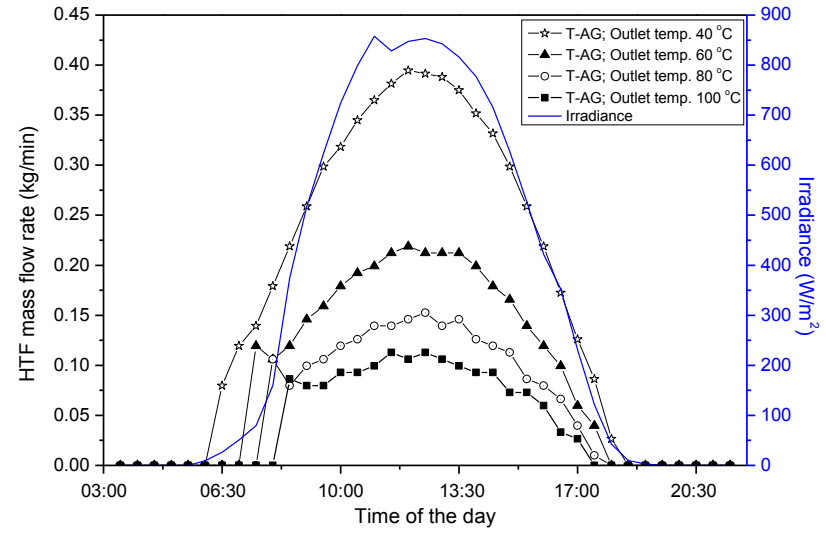

(a)

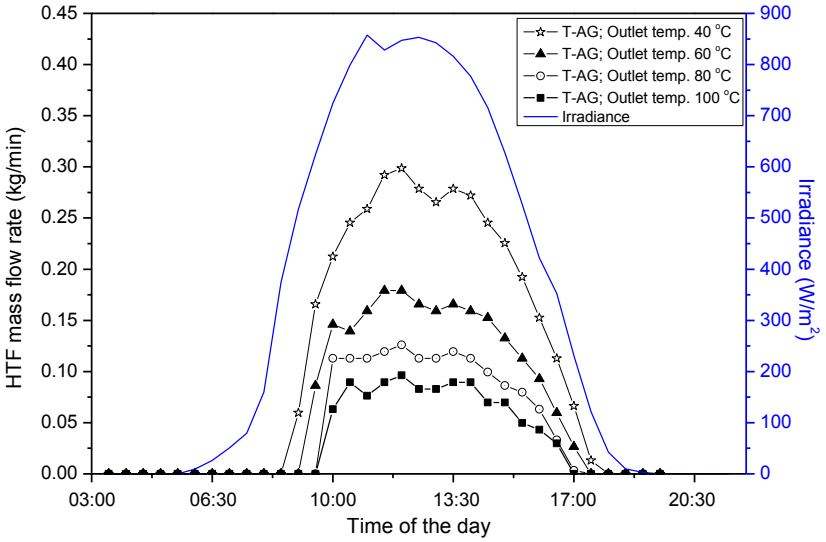

(b)

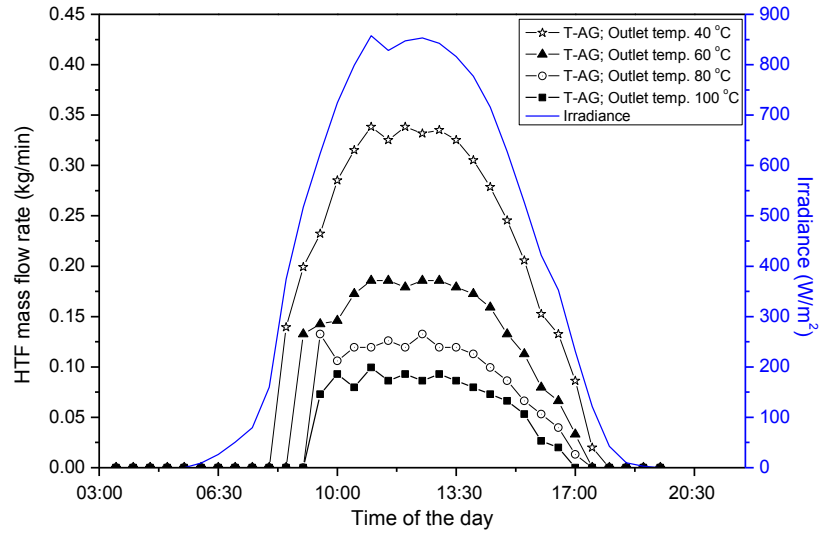

(c)

Fig. 3.33 *The mass flow rate of the output fluid at different targeted temperature from the thermal collector in Newcastle upon Tyne, UK; (a) on a sunny summer day, (b) on a sunny spring day and (c) on a sunny autumn day.*

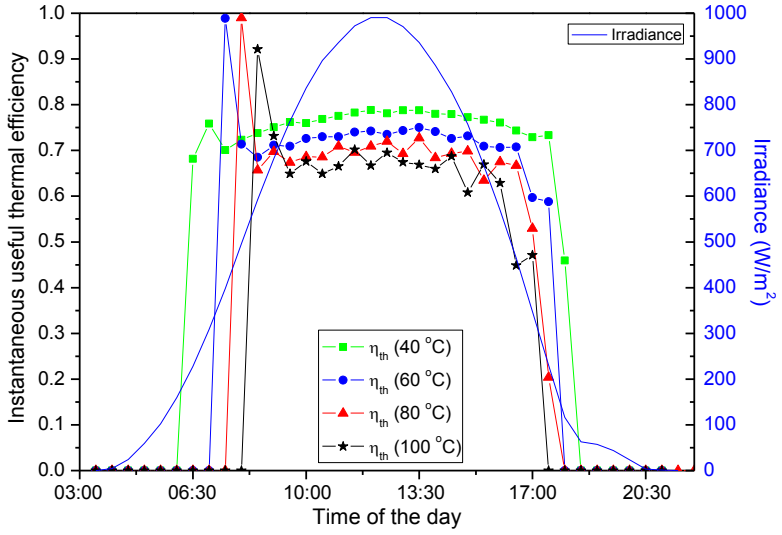

(a)

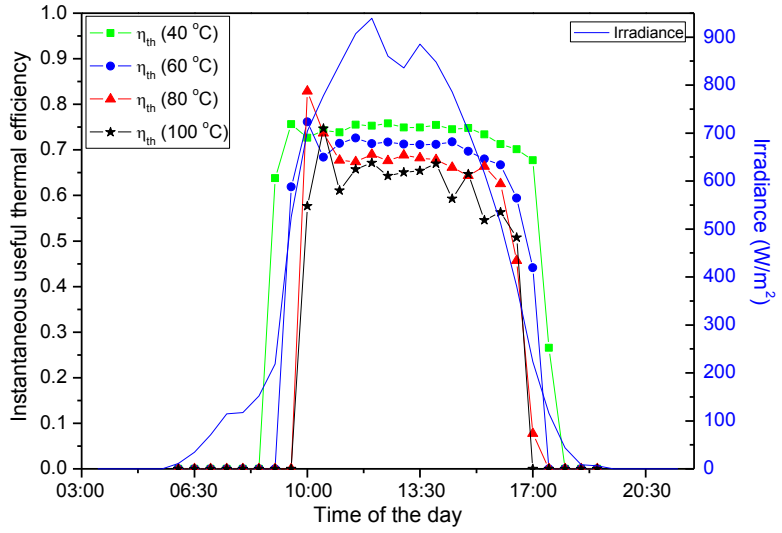

(b)

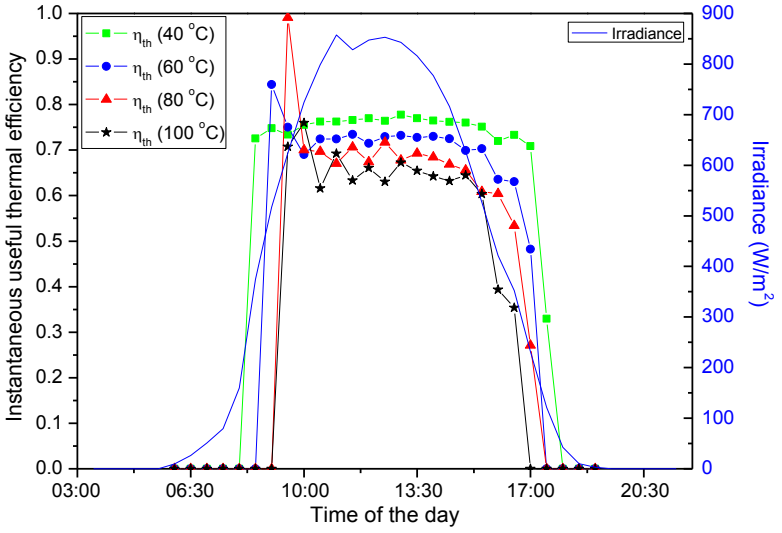

(c)

Fig. 3.34 *Instantaneous thermal efficiency of the thermal collector in Newcastle upon Tyne, UK; (a) on a sunny summer day, (b) on a sunny spring day and (c) on a sunny autumn day.*

3.5 Performance comparisons between PV, PV/T and thermal collector based on Newcastle upon Tyne weather

In this section, the solar energy conversion technologies studied in the previous section are compared with 4 different cases;

1. The PV and thermal collectors are installed with 50%/50% installation area (1-PV+1-T)
2. Two PV/Ts (with air gap) are installed (2-PV/T)
3. Two thermal collectors are installed (2-T) and
4. Two PV panels (2-PV) are installed

The total installation area of each case is equal (2 m^2) to explore the fare comparison results. Choosing the summer sunny day at the targeted output temperature (T_{out}) of 80 ^oC for the comparison, the electrical energy output of each case is presented in Fig. 3.35(a). The results show that installing 2-PV panels produce the highest electrical energy output, higher than the production from the 2-PV/T collectors case because the PV panel has better overall heat transfer from the PV layer to the ambient leading to lower PV cells temperature, unlike the PV/T which has the airgap as an air insulator for improving thermal efficiency although the two technologies has the same area of the PV cells. When the 1-PV+1-T case is considered, although the 50% of the installation area with the PV can perform the same conversion efficiency as the 2-PV case, it has only half of the PV cells area resulting in half of the electrical energy production compared with the 2-PV case. In summary, if the electrical energy is the priority, the available installation area may be entirely covered by only the PV panels. However, as the prior section suggested, if the PV/T is controlled to obtain T_{out} of less than 40 ^oC, the electrical energy output from the PV/T is higher than the PV (as shown in Fig. 3.35(b)) with additional thermal energy output as shown in Fig. 3.36 that the PV does not provide. The quality of the thermal output should be considered when choosing the conversion technology because the thermal energy output may not useful in some applications with more complicated systems which will be discussed in later sections.

Considering the thermal energy output from each technology as illustrated in Fig. 3.36, unsurprisingly, installing 2 thermal collectors (2-T case) delivers the highest thermal energy output compared to other cases. The 2-PV/T case provides lower thermal energy output than the 2-T case because part of the absorbed solar energy converted to the electricity. Therefore, if only the thermal energy output is of priority, the thermal collector is recommended if the quality of the HTF, namely T_{out}, is sufficiently high and the HTF is directly consumed, e.g.

domestic hot water usage, because of its highest total energy production as presented in Fig. 3.37 for the instantaneous total energy output and in Fig. 3.38 for the accumulation energy along the day.

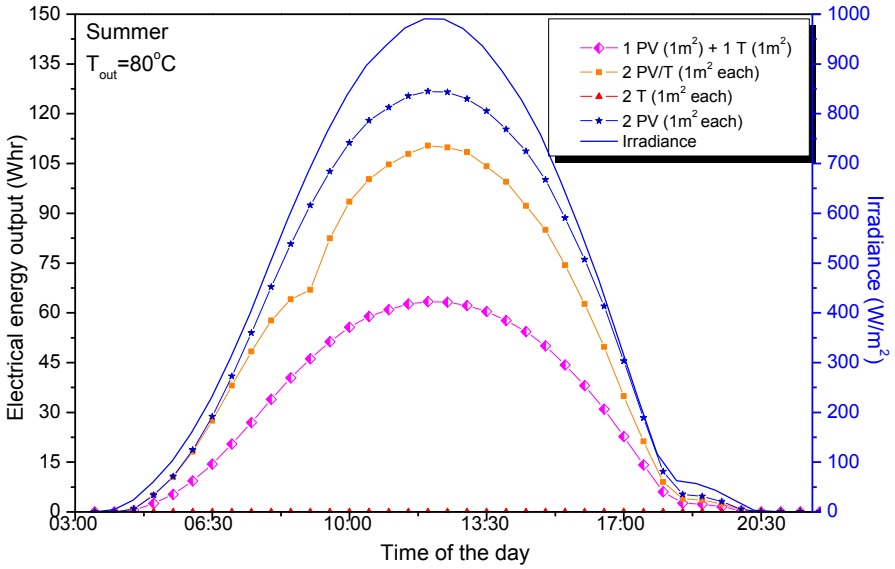

(a)

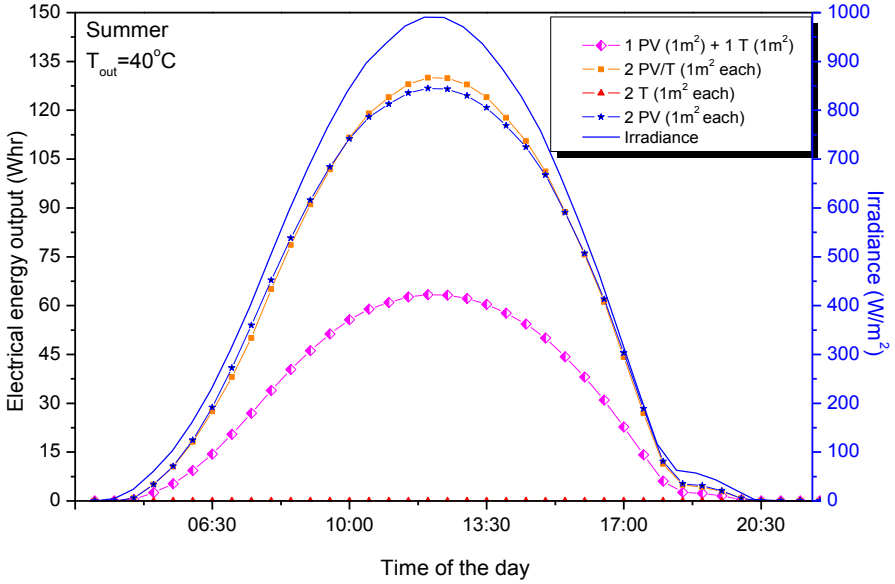

(b)

Fig. 3.35 *The electrical energy output comparison between PV, PV/T and thermal collector on a summer sunny day in Newcastle upon Tyne, UK; (a) at the targeted outlet temperature of 80 °C and (b) at the targeted outlet temperature of 40 °C.*

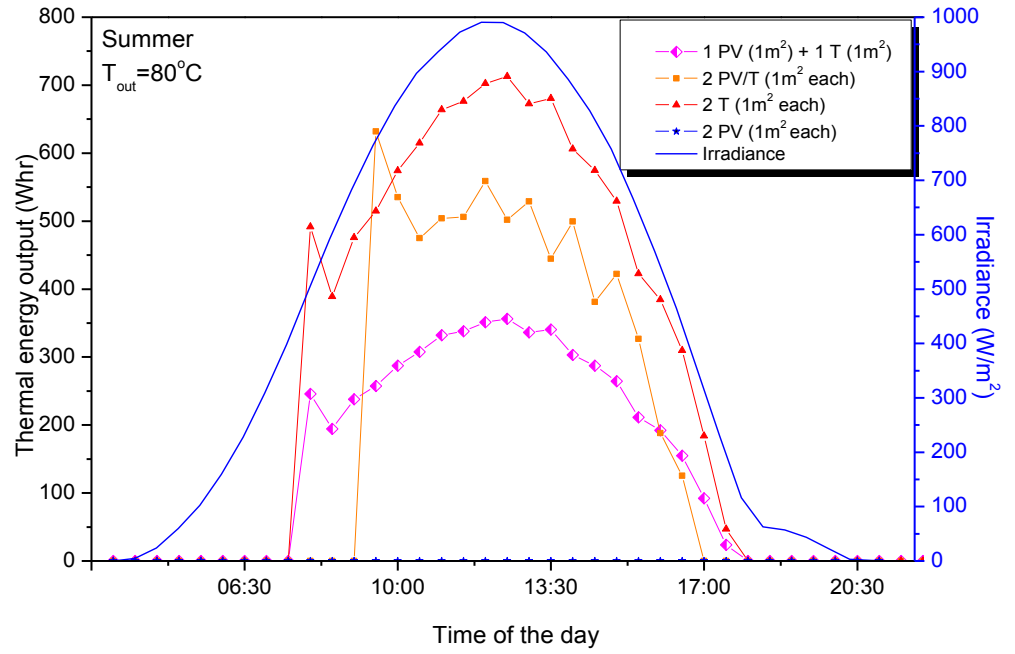

(a)

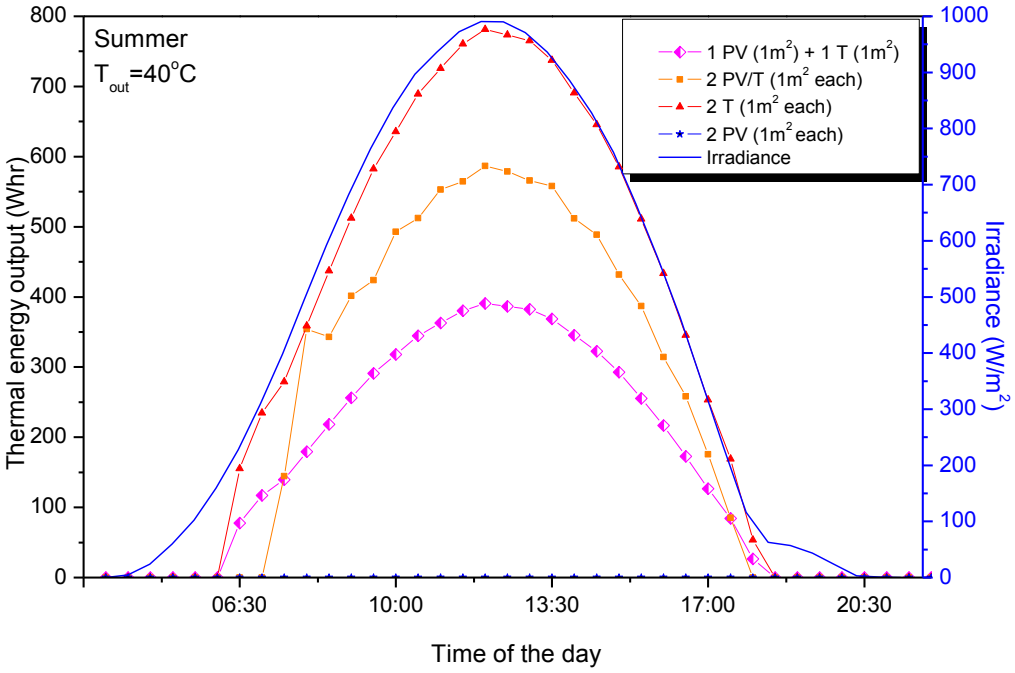

(b)

Fig. 3.36 *The thermal energy output comparison between PV, PV/T and thermal collector on a summer sunny day in Newcastle upon Tyne, UK; (a) at the targeted outlet temperature of 80 °C and (b) at the targeted outlet temperature of 40 °C.*

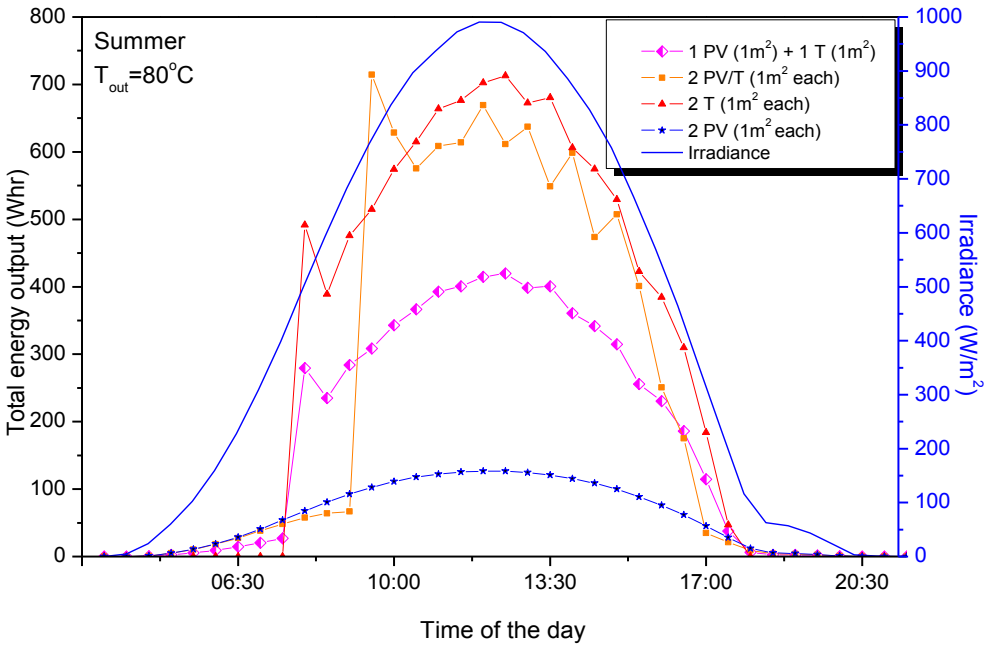

(a)

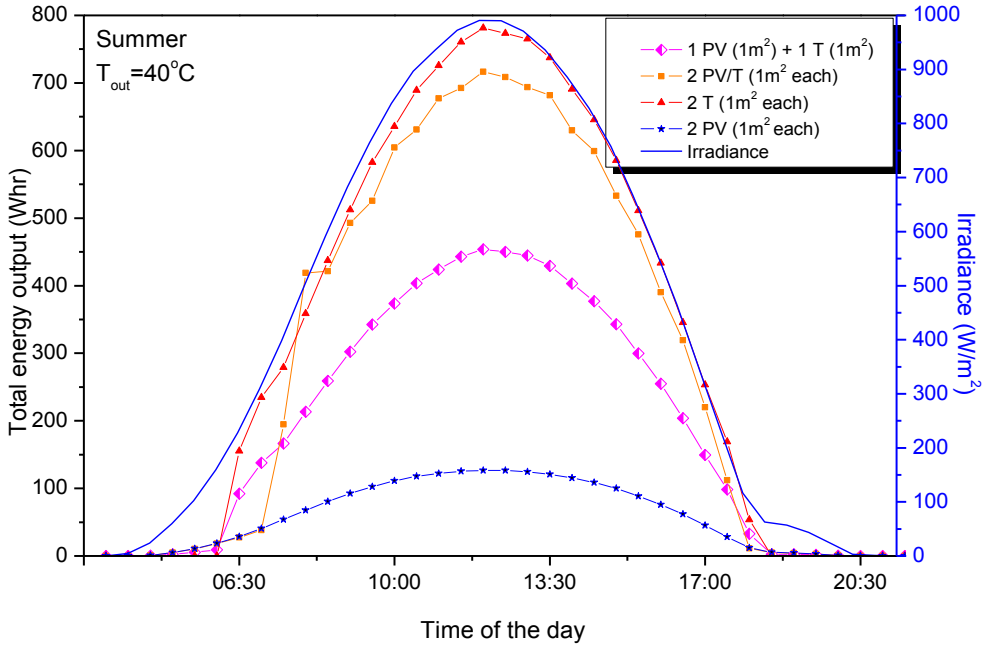

(b)

Fig. 3.37 *The total energy output comparison between PV, PV/T and thermal collector on a summer sunny day in Newcastle upon Tyne, UK; (a) at the targeted outlet temperature of 80 °C and (b) at the targeted outlet temperature of 40 °C.*

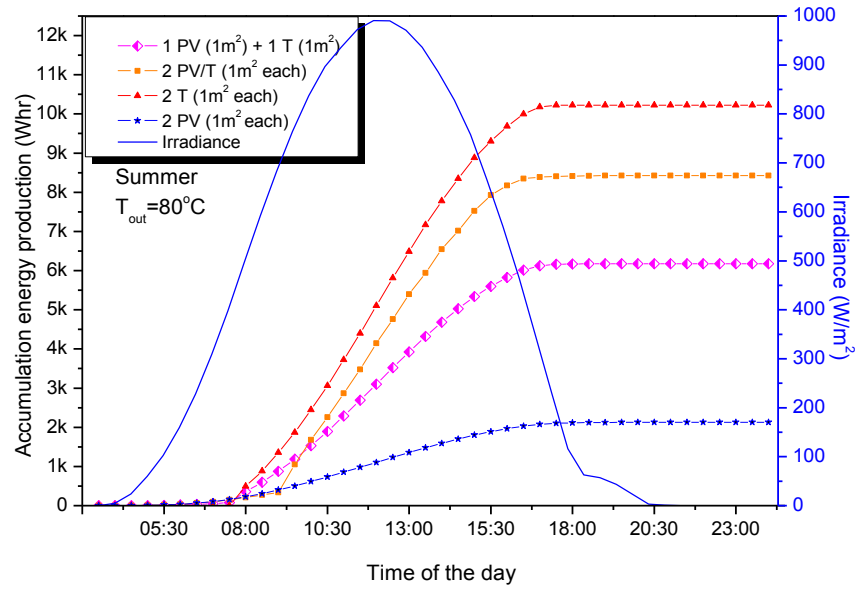

(a)

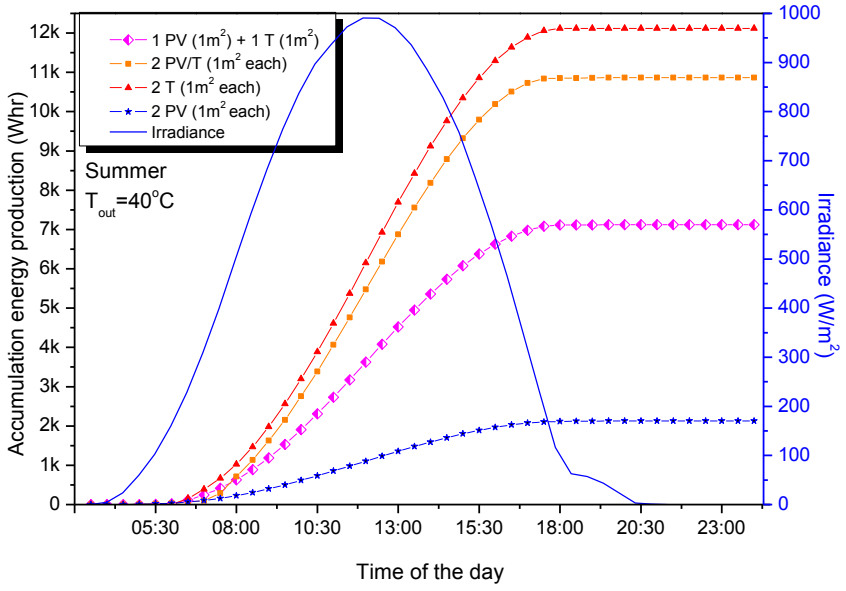

(b)

Fig. 3.38 *The comparison of the accumulative total energy output along the day between PV, PV/T and thermal collector on a summer sunny day in Newcastle upon Tyne, UK; (a) at the targeted outlet temperature of 80 °C and (b) at the targeted outlet temperature of 40 °C.*

The results seem to suggest that the thermal collector is the most promising technology especially when the thermal energy is highly demanded. For example, on a sunny summer day, the thermal collector produces 12.1 kWh of total energy output while the PV/T produces 10.86 kWh at T_{out} = 40 °C ($2m^2$ installation area). When higher temperature output is required, although the total energy output of all cases except the 2-PV case reduces, the thermal collector still performs better than other technologies. Interestingly, the efficiency of the thermal collector at higher T_{out} does not decrease as much as of the PV/T as shown by the bigger gap between the energy output from the thermal collector and the PV/T in Fig. 3.38(a).

Nevertheless, as the quality of energy has not been previously considered, the energy output from each technology may be useless although the amount of the energy output is considerable. Therefore, the exergy of each previous studied cased was calculated based on Eqs. (3.40) and (3.41) with the summer ambient temperature of 15.27 ^{o}C for the new comparisons as shown in Fig. 3.39. When the quality of energy is taken into account, it is obvious that the PV/T collector perform an outstanding performance being a solar energy conversion. Interestingly, the PV/T collector provide approximately high exergy output in a wide range of targeted temperature output (e.g. from 40 – 100 ^{o}C) while the PV collector generates constant exergy output as the PV collector generate pure electrical energy which is the exergy itself. Although the thermal collector has the highest energy conversion efficiency, the quality of its energy output is strongly varies depending on the output temperature. At low temperature, e.g. 40 ^{o}C, the thermal collector produced the highest energy output of 12.1 kWh in a sunny summer day; however, the exergy is only 0.96 kWh compared to the exergy of 2.14 kWh when the output temperature was 100 ^{o}C with the energy output of 10.23 kWh. Therefore, if the thermal collector is chosen, the results suggest that it should be operated so that to get as high-temperature output as possible. For the case of 1-PV + 1-T, the performance is moderate which is not very interesting to be further considered.

Furthermore, thermal collector usually generates thermal energy more than the daily demand in a rooftop area of a typical household thus hot water tank storage is normally integrated for short-term energy storage (last for 1 – 7 days). Therefore, PV/T provides the advantage of producing electricity as an additional form of energy to contribute both electrical and thermal energy demands in a domestic household. Moreover, as the main objective to store thermal energy from spring through autumn to use in winter, the long-term energy storage, the thermochemical energy storage, is integrated with the solar energy conversion technology which the threshold temperature of the supply thermal energy comes into consideration. The threshold temperature makes the PV/T technology becomes more promising as the electrical energy is required to drive the storage system in order to store sufficient thermal energy during charging state to use in winter.

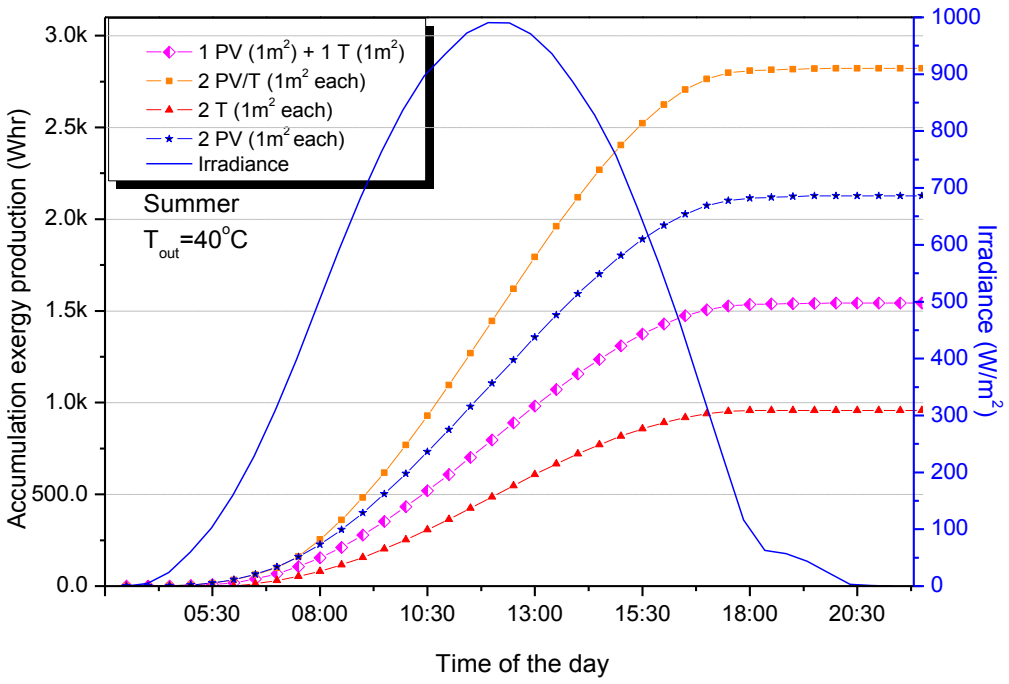
1 PV (1m²) + 1 T (1m²)
2 PV/T (1m² each)
2 T (1m² each)
2 PV (1m² each)
Irradiance
Summer
T_out=40°C
Accumulation exergy production (Whr)
Irradiance (W/m²)
Time of the day
3.0k
2.5k
2.0k
1.5k
1.0k
500.0
0.0
1000
900
800
700
600
500
400
300
200
100
0
05:30
08:00
10:30
13:00
15:30
18:00
20:30

(a)

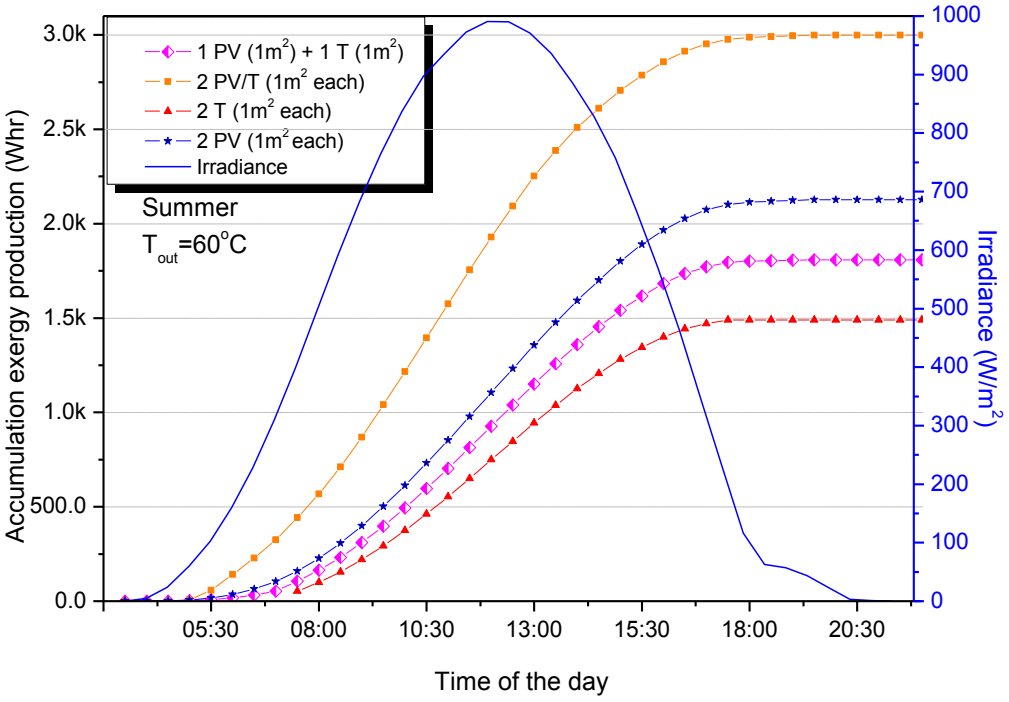
1 PV (1m²) + 1 T (1m²)
2 PV/T (1m² each)
2 T (1m² each)
2 PV (1m² each)
Irradiance
Summer
T_out=60°C
Accumulation exergy production (Whr)
Irradiance (W/m²)
Time of the day
3.0k
2.5k
2.0k
1.5k
1.0k
500.0
0.0
1000
900
800
700
600
500
400
300
200
100
0
05:30
08:00
10:30
13:00
15:30
18:00
20:30

(b)

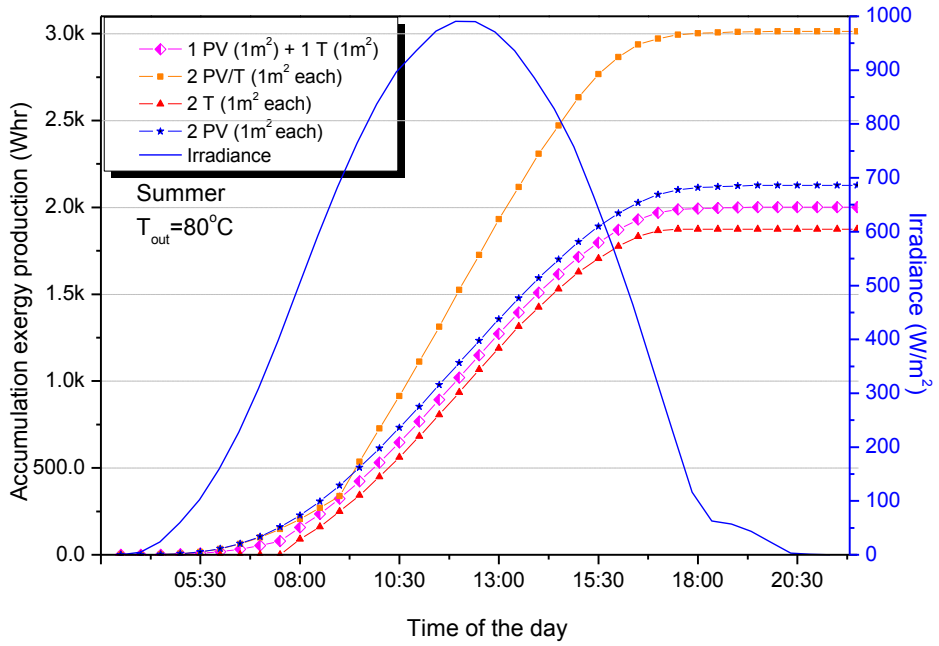

(c)

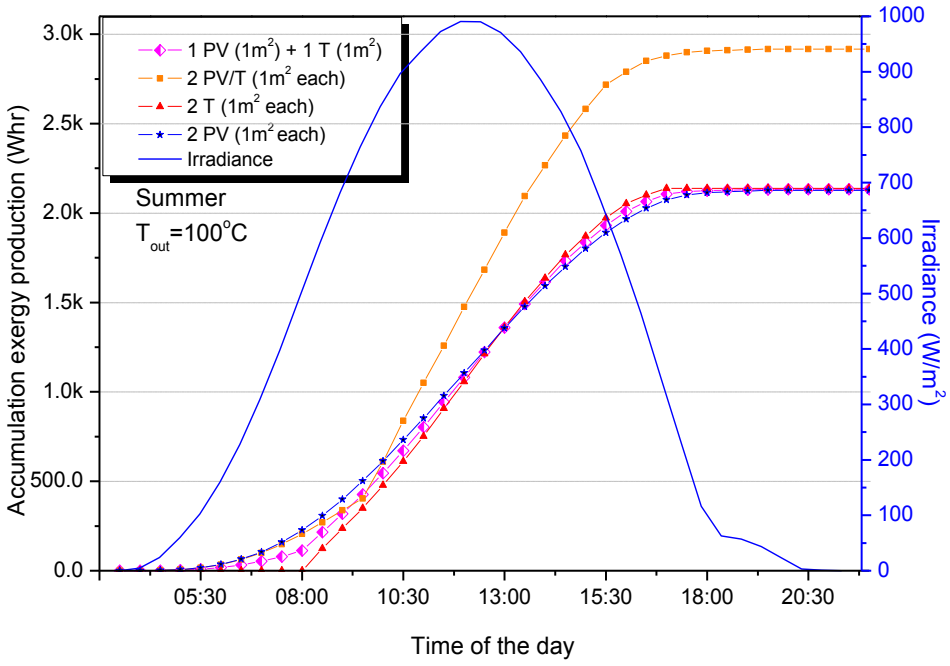

(d)

Fig. 3.39 *The comparison of the accumulative exergy output along the day between PV, PV/T and thermal collector on a summer sunny day in Newcastle upon Tyne, UK at the targeted outlet temperature of; (a) 40 °C, (b) 60 °C, (c) 80 °C and (d) 100 °C.*

For a typical UK household with approximately 30 m^2 rooftop area (a typical 4kWp of PV installation size) (Anon, 2015), the size of the PV/T-AG system installed at the optimum tilted angle was investigated to explore its potential of meeting the household hot water demand. In the context of Newcastle upon Tyne, the charging state including the spring sunny-day during March, April and May (27 days of production), the summer sunny-day during June and July

(18 days of production); and the autumn sunny-day during August, September and October (27 days of production) are used to represent the annual performance of each technologies.

The simulation results of the amount of water output at different temperature levels and the energy conversion efficiency by using the studied PV, PV/T-AG and thermal collectors were presented in Table 3.6, Table 3.7 and Table 3.8 for summer, spring and autumn respectively. On a typical summer sunny day in June in Newcastle, the amount of hot water production is from around 28 L/(day·m^2) to 133 L/(day·m^2) with the overall energy conversion efficiency from 45% to 66%, as the required output temperature ranging from 100 ^oC to 40 ^oC. For a sunny autumn day in September, the studied PV/T-AG collector can produce 19~98 L/(day·m^2) hot water depending on different required output temperature, with the overall energy conversion efficiency of 36%~59%, which is around 11%~18% lower than the efficiency obtained in summer.

Table 3.6 *Performance comparison between referenced PV, PV/T-AG and thermal collectors with 30 m^2 installation area in summer*

Type of Model	$T_{w,o}$ (°C)	m_w (liter/day/m^2)	Ave. η_{elec} (%)	Ave. η_{th} (%)	Total η (%)	Seasonal E_{elec} (kWh)	Seasonal E_{th} (kWh)	Seasonal E_{total} (kWh)
PV	-	-	12.97	-	12.97	574.42	-	574.42
PV/T-AG	100	27.97	9.88	34.79	44.68	437.51	1541.16	1978.67
	80	42.00	10.96	40.40	51.36	485.45	1789.82	2275.27
	60	68.18	12.03	46.56	58.59	532.73	2062.58	2595.31
	40	132.87	12.99	53.22	66.21	575.48	2357.53	2933.02
T-AG	100	45.58	-	57.38	57.38	-	2541.76	2541.76
	80	64.19	-	62.33	62.33	-	2761.04	2761.04
	60	98.73	-	67.60	67.60	-	2994.35	2994.35
	40	183.72	-	73.84	73.84	-	3271.01	3271.01

Table 3.7 *Performance comparison between referenced PV, PV/T-AG and thermal collectors with 30 m^2 installation area in spring*

Type of Model	$T_{w,o}$ (°C)	m_w (liter/day/m^2)	Ave. η_{elec} (%)	Ave. η_{th} (%)	Total η (%)	Seasonal E_{elec} (kWh)	Seasonal E_{th} (kWh)	Seasonal E_{total} (kWh)
PV	-	-	13.61	-	13.61	675.19	-	675.19
PV/T-AG	100	16.02	9.98	28.50	38.47	494.69	1413.30	1907.98
	80	25.18	11.05	35.38	46.42	547.79	1754.49	2302.28
	60	41.40	12.16	42.40	54.56	603.13	2102.80	2705.93
	40	75.74	13.16	48.70	61.85	652.37	2414.89	3067.26
T-AG	100	30.65	-	54.83	54.83	-	2719.31	2719.31
	80	42.20	-	58.94	58.94	-	2923.14	2923.14
	60	63.50	-	64.61	64.61	-	3204.04	3204.04
	40	109.08	-	70.25	70.25	-	3483.77	3483.77

Table 3.8 *Performance comparison between referenced PV, PV/T-AG and thermal collectors with 30 m^2 installation area in autumn day*

Type of Model	$T_{w,o}$ (°C)	m_w (liter/day/m^2)	Ave. η_{elec} (%)	Ave. η_{th} (%)	Total η (%)	Seasonal E_{elec} (kWh)	Seasonal E_{th} (kWh)	Seasonal E_{total} (kWh)
PV	-	-	13.17	-	13.17	652.81	-	652.81
PV/T-AG	100	17.82	9.89	29.69	39.58	490.07	1471.57	1961.65
	80	28.17	10.98	36.43	47.41	544.21	1805.82	2350.03
	60	48.67	12.05	44.29	56.34	597.14	2195.21	2792.35
	40	97.44	13.05	51.69	64.74	646.91	2562.03	3208.94

Type of Model	$T_{w,o}$ (°C)	m_w (liter/day/m^2)	Ave. η_{elec} (%)	Ave. η_{th} (%)	Total η (%)	Seasonal E_{elec} (kWh)	Seasonal E_{th} (kWh)	Seasonal E_{total} (kWh)
T-AG	100	33.24	-	55.28	55.28	-	2739.94	2739.94
	80	46.98	-	60.55	60.55	-	3001.30	3001.30
	60	73.55	-	66.57	66.57	-	3299.79	3299.79
	40	137.74	-	72.94	72.94	-	3615.60	3615.60

3.6 Summary

In this chapter, three solar conversion technologies which are photovoltaic collector, thermal collector and the hybrid photovoltaic-thermal collector were modelled and simulated to study the performances of each technology to reveal the possibility of the integration with the thermal energy storages for domestic application which will be done in the next chapter. The detailed model based on the one-diode model and the modified equations of RSH and RS were developed to couple with a CFD model for performance prediction of both thermal power and electrical power generation under various operating conditions. The validations were done against the manufacturing datasheet and real experimental data from Tsai (2012). The simulation suggested that the air gap is required in order to produce an HTF temperature of higher than 43 ^{o}C in the UK weather conditions.

Both thermal efficiency and electrical efficiency of the PV/T-AG collector is increased when it operates with lower outlet HTF temperature, The PV/T-AG can produce hot water at 100 °C in sunny summer days with lower total efficiency (44.68%) resulting from the high temperature of the panel leading to high heat loss and low electrical efficiency (9.88%). When considering the exergy output of each technology, PV/T is the most preferable technology because it has the highest exergy production in a wide range of operating temperatures (40-100 ^{o}C). Therefore, it is the chosen technology in this thesis to be integrated with the energy storage technology in the next chapter.

(This page intentionally left blank)

Chapter 4: Integration and optimisation of photovoltaic-thermal collector with thermochemical energy storage

4.1 The working principle for the integration of solar energy conversion with thermochemical energy storage

Normally on summer sunny days, the hot water and electricity productions from the PV/Ts are more than the normal household demand (Thinsurat *et al.*, 2019) so the electrical and thermal storages are required. There are various types of energy storage technology available currently and each technology has advantages and disadvantages depending on the main objective of its different applications as mentioned in the literature review chapter. Because of the advantages of the thermochemical sorption energy storage (TSES), e.g., higher energy density than other main thermal energy storage methods (i.e. sensible and latent heat storage), negligible long-term energy loss and abundance of raw materials leading to possible scale-up for seasonal storage, TSES were chosen in this thesis to reveal its potential for the integration of the PV/T with the TSES for a typical domestic household in Newcastle upon Tyne. Bao *et al.* (2016) proposed an interesting idea of storing thermal and electrical energy simultaneously in the form of a chemical reaction through a compressor-assisted thermochemical desorption process, which the working temperature can be reduced leading to the possibility of storing more thermal energy from the HTF that the PV/Ts produced.

If maximum storable energy is the priority of the operation, PV/Ts electrical output can be used to drive the compressor at its maximum compression ratio which may reduce the T_{eq} to be lower than the DHW temperature requirement. If the electrical grid is receiving high penetration of electricity from the PV in summer sunny days, the PV/Ts may be operated with higher HTF temperatures to reduce the electrical output and increase the useful thermal energy for thermochemical seasonal thermal storage to use in winter (Thinsurat *et al.*, 2019). As there has limited researches that pay attention to the integration of the PV/T collector with the compressor-assisted thermochemical sorption energy storage (CATSES), this thesis, therefore, reveal the optimum operating conditions for the integrated PV/Ts – thermochemical energy storage system where $T_{PV/T,}$ T_{eq} and T_{out} are the variable parameters and the constraints are the maximum compression ratio of the compressor, the available PV/Ts outputs and the DHW demand. The objective of the optimisation is to reveal the operational condition at maximum useful energy in different weather conditions and seasons.

4.1.1 The working principle of the basic thermochemical energy storage

A thermochemical process is based on reversible chemical reactions that produce or absorbs thermal energy in the exothermic adsorption process or endothermic desorption process, respectively. The basic solid-gas thermochemical sorption energy storage (TSES) unit consists of one solid sorbent reactor and one refrigerant container acts as a condenser in the charging phase (Fig. 4.1(a)) and an evaporator in the discharging state (Fig. 4.1(b)). The refrigerant container receives and condenses refrigerant vapour when the reactor desorbs refrigerant; in the reverse process, it converts to an evaporator while the reactor is adsorbing refrigerant vapour.

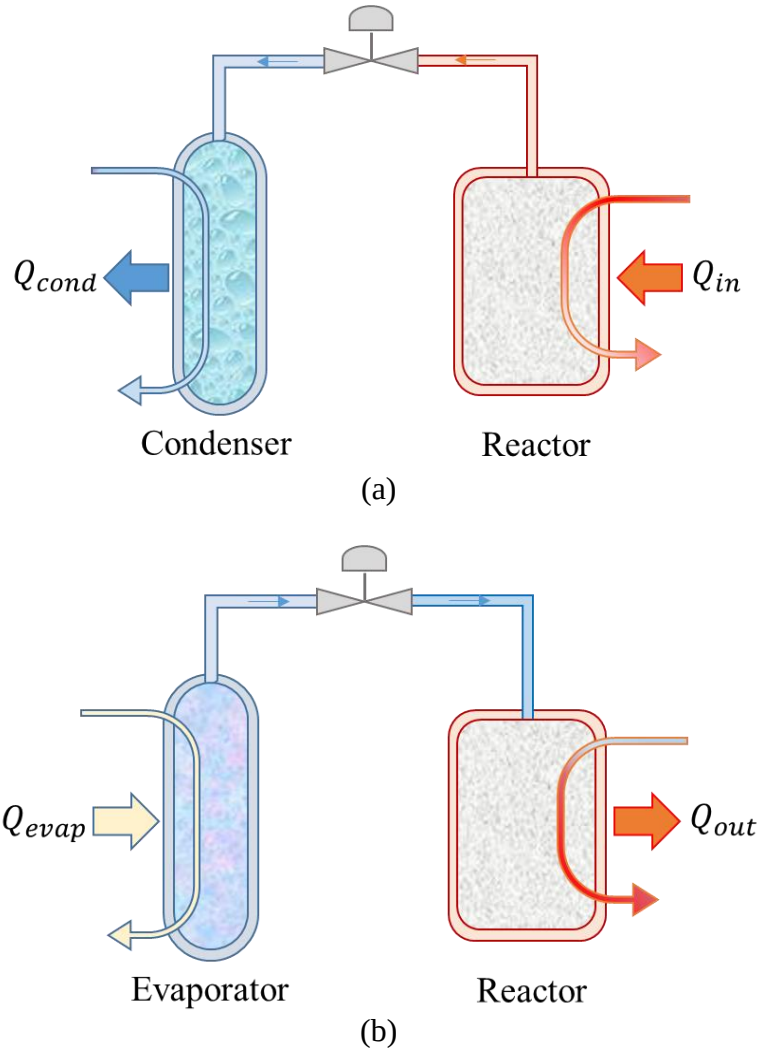

Fig. 4.1 *The sorption process of Salt/Ammoniates; (a) The desorption process during energy charging state and (b) The adsorption process during energy discharging state*

The reversible chemical reactions between salt ammines and NH_3 is expressed in Eq.(4.1). The basic thermochemical adsorption system consists of one solid adsorbent reactor and one refrigerant container. The adsorbent reactor absorbs thermal energy in endothermic desorption

as the first half cycle and produces thermal energy in the exothermic adsorption process as the second half cycle. The solid adsorbent studied in this work was the composite, a mixture of reactive salt and porous matrixes—expanded graphite (EG). Typically, reactive salt is impregnated into the porous matrix prior to drying and compressing/packing the mixture into the reactor. It was reported to effectively improve the thermal conductivity and gas permeability property of the adsorbent, as well as mitigating the swelling and agglomeration issues associated with pure salt adsorbent (Han *et al.*, 2000). The available reactive salt-ammonia working pairs as shown in Table 4.1 are analysed to reveal the suitable pair to use in the energy storage system.

$$SALT \cdot mNH_3 + \Delta H \leftrightarrow SALT \cdot nNH_3 + (m-n)NH_3 \quad (4.1)$$

where m is the fully adsorbed ammonia mole per salt mole (mole)

n is the fully desorbed ammonia mole per salt mole (mole)

Table 4.1 *The number of ammonia molecule adsorbed by reactive salts at fully-adsorption state 'm' and non-adsorption state 'n' with their reaction enthalpy, entropy, heat capacity and molar mass*

Reactive salts	m	n	ΔH_R (J/ammonia mole)	ΔS_R (J/ammonia mole ·K)	C_p (J/ mole ·K)	Molar mass (g/ mole)
NH_4Cl	3	0	29433	207.9	84.1	53.49
$PbCl_2$	8	3.25	34317	223.6	55.2	278
NaBr	5.25	0	35363	225.2	36.34	102.9
$BaCl_2$	8	0	38250	232.4	75.30	208.2
LiCl	4	3	36828	224.6	33.25	42.39
$CaCl_2$	8	4	41013	230.1	59	110.98
NaI	4.5	0	39339	224.5	36.64	149.89
$BaBr_2$	8	4	41850	229.8	76	297.15
$SrCl_2$	8	1	41432	228.6	77.52	158.53
$CaCl_2$	4	2	42269	229.7	59	110.98
$SrBr_2$	8	2	45617	229.3	130	247.43
$MnCl_2$	6	2	47416	227.9	152	125.7
$CaBr_2$	6	2	48965	230.4	156	199.8
$FeCl_2$	6	2	51266	227.8	186	126.6

Reactive salts	m	n	ΔH_R (J/ammonia mole)	ΔS_R (J/ammonia mole ·K)	C_p (J/ mole ·K)	Molar mass (g/ mole)
$MnBr_2$	6	2	53066	228.3	200	214.7
$CoCl_2$	6	2	53987	227.9	210	94.3
$MgCl_2$	6	2	55661	230.4	214	95.1
$FeBr_2$	6	2	55828	228.1	226	215.6
CaI_2	6	2	58590	231.0	237	293.8
$CoBr_2$	6	2	58590	227.5	253	218.7
$NiCl_2$	6	2	59218	227.6	259	219.5
MnI_2	6	2	59301	227.4	260	308.7
FeI_2	6	2	60683	227.5	272	309.6
$MgBr_2$	6	2	63612	230.2	285	184.1
$NiBr_2$	6	2	64240	227.2	306	218.5
NiI_2	6	2	65453	224.1	334	312.5

4.1.2 The working principle and system operation of the integration system of the Photovoltaic-thermal collector with the thermochemical energy storage

In the compressor-assisted thermochemical sorption energy storage (CATSES) studied in this thesis as shown in Fig. 4.2(b), one compressor is installed in between the adsorbent reactor and the refrigerant container, compared to the basic system in Fig. 4.2(a) for charging phase and Fig. 4.2(c) for discharging phase. The compressor introduces electrical energy input to assist the pressurization during the desorption process, so as to enable a wider range of operating conditions. The compressor reduces the pressure on the reactor side leading to lower salt equilibrium temperature; therefore, lower heat source temperature can be supplied for the desorption process. Simultaneously, the compressor may increase the pressure on the condenser side resulting in a higher rate of ammonia condensation which maintains the desired reaction rate in the reactor. The desorption process in the charging state of the CATSES is driven by the thermal and electrical energy output from the PV/T; however, when there is unfavourable weather conditions which cause the insufficient collective amount of two types of energy outputs from the hybrid solar PV/T collector to activate the desorption, the electricity from the grid can be provided to the compressor to assist the desorption process.

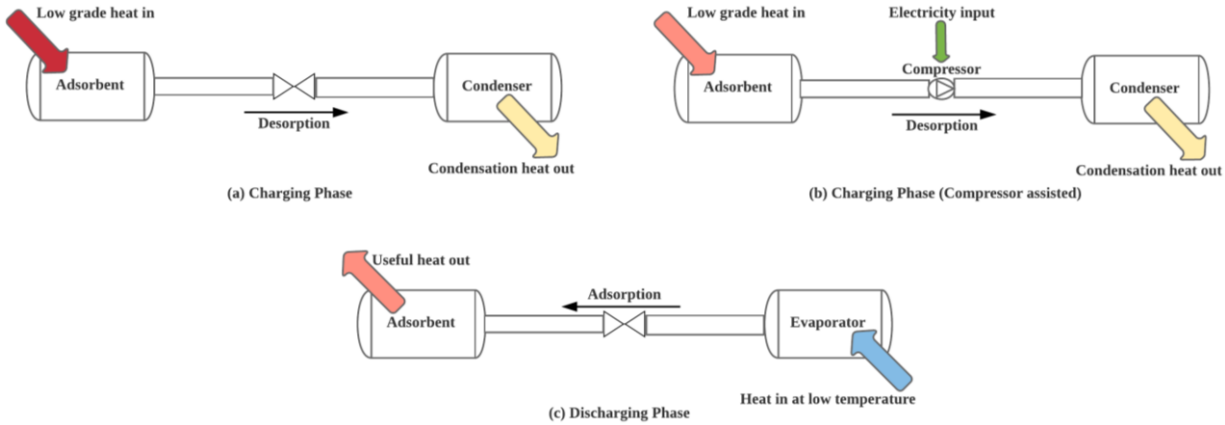

Fig. 4.2 *Thermochemical sorption systems for energy storage*

The hybrid compressor-assisted thermochemical sorption energy storage (CATSES) system implements energy charging in summer (Fig. 4.3 (a)) and energy discharging in winter (Fig. 4.3 (b) and (c)) is proposed in this thesis. Fig. 4.4 presents two system layouts of the whole domestic heating system employing the proposed integrated system. In this thesis, the daily sum of energy demand and supply of each element were considered instead of the real-time variation along the day to reduce the complication of the optimisation of the integrated system. With the assumption that if the system is operated one day prior to the initial day of supplying the household energy, the short-term DHW storage can be used to supply the DHW demand regardless of the demand variation along the day because the DHW storage tank is chosen to sufficiently store the DHW demand volume for at least 3 consecutive days. Moreover, on a typical sunny day during the charging period, the PV/T with 30 m^2 installation area produces more DHW than the demand as the results from the previous chapter suggested. Therefore, optimising the integrated system by considering the total daily energy of each component is reasonable.

In summer, for the first layout (case#1) illustrated in Fig. 4.4 (a), the HTF (water) heated by the solar panel heads to the thermochemical reactor that contains adsorbent and releases heat for endothermic desorption of the adsorbent. The water flow rate is adjusted to achieve the targeted temperature at the outlet of the PV/T collectors so that to meet the temperature requirement of the endothermic decomposition. The ammines adsorbent in the reactor decomposes and releases ammonia vapour, whilst the electrical yield drives the compressor to pressurise and liquidize the ammonia vapour in the condenser, as shown in Fig. 4.3 (a). In this case, both the solar thermal and electrical energy is stored in the form of chemical potential, which has minimum energy loss over long term storage. The warm water drained from the reactor is split into two streams, one stream is collected in a reused water tank, which will be

part of thermal energy carrier for the next day operation, and the other one stream is saved in the domestic hot water (DHW) tank for daily use. Depending on the feed-in temperature of the DHW tank, either a standby electric heater or an inline mixer performs to make sure the water temperature is in the right range for daily use. The standby electric heater can also be powered by the electricity generated by the solar PV/T. For the second system layout (case#2) in Fig. 4.4 (b), the heated water from the solar panels firstly fed into the DHW tank until it stored for 3-day autonomy in case of no solar energy available. Afterwards, the residual hot water from the PV/T collectors is used to charge the thermochemical unit, then the exhaust water from the reactor will be collected in the reused water tank and used as the inlet water of the PV/T collector for the next day operation. In this instance, the daily hot water use is prioritised, and the excess solar heat is stored over seasons. Another arrangement including a standby electric heater and the inline mixer is the same with the case#1.

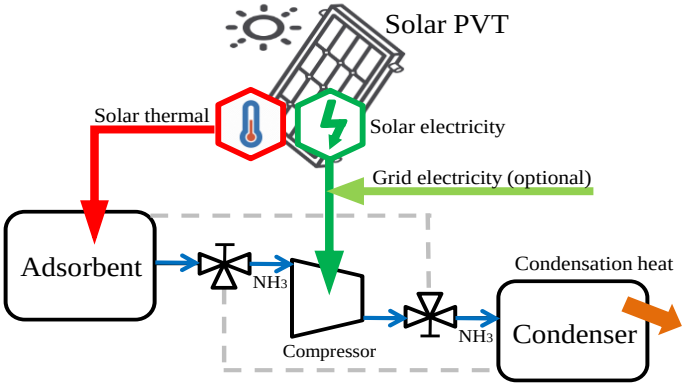

(a)

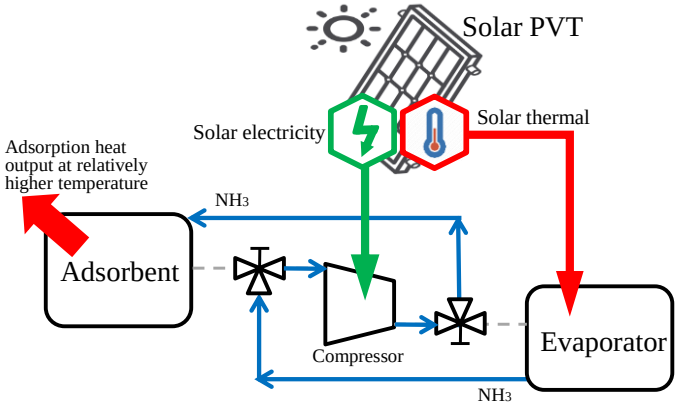

(b)

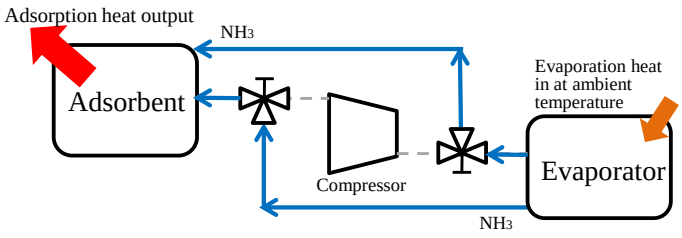

(c)

Fig. 4.3 *Thermochemical sorption storage system performs (a) energy charging in the compressor-assisted mode in summer; (b) energy discharging in the compressor-assisted mode in winter; (c) energy discharging in the basic mode in winter.*

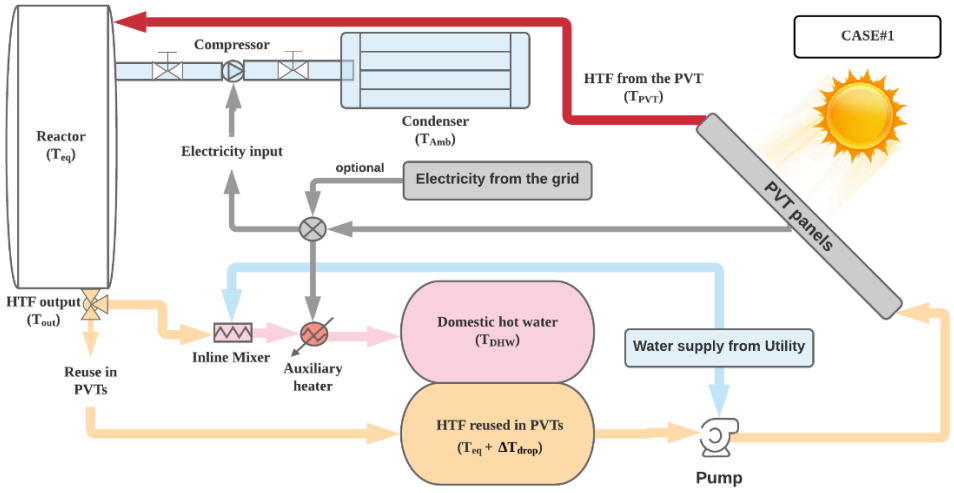

(a)

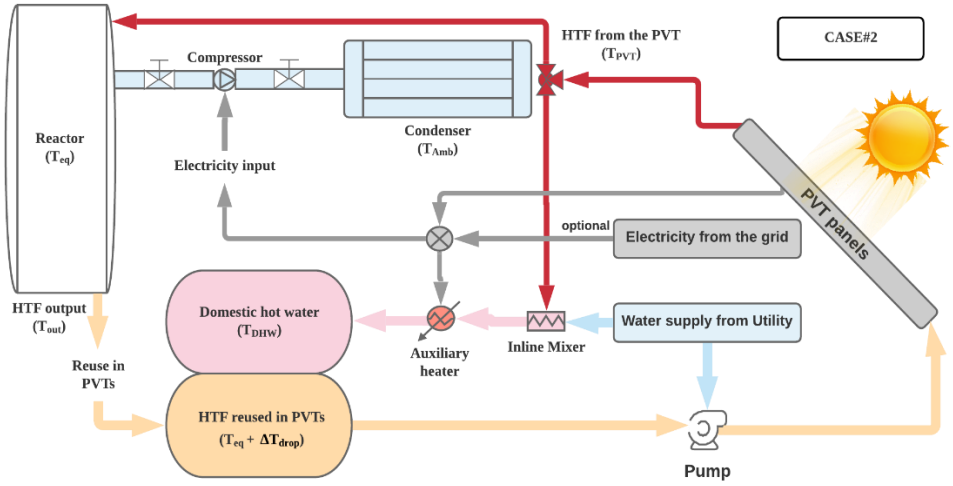

(b)

Fig. 4.4 *Two layouts of the domestic heating system using the integrated energy storage system in summer. (a) case#1: the heated water from the PV/T runs through the reactor for energy storage prior to feeding into the DHW tank; (b) case#2: the heated water from the PV/T firstly fills up the DHW tank then the excessive part is stored over seasons.*

It is worth noting that, in order to meet the energy input required for the desorption in the CATSES unit, the water flow rate that carries away the generated heat from the PV/T panel is to be adjusted to obtain the different quantity and quality of thermal energy. In response, the electrical output varies correspondingly as aforementioned that the PV cell temperature affects the electrical conversion efficiency. The PV/T cell that retains low temperature has relatively higher electrical efficiency; however, the electrical product is compromised if the thermal output is required at relatively higher temperature level. On the other side, the CATSES unit as the downstream unit is capable to adapt to either scenario, namely, it can effectively harness low-temperature thermal energy while consuming more electricity for compression process, or it uses high-temperature heat input with comparatively less electricity input for compression or even no electrical compression at all. Therefore, it is critical to study the optimal operating conditions of the PV/T collector and the CATSES unit when they integrate with each other, to provide the maximum efficiency for both units, i.e. maximising the energy conversion efficiency of the PV/T collector and maximising the solar fraction of domestic heating demands. The key question is how to tactically control the water flow rate to meet the requirement of both thermal and electrical energy by the CATSES unit and at the same time strike the balance between the thermal and electrical generation of the solar PV/T collector.

In winter, the proposed storage system is expected to deliver the heating demands, including the domestic how water (DHW) use and the space heating (SPH), without extra consumption of natural gas and the electricity from the national grid. In the best scenario of making the best use of solar devices, as shown in Fig. 4.3 (b), the solar PV/T collectors still produce thermal and electrical energy to boost the energy discharging process if there is useful solar energy available in winter. In this case, the solar thermal energy can be used for ammonia evaporation in the CATSES evaporator and simultaneously the electrical power drives the compressor to further pressurise the ammonia vapour. In this instance, the adsorption takes place in the CATSES reactor at a relatively higher temperature and pressure, leading to the release of adsorption heat at a high temperature for heating purposes. This best scenario may not be applicable in the context of the high-latitude regions like the UK city of Newcastle upon Tyne with weak solar radiation and limited insolation duration during the winter, then the second scenario as illustrated in Fig. 4.3 (c) has been studied in this thesis, as the basic thermochemical sorption heat pump performs, and the compressor is bypassed.

This thesis analysed several potential kinds of reactive salts that are able to work with the PV/T temperature output range and also able to provide sufficient high-temperature output in

winter for mentioned applications in a household. Individual reactive salt has the equilibrium reaction temperature depending on its property and working pressure; therefore, for the desorption process, the HTF temperature, even at the outlet of the reactor (T_{out}), should be kept higher than the T_{eq} to maintain the reaction. T_{eq} is normally higher than the cold-water supply from a utility so the output HTF from the reactor may be used for other applications as already mentioned in case#1 and case#2. Assuming that the DHW requires 60 ^{o}C, if the reactive salt has the T_{eq} higher than the DHW temperature, the temperature of the HTF output from the reactor will be higher than the requirement so it may be mixed with the supplied cold water to reduce the temperature to 60 ^{o}C then stored for the daily DHW use. If the temperature of the HTF output from the reactor is lower than the desired DHW temperature, the auxiliary electrical heater may be installed and heat up the output HTF from the reactor to 60 ^{o}C just for the demand amount of DHW and the rest of the HTF output may be reused in the PV/Ts for the next day.

4.1.3 Mathematical analysis of the thermochemical energy storage cycle used for examining the optimal conditions when integrated with the PV/T technology

In the CATSES system studied in this work, one compressor is installed in between the sorbent reactor and the condenser/evaporator. The introduction of a compressor enables the electrical or mechanical-driven pressurisation, consequently, enables comparatively lower temperature heat sources to be used for desorption in the energy charging process compared to the basic cycle using the given reactive salt. Alternatively, with the same heat source, ammines those have higher desorption equilibrium temperature can be employed in the compressor-assisted cycle, which has also higher adsorption equilibrium temperature, i.e. higher temperature heat output in energy discharging process. Such a hybrid cycle enhances heat pumping performance, as it has the collective effect of a thermochemical sorption heat pump and a conventional vapour compression heat pump.

The basic thermochemical cycle and the compressor-assisted cycle at a non-equilibrium cycle, contrasted with the equilibrium based on the Van't Hoff equation (Eq. (4.2)), are plotted in the P-T diagram of Fig. 4.5 using the working pair $SrCl_2/NH_3$ as an example. The difference between the equilibrium states and the non-equilibrium conditions is the main driver of the reaction, dominating the reaction rate. This thermodynamic difference is commonly termed as equilibrium drop and can be expressed either in pressure term or in temperature term as Eq.(4.3)) (Bao, Ma & Roskilly, 2016). The higher the equilibrium drop, the faster the reaction rate. If the equilibrium temperature drop is preset as 5 °C and the pressure equilibrium drop is at least 1 bar, the minimum desorption temperature is required as 87 °C (at point B) since the

surrounding as the heat sink environment is at 15 °C (point A) in summer, and the highest adsorption temperature can be achieved as 68 °C (point C) if the average ambient temperature is 5 °C in winter (point D), as the A-B-C-D loop represents the basic cycle at non-equilibrium condition. In the compressor-assisted cycle (A-B'-C'-C-D loop), if the compression ratio is 4 as the curve C'-B' represents the electrical or mechanical-driven compression process, and the discharge temperature denoted by point B' is controlled no higher than the commonly recommended level of 170~180 °C, the desorption temperature (at point C') can be effectively reduced by 30 °C compared to the basic cycle.

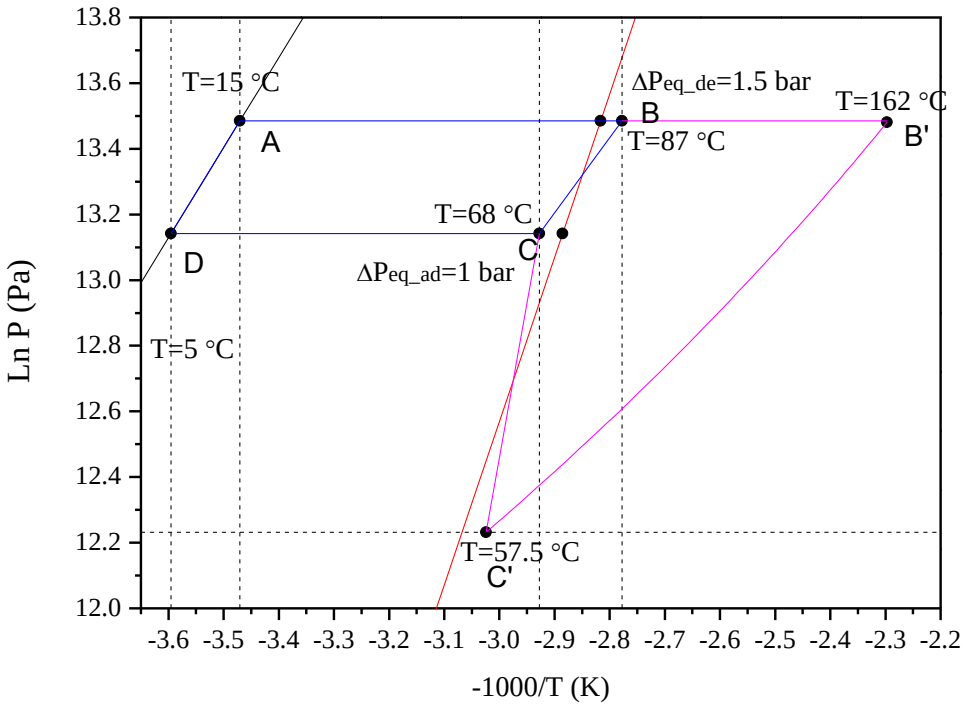

Fig. 4.5 *Clapeyron diagram of the basic thermochemical sorption cycle and the compressor-assist sorption cycle.*

Depending on the compression ratio (CR) calculated from Eq.(4.4), the inlet pressure of the compressor (P_{inlet}) can be represented by the reactor operating pressure (P_r at point C' in Fig. 4.5) where the reactant temperature (T_r) is 5 °C higher than the equilibrium temperature (T_{eq}). The electrical energy demand for the compressor (E_{comp}) is calculated in Eq. (4.5) as the enthalpy change of the ammonia gas from the inlet to the outlet of the compressor. The ammonia real gas properties for calculation were sourced from the free software called Cool Prop which used the method presented by Bell *et al.* (2014). The compression ratio was discussed in the range of 1~16 in this thesis.

$$\ln\left(P_{eq}\right) = -\frac{\Delta H}{RT} + \frac{\Delta S}{R} \tag{4.2}$$

$$\Delta P_{eq} = P_c - P_{eq} \quad \text{or} \quad \Delta T_{eq} = T_c - T_{eq} \tag{4.3}$$

$$\text{CR} = \frac{P_{outlet}}{P_{inlet}} = \frac{P_{B'}}{P_{C'}} \tag{4.4}$$

$$E_{comp} = h_{outlet} - h_{inlet} \tag{4.5}$$

The heat input to the CATSES unit in summer, Q_{in}, calculated in Eq. (4.6), represents the heat released by the HTF without heat transfer loss. Assuming 100% desorption with no heat loss to the ambient due to good insulation around the reactor, the Q_{in} is mainly consumed by sensible heat load of solid composite adsorbent, ammonia and the desorption heat of the ammines. T_{PVT} is the targeted HTF temperature at the outlet of the PV/T collector, i.e. the inlet HTF temperature of the CATSES reactor when assuming no heat loss through the pipes. T_{out} is the HTF temperature at the outlet of the reactor, and it is predefined 5 ºC higher than the equilibrium desorption temperature that corresponds to the inlet pressure of the compressor ($T_{eq}(P_{inlet})$), under the assumption that the maximum heat transfer takes place between the HTF and the reactor without heat transfer loss, but the equilibrium drop (5 ºC) is still guaranteed. The amount of HTF (m_{HTF}) produced by the PV/T collector varied because the HTF flow rate was adjusted in order to achieve the targeted T_{PVT} under the varying weather condition (Thinsurat *et al.*, 2019). The total mass of the HTF that delivers heat to the reactor ($m_{PVT\text{-}React}$) can be calculated according to Eq. (4.7) for two different layouts, where the $m_{PVT\text{-}DHW}$ is the total quantity of the HTF that directly fills up the hot water tank before the rest of the HTF heads to the reactor.

To explore the theoretical performance and maximum potential of the proposed storage system, the influence of external devices and peripheral equipment, such as thermal mass of metallic container and heat transfer coefficient of the heat exchanger on the cyclic performance is not taken into consideration, which varies for different reactor design with various preference and specific considerations. Therefore, only the adsorbent and the ammonia gas are included in the performance analysis. Part of the reactor heat input (Q_{in}) is consumed by the sensible heat load of the solid composite and ammonia and only the desorption heat of the ammines is the stored energy (Q_{stored}) which is rewritten in Eq. (4.8).

$$Q_{in} = m_{PVT\text{-}React} \cdot c_{p\text{-}HTF} \cdot \left(T_{PVT} - T_{out}\right) = n_R x_R \Delta H_R + \int_{T_{amb\_sum}}^{T_{out}} \left[\left(m \cdot c_p\right)_{salt} + \left(m \cdot c_p\right)_{EG} + \left(m \cdot c_p\right)_{NH3}\right] \cdot dT \tag{4.6}$$

$$Case1: m_{PVT-React} = m_{HTF} \quad (4.7a)$$

$$Case2: m_{\text{PVT-React}} = m_{\text{HTF}} - m_{\text{PVT-DHW}} \quad (4.7b)$$

$$Q_{\text{stored}} = n_{\text{NH3\_R}} X_R \Delta H_R \quad (4.8)$$

In this thesis, the reactor heat source in the charging state is from the HTF heated up by the PV/T. The present of the compressor in the CATSES allows flexible operations for energy charging process which introduce the advantages of the CATSES over the TSES as described below.

Option#1: The HTF output temperature from the PV/T (T_{pvt}) is higher than the T_{out}. The PV/T electrical power production is reserved for household usage. Thus, the reactor heat input (Q_{in}) can be utilised in the storage systems. In this case, when there is no electricity support from the PV/T for the compressor, the TSES and the CATSES can store the same amount of thermal energy from the PV/T.

Option#2: The HTF output temperature from the PV/T (T_{pvt}) is higher than the T_{out} and the PV/T electrical power production is more than household electrical demand. In this case, the excess electrical energy may be used to drive the compressor for the CATSES resulting in lower T_{out}. The TSES is able to absorb thermal energy with the same amount as option#1. It can be illustrated in Fig. 4.6 that when the T_{des} is lower, a considerable amount of thermal energy can be additionally stored.

Option#3: The HTF output temperature from the PV/T (T_{pvt}) is lower than the T_{out}; however, the grid electricity is available at an acceptable price. In this case, the TSES cannot store thermal energy from the PV/T but the CATSES may use the grid electricity to drive the compressor which enables the low-temperature HTF from the PV/T collectors to be used for desorption. It also applies to the day of no PV/T output but grid electricity is excessive; if the compression ratio of the compressor is able to lower the reactor pressure that the T_{out} is lower than T_{amb}, the ambient air can be used as a heat source instead of the PV/T with the facilitation of the grid electricity. Therefore, the abundant heat from the ambient can be effectively utilised and the surplus renewable electricity which cannot be accommodated by the grid is simultaneously converted and stored. This operation mode reduces the constraint payment for the "wrong time" production and benefits to shortening the investment return time on the renewable power stations. The grid electricity can be used to store

more thermal energy. As electricity in summer is cheaper than in winter, it is still a cost-effective solution to use cheap electricity in spring, summer or autumn rather than the expensive energy at the peak time in winter to supply the domestic heating demand; therefore, the year-round energy bill is effectively saved.

To illustrate the examples of the abilities to store thermal energy in the two storage systems (TSES vs CATSES) with the PV/T using Eq. (4.6), the reactor containing the $SrCl_2$ adsorbent at the ambient temperature of 15 ^oC is used. When the compressor is not integrated (CR = 1), the T_{out} (=T_{eq}) is around 85 ^oC. In this case, only the HTF with the temperature of higher than 85 ^oC that can be used for the TSES and the amount of input thermal energy is very limited as shown in the red area of Fig. 4.6(a). If the compressor is used in the CATSES with the CR of 16, it can reduce the T_{out} to around 30 ^oC, 55 ^oC lower than the TSES, leading to the enormous increase of thermal energy input in the CATSES as shown in Fig. 4.6(b).

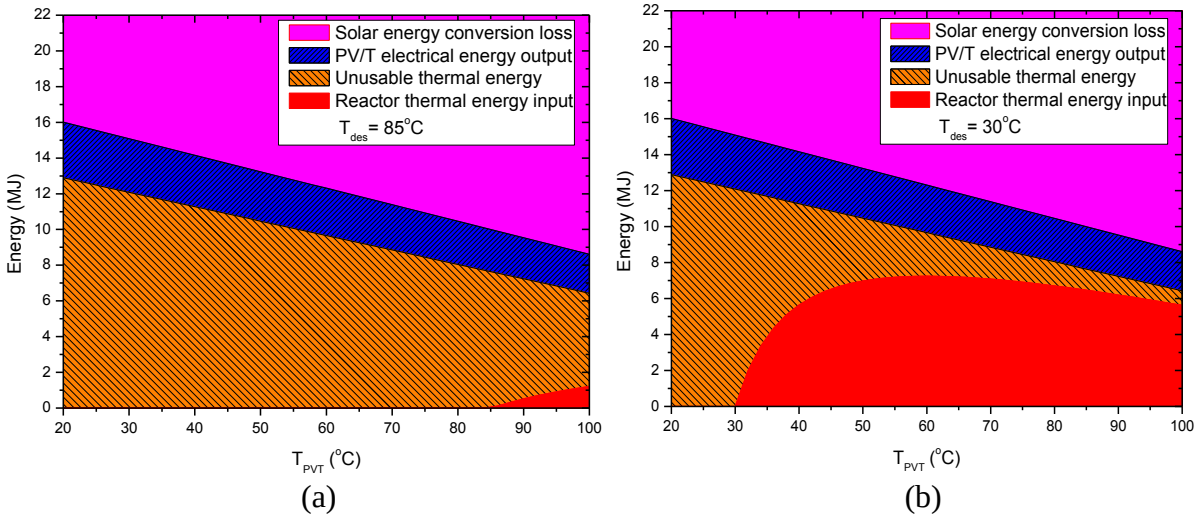

Fig. 4.6 *The comparison of reaction energy input at two different desorption temperature (a) T_{out} = 85 ^oC (@CR=1), (b) T_{out} = 30 ^oC (@CR=16) when $SrCl_2$ is used at the ambient temperature of 15 ^oC*

In winter, the exothermic adsorption takes place in the reactor and releases heat to the HTF (Q_{useful}) after being consumed by the sensible heat load in the reactor as presented in Eq. (4.9). Again, when the heat exchanger has large enough exchange area and good insulation, the maximum HTF temperature obtained was assumed 5 ^oC lower than the equilibrium adsorption temperature in the reactor, as the equilibrium drop is guaranteed as the drive of the reaction. Since the heat input Q_{in} in summer cannot be fully exploited to be the useful heat output Q_{useful} in winter, the storage efficiency ($\eta_{storage}$) is calculated as Eq. (4.10).

$$Q_{\text{useful}} = n_{\text{R}} x_{\text{R}} \Delta H_{\text{R}} - \int_{T_{\text{amb\_win}}}^{T_{\text{release}}} \left[\left(m \cdot c_p \right)_{\text{salt}} + \left(m \cdot c_p \right)_{\text{EG}} + \left(m \cdot c_p \right)_{\text{NH3}} \right] \cdot dT \quad (4.9)$$

$$\eta_{\text{storage}} = \frac{Q_{\text{useful}}}{Q_{\text{in}}} \quad (4.10)$$

4.1.4 Domestic hot water and space heating demands and supplies

Energy production should be used instantly to avoid losses. Therefore, the hot water produced from the PV/T is firstly used to supply domestic thermal demands and the excessive amount is then stored in the seasonal storage. However, during spring to autumn time (March to October), space heating is normally not required for domestic households. In winter (November to February), the PV/T cannot produce high-temperature hot water, so this thesis assumed that the DHW and the SPH are supplied from the thermal storage with no PV/T support. The DHW and SPH demand and supply can be calculated from the followings.

A. Domestic hot water (DHW)

The monthly data of the DHW consumption (m_{DHW}) in a typical UK household and the temperature of the cold water supplies (T_{cold}) from the utility was reported in (Ma, Bao & Roskilly, 2018) as presented in Table 4.2. Therefore, the volume of the hot water tank is designed around 0.4 m^3 to not only meet the daily use but also have extra capacity to store some water for the next couple of days in case of no useful solar energy available. The reused water tank for the PV/T reusable HTF is approximately 2 m^3 to be able to store the HTF in the most peak sunny day in summer (as the results suggested). In general, the heating demand for the DHW can be obtained as Eq. (4.11). For two different operation modes studied in this work in summer, the equation should be modified as eqn Eq. (4.12) to specify the shares between the hot water tank and the thermochemical unit, and also include the electrical input if applicable. If $T_{PV/T}$ or T_{out} is already higher than the required T_{DHW}, it can be mixed with cold water and the required amount of cold water is calculated from Eq. (4.13) to keep the temperature at the safe level. In winter, the storage system releases adsorption heat that is expected to fully cover the heating demands without additional electrical supply.

$$Q_{DHW\_demand} = m_{DHW} \cdot C_{P-HTF} \cdot (T_{DHW} - T_{cold}) \quad (4.11)$$

Summer: Case#1; $Q_{DHW_{supply}} = m_{PVT-DHW} \cdot C_{P-HTF} \cdot (T_{DHW} - T_{out}) + E_{heater(optional)}$ (4.12a)

Summer: Case#2; $Q_{DHW_{supply}} = m_{DHW} \cdot C_{P-HTF} \cdot (T_{DHW} - T_{PV/T}) + E_{heater(optional)}$ (4.12b)

$$m_{w-cold} = m_{PVT-DHW} \cdot \frac{T_{PVT} - T_{DHW}}{T_{DHW} - T_{w-cold}} \quad (4.13)$$

Table 4.2 *The mean domestic hot water used and the monthly averaged cold-water temperatures in a typical household in Newcastle upon Tyne, UK (Ma, Bao & Roskilly, 2018)*

Month	JAN	FEB	MAR	APR	MAY	JUN	JUL	AUG	SEP	OCT	NOV	DEC
T_{cold} (ºC)	9.62	9.32	10.70	13.70	15.32	17.26	19.33	18.67	17.88	15.55	12.22	10.51
DHW consumption (L/day)	116.86	124.64	125.71	114.74	122.88	116.50	98.44	105.52	112.61	123.58	127.84	133.16
T_{amb} (ºC)	3.0	3.1	5.1	7.1	9.9	13.0	14.5	14.4	12.6	9.6	6.0	3.8

B. Space heating (SPH)

The space heating demand depends mostly on the overall heat loss coefficient of the household, the ambient temperature and the required indoor temperature, and it can be calculated from Eq. (4.14) as the Q_{SPH} represents the energy demand for space heating. The overall heat loss coefficient ($\overline{UA}$) varies depending on floor area, insulation and wind speed and the value ranges between 50 to 300 W/K for the typical UK households (Johnston & Siddall, 2016). The room temperature (T_{room}) is normally set to approximately 21 ºC for most of the existing household (Ma, Bao & Roskilly, 2018; Kane, Firth & Lomas, 2015). To provide space heating through water radiator, the supply and return temperatures of the HTF to the radiator vary from country to country following the national code of practice range from 70-95 ºC for the supply temperature and 40-75 ºC for return temperature (Skagestad, Bard and Mildenstein, 2002). Currently, in the UK, it is common to use the supply temperature of 60-80 ºC and the return temperature as low as 35 ºC (YouGen, n.d.). In this thesis, the storage discharging capability is designed to supply hot water (T_{RST}) at least 60 ºC and the radiator return temperature (T_{RRT}) is considered to be 40 ºC, and the $\dot{m}_{SPH}$ is the mass flow rate of the HTF. It was assumed the heating time (t) was averagely 10 hours per day in winter.

$$Q_{SPH} = \overline{UA} \cdot \left(T_{room} - T_{amb}\right) \cdot t = \dot{m}_{SPH} \cdot c_{p\text{-}HTF} \cdot \left(T_{RST} - T_{RRT}\right) \cdot t \tag{4.14}$$

4.1.5 Objectives and constraints for the optimisation

The objective in this thesis is to maximise the net useful energy in the charging period (during spring, summer and autumn) with the schematic that provides more storable thermal energy. The net useful energy (E_{total}) is defined as the total usable energy from the PV/T in the

considered charging day expressed in Eq. (4.15) which is constrained by the following condition

- Storable energy is supplied by the HTF from the PV/Ts (schematic 1 and 2 provides a different amount of the reactor heat input ($Q_{reactor\text{-}in}$))
- The compressor is used at the compression ratio that supports 100% winter solar fraction (SF) but not more than 16; SF can be calculated from Eq. (4.16)
- Electrical energy output from the PV/Ts is used to drive the compressor and the DHW via the auxiliary heater if required

$$E_{total} = Q_{\text{reactor}-\text{in}} + E_{PVT-elec} - E_{comp} - E_{heater} \quad (4.15)$$

$$SF = \frac{Q_{DHW\_supply} + Q_{SPH\_supply}}{Q_{DHW\_demand} + Q_{SPH\_demand}} \quad (4.16)$$

Because of the involvement of the compressor, the potential desorption temperature spans a wider range. The compressor is powered either by the PV/T or the grid electricity, the storable thermal energy varies when $T_{PV/T}$ varies.

4.2 Domestic hot water and space heating demands

To assess the annual performance and preliminary sizing of the integrated system for a typical domestic household in high latitude regions, the monthly lump sum of the thermal energy demand in a household in Newcastle upon Tyne, UK was determined as follows.

4.2.1 Domestic hot water (DHW)

According to the average DHW consumption per day for a typical household in Newcastle and the mean cold-water temperature supplied by a water utility (as presented in Table 4.2), the DHW energy demand could be calculated from Eq. (4.11) and the result is presented in Table 4.3. The DHW is consumed at its peak in winter with the maximum consumption of 4.13 m^3/month in December in addition to low cold-water temperatures resulting in higher thermal energy demand. In wintertime from November to February, the total DHW energy demand is approximately 3.13 GJ which will be used to calculate the winter solar fraction of the storage system. The DHW energy demand in the charging period from March to October is supplied by the PV/T's thermal energy output and heated up to 60 ^oC by the electrical auxiliary heater driven by the PV/T electrical output if required. The DHW tank was used to store hot water for

the DHW demand of up to 3 consecutive days which is approximately 0.4 m^3. The DHW thermal energy demand of 5.20 GJ in the energy charging period (in spring, summer and autumn from March to October) was also supplied by the PV/T with the two cases of integrated layout in Fig. 4.4 before storing the excessive amount in the CATSES.

4.2.2 Space heating (SPH)

For the space heating (SPH) energy demand, following the assumptions that the comfortable room temperature is 21 ^oC, the overall heat loss coefficient ($\overline{UA}$) of 125 W/K and the average heating hour per day of 10 hours, the thermal energy demand for the space heating could be calculated using Eq. (4.14) with the average ambient temperature in Newcastle upon Tyne at 6 ^oC, 3.8 ^oC, 3.0 ^oC and 3.1 ^oC from November to February respectively in winter (in Table 4.2). By following the mentioned assumptions, the SPH energy demand was presented in Table 4.3.

Combining 3.13 GJ of DHW energy demand and 9.19 GJ of SPH energy demand in winter, 12.32 GJ of winter heating energy demand for a typical UK household was used for further calculations.

Table 4.3 *Heating demands in a typical household in Newcastle upon Tyne, UK*

Month	**JAN**	**FEB**	**MAR**	**APR**	**MAY**	**JUN**	**JUL**	**AUG**	**SEP**	**OCT**	**NOV**	**DEC**
DHW consumption (m^3/month)	3.62	3.49	3.90	3.44	3.81	3.50	3.05	3.27	3.38	3.83	3.84	4.13
DHW energy demand (GJ/month)	0.76	0.74	0.80	0.67	0.71	0.63	0.52	0.57	0.60	0.71	0.77	0.86
SPH energy demand (GJ/month)	2.51	2.26	-	-	-	-	-	-	-	-	2.03	2.40

4.3 PV/T energy production summary

According to the PV/T geometry described in Chapter 3 and the weather condition of Newcastle upon Tyne, the mass flow rate of the HTF in the PV/T was controlled in the simulation to produce targeted output temperatures ($T_{PV/T}$) range from 40 to 100 ^oC. Autumn days produce less thermal energy than summer days roughly 27-36% at $T_{PV/T}$ of 40 ^oC and 100

^{o}C respectively. Spring days provide slightly less thermal energy than autumn days and lastly, PV/T cannot produce HTF with the $T_{PV/T}$ higher than 40 ^{o}C in winter days as illustrated by the amount of HTF in Fig. 4.7. Apart from the weather effect, when $T_{PV/T}$ was low, the thermal energy efficiency of the PV/T is relatively higher, meaning it can deliver more amount of thermal energy, compared to the case of higher $T_{PV/T}$, as also illustrated in Fig. 4.7, PV/T produced the highest amount of HTF with approximately 130 kg/m^2 at 40 ^{o}C and 28 kg/m^2 at 100 ^{o}C on a summer sunny day in Newcastle upon Tyne.

It is obvious that PV/Ts can produce the highest electrical energy in summer, spring days can produce slightly more electrical energy than autumn days as shown in Fig. 4.8 because the average ambient temperature in spring days is lower than that in autumn days. There is about 805 Whr/m^2 electricity output with $T_{PV/T}$ at 100 ^{o}C, about 25% less than the production at 40 ^{o}C temperature output, which is about 1070 Whr/m^2 on a summer sunny day in Newcastle upon Tyne. In winter cloudy or rainy or snowy days which averagely accounts for 50-75% of the wintertime depending on years, electrical energy and hot water production from the PV/T is negligible; therefore, the storage and utilities are the energy supplies for the household demands.

Statistical data of Newcastle weather suggests that there are only around 9 sunny days per month in the summer, and 7-10 sunny days per month in spring and autumn; for the rest of the time, there would be barely recoverable solar energy. Therefore, this work assumed that there was only 9-day-per-month availability of solar energy in three seasons (from March to October) that was converted not just for daily use in these three seasons but also to be stored for winter use (from November to February) as well. Therefore, the PV/T energy productions shown in Fig. 4.7 and Fig. 4.8 were used in later sections with the number of production days in each mentioned season. As the results in later sections of this chapter suggested that the optimum HTF temperature from the PV/T are normally more than 40 ^{o}C; therefore, the PV/T energy productions shown in Fig. 4.7 and Fig. 4.8 were simulated starting from 40 ^{o}C and the HTF temperature lower than 40 ^{o}C is not considered in this thesis.

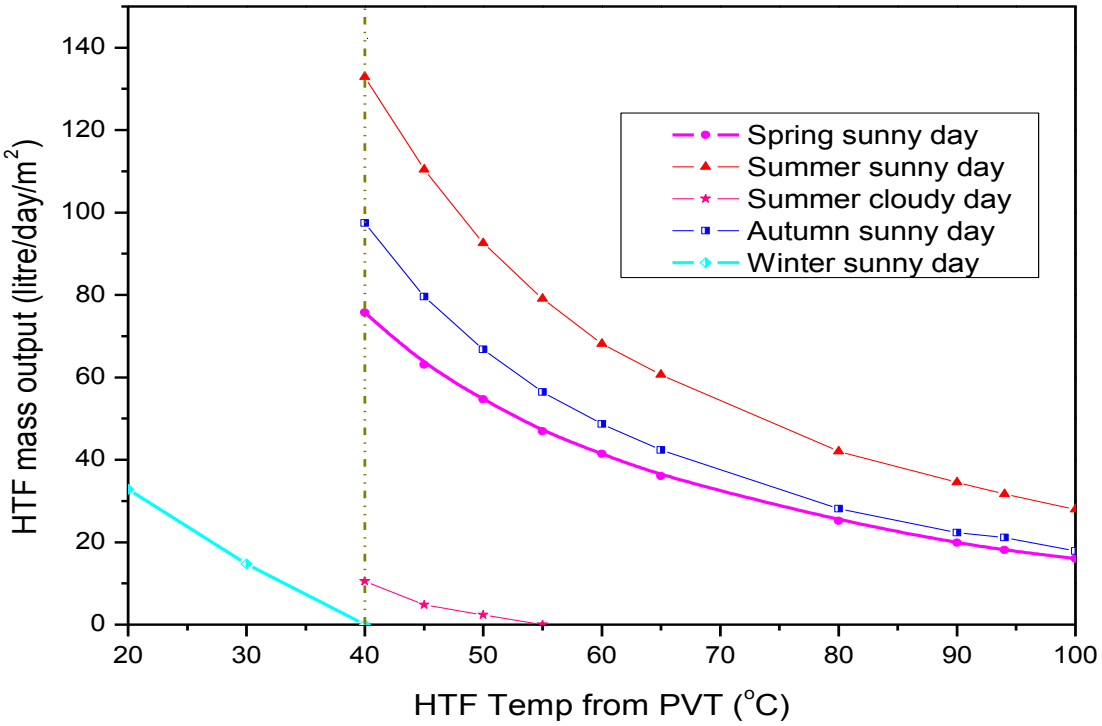

Fig. 4.7 *The amount of HTF output from the AG-PV/T on different weather conditions and time of the year*

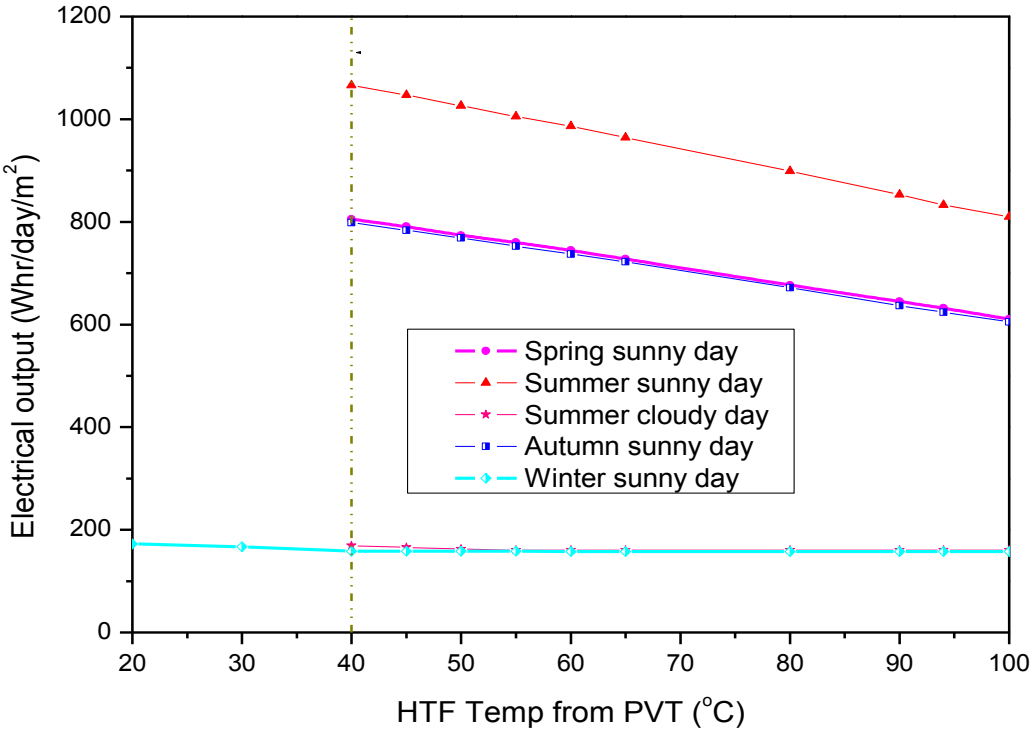

Fig. 4.8 *The electrical energy production from the AG-PV/T on different weather conditions and time of the year*

4.4 Reactive salt selection

In order to identify the suitable ammines for the proposed system, it should, first of all, determine the operating conditions like the real weather conditions and the targeted performance. According to the weather in the city of Newcastle upon Tyne, the average ambient temperature (T_{amb}) in spring (March-May) is 8.1 ^{o}C, 15.5 ^{o}C in summer (June – July) and 12.3 ^{o}C in autumn (August – October). The winter (November - February) has the T_{amb} around 5 ^{o}C with 11 days in the last 5 years suffered from the coldest weather between -5 and -7 ^{o}C. That implies during these coldest days with the minimum working pressure (i.e. synthesis pressure) was around 3.3-3.5 bar (NH_3 evaporation pressure at -5 ~ -7 ^{o}C), the system should still be able to deliver hot water at least 60 ^{o}C if equipped with high-temperature heating facilities, e.g. water radiator, or 40-50 ^{o}C if low-temperature heating facilities is used e.g. the floor heating or air-fanned radiator. With this baseline of heating performance in winter, some salts can be shortlisted for a basic cycle and water radiator heater, such as $CaCl_2$(8/4), NaI, $BaBr_2$, $SrCl_2$, $CaCl_2$(4/2), $SrBr_2$, $MnCl_2$ and so on, because their adsorption temperature corresponding to the evaporation pressure is higher than 60 ^{o}C, as shown in Table 4.4.

For the energy charging process, since the PV/T-AG panel typically generates thermal energy up to 100 ^{o}C in a sunny day, that sets the threshold of desorption temperature and only $CaCl_2$(8/4), NaI, $BaBr_2$, $SrCl_2$ and $CaCl_2$(4/2) in Table 4.4 can apply to the non-compressor system. However, for the compressor-assisted system, there are more options of ammines because the threshold of desorption temperature (i.e. heat source temperature) can be significantly declined due to the further pressurising process by the compressor. For example, if a compressor with the CR of 8 is used, the minimum desorption temperature required can be brought down as shown in the last column of Table 4.4. Therefore, $SrBr_2$, $MnCl_2$ and $CaBr_2$ enter the shortlist to be studied and compared with the other aforementioned potential candidates, as the feasibility, practical performance and the optimal operating conditions of the proposed system using these candidates under the real weather condition is evaluated and discussed in more details.

The investigation and evaluation on such a highly hybridized systems has been carried out in a wide operating conditions to explore the boundaries and maximum potential of the concept, with the CR value between 1 and 16 as well as effective recovery or release of compression heat so that the compression discharging temperature is controlled under 180 ^{o}C as recommended by most manufacturers.

Table 4.4 *The characteristics of the thermochemical sorption working pairs considering the ambient temperature of 15 ^oC and 5 ^oC in summer and winter respectively.*

Reactive salts	Mass ratio (kg NH_3 /kg salt)	Energy density (kJ/kg salt)	Adsorption temperature (^oC)	Desorption temp (^oC) No compressor (CR =1)	Desorption temp (^oC) compressor-assisted (CR =8)
NH_4Cl	0.9568	1,653.54	25.55	34.52	-6.85
$PbCl_2$	0.4901	586.35	27.25	35.00	-1.01
NaBr	0.8689	1,804.23	32.13	39.89	3.73
$BaCl_2$	0.6544	1,469.74	37.73	45.16	10.41
LiCl	1.6105	870.64	46.44	54.60	16.32
$CaCl_2(8/4)$	1.2297	1,480.61	66.54	74.82	35.64
NaI	0.5113	1,180.96	68.52	77.26	35.95
$BaBr_2$	0.4586	563.45	74.34	82.82	42.54
$SrCl_2$	0.8602	1,830.96	74.33	82.90	42.23
$CaCl_2(4/2)$	0.6148	762.98	78.11	86.69	45.88
$SrBr_2$	0.5507	1,106.31	107.19	116.52	71.79
$MnCl_2$	0.8129	1,508.86	126.86	136.79	88.93
$CaBr_2$	0.5114	980.28	131.40	141.23	93.74
$FeCl_2$	0.8072	1,619.78	159.71	170.46	-
$MnBr_2$	0.4759	988.65	173.02	184.06	-
$CoCl_2$	1.0836	2,290.01	182.30	193.60	-
$MgCl_2$	1.0745	2,341.16	186.72	197.89	-
$FeBr_2$	0.4740	1,035.77	197.03	208.69	-

4.5 PV/T-CATSES integration results

To be clear, this thesis does not use any optimisation algorithms but trialled the overall range of operating conditions then select the optimum operating points corresponding to the global maximum value of the objective parameter. This section reveals the optimisation results for different reactive salts to suggest the promising ones to be deployed for the integrated system that can annually supply energy for the heating demands to a typical UK household

using only the solar energy resource. Additionally, the required installation area of the PV/T system and the material volume for the storage system will be discussed. The energy productions from the PV/T from chapter 4 and the reactor designed in chapter 5 were used for the system performance evaluation in this chapter.

Fig. 4.9 exemplifies the profiles of the electrical and thermal production from the PV/T, the compressor electricity demand, DHW energy demand the storable thermal energy and the net useful energy using the $SrCl_2$(8-1)/NH3 working pair and a compressor with a (CR) value of 8, when the PV/T output temperature ($T_{PV/T}$) varies from 40 to 100 ^oC, and the heat sink temperature, i.e. condensation temperature, was at 15 ^oC. There are three energy output curves in the positive zone above the x-axis, which is the reactor heat input ($Q_{in\text{-}reactor}$), pure electrical output (E_{out}) and the net useful energy gain (E_{total}) which is algebraic sum of all energy outputs and all energy consumptions within the system. The negative zone below the x-axis encompasses two energy consumption curves, one is electricity consumption by the compressor (E_{comp}), and the other one is for the standby electric heater (E_{heat}) that is only put in use when the hot water temperature for daily use is unsatisfactory. The intersection point of the storable thermal output curve and the x-axis indicates the threshold of desorption temperature of the thermochemical sorption cycle with the assistance of the compressor, which is 43.40 ^oC (i.e. $T_{eq}+ \Delta T_{drop}$ in non-equilibrium conditions and equilibrium drop is pre-set at 5 ^oC), reduced by 38.57 ^oC compared to the basic cycle at 81.97 ^oC. With the same weather data, the pure electrical output is only related to the PV temperature, represented by the HTF temperature, therefore, the blue line has the same profile in both cases in Fig. 4.9(a) and Fig. 4.9(b).

For the operation mode of case#1 shown in Fig. 4.4(a), the entire HTF carrying thermal outputs from the PV/T heats the reactor for desorption prior to being collected in the hot water for daily use and its temperature when it arrives in the hot water tank never reaches the desired level (60 ^oC) under all the conditions studied in this work, then the standby electric heater has to consume part of the electricity generated by the PV/T panel to heat the water up, which is depicted by the orange curve. In the case#2, the daily DHW directly comes from the PV/T and there is no extra electricity consumption once the outlet HTF temperature is controlled higher than T_{DHW} (60 ^oC).

For the $Q_{in\text{-}reactor}$ curves, there are two factors influencing the tendency, accordingly which also explains the variation profile of electricity consumption by the compressor, since they are closely related. With the fixed HTF temperature at the outlet of reactor, the higher the targeted HTF temperature at the outlet of the PV/T (i.e. the inlet of the reactor), the more thermal input

towards the reactor, leading to more amount of the desorbed ammonia and more energy stored in the form of chemical potential. In the meantime, the higher HTF temperature not just decreases the electricity efficiency but also abates the thermal efficiency of the PV/T. These two conflicting factors create an optimal operating point of the HTF temperature for maximising the storable thermal energy. In principle, if based on the net energy gain, there should be another different optimal operating point as plotted in dash lines in Fig. 4.9, although there is not much difference between the values of these two optimal points under the conditions studied in this work, depending on the compression ratio. For example, as shown in Fig. 4.9 with CR=8, the optimum HTF temperatures are 88.68 and 87.27 ^{o}C with the maximum net energy gain of 243.06 MJ and 235.09 MJ per 30 m^2 PV/T installation per day in case 1 and 2, respectively, on a typical summer sunny day. The optimal HTF temperature of case 1 and 2 for maximum storable thermal energy under the same conditions is 90.10 and 91.51 ^{o}C, respectively. Case#1 can store considerably more thermal energy than the case#2, leading to a larger flow of the desorbed ammonia and more electricity consumption by the ammonia compression process. The electricity consumption curves have their negative peaks when the stored thermal energy curves have their positive peaks. Together with larger electricity consumption on an electric heater, there is no impediment superior of the case#1 over the case#2 in terms of net energy gain. For further comparisons, the profiles of spring sunny day (in Fig. 4.10) and autumn sunny day (in Fig. 4.11) are also presented with the CR of 1, 4 and 16 when using $SrCl_2/NH_3$ working pair.

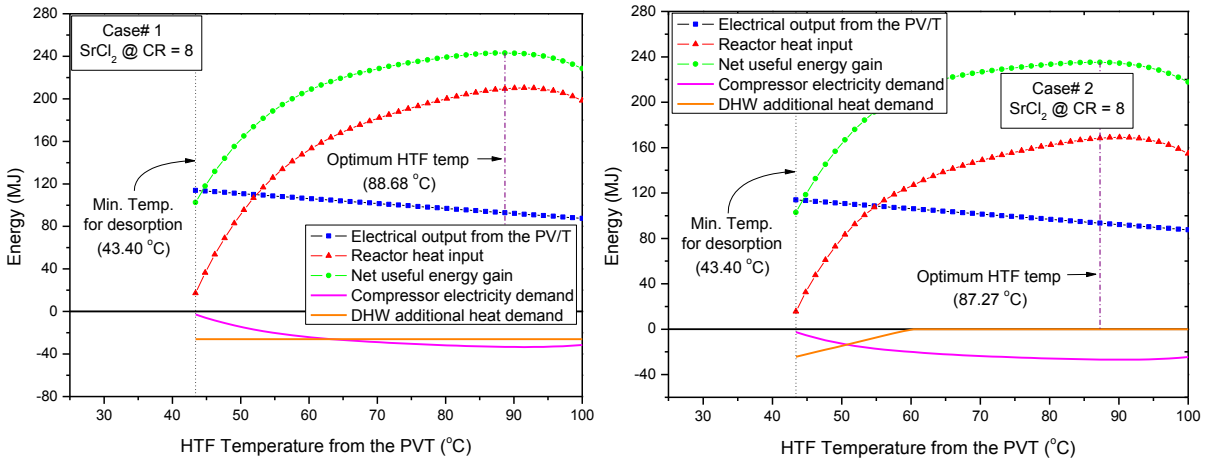

Fig. 4.9 *The energy variation profiles with different HTF temperatures on a sunny summer day when using $SrCl_2/NH_3$ working pair and the CR of 8: (a) case 1 (b) case 2.*

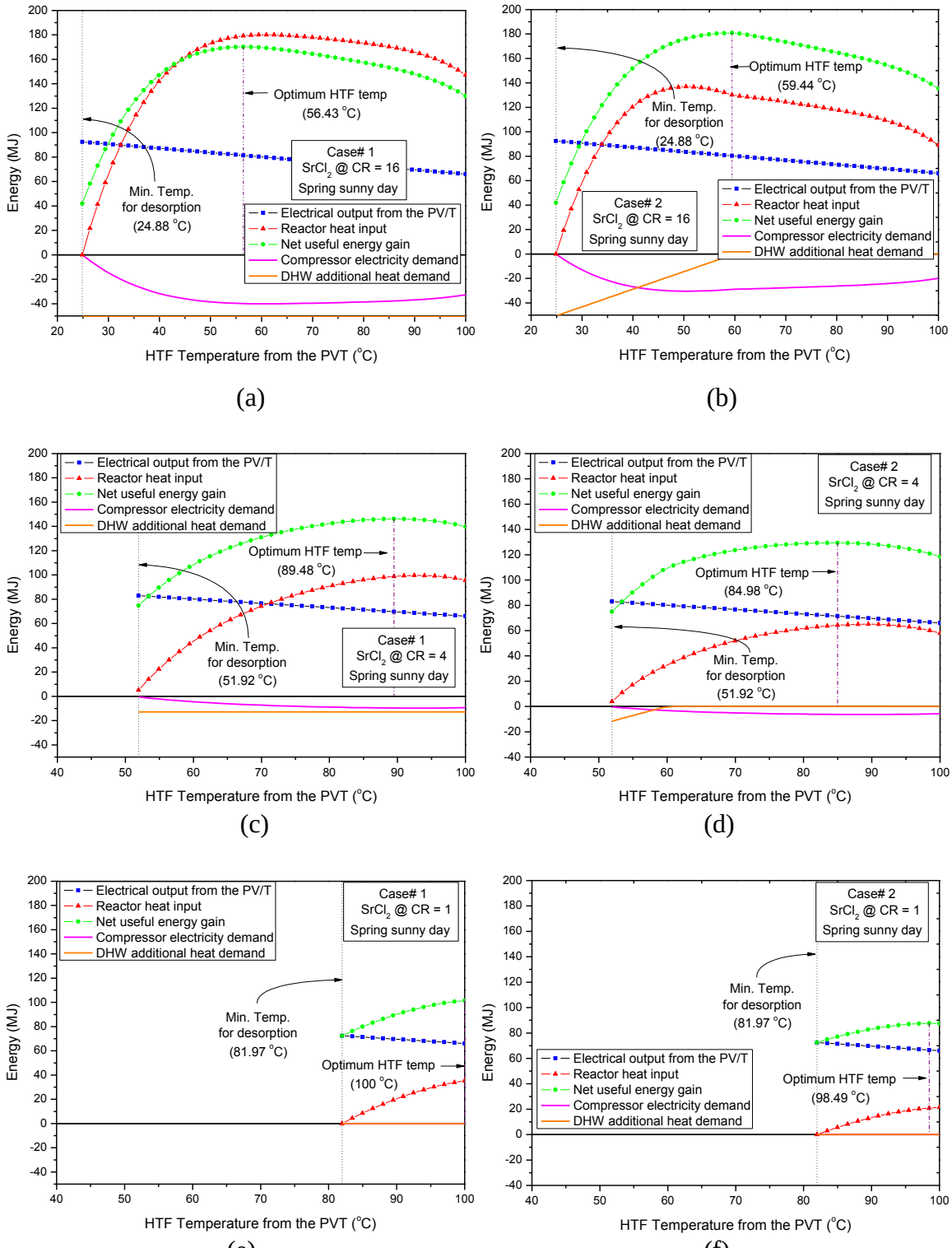

Fig. 4.10 *The energy variation profiles with different HTF temperatures on a sunny spring day when using $SrCl_2/NH_3$ working pair: (a) case 1 with the CR of 16, (b) case 2 with the CR 16, (c) case 1 with the CR of 4, (d) case 2 with the CR of 4, (e) case 1 with the CR of 1, (f) case 2 with the CR of 1.*

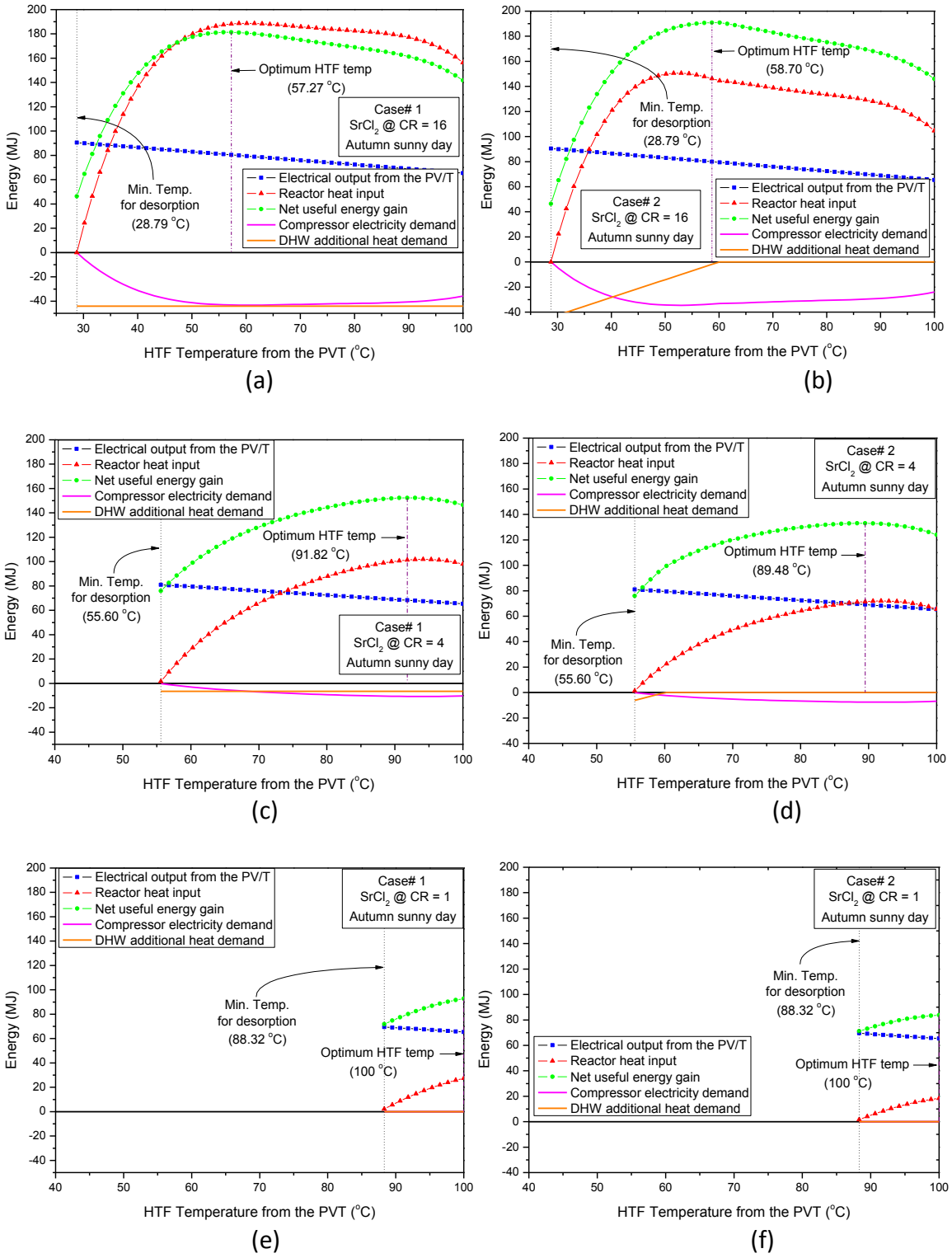

Fig. 4.11 *The energy variation profiles with different HTF temperatures on a sunny autumn day when using $SrCl_2/NH_3$ working pair: (a) case 1 with the CR of 16, (b) case 2 with the CR 16, (c) case 1 with the CR of 4, (d) case 2 with the CR of 4, (e) case 1 with the CR of 1, (f) case 2 with the CR of 1.*

Fig. 4.12 presents more comparison between the two cases with different CRs. The cumulative summation clearly display the relationship between the energy output and energy consumption, as the light (E_{comp})/dark (E_{heat}) grey zones denote energy consumption by

compressor/electric heater, the magenta zones represent thermal energy storage and the pink area (E_{net}) means redundant electricity that can be traded into the grid or used for other appliances, the only one blue strip in Fig. 4.12(a) suggests the deficit of electricity ($E_{deficit}$), meaning the electrical generation by the solar PV/T panel cannot 100% satisfy the total electricity consumption within the systems but requires import from the grid.

By using higher CRs, more thermal energy can be effectively recovered and stored regardless of the operation modes (case 1 or case 2), because it enables the utilisation of the relatively lower temperature heat for endothermal desorption. Correspondingly, there exists an optimum operating condition with lower HTF temperature which is favourable to the longevity of the PV/T panel. If the primary goal is to increase the solar fraction of domestic space heating, it is noticeable in Fig. 4.12 that case1 has prominent superiority to case 2.

The maximum potential of the reactor heat input and net energy gain for each case using different CR values from 1 to 16 is summarised in Fig. 4.13 for summer, spring and autumn for the system operating with $SrCl_2/NH_3$ working pair. Again, the case 1 stores more thermal energy than case 2, the storage capacity gap expands with the increasing CR values, For the net energy gain, two curves in Fig. 4.13(b), (d) and (f) cross over each other at the point of CR = 11.5, 8.5 and 9.5 on the summer, spring and autumn sunny days respectively. Consider the summer sunny day, The case 1 can yield more net useful energy than the case 2.if the CR value is lower than 11.5 and the maximum gap exists between CR=3 and 4 as the gap gradually narrows down with the increasing CR value; over the point of CR=11.5, it becomes opposite as the case 2 marginally beats the case 1. The operating conditions with higher CR enable desorption to occur at a lower equilibrium temperature, leading to lower HTF temperature at the outlet of the reactor in the case1, which is subsequently received by the hot water tank. In this instance, there is not just the compressor that consumes more electrical power due to the higher CR but also the electric heater which is activated and consumes more electricity for lifting the water temperature to the required level of daily use. For example, as shown in Fig. 4.12(a), with the CR value at 16, the optimum HTF temperature is determined at around 60 ^{o}C when the two electricity consumptions combined exactly offset the electrical yield from the PV/T panel, at which point the net energy gain is merely represented by the amount of thermal energy stored. However, for the case2, running the system with the HTF temperature at the optimum point- similarly to the case 1, at around 60 ^{o}C, there is a substantial share of net electricity output plus $Q_{in\text{-}reactor}$ to represent the net useful energy gain (E_{total}).

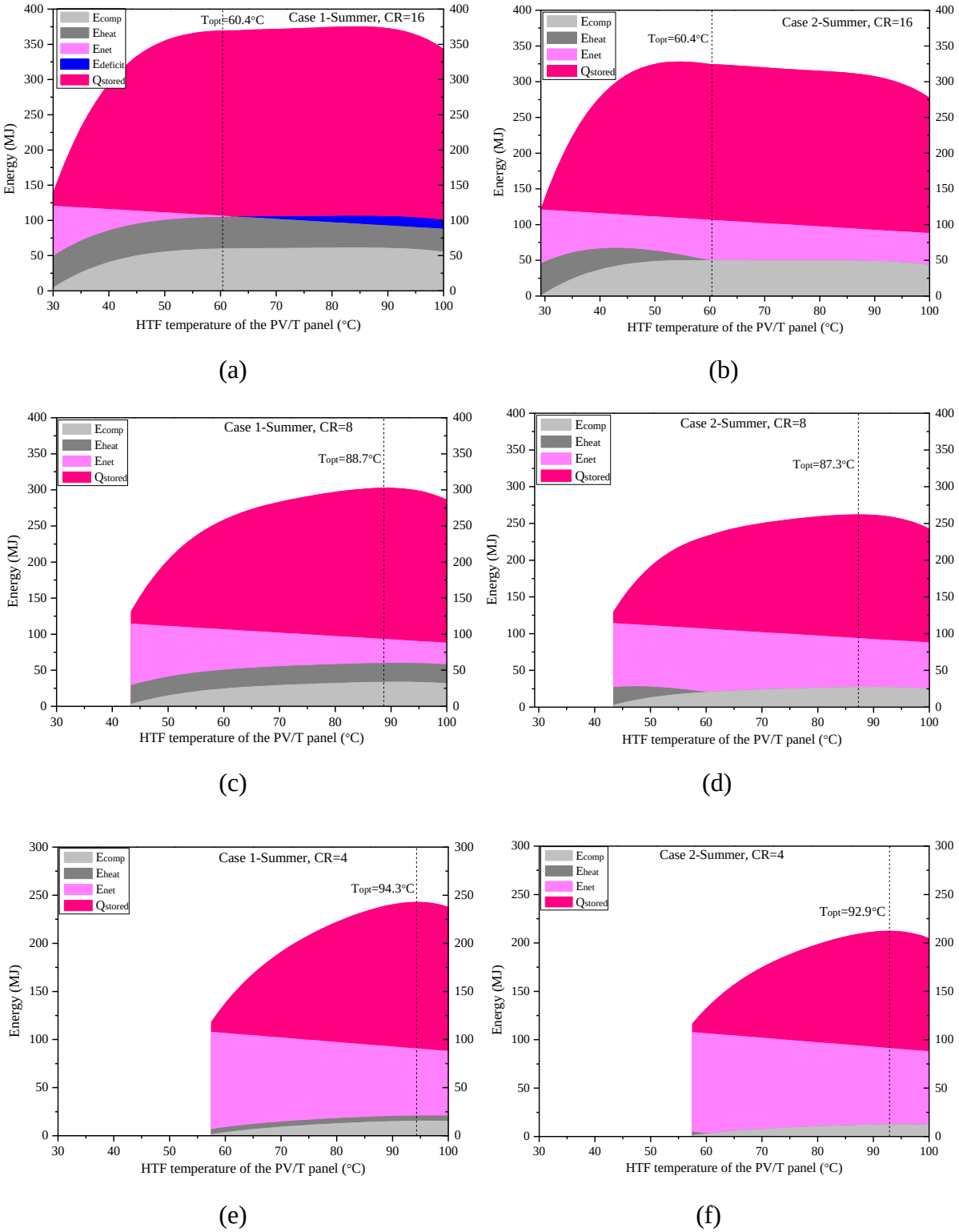

Fig. 4.12 *The energy variation profiles VS different HTF temperatures on a sunny summer day when using $SrCl_2/NH_3$ working pair and the CR of 4, 8 and 16 in two different operation modes.*

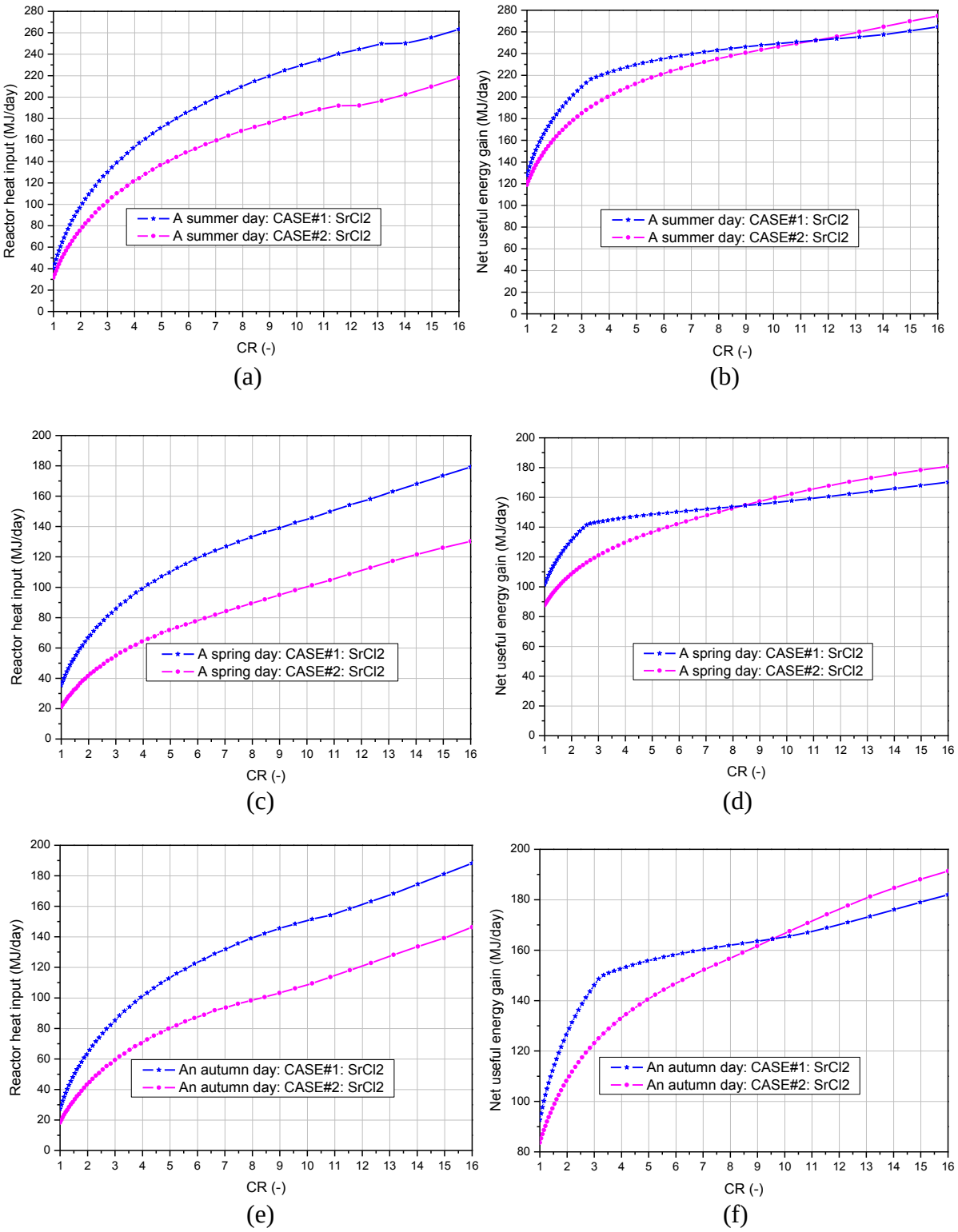

Fig. 4.13 *The correlations when using $SrCl_2$ as an adsorbent: (a) CR vs reactor heat input in a summer sunny day, (b) CR vs Net useful energy gain in a summer sunny day, (c) CR vs reactor heat input in a spring sunny day, (d) CR vs Net useful energy gain in a spring sunny day, (e) CR vs reactor heat input in an autumn sunny day, (f) CR vs Net useful energy gain in an autumn sunny day.*

The following sections focus on case 1 to explore the potential of the system using different potential reactive salts since the storage capacity is prioritised in this work. Fig. 4.14 show the

optimum PV/T operating conditions (HTF temperature) and the net energy gain when using 7 reactive salt candidates, which are $CaCl_2$(8-4), $SrCl_2$(8-1), NaI(4.5-0), $BaBr_2$(8-4), $SrBr_2$(8-2), $MnCl_2$(6-2) and $CaBr_2$(6-2). Among all, using $CaCl_2$(8-4) and NaI(4.5-0) working pairs similarly provide the best performance with the lowest HTF temperature at the optimum condition since they have very similar equilibrium characteristics, which is followed by the $SrCl_2$(8-1) and $BaBr_2$(8-4) cases. Because $CaCl_2$(8-4) and NaI(4.5-0) working pairs have lower equilibrium temperature than the $SrCl_2$(8-1) and $BaBr_2$(8-4) cases under the same working pressure, the former two can use relatively lower temperature heat for desorption, namely it allows lower PV cell temperature to ensure higher energy conversion efficiency, leading to more thermal and electrical energy output from the PV/T panel. On the other hand, although the $CaCl_2$(8-4) and NaI(4.5-0) cases are advantageous at the quantity of the heat stored, but the $SrCl_2$(8-1) and $BaBr_2$(8-4) cases are more secure in terms of delivering qualified heat in the winter, ensuring the heating at the desired temperature level even in case of unexpected record-breaking cold weather.

The plunge on $CaCl_2$(8-4) and NaI(4.5-0) curves from CR=9 to CR=10 could be explained when referring to Fig. 4.15 as when the CR is low, the desorption temperature is high resulting in high dominate on ΔT ($T_{PV/T} - T_{out}$) rather than the amount of HTF ($m_{PV/T\text{-}react}$) produced from the PV/T at $T_{PV/T}$ when calculating the heat stored from the HTF (at $T_{PV/T}$) to the reactor (at T_{out}). When CR is sufficiently high so that the desorption temperature is low enough, $Q_{in\text{-}reactor}$ is quite linear as shown in Fig. 4.12(a). At those CRs, operating the PV/T at 90 or 60 ^oC gives similar results on the amount of useful energy. Then when higher CRs than the critical point were operated, the optimum point suddenly moves to lower temperatures as $m_{PV/T\text{-}react}$ plays more important roles than the ΔT as the energy loss is lower with low temperatures operation. Correspondingly, there is a sudden steeply rise on the net energy gain curve at the same CR point. The $BaBr_2$(8-4) case is slightly inferior to the $SrCl_2$(8-1) one, and the inferiority grows with the increasing CR values, especially when the $SrCl_2$(8-1) curve has the similar plunge when the CR value higher than 13. The other three working pairs, i.e. $SrBr_2$(8-2), $MnCl_2$(6-2) and $CaBr_2$(6-2), fail to meet the criteria of substantial reduction of the required HTF temperature even though the CR is already as high as 16, these working pairs were ruled out for further comparison and evaluation in the following sections.

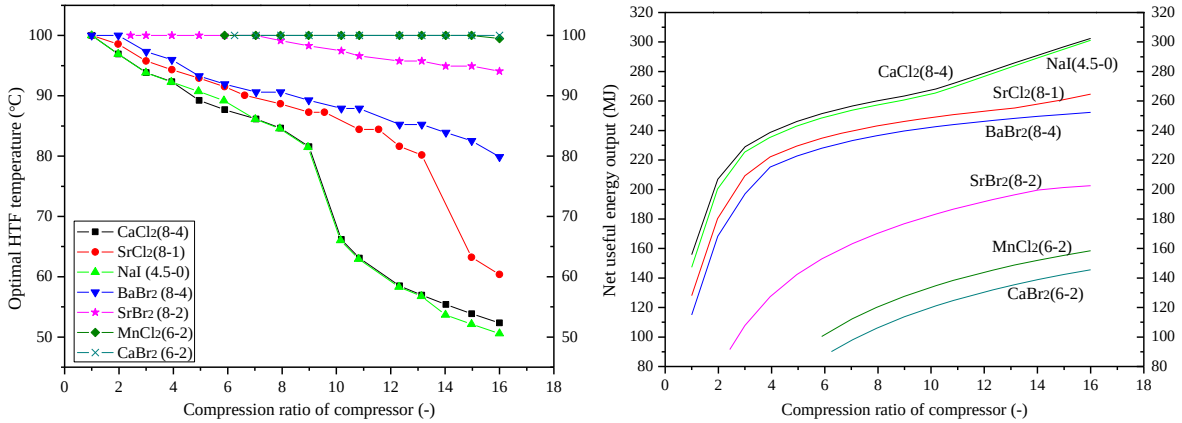

(a) (b)

Fig. 4.14 *(a) CR vs optimum HTF temperatures and (b) CR vs Net useful energy for all viable reactive salts in a summer sunny day*

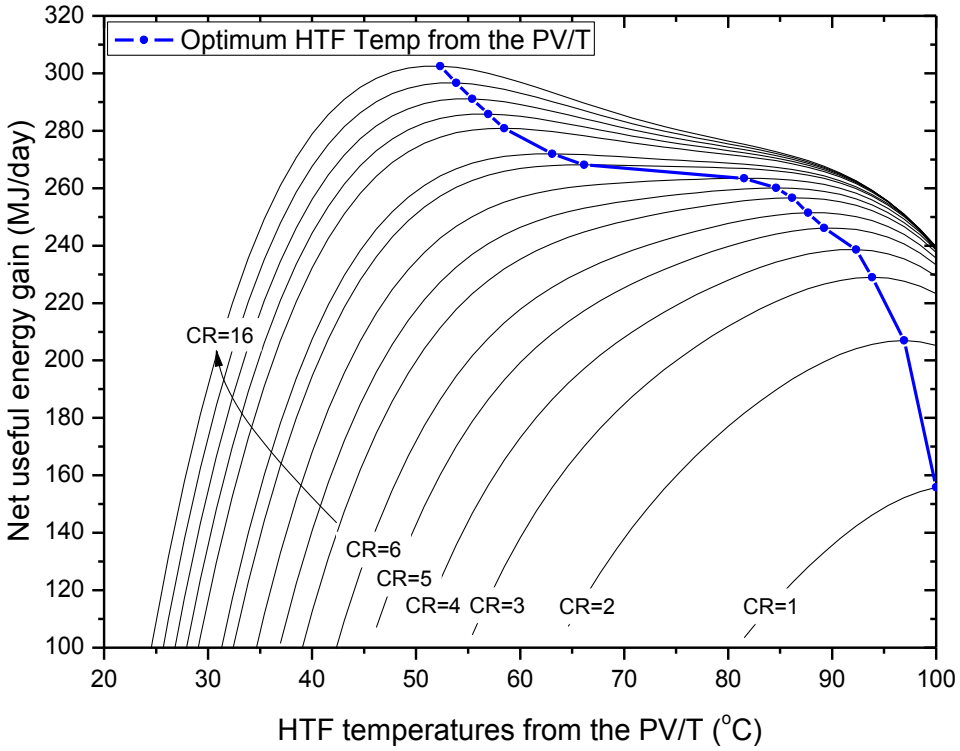

Fig. 4.15 *The optimal HTF temperatures considering the net useful energy gain when CR ranges from 1 to 16 on a summer sunny day when using $CaCl_2$(8-4) as a reactive salt*

From the four potential reactive salt candidates, the energy variation profiles with different HTF temperatures for different days of the year of $CaCl_2$(8-4), NaI(4.5-0) $BaBr_2$(8-4) and $SrCl_2$(8-1) when using case 1 are presented in Fig. 4.16, Fig. 4.17 Fig. 4.18 and Fig. 4.19 respectively. Moreover, focusing on case 1, the correlations between the CR and the reactor heat input are compared with the correlation between the CR and the net useful energy gain are

presented in Fig. 4.20, Fig. 4.21 and Fig. 4.22 for $CaCl_2$(8-4), NaI(4.5-0) and $BaBr_2$(8-4) respectively.

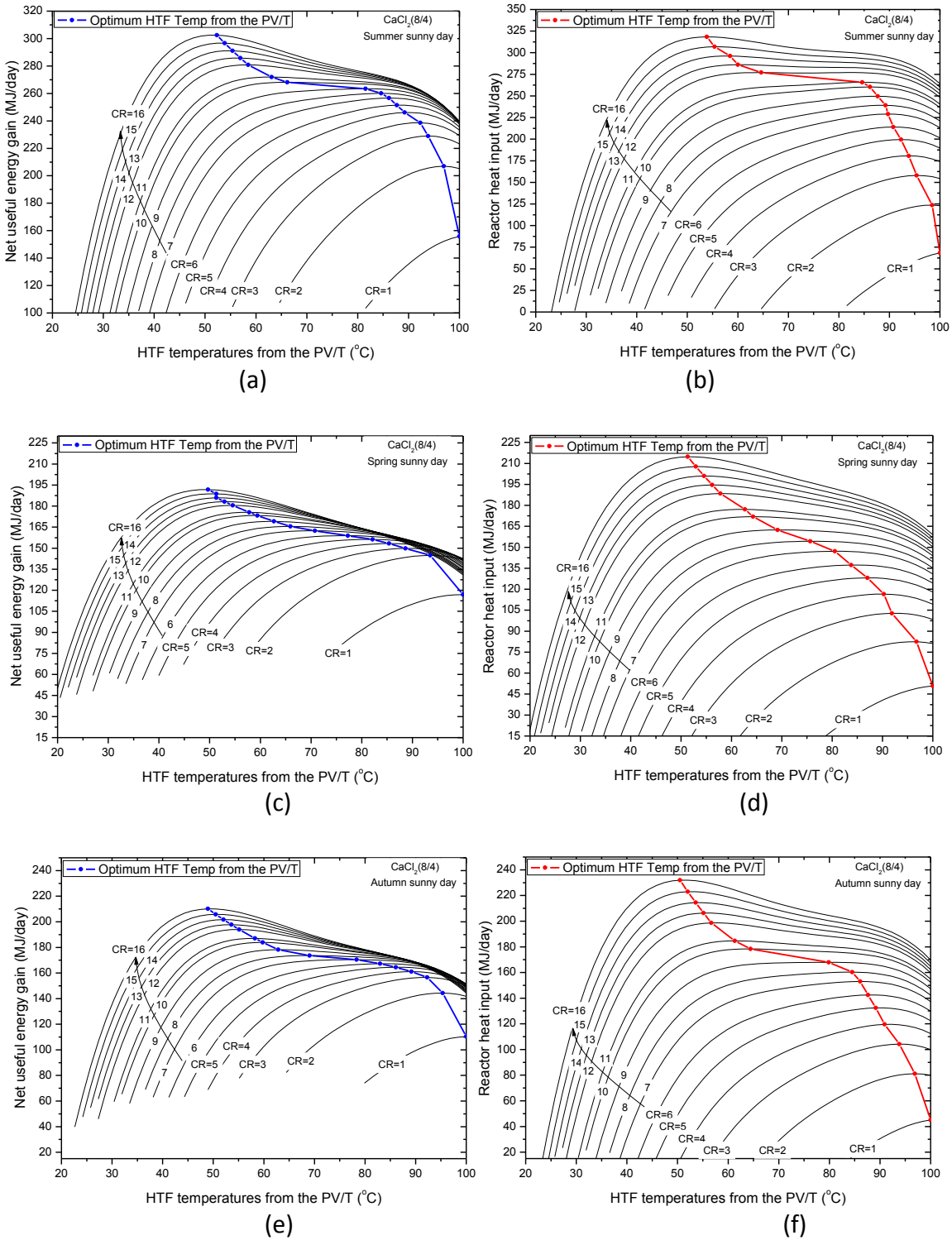

Fig. 4.16 *The energy variation profiles with different HTF temperatures and CRs when using $CaCl_2$(8-4)/NH_3 working pair of case 1: (a) the net useful energy gain on a summer sunny day, (b) the reactor heat input on a summer sunny day, (c) the net useful energy gain on a spring sunny day, (d) the reactor heat input on a spring sunny day, (e) the net useful energy gain on an autumn sunny day, (f) the reactor heat input on an autumn sunny day.*

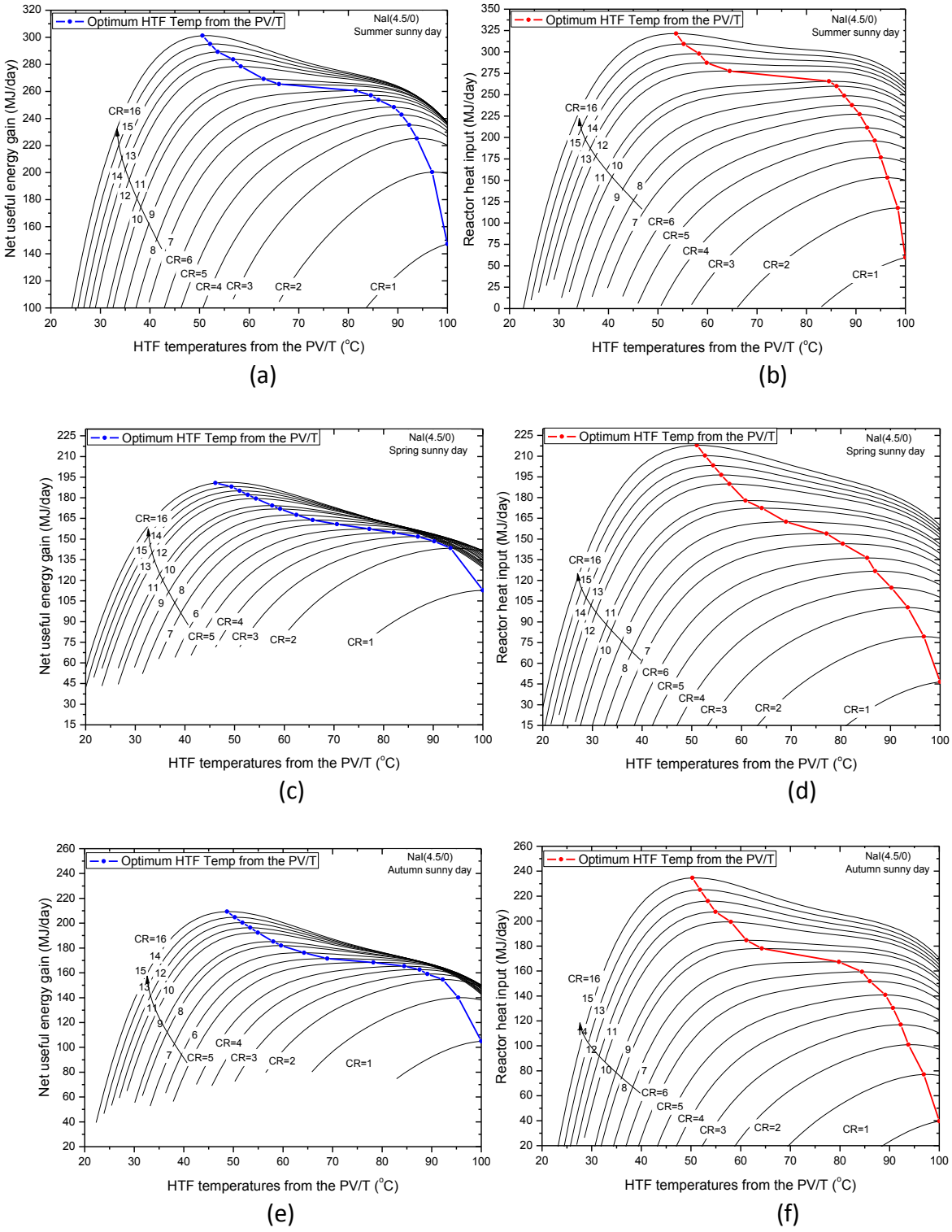

Fig. 4.17 *The energy variation profiles with different HTF temperatures and CRs when using NaI(4.5-0)/NH_3 working pair of case 1: (a) the net useful energy gain on a summer sunny day, (b) the reactor heat input on a summer sunny day, (c) the net useful energy gain on a spring sunny day, (d) the reactor heat input on a spring sunny day, (e) the net useful energy gain on an autumn sunny day, (f) the reactor heat input on an autumn sunny day.*

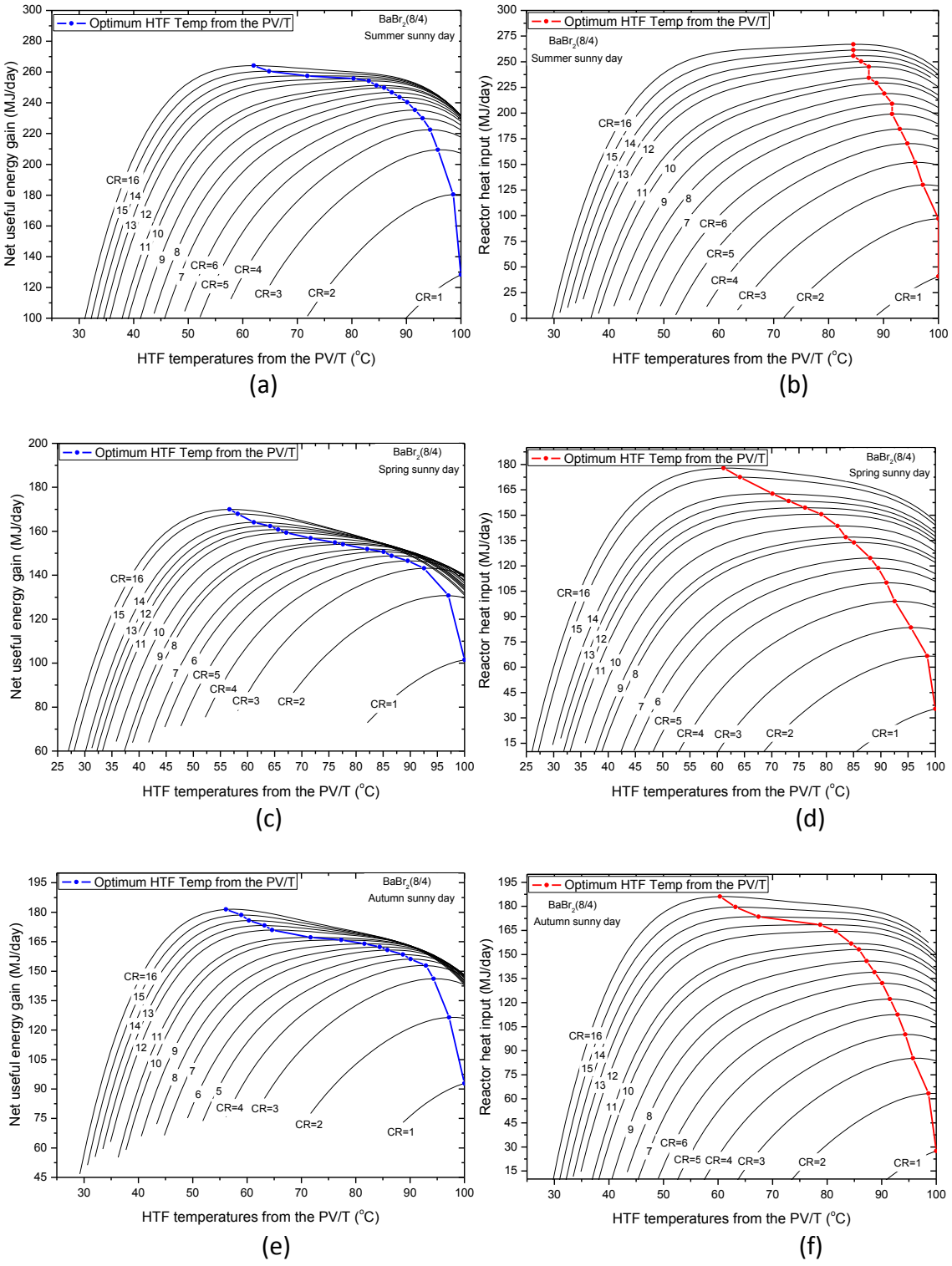

Fig. 4.18 *The energy variation profiles with different HTF temperatures and CRs when using $BaBr_2$(8-4)/NH_3 working pair of case 1: (a) the net useful energy gain on a summer sunny day, (b) the reactor heat input on a summer sunny day, (c) the net useful energy gain on a spring sunny day, (d) the reactor heat input on a spring sunny day, (e) the net useful energy gain on an autumn sunny day, (f) the reactor heat input on an autumn sunny day.*

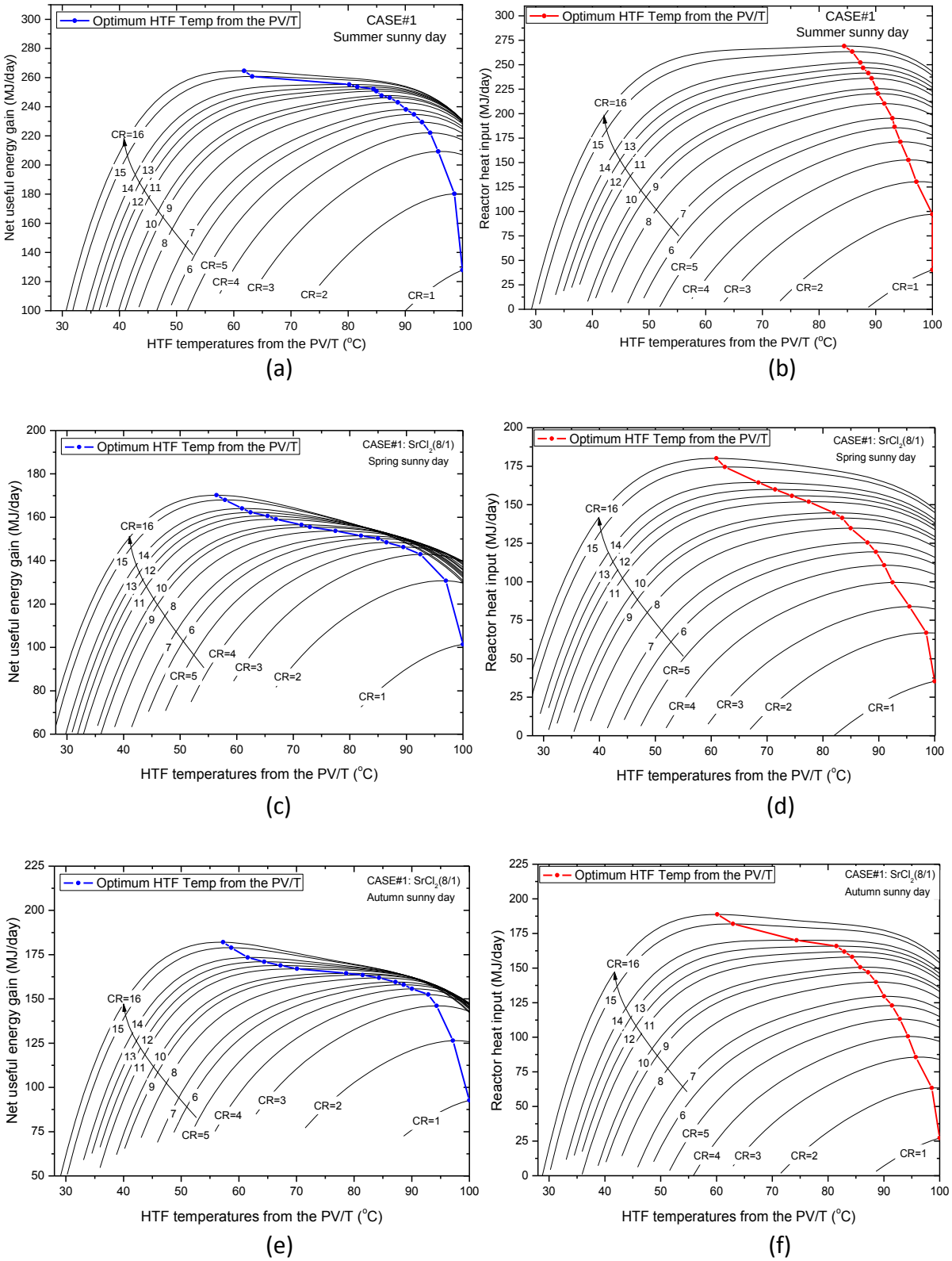

Fig. 4.19 *The energy variation profiles with different HTF temperatures and CRs when using $SrCl_2$(8-1)/NH_3 working pair of case 1: (a) the net useful energy gain on a summer sunny day, (b) the reactor heat input on a summer sunny day, (c) the net useful energy gain on a spring sunny day, (d) the reactor heat input on a spring sunny day, (e) the net useful energy gain on an autumn sunny day, (f) the reactor heat input on an autumn sunny day.*

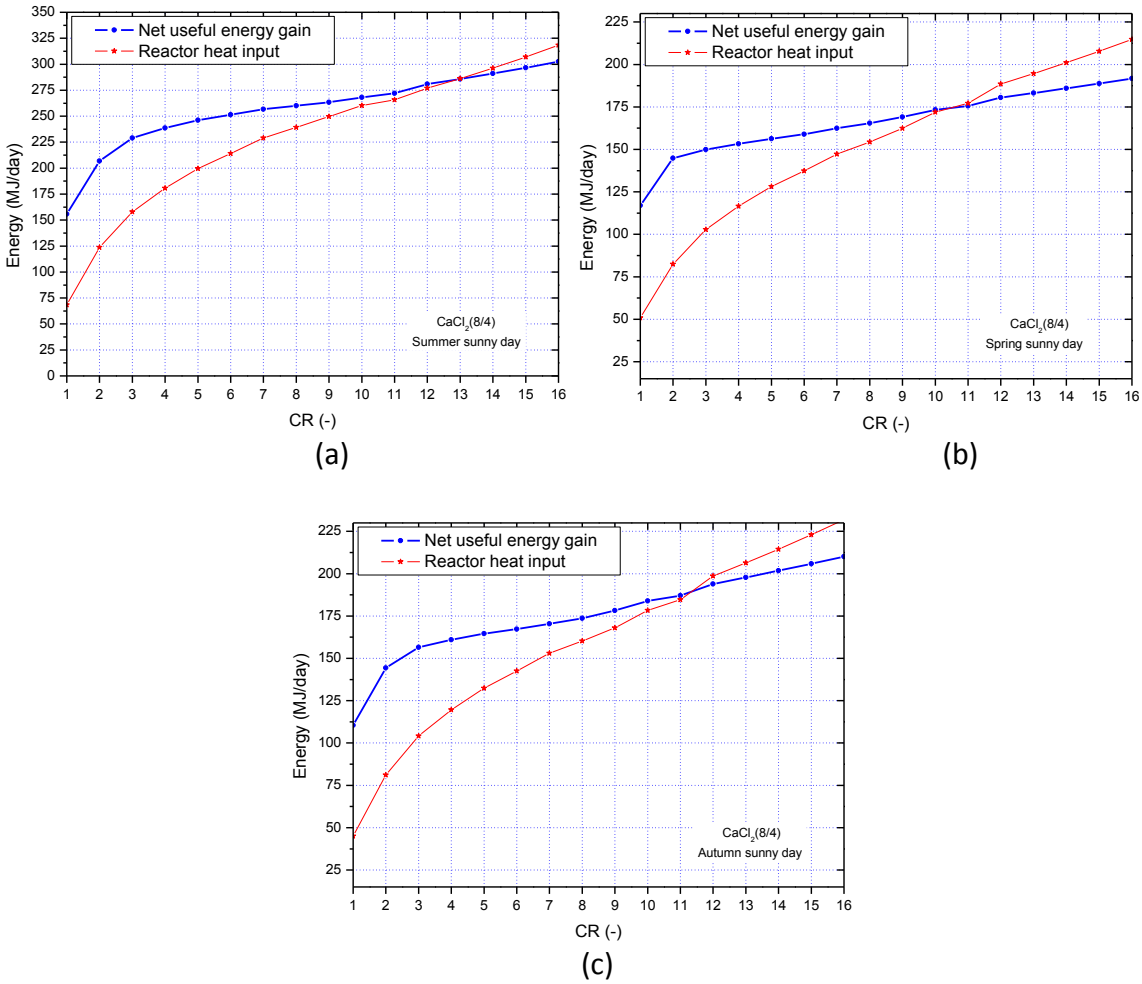

Fig. 4.20 *The comparisons of the reactor heat input and the net useful energy gain vs CR when using $CaCl_2$(8-4) as an adsorbent: (a) a summer sunny day, (b) a spring sunny day, (c) an autumn sunny day.*

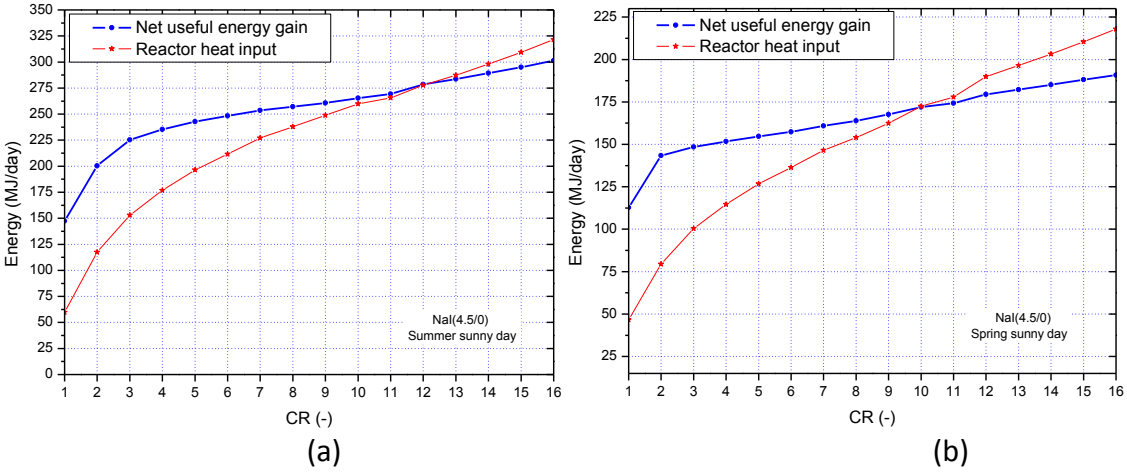

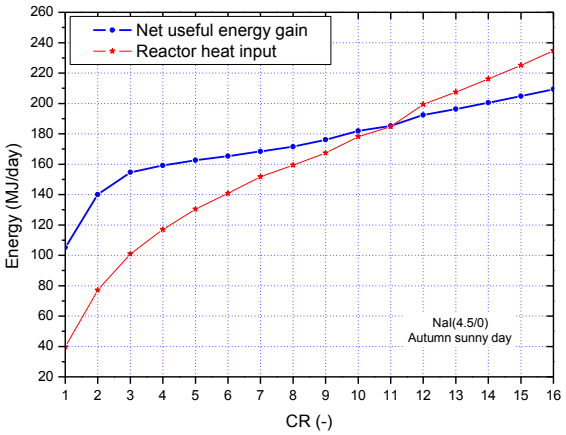

(c)

Fig. 4.21 *The comparisons of the reactor heat input and the net useful energy gain vs CR when using NaI(4.5-0) as an adsorbent: (a) a summer sunny day, (b) a spring sunny day, (c) an autumn sunny day.*

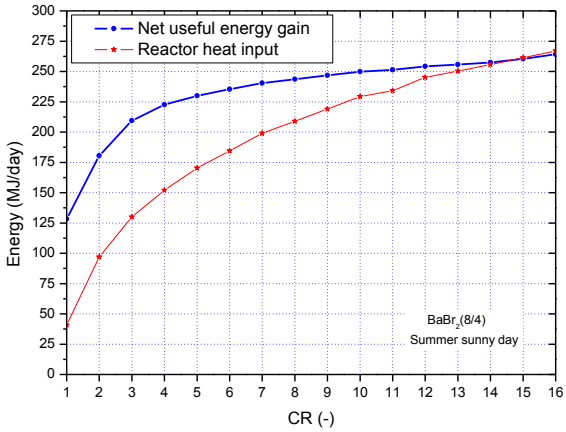

(a)

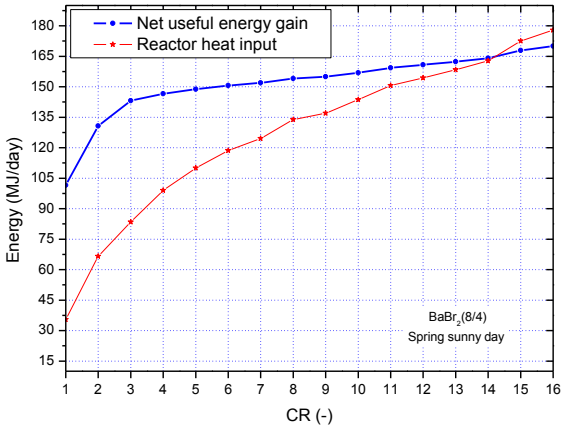

(b)

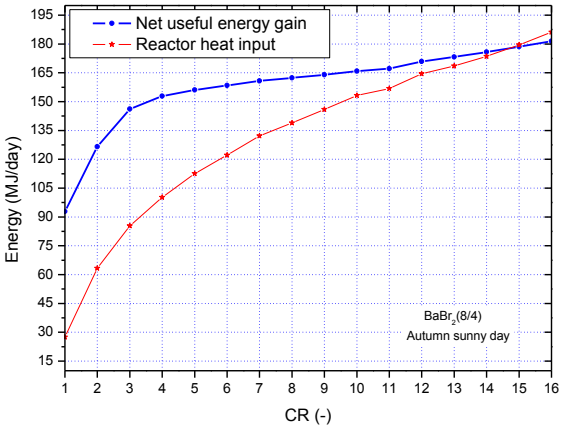

(c)

Fig. 4.22 *The comparisons of the reactor heat input and the net useful energy gain vs CR when using BaBr2(8-4) as an adsorbent: (a) a summer sunny day, (b) a spring sunny day, (c) an autumn sunny day.*

4.6 Optimisation results of the overall system, reactive salt selection and its annual performances for a typical household in Newcastle upon Tyne

The energy storage density and the potential annual performance of the integrated system using four different reactive salts that were shortlisted in above sections have been investigated to determine the required scale of system installation in order to achieve 100% solar fraction of domestic space heating for a typical single household in Newcastle upon Tyne. The size of each main component, i.e. solar PV/T panel and thermochemical sorption unit, as well as the compressor specifications were also discussed.

The storage efficiency ($\eta_{storage}$) calculated from Eq. (4.10) by using potential four reactive salts were presented in Table 4.5. The $\eta_{storage}$ value ranges from the lowest of 0.774 for $BaBr_2$(8/4) to the highest of 0.8795 for NaI(4.5/0). The energy storage density presented in this work was based on the thermochemical material volume, as the adsorbent composite density of 450 kg/m^3 and the salt/EG mass ratio of 3:1. Again the case using $BaBr_2$(8/4) is at the bottom of the pile, in contrast, the $SrCl_2$(8/1) case has more than triple the energy density of the $BaBr_2$(8/4) one and outranks the other two as well. Therefore, in order to meet the heating demand in winter with solely solar energy sources (SF=1) collected by a 30 m^2 solar PV/T panel in summer, the $SrCl_2$(8/1) system potentially can be the most compact one as it requires the smallest volume, about 22 m^3, of adsorbent materials. The NaI(4.5/0) system requires the compressor to have the CR of at least 8.17 and a thermochemical unit containing 34 m^3 adsorbent materials (V_{ads}), in the meantime with the most net electricity yield that could be used for other domestic appliances. Comparatively, the $BaBr_2$(8/4) system is much demanding as it requires the CR no smaller than 15 that cannot be satisfied by the electrical output from solar PV/T system but need import from the grid, let alone it triples the volume of the thermochemical unit compared to the smallest one.

In another study scenario to explore the threshold of the required area of solar PV/T panel to meet the goal of SF=1, the performances with the installation area of 23m^2, 26 m^2 and 30 m^2 are shown and compared in Fig. 4.23. If the PV/T is installed with the area of 26 m^2, the $CaCl_2$(8/4), NaI(4.5/0) and $SrCl_2$(8/1) systems are able to accomplish 100% solar fraction with the CR of 12.5, 11.0 and 15.9 respectively. The $BaBr_2$(8/4) system cannot deliver 100% solar fraction with the installation area of less than 30 m^2 if the CR is limited at 16 as studied in this work. Because of the reduction of the PV/T panel area, it produces less thermal energy as well as less electricity that is used to power the compressor and auxiliary heater, leading to the negative value of the electricity output curves shown in Fig. 4.23, in other words, the grid electricity is needed to complete the energy charging process in summer. If with the fixed CR

at 16 and no limitation of using the grid electricity, the minimum required PV/T installation area to acquire 100% solar fraction for each reactive salt is presented in Table 4.5. For further investigation, it can be an interesting subject to study whether a bigger installation if the roof area allows or importing more electricity from the grid has a shorter payback time for the overall system.

Table 4.5 *Performance for PV/T-DHW-TCSS of each viable reactive-salts with 30 m^2 PV/T installation area and the adsorbent has the properties of 450 kg/m^3 with Salt/EG mass ratio = 3:1*

Reactive Salt	**$\eta_{storage}$***	**Minimum CR for winter SF = 1**	**Adsorbent Energy Density (MJ/m^3)**	**V_{ads} for SF = 1 (m^3)**	**E_{left} for SF = 1 (MJ)**	**Estimate price of reactive salt ($/ton)*** **	**Minimum $A_{PV/T}$ for SF=1 and CR = 16 (m^2)**
$CaCl_2$(8/4)	0.8229	9.44	499.71	28.52	659.17	80-120	22.31
NaI(4.5/0)	0.8795	8.17	398.57	34.00	936.78	3,600-4,000	20.87
$BaBr_2$(8/4)	0.7740	14.99	190.16	77.97	-3.41**	3,000-3,260	29.00
$SrCl_2$(8/1)	0.8761	11.35	617.95	21.91	649.79	672-842	25.80
$CaCl_2$(4/2)	0.7326	>16	257.51	59.83	-	80-120	>30
$SrBr_2$(8/2)	0.7746	>16	373.38	39.06	-	1,000-7,000	>30
$MnCl_2$(6/2)	0.7022	>16	509.24	30.52	-	1,500-2,400	>30
$CaBr_2$(6/2)	0.6831	>16	330.84	47.76	-	1,565-1,950	>30

* Note that the efficiency slightly changes depending on the working CR; the values presented in this column were calculated from CR=8.

** The negative value means electricity was imported from the grid to work at the minimum CR for winter SF of 1

*** The prices are based on the wholesale price per metric ton from www.alibaba.com.

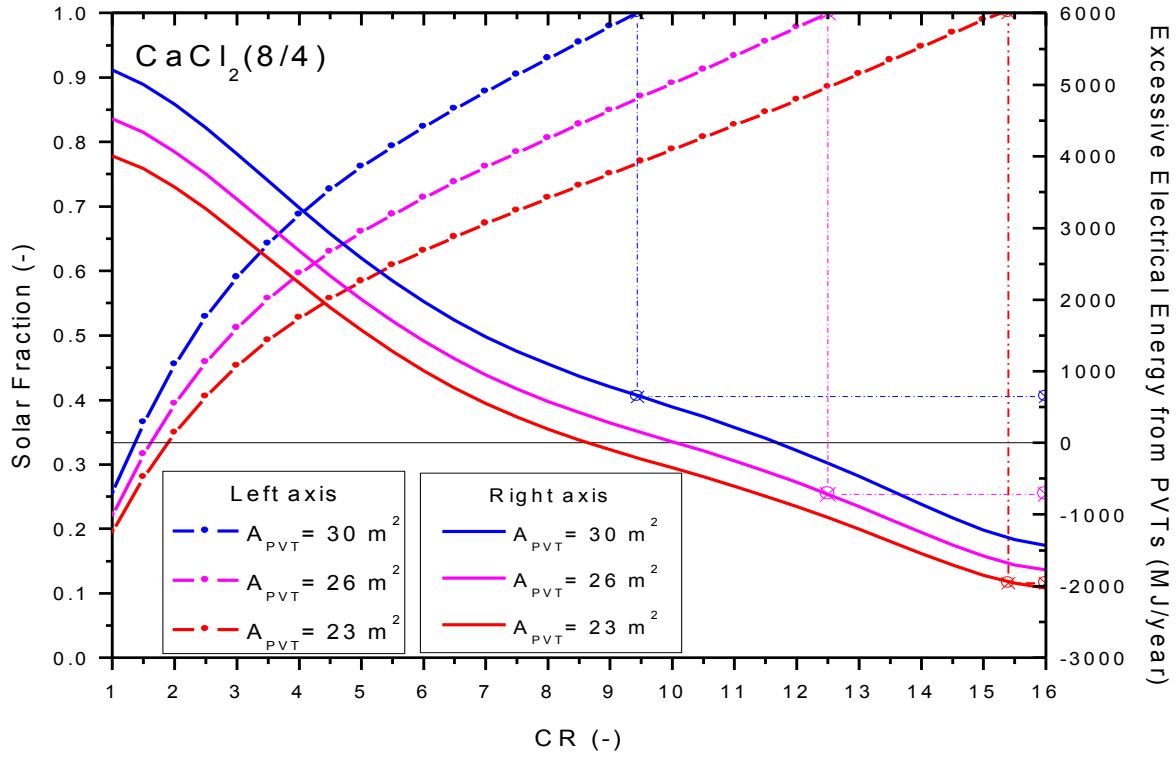
CaCl2(8/4)
Solar Fraction (-)
Excessive Electrical Energy from PVTs (MJ/year)
CR (-)
Left axis
A PVT= 30 m2
A PVT= 26 m2
A PVT= 23 m2
Right axis
A PVT= 30 m2
A PVT= 26 m2
A PVT= 23 m2

(a)

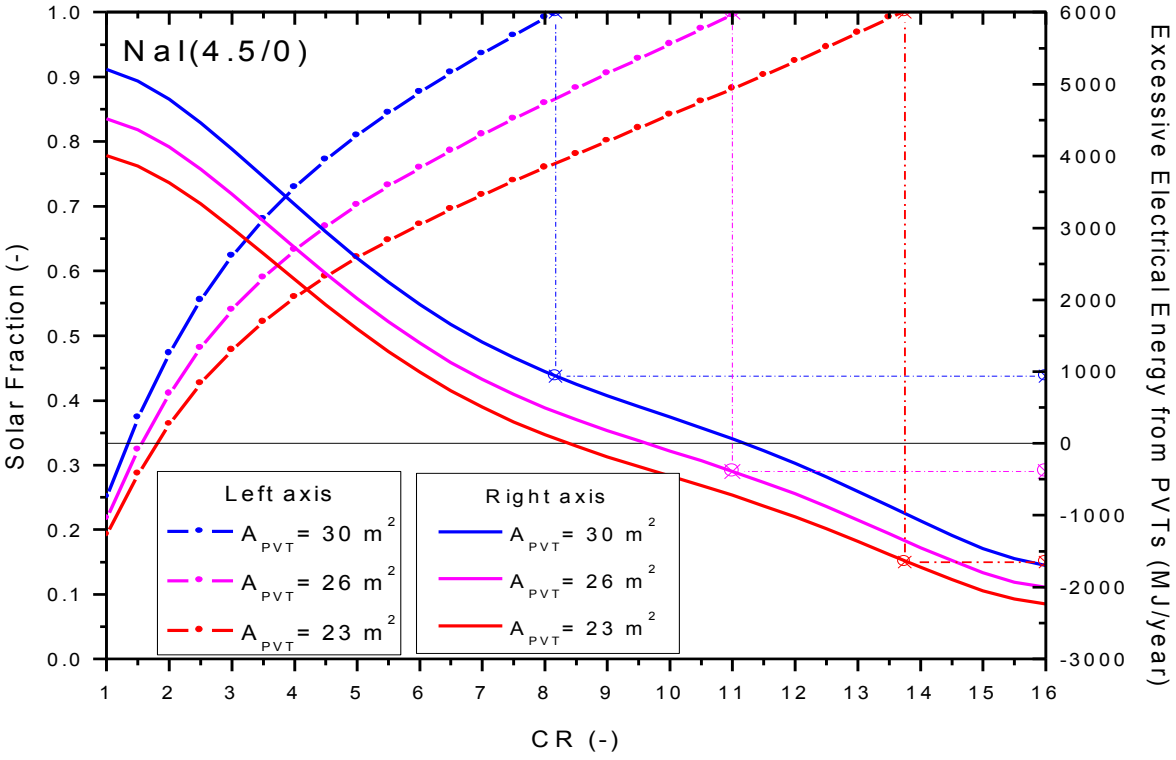
NaI(4.5/0)
Solar Fraction (-)
Excessive Electrical Energy from PVTs (MJ/year)
CR (-)
Left axis
A PVT= 30 m2
A PVT= 26 m2
A PVT= 23 m2
Right axis
A PVT= 30 m2
A PVT= 26 m2
A PVT= 23 m2

(b)

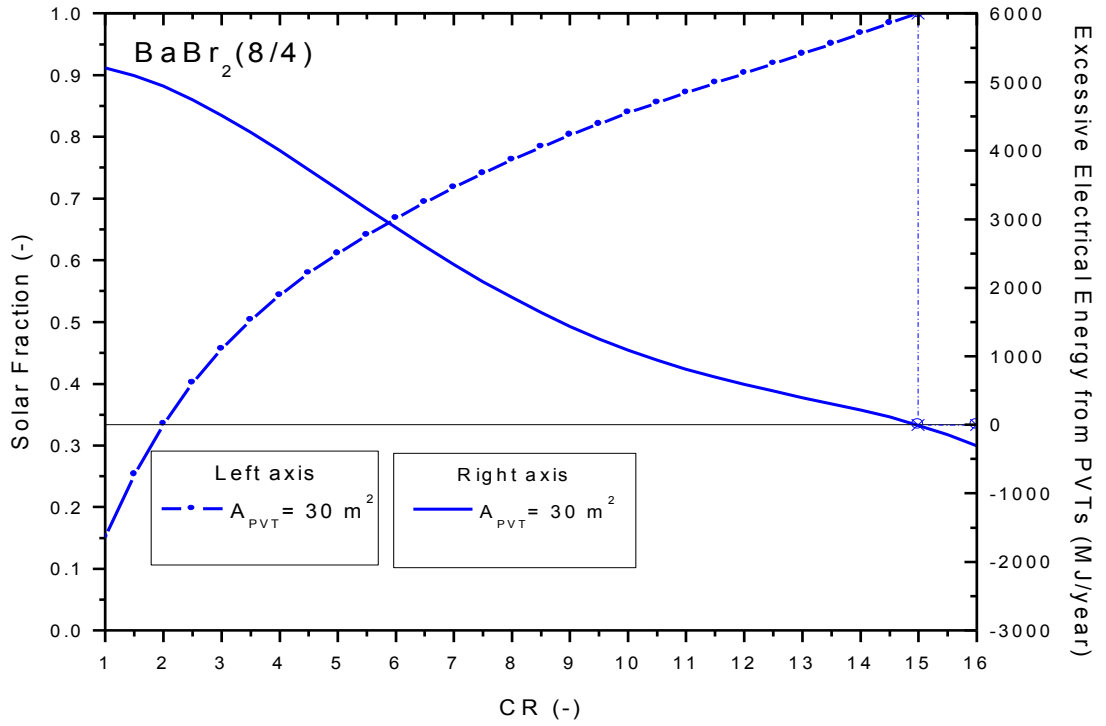

(c)

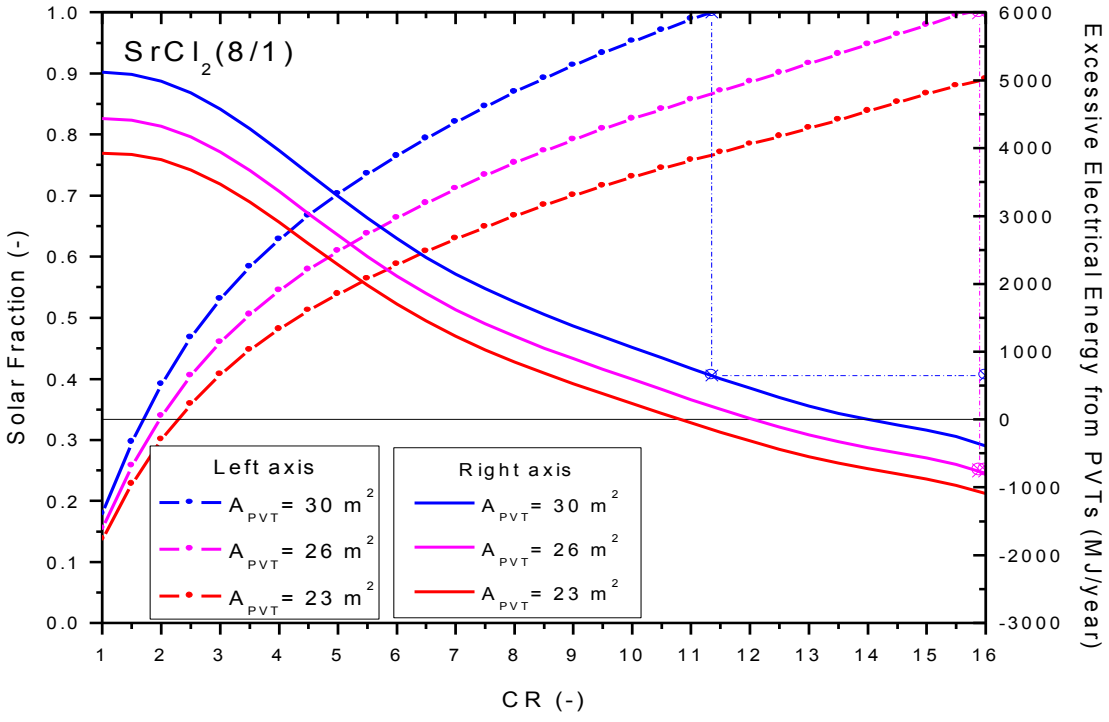

(d)

Fig. 4.23 *Winter solar fraction and the excessive electrical energy when different PV/T installation areas were employed for (a) $CaCl_2$(8/4), (b) NaI(4.5/0), (c) $BaBr_2$(8/4) and (d) $SrCl_2$(8/1)*

For all the performance figures summarised in Table 4.5, the $CaCl_2$(8/4) system does not lead in any comparison but just being slightly inferior to the best one, which is good enough to some degree. Nevertheless, it is essentially crucial that it is the cheapest material among all. On the other side of the cost spectrum, being prohibitively expensive can significantly hinder the application of the chemicals NaI(4.5/0) and $BaBr_2$(8/4) in every area. Despite winning out at energy density and storage efficiency, the SrCl2(8/1) is still at a disadvantage against the CaCl2(8/4) from the economic point of view, unless there raises massive demand in the market and it potentially could alter the economic competition.

It is worth noting that, in practice for a real system with industrial packing machine, the adsorbent material can be compressed with higher density ranges typically from 600 to 1200 kg/m^3 (Jiang & Roskilly, 2019). For example, Jiang *et al.*(2017) used $SrCl_2$-EG adsorbent with a density of 500-600 kg/m^3; Zamengo, Ryu & Kato (2013) packed $Mg(OH)_2$ with the bulk density of 625.8 kg/m^3 and the mass ratio of 4:1 to study for its thermal characteristics but no sorption performance was done. EG treated with sulfuric acid was able to be compressed to the density of 831 kg/m^3 by Wang *et al.* (2011) with the compressing pressure of around 4 MPa. Those aforementioned examples ensure that the composite sorbent can be packed with a higher density than reported in this thesis when a proper compressing machine is available. If the adsorbent density in this thesis is 900 kg/m^3 (2 times of the valued used to calculate the performances reported in Table 4.5) and $CaCl_2$(8/4) is used with the same salt:EG mass ratio (4:1), the energy density may reach 277.62 kWh/m^3 with the required storage volume of 14.26 m^3. If $SrCl_2$ is used, the energy density can get up to 343.3 kWh/m^3 with the required storage volume of only around 11 m^3. Therefore, the integrated system purposed in this thesis with high packing adsorbent density could potentially outperform the systems reported by several other works. For instance, LiBr-H_2O system with energy density for heating of 110 kWh/ m^3 with 43 ^oC temperature output from (Zhang *et al.* (2014a), $SrCl_2$-NH_3 system from Jiang *et al.* (2017) who used the mass ratio of up to 5:1 which could perform a heat storage density of up to 274.67 kWh/m^3, etc.

4.7 Summary

The PV/T-AG was integrated with the CATSES for short-term and long-term thermal energy storages for a typical household in the UK. The components of the integrated system are PV/T collectors, a reactor, a compressor, an inline mixer, an auxiliary heater, a domestic hot-water tank and a reused hot-water tank. Based on the temperature requirements for the

DHW and SPH applications, $CaCl_2$, NaI, $BaBr_2$ and $SrCl_2$ are the four applicable reactive salts to be used in the UK.

By using different salts at different CR, the optimum operating temperature for the PV/T varies. For example, when $SrCl_2$ was chosen to work with the CR of 1, 4, 8, 12 and 16, the optimum HTF temperature for operating the PV/T were 100, 95.76, 91.51, 88.68 and 84.44 ^oC in a sunny summer day. With different weather conditions (spring and autumn), the optimum HTF temperature of operating the PV/T is different; therefore, the optimum operating point of the integrated system is weather dependent.

If the kinetic analysis of the reactor is not considered, the minimum CR required to supply the winter heating demand with 100% solar fraction for NaI, $CaCl_2$, $SrCl_2$ and $BaBr_2$ are 8.17, 9.44, 11.35 and 14.99 respectively. NaI works at the lowest CR which is preferable; however, because of its low energy density and high price, it may not be able to be economically deployed. Therefore, the most promising reactive salts for the integration between the PV/T and the CATSES are $CaCl_2$ and $SrCl_2$. $SrCl_2$ may be preferable with its highest energy density which required only 21.91 m^3 storage material volume with 87.61% storage efficiency compared to 28.52 m^2 with 82.29% efficiency of $CaCl_2$(8/4). $CaCl_2$ works with lower CR of 9.44 compared with 11.35 for $SrCl_2$ for 100% solar fraction which is admirable and the budget is much cheaper than other salts (around 6 times less than $SrCl_2$). The two competitive salts $CaCl_2$ and $SrCl_2$ meet the requirement to produce the winter temperature of the HTF at 66.54 and 74.33 ^oC respectively, more than 60 ^oC for heating applications. If the compressor is able to work at CR of 16, the installed PV/T area can be reduced to meet the 100% winter fraction, however, the grid electricity may be required in the charging stage as less PV/T area produces less electricity to supply the compressor.

Chapter 5: Simulation, validation and kinetic performance of the compressor-assisted thermochemical energy storage

5.1 Introduction

The previous chapter illustrated that the compressor-assisted thermochemical sorption energy storage (CATSES) has the ability to store thermal energy supplied from the PV/T collector which has the temperature ranges from 40 ^{o}C to 100 ^{o}C. Moreover, the previous chapter also suggested the optimum temperature of the HTF produced from the PV/T in different seasons. This chapter will further analyse the dynamic performance of the reactor to uncover the time-dependence performance of the integrated system.

Among all potential candidates of working pairs (salt-ammoniates) studied and evaluated, the $SrCl_2$-$8NH_3$ were selected to further study the dynamic performances of the integrated system. In energy charging state, the CATSES was studied on how fast that the desorption can perform at different levels of input temperature from the PV/T and its efficiency. In the energy-releasing stage, the CATSES was studied on the ability to support the heating demand in a typical household in the UK. With the kinetic study of the $SrCl_2$-$8NH_3$ salt-ammoniate, the proper reactor designs can be conducted to meet the energy charging and discharging requirements in different areas for future works.

5.2 Theoretical analysis of reaction kinetics

In this section, the global kinetic performances of sorption processes were analysed. The reaction rate (dx/dt) is the rate of change of the degree of conversion 'x' which x equals to 1 when ammonia is fully adsorbed by reactive salts and equals to 0 when the ammonia is fully desorbed. The reaction rate varies as a function of two main parts which are the operating conditions (k(P, T)) and the progression of the reaction (f(x)), presented in Eq. (5.1) by Mazet, Amouroux and Spinner (1991). With different operating conditions, the k(P, T) is different and with different reaction directions (adsorption or desorption), the f(x) may be different.

$$\frac{dx}{dt} = f(x) \cdot k(P,T) \tag{5.1}$$

The reaction progression, f(x), and the operating condition, k(P, T), in Eq. (5.1) has been reported in several pieces of literature for different kinds of reactive salt with parameters validated from their experimental results which vary depending on the reaction direction

(desorption or adsorption), the reactor design, and the type and mixture of reactive salts. Therefore, different references reported different reaction rate equations and reaction parameters as presented in Table 5.1.

5.2.1 Adsorbent mixture for thermochemical storage

Commonly in many pieces of research, reactive salt was impregnated into the porous matrix (EG) to improve the thermal conductivity and gas permeability property of the adsorbent, as well as mitigating the swelling and agglomeration issues associated with the pure salt adsorbent (Han *et al.*, 1998; Oliveira & Wang, 2007; Kim, Ryu & Kato, 2013; Wu *et al.*, 2018). The mass ratio of the salt and expanded graphite is 3:1 (kg salt/kg EG) in this work but the mass ratio of 2:1 was used for the validation with the experiments from Yuan *et al.* (2018). Graphite can be expanded to get a suitable porous structure by heating up to the temperatures higher than 600 ^{o}C (Han *et al.*, 1998). To be specific, Oliveira and Wang (2007) suggest that performing the heat treatment of graphite using 10 minutes with 700 ^{o}C provides exceptional apparent density for impregnated adsorbent at the minimal time of heating treatment. Although the test rigs expected to use to compare the experimental results with the simulation results in this thesis is not ready yet due to technical problem about releasing valves, the preparations of the adsorbent mixtures of $SrCl_2$ and $MnCl_2$ are attached in Appendix D for the illustration.

Table 5.1 *The global reaction rate equations and their parameters for different reactive salts*

Desorption Reaction rate (dx/dt)	Adsorption Reaction rate (dx/dt)	Reactive salt	Parameters			Reference
			Symbol	Desorption	Adsorption	
$\frac{dx}{dt} = Ar \cdot x^m \cdot \frac{P_c - P_{eq}(T_r)}{P_c}$ ---------- (5.2)-A ---------- (Mazet, Amouroux & Spinner, 1991)	$\frac{dx}{dt} = Ar \cdot (1-x)^m \cdot \frac{P_c - P_{eq}(T_r)}{P_c}$ ---------- (5.2)-B ---------- (Mazet, Amouroux & Spinner, 1991)	$MnCl_2$ (6-2) NH_3	Ar	0.027	0.031	(Neveu & Castaing-Lavignottes, 1997)
			m	1		
			Ar	0.0010187		(Han *et al.*, 2000)
			m	1.185		
			Ar	0.0033		(Dutour *et al.*, 2005)
			m	1.0		
			Ar	-	0.003	(Azoumah, Neveu & Mazet, 2007)
			m		1	
			Ar	0.0028	0.001019	(Lyakh et al., 2013)
			m	1.0	1.185	
		$BaCl_2$ (8-0) NH_3	Ar	0.0033		(Le Pierrès, Mazet & Stitou, 2007)
			m	1.0		
			Ar	0.0001		(Le Pierrès, Driss & Nathalie, 2008)
			m	1.0		
			Ar	0.0195	0.0125	(Lyakh et al., 2013)
			m	1.005	2.104	
			Ar	0.0045	0.0287	

Desorption Reaction rate (dx/dt)	Adsorption Reaction rate (dx/dt)	Reactive salt	Parameters			Reference
			Symbol	Desorption	Adsorption	
		$CaCl_2$ (4-2) NH_3	m	0.468	1.78	(Wang, Zhang & Wang, 2010)
		$CaCl_2$ (8-4) NH_3	Ar	0.0125	0.0195	
			m	2.104	1.005	
		$NiCl_2$ (6-2) NH_3	Ar	0.018	0.0095	(Neveu & Castaing-Lavignottes, 1997)
			m	1		
		$MgCl_2$ (6-2) NH_3	Ar	-	0.006036	(Mofidi & Udell, 2017)
			m		1.185	
$\frac{dx}{dt} = (Ar + Ad \cdot T_r) \cdot x^m \cdot \frac{P_c - P_{eq}(T_r)}{P_c}$ ---------- (5.3)-A ----------	$\frac{dx}{dt} = Ar \cdot (1-x)^m \cdot \frac{P_c - P_{eq}(T_r)}{P_c}$ ---------- (5.3)-B ----------	$SrCl_2$ (8-1) NH_3	Ar	x>0.8: 0.02413 / x<0.8: 0.0004598		0.001631	(Yuan *et al.*, 2018)
			Ad	$-6.2e{-8}$		-	
			m	1.1		2.071	
$\frac{dx}{dt} = s \cdot x^m \cdot exp\left(\frac{-E}{RT}\right) \cdot \frac{P_c - P_{eq}(T_r)}{P_c}$ ----------	$\frac{dx}{dt} = s \cdot (1-x)^m \cdot exp\left(\frac{-E}{RT}\right) \cdot \frac{P_c - P_{eq}(T_r)}{P_c}$ ----------	$SrCl_2$ (8-1) NH_3	k_0	0.125	0.019	(Huang *et al.*, 2004)
			E	9000	6921	
			m	3.02	2.96	

Desorption Reaction rate (dx/dt)	Adsorption Reaction rate (dx/dt)	Reactive salt	Parameters			Reference
			Symbol	Desorption	Adsorption	
(5.4)-A	(5.4)-B					
$\frac{dx}{dt} = k \cdot x \cdot exp\left(\frac{-E_0}{T_r}\right) \cdot \ln\left(\frac{P_c}{P_{eq}(T_r)}\right)$ (5.5)-A	$\frac{dx}{dt} = k \cdot (1-x) \cdot exp\left(\frac{-E_0}{T_r}\right) \cdot \ln\left(\frac{P_c}{P_{eq}(T_r)}\right)$ (5.5)-B	$MnCl_2$ (6-2) NH_3	k	0.59	0.92	(Neveu & Castaing-Lavignottes, 1997)
			E_0	1390		
		$NiCl_2$ (6-2) NH_3	k	0.26	0.43	
			E_0	1404		

where Ar is the Arrhenius term [-]; x is the degree of conversion [-]; m is the reaction pseudo-order [-]

P_c is the pressure in the reactor dominated by the condenser/evaporator [Pascal]

$P_{eq}(T_r)$ is the thermodynamic equilibrium pressure which is a function of the reactant temperature, T_r [Pascal]

E is the activation energy [J/mol]

k_0 is the pre-exponential factor of Arrhenius (1/s)

5.2.2 Heat transfer analysis of water-jacket reactor

To analyse the performances when using the $SrCl_2$ as an adsorbent, the water-jacket reactor as shown in Fig. 5.1 was chosen for the modelling because of its simplicity and availability of experimental data for validation. It is well known that the finned-tubes reactor as presented in Fig. 5.2 has better heat transfer properties, the test rigs are not ready for the experiment yet; therefore, the finned-tube reactor is suggested to be future work to explore the influence of the reactor design on the storage performance but not yet considered in this thesis. The global kinetic equations from Mazet, Amouroux & Spinner (1991) was used for $MnCl_2(6\text{-}2)NH_3$ reactor with the parameters reported in Lyakh *et al.* (2013) in the simulation model. For $SrCl_2(8\text{-}1)NH_3$ reactor, the global kinetic equations and parameters from Huang *et al.* (2004) were used in the simulation model.

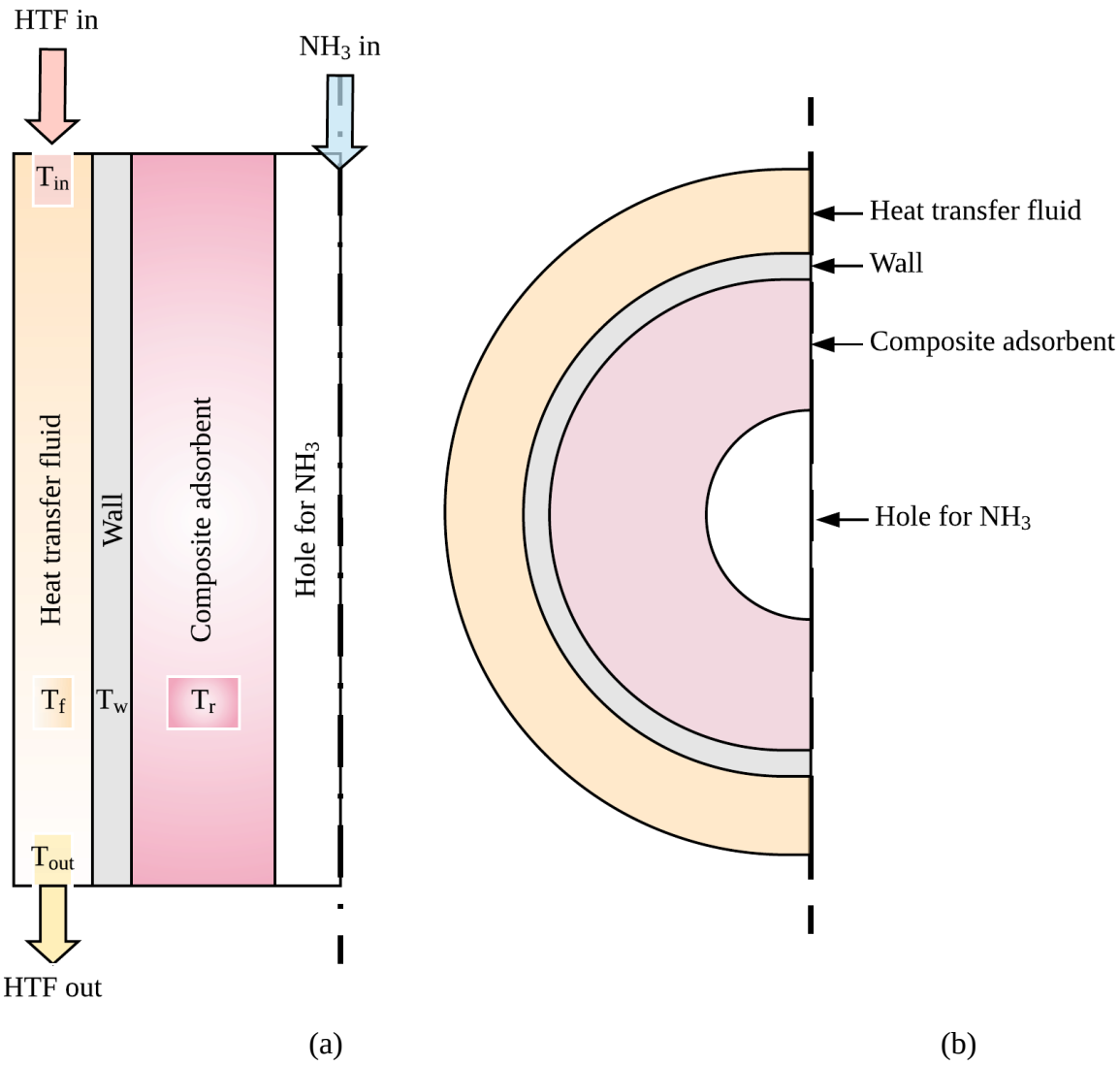

Fig. 5.1 *The simple reactor layers for heat transfer analysis of the sorption reactions (a) longitudinal view (b) cross-sectional view*

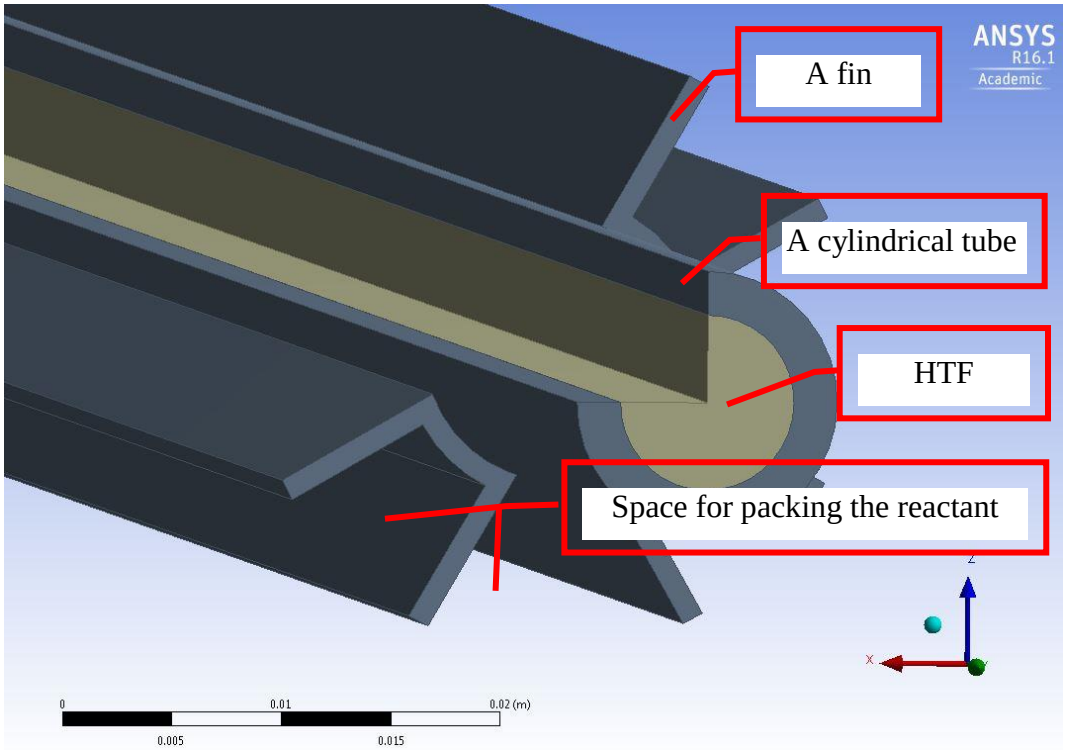

(a)

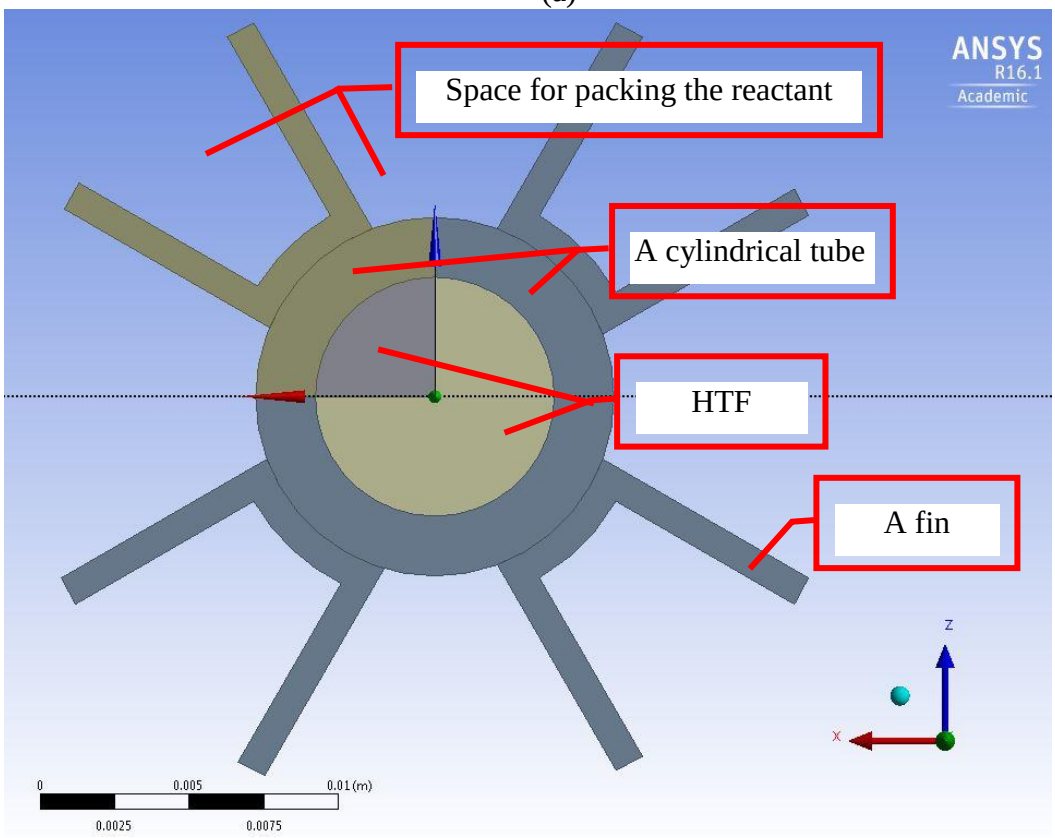

(b)

Fig. 5.2 *The finned tube for packing the adsorbent in the thermochemical sorption reactors; (a) Isometric view, (b) Cross-sectional view*

As the global kinetic analysis was considered, the one-dimensional analysis is performed on the longitudinal cross-sectional plane of the reactor. Each layer in Fig. 5.1 were considered as a single mass with no temperature gradient on its layer. The fins were treated by using the increasing contact area between the tube wall and the reactant. To obtain the average temperature difference between the HTF layer and the wall, logarithm-mean- temperature difference (ΔT_{fw}) can be determined by Eq. (5.6). The simple idea of global kinetic analysis is that the transient temperature in each layer occurs because of the imbalance of the energy-in and energy-out in the considered layers.

$$\Delta T_{fw} = \frac{T_{in}-T_{out}}{ln\left(\frac{T_{in}-T_w}{T_{out}-T_w}\right)} \tag{5.6}$$

Considering the desorption kinetics of the $SrCl_2$ reactor, the reaction rate of the reactor with Eq. (5.4)-A is chosen because the reactor designed is the water-jacket reactor which is used in the modelling in this thesis. P_{eq} can be obtained by Eq. (4.2) which is a function of reactant temperature and P_c is the operating reactor pressure dominated by the condenser during the desorption stage. Heat sink temperature defines the operating pressure inside the condenser. Initially, the degree of conversion 'x' is 1 and T_r is equal to the ambient temperature which make the P_{eq} less than P_c. It means that the condition does not activate the desorption reaction yet.

To initiate the endothermic desorption reaction, the reactant needs to be heated from ambient temperature to the temperature of higher than T_{eq}. When T_r is greater than T_{eq}, P_{eq} in Eq. (5.4)-A is higher than the P_c. This mean that the desorption process is occurring, leading to the reduction of the degree of conversion 'x' of the reactant. If there is sufficient HTF produced from the PV/T or thermal collectors, the reaction is going to finish when the degree of conversion equals to zero which is at the full desorption state for the ideal case. However, the full desorption state hardly reaches 'x=0' and the full adsorption state also hardly achieves 'x=1' as when the conversion approach 0 or 1, the reaction rates slow down dramatically and it may not worth trying to get the full adsorption or desorption. In real application, the reactor may be designed to contain more amount of composite adsorbent to deal with the energy demand with the degree of conversion range from 0.9 to 0.1. In this case, only 80% of the adsorbent is actually active.

For the adsorption process in winter, referring to Eq. (5.4)-B used for the adsorption kinetics of the $SrCl_2$ reactor, the degree of conversion 'x' is zero at an initial time and T_r equals

to the ambient temperature which makes the P_{eq} less than P_c resulting in the positive conversion rate. As it is in the full desorption state, the exothermic adsorption process starts immediately after the valve between the evaporator and the reactor is opened. The adsorption heat increases the reactant temperature and transfers through the wall to the HTF. The temperature of the HTF output (T_{out}) from the reactor is always lower than the salt equilibrium temperature, T_{eq}, to maintain the adsorption process. If T_{out} gets close to T_{eq}, the reaction slows down and the adsorption heat reduces. If the HTF is pumped to the reactor slow enough that heat transfer from the reactant is less than the exothermic heat, temperature of the reactant T_r can get close to the equilibrium temperature T_{eq}. There is no reaction heat produced by the reaction when the reactant temperature T_r is equal to its equilibrium temperature.

To calculate the transient wall and reactant temperatures corresponding to the temperature input and output of the HTF, energy balance in HTF layer, wall layer and reactant layer were obtained in Eq. (5.7), Eq. (5.8) and Eq. (5.9) respectively. The overall heat exchange coefficient between the HTF and the wall is calculated from Eq. (5.10) and the overall heat exchange coefficient between the wall and the reactant is obtained from Eq. (5.11). Because the reactant contains multi-substance, to achieve a higher degree of accuracy in the reactor model, the heat capacity and the porosity of the reactant were proposed by Han *et al.* (2000) as presented in Eq. (5.12) and Eq. (5.13) respectively. All the mathematical equations for modelling the reactor are modelled in MATLAB as presented in Appendix E.

$$m_f C_{pf} \frac{\partial T_f}{\partial t} = \dot{m} C_{pf} (T_{in} - T_{out}) - (UA)_{fw} \Delta T_{fw} \tag{5.7}$$

where m_f is the mass of the HTF [kg]

C_{pf} is the specific heat capacity of the HTF [J/kg·K]

T_f is the HTF temperature [K]

$\dot{m}$ is the mass flow rate of the HTF [kg/s]

$(UA)_{fw}$ is the overall heat exchange coefficient between the HTF and the wall [W/K] calculated from Eq. (5.10)

$$m_w C_{pw} \frac{\partial T_w}{\partial t} = (UA)_{fw} \Delta T_{fw} - (UA)_{wr} (T_w - T_r) \tag{5.8}$$

where m_w is the mass of the wall [kg]

C_{pw} is the specific heat capacity of the wall [J/kg·K]

T_w is the wall temperature [K]

T_r is the reactant temperature [K]

$(UA)_{wr}$ is the overall heat exchange coefficient between the wall and the reactant [W/K] calculated from Eq. (5.11)

$$m_r C_{pr} \frac{\partial T_r}{\partial t} = (UA)_{wr}(T_w - T_r) + n_{NH3\_R} \Delta H_R \frac{dx}{dt} \quad (5.9)$$

where m_r is the mass of the reactant [kg]

C_{pr} is the specific heat capacity of the reactant [J/kg·K]

C_{pr} is calculated from Eq. (5.12)

n_{NH3_R} is the reactive ammonia mole [mol]

ΔH_R is the reaction enthalpy of the salt-ammonia working pair [J/mol]

$$\frac{1}{(UA)_{fw}} = \frac{1}{h_{fw} A_{fw}} + \frac{\delta_w/2}{\lambda_w A_{fw}} \quad (5.10)$$

where h_{fw} is the heat transfer coefficient between the HTF and the wall [W/m^2/K]

A_{fw} is the contact area between the HTF and the wall [m^2]

δ_w is the wall thickness [m]

λ_w is the thermal conductivity of the wall [W/m/K]

$$\frac{1}{(UA)_{wr}} = \frac{\delta_w/2}{\lambda_w A_{wr}} + \frac{\delta_r/2}{\lambda_r A_{wr}} \quad (5.11)$$

where A_{wr} is the contact area between the wall and the reactant [m^2]

δ_r is the reactant thickness [m]

λ_r is the thermal conductivity of the reactant [W/m/K]

$$C_{pr}(x) = \frac{V_{EG}}{V_b} C_{p,EG} + \frac{v_{s_{de}}}{V_b} \frac{m_S}{M_{s_{de}}} (1 - x) C_{p,s_{de}} + \frac{v_{s_{ad}}}{V_b} \frac{m_s}{M_{s_{ad}}} x C_{p,s_{ad}} + \varepsilon(x) C_{p,NH3} \quad (5.12)$$

where V_{EG} is the expanded graphite volume in the adsorbent [m^3]

V_b is the adsorbent (bulk) volume [m^3]

$v_{s_{de}}$ is the molar volume of the salt at fully desorption state [m^3/mol]

$v_{s_{ad}}$ is the molar volume of the salt at fully adsorption state [m^3/mol]

$C_{p,EG}$ is the specific heat capacity of the expanded graphite [J/kg·K]

$C_{p,s_{de}}$ is the specific heat capacity of the salt at fully desorption state [J/kg·K]

$C_{p,s_{ad}}$ is the specific heat capacity of the salt at fully adsorption state [J/kg·K]

$C_{p,NH3}$ is the specific heat capacity of ammonia [J/kg·K]

m_S is the mass of the salt [kg]

$M_{s_{de}}$ is the molecular weight of the salt at fully desorption state [g/mol]

$M_{s_{ad}}$ is the molecular weight of the salt at fully adsorption state [g/mol]

$\varepsilon(x)$ is the porosity of the adsorbent [-]

$\varepsilon(x)$ is calculated from Eq. (5.13)

$$\varepsilon(x) = 1 - \frac{\rho_b}{\rho_{EG}} - \left(\frac{1 - f_{EG}}{f_{EG}}\right)\left[v_{s_{de}} + (v_{s_{ad}} - v_{s_{de}})x\right]\frac{\rho_b}{M_{s_{de}}} \quad (5.13)$$

(Han *et al.*, 2000; Bao, Wang & Roskilly, 2014)

where ρ_b is the density of the adsorbent [kg/m^2]

ρ_{EG} is the density of the expanded graphite [kg/m^2]

f_{EG} is the mass-fraction of the expanded graphite [-]

5.2.3 Heat sources and heat sinks for the thermodynamic cycle of the energy storage system

In order to complete the thermodynamic cycle of the designed energy storage system, heat must be removed/absorbed at condensation/evaporation processes. There are two types of natural heat reservoir available which are ambient air and underground. The temperature of the underground soil is more reliable as it does not dramatically change daily and seasonally. It has almost constant temperature all year long at a certain depth. Moreover, in summer, underground soil at certain depth has a much lower temperature than air resulting in higher heat transfer efficiency. Popiel, Wojtkowiak and Biernacka (2001) referred to Baggs's formula (Baggs, 1983) which predicted underground temperatures which highly depend on average ambient air temperature in the upper layer and it is approximately constant after 3 meters depth. Temperature distribution which is a function of depth and time is expressed in Eq. (5.14). However, to simplify the pilot system, the ambient air heat sink/source is chosen in this thesis to better understand the fundamental possibility of the system before adding more complicated alternative heat sink/source in the future.

$$T(x,t) = (T_m \pm \Delta T_m) - 1.07 \cdot k_v \cdot A_s \cdot exp(-0.00031552 \cdot x \cdot \alpha^{-0.5}) \cdot cos\left(\frac{2\pi}{365}(t - t_0 + 0.018335 \cdot x \cdot \alpha^{-0.5})\right) \quad (5.14)$$

where $T(x,t)$ is temperature distribution (^oC)

T_m is the average annual ambient air temperature (^oC)

ΔT_m is the difference between the ground temperature at 10-meter depth and the average annual ambient air temperature (^oC)

Note: 10 meters is used as it is usually the depth where the ground temperature starts to be stable

k_v is the vegetation coefficient which varies from
1 if the considered ground area is naked and
0.22 if the considered ground area is fully covered

A_s is the amplitude of surface temperature from T_m (K)

x is the depth of ground (m)

α is the annual average soil thermal diffusivity for homogeneous undisturbed ground (m^2/s) where $\alpha = \frac{\lambda}{C_v}$

λ is the thermal conductivity ($W/(m \cdot K)$)

C_v is the volumetric heat capacity ($J/(kg \cdot K)$)

t is the time of the considered year from day 1 which is Jan 1st (day)

t_0 is the day when the average ambient air temperature is at its minimum

5.3 Water-jacket reactor model validation

The adsorption and desorption of the water-jacket models were validated with the experimental data from (Yuan *et al.*, 2018). Yuan *et al.* (2018) used a mixture ratio between $SrCl_2$ and EG of 2:1 which was set in this thesis model for the validation cases. The simulation conditions were set associating with the experiment setups as follow.

Table 5.2 *The simulation model setups to follow the experimental setups for model validations*

Experimental setups from (Yuan *et al.*, 2018)	**This thesis simulation models setup**
The desorption process	
The connection valve between the condenser and the reactor was closed until the HTF temperatures reach the desired levels; 90 ^{o}C, 100 ^{o}C and 110 ^{o}C	The HTF input temperature was pre-set at three levels. The simulation was done in three cases following the available experimental data; 90 ^{o}C, 100 ^{o}C and 110 ^{o}C

The condenser temperature is being kept at 20 ^{o}C (±1 ^{o}C)	The ambient temperature which dominants the condensation pressure in the condenser was set at 20 ^{o}C
The valve was opened and the HTF at desired temperature was run into the reactor. The reaction rate was monitored using the differential pressure sensor. The experiment finished when the sensor indicates no more change.	The simulation was run with the reaction time of 2 hours following the results from (Yuan *et al.*, 2018).
The adsorption process	
The evaporator was kept at 0 ^{o}C (±1 ^{o}C)	The ambient temperature which dominants the evaporation pressure in the evaporator was set at 0 ^{o}C
The valve was closed then the reactor was cooled down to 0 ^{o}C to represent the winter-like temperature condition.	The initial condition of every part in the reactor was set at 0 ^{o}C.
The valve was opened for the adsorption process and the HTF at 20 ^{o}C was run into the reactor to absorb the exothermic adsorption heat.	The simulation started with the initial HTF temperature of 20 ^{o}C.

5.3.1 The adsorption model's validation

With the model setup described in Table 5.2 and the parameters shown in Table 5.3, the simulation and experimental results were compared with the presented deviation in Fig. 5.3. The largest deviation happens at the first half-hour of the reaction time which can be described into two parts. The simulation results during the first ten minutes have the deviation of more than 10% because the global conversion is almost zero resulting in a large percentage of the deviation as the reference value gets close to zero although the simulation result is fitting well with the experimental result. During ten to thirty minutes of the reaction time, the deviation is about 10% to 17% which is considerably large. The global conversion of the simulation indicates the faster reaction rate than the experiment. The reason may be because of the ideal property of the heat transfer coefficient between the adsorbent bed and the tube wall resulting in greater heat transfer rate between the adsorbent bed and the tube wall in the simulation than the experiment. Practically, the adsorbent bed may not be able to make good contact with the tube wall resulting in lower heat transfer from the adsorbent bed to the tube wall. Consequently, the adsorbent temperature may get closer to its equilibrium temperature which makes the

reaction rate lower. The model simulation may be improved to obtain higher accuracy if the real heat transfer coefficient between the mentioned surface-contact is known. However, after half an hour, the simulation results fit well with the experimental results with the global conversion of around 0.86 with 1.30% deviation.

Table 5.3 *The parameters used in the adsorption and desorption models for validations*

Parameters	Value	Unit
Physical properties of materials		
$SrCl_2$ mass per tube	0.18	kg
The weight fraction of salt/EG	2:1	-
Expanded graphite weight	0.09	kg
Composite adsorbent density	250	kg/m^3
Pure $SrCl_2$ density	3052	kg/m^3
Graphite density	2260	kg/m^3
Molar weight of $SrCl_2$	158.53	g/mol
Molar weight of NH_3	17.03	g/mol
Wall material (situated between adsorbent and water layers)	Stainless steel (type 430)	
Wall density	7740	kg/m^3
Geometry		
NH_3 hole diameter	12	mm
Wall thickness	1	mm
Composite adsorbent thickness (adsorbent layer)	20.25	mm
Water layer thickness	3	mm
Length of the water-socket reactor	0.5264	m
Thermal properties of materials		
Wall's thermal conductivity	26.1	W/(m· K)
Composite adsorbent's thermal conductivity (Huang *et al.*, 2004)	For adsorption: 19.1 For desorption: 13.7	W/(m· K)

Parameters	Value	Unit
Wall's specific heat	460.55	J/(kg· K)
Water's specific heat	4186	J/(kg· K)
NH_3's specific heat	2172.64	J/(kg· K)
Graphite's specific heat	720	J/(kg· K)
Initial composite adsorbent's specific heat (Huang *et al.*, 2004)	At fully desorption stage: 576	J/(kg· K)
Convective heat transfer coefficient between water and wall	500	W/(m^2 · K)
Heat transfer coefficient between composite adsorbent and wall (Huang *et al.*, 2004)	For adsorption: 249 For desorption: 165	W/(m^2 · K)

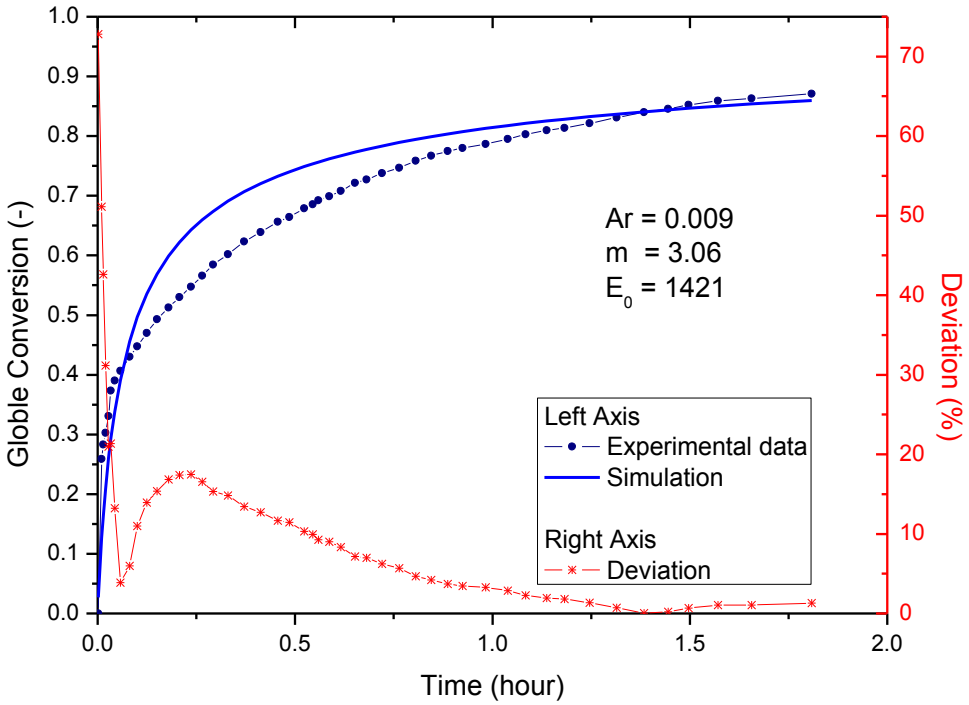

Fig. 5.3 *The adsorption comparison between the simulation results in this thesis and experimental results from* (Yuan *et al.*, 2018) *with the deviation*

5.3.2 The desorption model's validation

By setting the simulation for the desorption process as described in Table 5.2, the validations were performed against two experimental cases; 1) 100-20 case which is the case that the input HTF temperature was 100 ^oC and the ambient temperature is at 20 ^oC as shown

in Fig. 5.4. 2) 110-20 case which is the case that the input HTF temperature was 110 ^{o}C and the ambient temperature is at 20 ^{o}C as shown in Fig. 5.5. In the 110-20 case, the simulation was assumed that the pressure in the HTF tube is sufficiently high to keep the HTF as liquid phase and there is no phase change analysis involved. The desorption model produces a considerably good match with the experimental results with the parameters shown in the figures. The per cent deviations of the simulation results from the experimental results are larger when the global conversion approaches zero which is because the reference value (global conversion from the experiments) gets close to zero leading to large per cent deviations. However, the accuracy of the simulation results is still acceptable with the per cent deviation of less than 10% when the global conversion is greater than 0.2. Consequently, the water-jacket desorption model with the Arrhenius number of 0.125, the exponential term of 1.52 and the activation energy of 14000 obtained by validating the models developed in this thesis with the experimental results from Yuan *et al.* (2018) is used for the rest of the study.

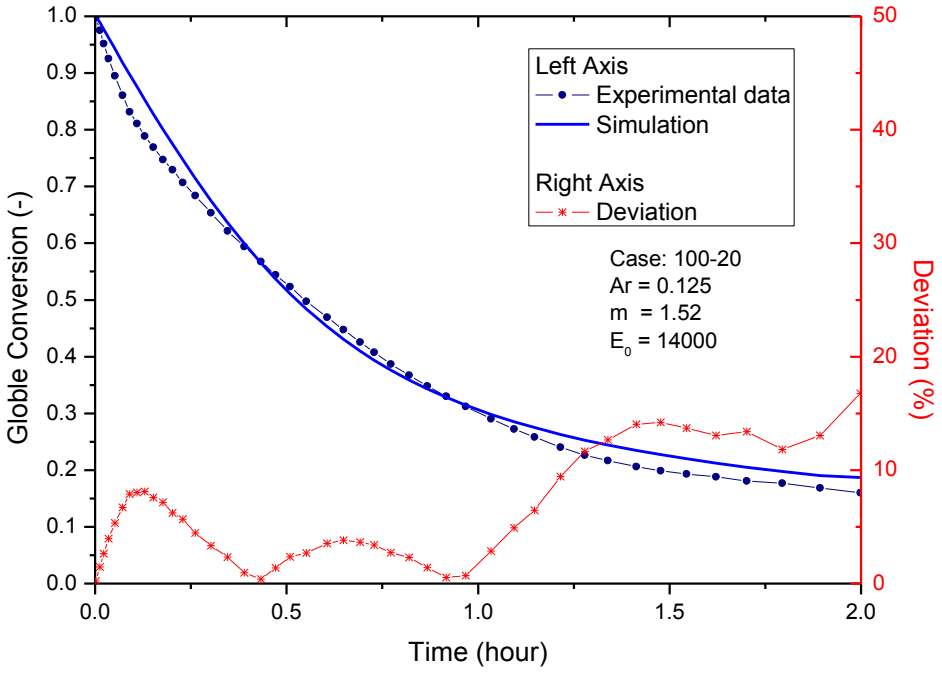

Fig. 5.4 *The desorption (case 100-20 ^{o}C) comparison between the simulation results in this thesis and experimental results from* (Yuan *et al.*, 2018) *with the deviation*

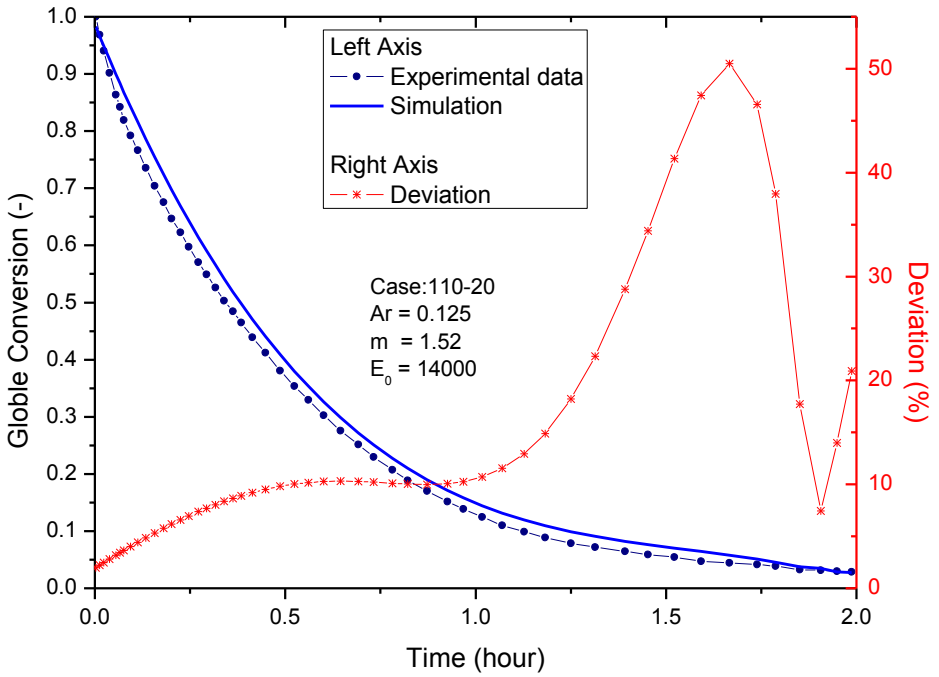

Fig. 5.5 *The desorption (case 110-20 °C) comparison between the simulation results in this thesis and experimental results from* (Yuan *et al.*, 2018) *with the deviation*

5.4 Compressor-assisted thermochemical sorption energy storage simulation results

The simulations were done with the initial conditions different from the validated models as described by the following;

1. In this simulation, the compressor will be integrated into the model by adjusting the operating pressure according to the considered CR as described in the previous chapter.
2. The salt to EG mass ratio is 3:1 rather than 2:1 in the validation cases due to the more energy density while still keeping acceptable heat transfer properties.
3. The adsorbent bed density is 450 kg/m^3 rather than 300 kg/m^3 in the validation cases because of the more effective compression process. Moreover, many published works report higher mass density of the adsorbent bed while still keeping even material distribution and gas permeability. This thesis used 450 kg/m^3 because the laboratory for the future work was able to deal with this density level.
4. The heat source for the desorption process in the following studies is from the PV/T according to the real weather data. Therefore, the amount of HTF used as the heat source was limited according to the real production results from the last chapter. Compared to the validation cases, the amount of HTF was not limited.

5. The mass flow rate of the HTF flowing into the reactor in the following studies was controlled to see the performances in many conditions. Compared to the validation cases which were done with fixed mass flow rates.

5.4.1 Water-jacket reactor performance using SrCl2 composite adsorbent: The desorption performance

The desorption process in the simulation will be done after sunset to get the advantage of lower desorption pressure from the lower ambient temperature. After 9 PM in summer at Newcastle upon Tyne, although there is still solar irradiance, the PV/T collector is unable to produce useful energy output; therefore, the daily HTF produced from the day is collected in the tank ready for the desorption process to be started at 9 PM. As an example, Fig. 5.6 shows the temperature responses at each component of the reactor under the conditions of the CR=12, the temperature equilibrium drop = 5^{o}C, the HTF temperature from the PV/T (which will call the reactor heat input temperature from now as this chapter more focuses on the reactor) = 90^{o}C and the ambient temperature on the studied summer sunny day of 13.43 ^{o}C. At the system starting time, the HTF was fed into the reactor occupying the volume of the inside tube at stationary state (as presented with zero mass flow rate in Fig. 5.7 for the first few minutes transient response) until the temperature of the HTF reduces to 5 ^{o}C higher than the salt equilibrium temperature. Heat conductively transfers from the HTF through the wall to the reactant resulting in temperatures rise in the wall and reactant with temperature decreases in the HTF as shown in Fig. 5.6 in the first 6 minutes. After 6 minutes, the HTF flows into the reactor at the mass flow rate that maintains the outlet temperature at 5 ^{o}C higher than the salt equilibrium temperature until 6 AM of the next day.

It can be seen in Fig. 5.6 that the global conversion reduces rapidly in the first few minutes due to the high temperature difference from the reactant temperature response ($T_{eq} - T_{reactant}$) introducing large pressure drop (dP_{drop}) as shown in Fig. 5.8 before it reaches steady state. Note that, although the HTF temperature at the outlet of the reactor remains at 5 ^{o}C higher than the salt equilibrium temperature, the reactant temperature is slightly less than 5 ^{o}C as seen in Fig. 5.6 after 6 minutes. The temperature differences between the inlet HTF and the outlet HTF temperatures influent different temperature response characteristics of the component temperatures. If the outlet HTF temperature (T_{outlet}) is slightly lower than the inlet HTF temperature (T_{inlet}), in case of low compression ratios when T_{outlet} is kept at high temperature to maintain the desorption, the reactant temperature responses as the overdamped (or critical

damped) characteristic (which also happen with the pressures as shown in Fig. 5.9). When the CR is high, T_{outlet} could be maintained to be low and the temperature difference between T_{outlet} and T_{inlet} is considerably high which make the reactant temperature response to be underdamped characteristic (as shown in Fig. 5.8) as the temperature differences between T_{eq_salt} and $T_{reactant}$ ($dT_{drop\_actual} = T_{eq\_salt} - T_{reactant}$) shown in Fig. 5.10 when CR is equal to or higher than 8. The dT_{drop_actual} of each CR introduces the different pressure drop in the reactor as presented in Fig. 5.11.

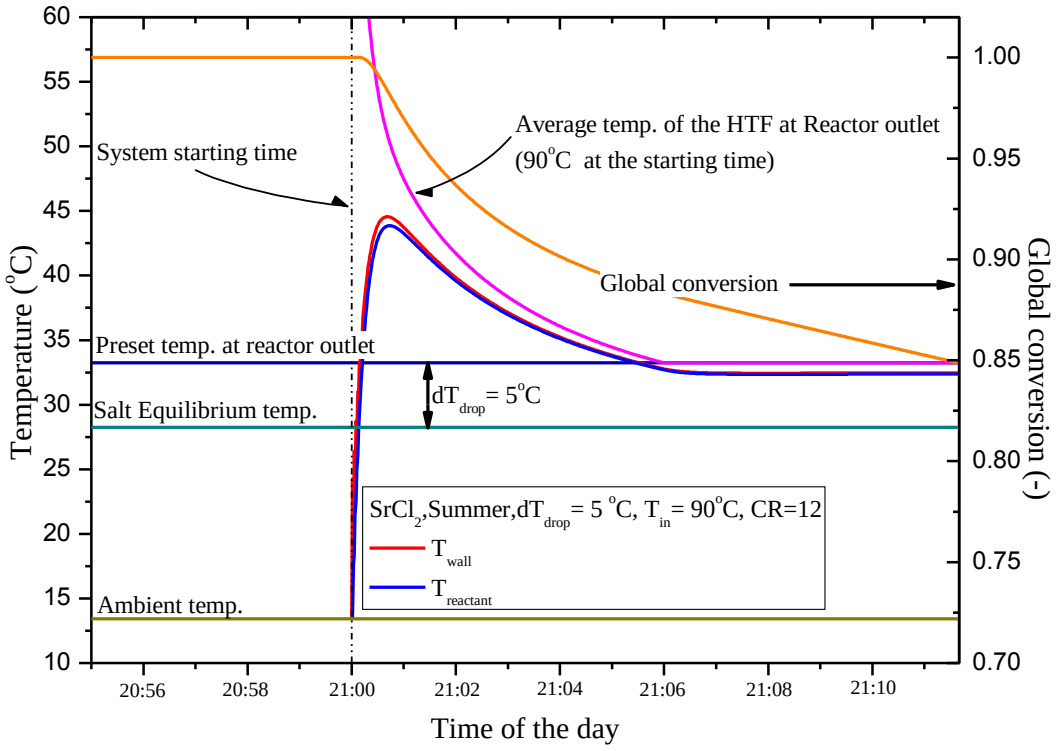

Fig. 5.6 *The first few minutes temperature responses of reactor components and the global conversion when using $SrCl_2$-EG at 5 °C temperature equilibrium drop, 90 °C reactor input temperature at CR = 12.*

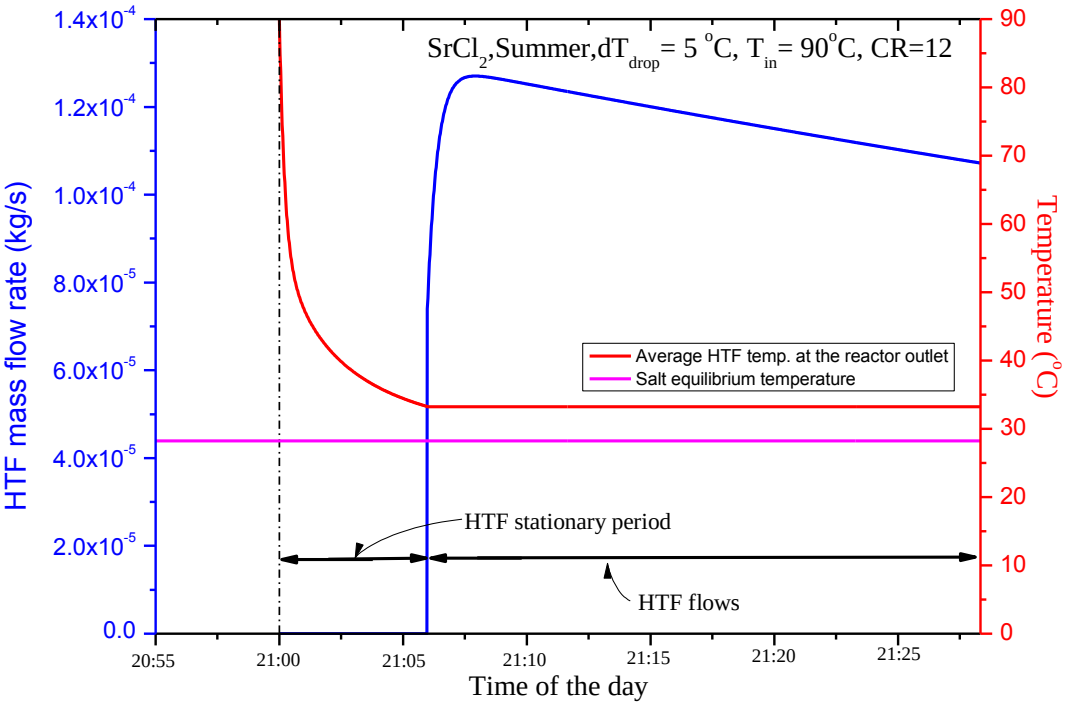

Fig. 5.7 *The HTF mass flow rate and its temperature at the reactor outlet (T_{out}) showing that the HTF flow starts after the T_{out} reduces to 5 °C higher than the T_{eq} when using $SrCl_2$-EG at 5 °C temperature equilibrium drop, 90 °C reactor input temperature at CR = 12.*

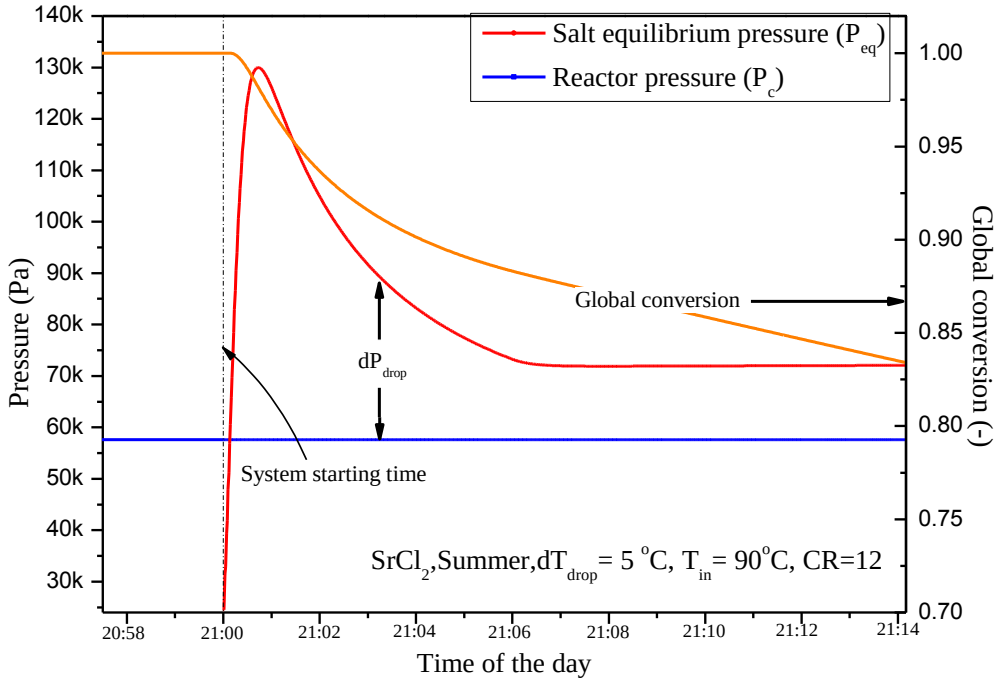

Fig. 5.8 *The salt equilibrium pressure and the reactor pressure showing the pressure difference (dP_{drop}) that introduce the desorption process as seen by the reduction of the global conversion when P_{eq} is higher than P_c for the $SrCl_2$-EG reactant at 5 °C temperature equilibrium drop, 90 °C reactor input temperature and CR = 12. The salt equilibrium pressure responses as the underdamped characteristic.*

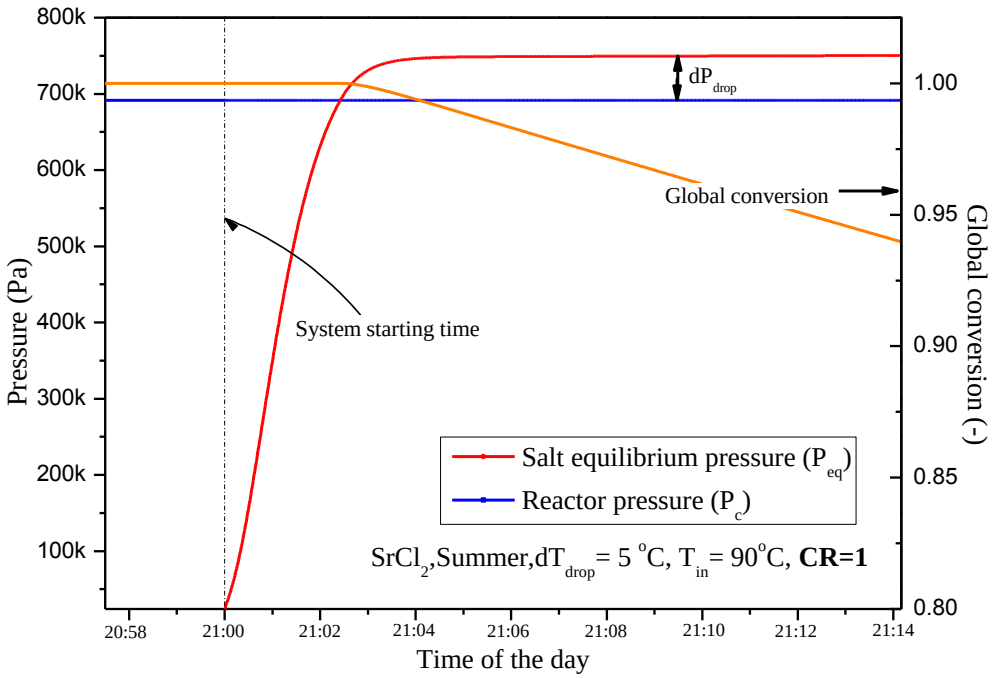

Fig. 5.9 *The salt equilibrium pressure and the reactor pressure showing the pressure difference (dP_{drop}) that introduce the desorption process as seen by the reduction of the global conversion when P_{eq} is higher than P_c for the $SrCl_2$-EG reactant at 5 ^oC temperature equilibrium drop, 90 ^oC reactor input temperature and CR = 1. The salt equilibrium pressure responses as the overdamped (or critical damped) characteristic.*

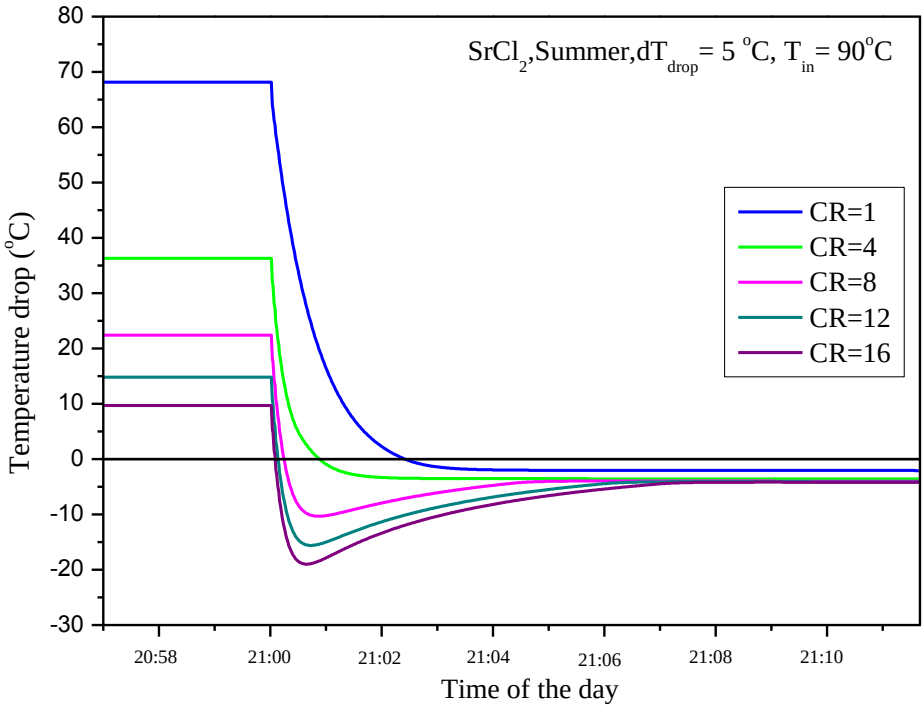

Fig. 5.10 *The transient temperature drop ($dT_{drop\_actual} = T_{eq\_salt} - T_{reactant}$) of the $SrCl_2$ reactor at different CR for the first few minutes before reaching the steady states. (Negative values mean that the reactant temperature is higher than the salt equilibrium temperature resulting in desorption reaction.*

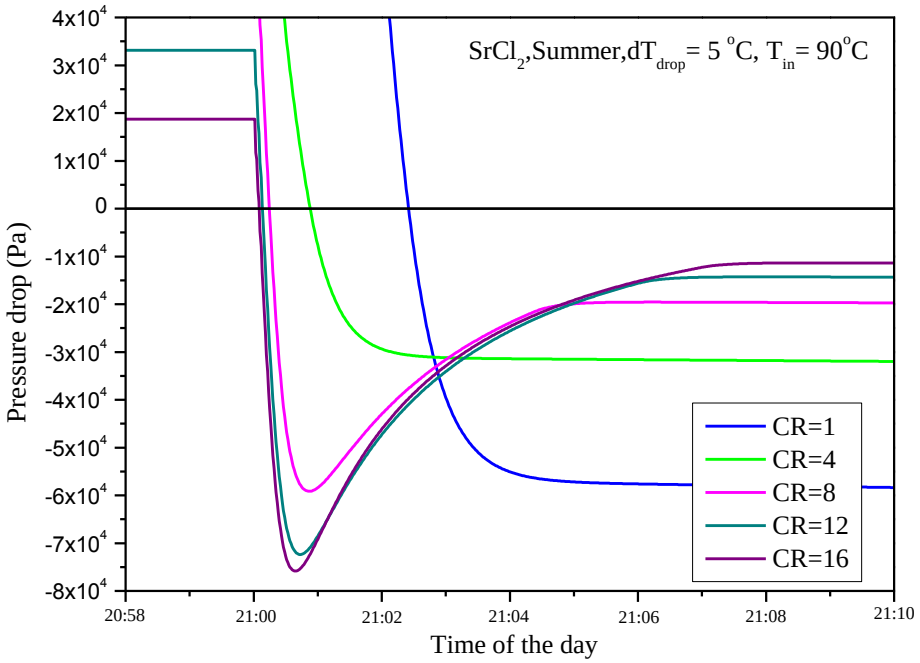

Fig. 5.11 *The transient pressure drops ($dP_{drop} = P_c - P_{eq\_salt}$) of the $SrCl_2$ reactor at different CR for the first few minutes before reaching the steady states. (Negative values mean that the salt equilibrium pressure is higher than the reactant pressure resulting in desorption reaction.*

To keep the 5 °C difference (dT_{drop}) between the outlet HTF temperature and the T_{eq}, the mass flow rate of the HTF was adjusted as shown in Fig. 5.12. At CR =1, the non-equilibrium reactant temperature has to be maintained at 84.75 °C leading to the very fast mass flowrate depicted with the blue line. Therefore, with the limited amount of HTF produced by the PV/T collectors, the storage system without the compressor-assist component (CR=1), thermal energy produced from the PV/T collector can be hardly stored in the TSES system. With the assistance of the compressor (CR>1), the HTF mass flow rate reduces considerably; for example, at the CR of 4, the maximum mass flow rate reduces from 18e-4 to around 2.5e-4 kg/s because the reactant temperature can be kept at 54.36 °C to maintain the non-equilibrium state for the desorption process. For higher CR, lower reactant temperatures can be used to maintain the desorption process leading to a greater amount of thermal energy being utilised from the PV/T thermal production. Fig. 5.12 also shows that using higher CR introduces lower reactant temperature which adds the other benefit as the sensible heat is lesser resulting in more thermal energy being used in the desorption reaction rather than the unstorable thermal mass consumption in the storage system as shown with the per cent of desorption heat. The storage system operated at the CR = 16 may store 94% of the thermal energy supplied from the PV/T, comparing to just around 78% with the CR = 1. The rest of the thermal energy is consumed as sensible heat with the assumption of no energy loss to the ambient.

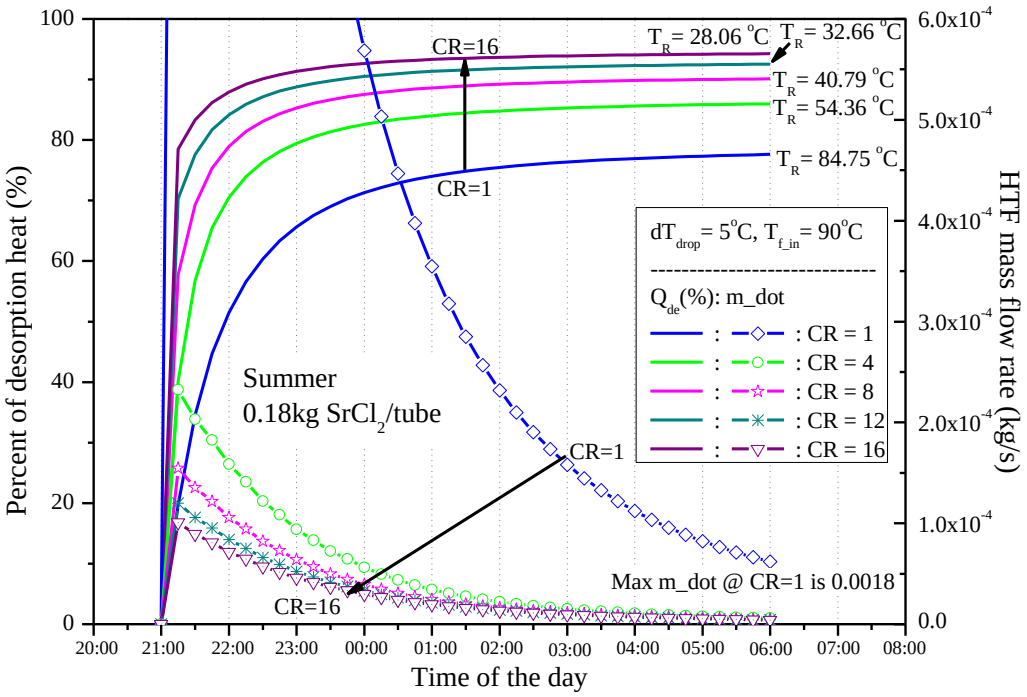

Fig. 5.12 *The per cent of the desorption heat and the HTF mass flow rate to maintain the non-equilibrium state of the desorption when different CRs are used in the desorption process. The reactant temperatures (T_R) presented at each CR indicate that the higher the CR, the lower the T_R, leading to a higher per cent of desorption heat as the sensible heat is lower.*

The per cent of desorption heat is used to indicate the coefficient of performance (COP) for the desorption system when different CRs are used as shown in Fig. 5.13. Because of the higher COP and larger temperature gap between the HTF and T_R when higher CR is used, the amount of HTF used for the desorption is presented in Fig. 5.13 for one reactant tube containing 0.18kg of $SrCl_2$ with 3:1 salt/EG ratio. It can be seen that when CR = 1, the amount of 90°C HTF of 22.24kg is required to maintain the non-equilibrium desorption process for 9 hours from 21:00 until 06:00 on the next day. If the CR = 4, the 90°C HTF of only 2.17kg is needed which is less than 10 times of the amount needed when there is no compressor assistance.

After 9 hours of desorption from 21:00 (after sunset of the HTF production day from the PV/T collector) to 06:00 of the next day (before the HTF is reused in the PV/T collector), the overall global conversions of the reactant of 0.18kg $SrCl_2$ (1 water-jacket reactant tube) are presented in Fig. 5.14. It can be seen from the global conversions when using different CRs that after 9 hours, the reactant could be desorbed more than 90%. The best performance happened when using CR=4 with 93.8% desorption following by 93.3%, 92.6%, 92.6% and 92.1% when CR=8, 12, 1 and 16 respectively. Thermal energy consumed for the per cent conversion at each CR is presented in Fig. 5.14 as well. Note that, when the lower CR is used, the amount of thermal energy input is required more than the cases that the higher CR is implemented. It is

because less sensible heat is needed when higher CR is used as the operating reactant temperature is lower. Therefore, using higher CR tend to provide higher storage efficiency.

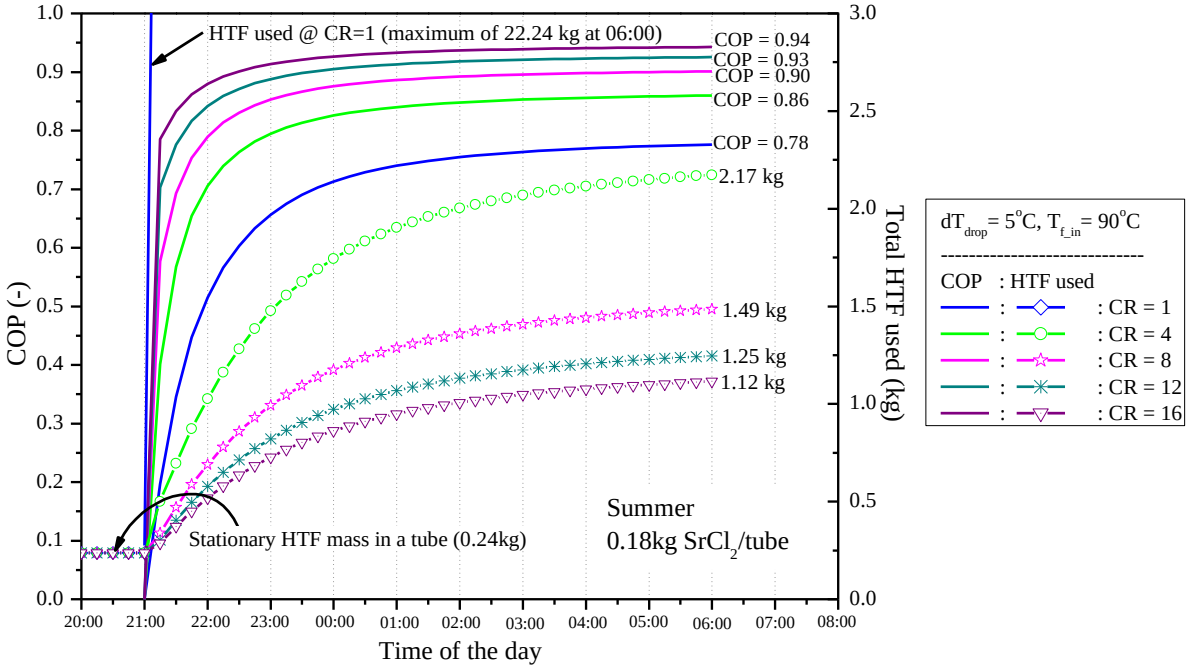

Fig. 5.13 *The COP and the amount of HTF used for 9-hour desorption of a reactant tube with 0.18kg of $SrCl_2$-EG in a reactor when different CRs are used.*

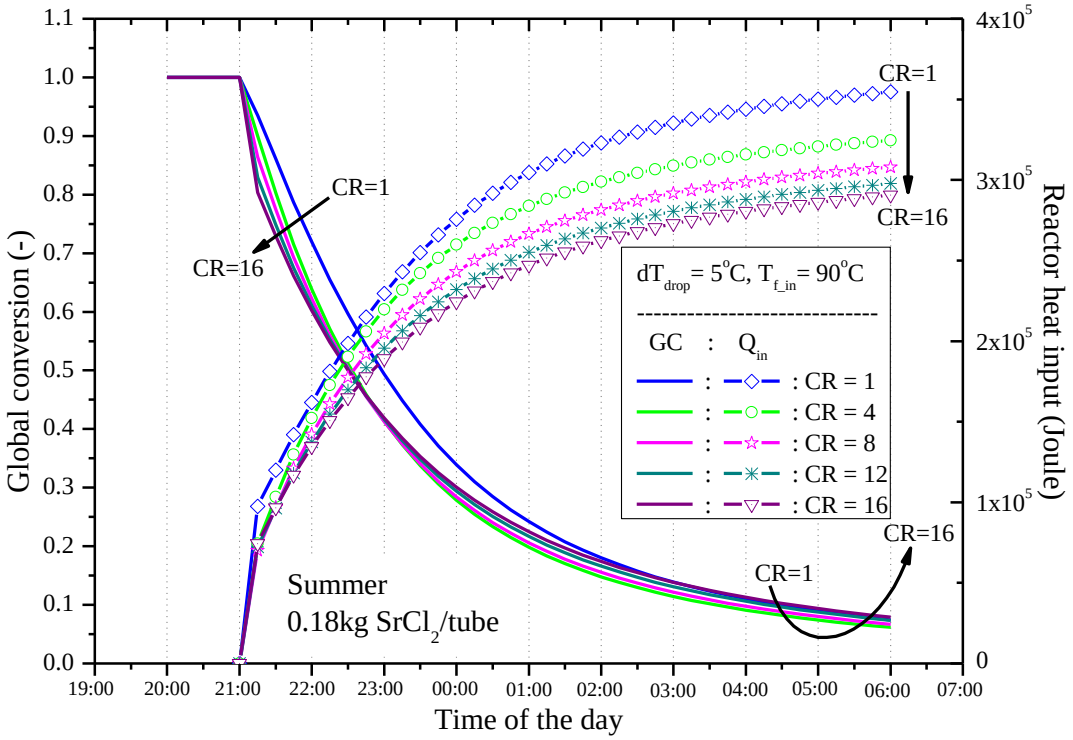

Fig. 5.14 *The global conversion (GC) and its corresponding required heat input (Q_{in}) at different compression ratio (CR) of a single water-jacket tube in the reactor with 5 °C equilibrium temperature drop and the HTF input temperature is 90 °C in a sunny summer day.*

Along the desorption process, the rate of conversion trends at different CRs were not consistent as shown in Fig. 5.15 for the entire 9-hour desorption and Fig. 5.16 for the transient responses of the first 15-minutes. Because of different characteristics of temperature responses at different CRs, using CR=16 makes the biggest pressure drop during the first few minutes resulting in the highest reaction rate and the reaction rates reduce when using lower CRs as shown in Fig. 5.16. However, when the reactions progress toward the steady states, using lower CRs give higher reaction rates as shown in Fig. 5.15 and Fig. 5.16. These reaction rate responses contribute to the degree of conversion as mentioned and presented in Fig. 5.14. As the reactions progress, the porosity and the specific heat capacity of the reactant change according to the degree of conversion as presented in Fig. 5.17.

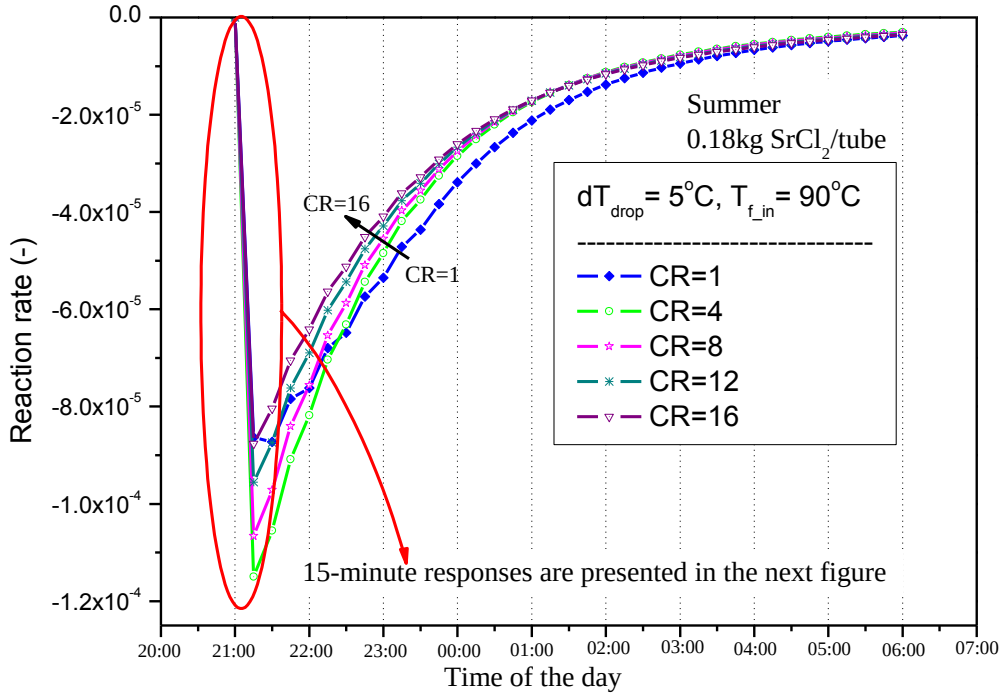

Fig. 5.15 *The 9-hour reaction rates of a reactant tube with 0.18kg of $SrCl_2$-EG in a reactor when different CRs are used.*

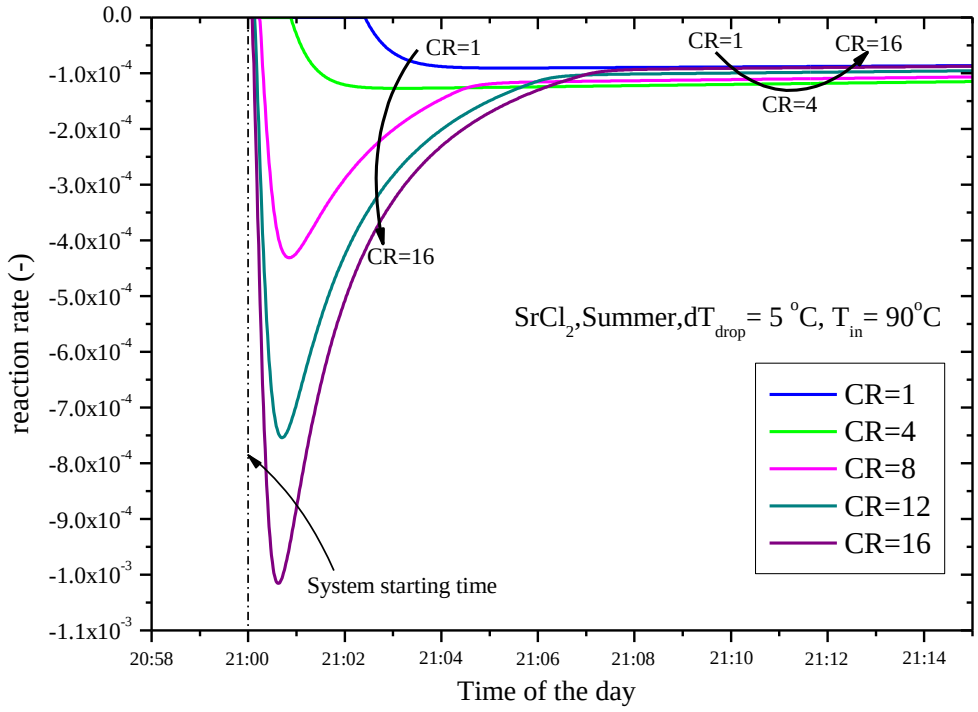

Fig. 5.16 *The 15-minute reaction rates of a reactant tube with 0.18kg of $SrCl_2$-EG in a reactor when different CRs are used.*

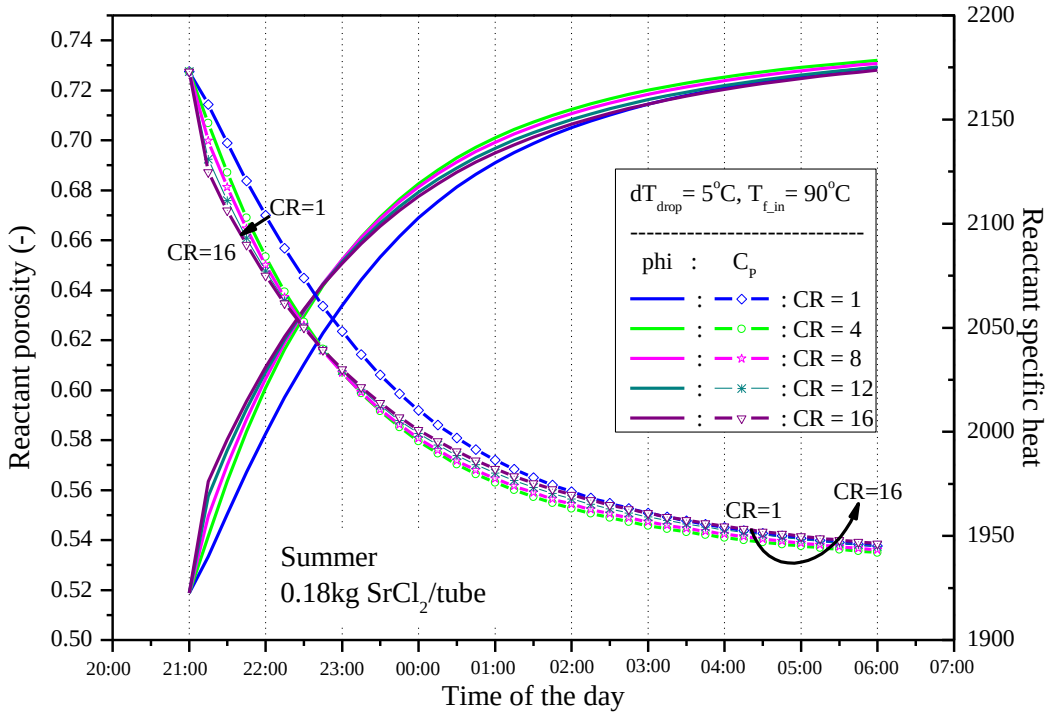

Fig. 5.17 *The reactant porosity and specific heat of a reactant tube with 0.18kg of $SrCl_2$-EG in a reactor when different CRs are used.*

5.4.2 Water-jacket reactor performance using SrCl2 as a reactive bulk: The adsorption model results

Assuming that a household starts the space heating system at 6 AM in winter days; therefore, the following studies use a typical cloudy winter day in Newcastle upon Tyne as an example to demonstrate the dynamic response of the reactor for supplying the heating demand in a typical household in Newcastle upon Tyne. The results are based on the water-jacket reactor containing a 0.18 kg of $SrCl_2$ mixed with the EG of 3:1 salt:EG mass ratio and 450 kg/m^3 adsorbent density. Because the adsorption process (discharging state) normally occurs after the desorption process (charging state), the initial global conversion of the reactant should be set based on the global conversion after the desorption presented in the previous section. With different CRs used in the desorption state, the final global conversions for each CR were around 0.1 which is used as the initial global conversion in this section for the adsorption process.

Following one of the main objectives in this thesis which is not using additional electricity in winter to drive the system while maintaining the temperature level of the HTF output for heating demands, the CR of the adsorption process was kept at 1 for all cases. The output temperature of the HTF was varied from 55 ^{o}C to 75 ^{o}C to explore the performances of the system. To maintain the HTF temperature output at each desired level, the mass flow rate of the HTF was adjusted along the day as shown in Fig. 5.18. It is obvious that the HTF mass flow rate is higher when lower HTF temperature output is required. To maintain the output temperature, the mass flow rate was decreased because the heating power output of the reactant reduces when the adsorption progresses as shown in Fig. 5.19. Note in Fig. 5.19 that there are the sudden increases of the reactor heating power output at the time of the first mass flow rate at each T_{out}. Those changes are because of the change from conductive heat transfer during the stationary period to be convective heat transfer when the mass flow rate is not zero. Naturally, the convective heat transfer coefficient is higher than the conductive heat transfer coefficient resulting in sudden increases in the thermal power output as mentioned.

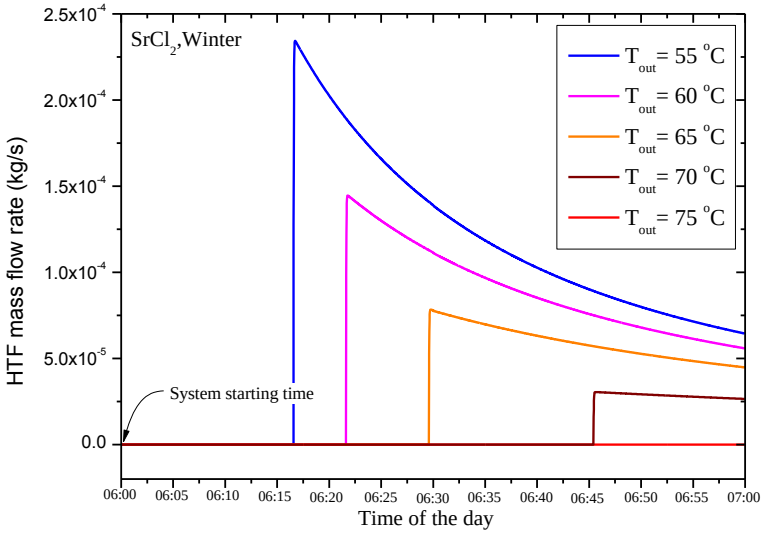

(a)

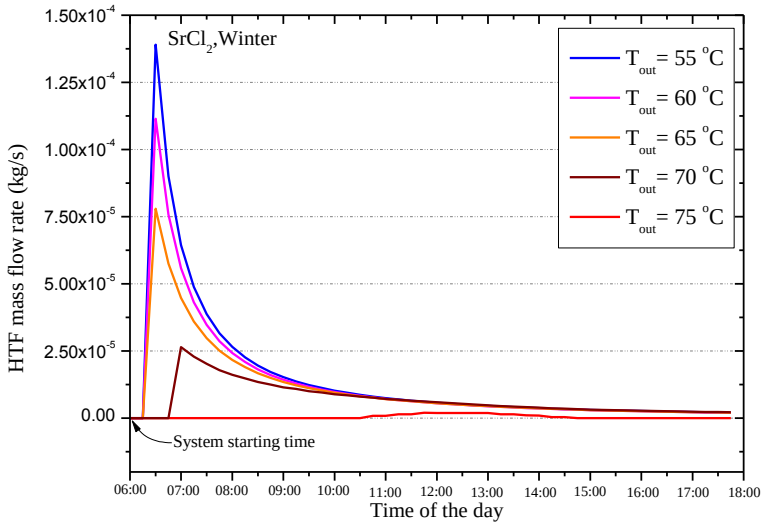

(b)

Fig. 5.18 *The HTF mass flow rate along a typical winter cloudy day at Newcastle upon Tyne when different HTF output temperatures were set; (a) at the first one hour of the reaction, (b) the entire day.*

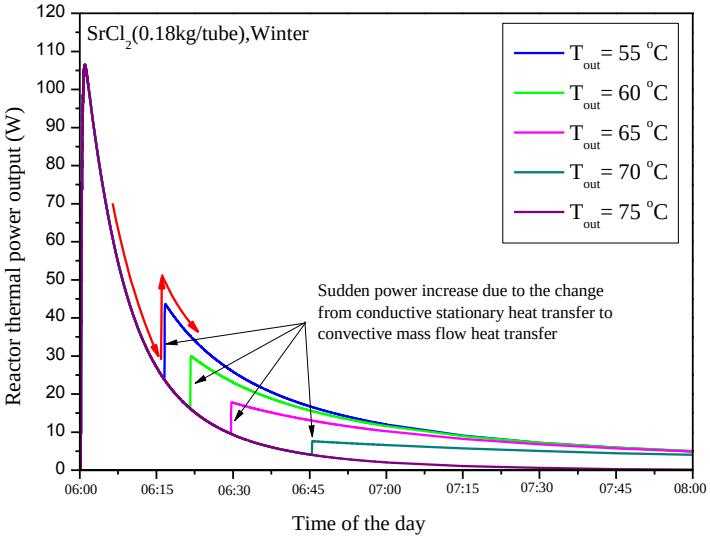

(a)

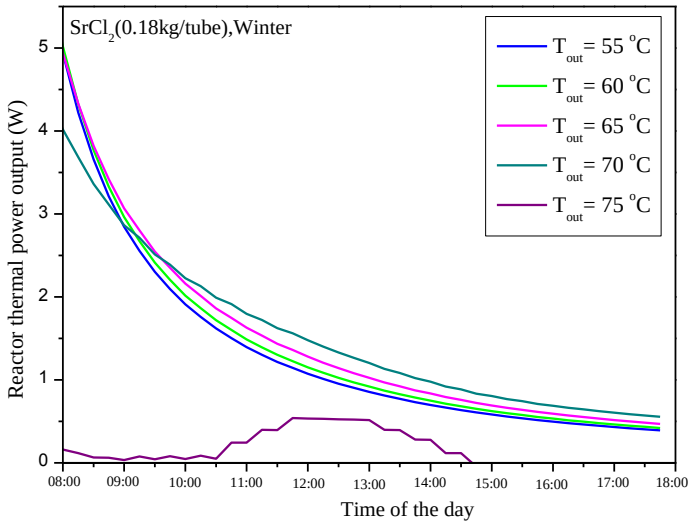

(b)

Fig. 5.19 *The useful thermal power output at the first 2-hour adsorption from a one-tube of 0.18kg of $SrCl_2$ in the reactor at Newcastle upon Tyne when different HTF output temperatures were set ; (a) at the first two hours of the reaction, (b) from 08:00 to 18:00.*

It is noticeable in Fig. 5.18 and Fig. 5.19 that at T_{out} = 75 °C before 10:30, the reactor could not produce the HTF at the desired temperature. The reason is that the desired output temperature at 75 °C is slightly higher than the salt equilibrium temperature (74.9 °C) corresponding to the ambient temperature in the morning as shown in Fig. 5.20. Therefore, when the adsorption progresses, the reactant temperature rises until it approaches the salt equilibrium temperature which makes the reaction stops because the equilibrium state is reached as presented by the reaction rate in Fig. 5.21.

However, at noontime when the ambient temperature is sufficiently high, the salt equilibrium temperature goes higher than the desired HTF temperature output resulting in the HTF is being flowed at 10:45 as shown in Fig. 5.18. If the desired HTF temperature output is not close to the salt equilibrium temperature, the issue of the reaction reaching its equilibrium state, which is not desirable, may not happen when setting the T_{out} to be 70 ^{o}C or lower as illustrated with the case of T_{out} = 55 ^{o}C in Fig. 5.22. Fig. 5.22 shows that the reactant temperature never reaches the salt equilibrium temperature leading to the continuous reaction which produces the thermal power output throughout the day as shown in Fig. 5.19. Fig. 5.19 also suggests that setting the T_{out} at a lower temperature can start powering the thermal energy demands in a household earlier. Nevertheless, the output temperature is restricted by the application requirement such as the 60 ^{o}C for the DHW demand. Setting the output temperature lower than the application requirement may lead to additional auxiliary heater operation which is not desired in this thesis although the COP of both energy charging and discharging states are higher as presented in the previous section for the energy charging state and in Fig. 5.23 for the energy discharging state.

Referring back to the reaction rate, the two main parameters that affect the reaction rate are the pressure drop (dP_{drop}) and the degree of conversion of the adsorbent (or global conversion). The dP_{drop} is the pressure difference between the reactor pressure (dominate by the evaporation pressure in the evaporator connected to the reactor) and the salt equilibrium pressure as shown in Fig. 5.24. The reactor pressure varies depending on only the ambient temperature and the salt equilibrium pressure depends on the reactant temperature. If the salt equilibrium temperature is lower than the reactor pressure, the pressure drop is positive, and the exothermic adsorption progresses. At the beginning of the day, when the adsorption has just started, the initial reactant temperature is at ambient temperature providing the low salt equilibrium pressure (in Fig. 5.24) leading to the fast reaction rate previously shown in Fig. 5.21. When the exothermic adsorption provides the thermal energy to the reactant mass until it reaches the state that T_{out} is achieved, the HTF flows with the accordance mass flow rate to maintain the desired output temperature providing the stable salt equilibrium pressure which maintains the pressure drop associated with the T_{out} as presented in Fig. 5.25. The pressure drop is directly related to the temperature drop which is the temperature difference between the salt equilibrium temperature and the reactant temperature as shown in Fig. 5.26.

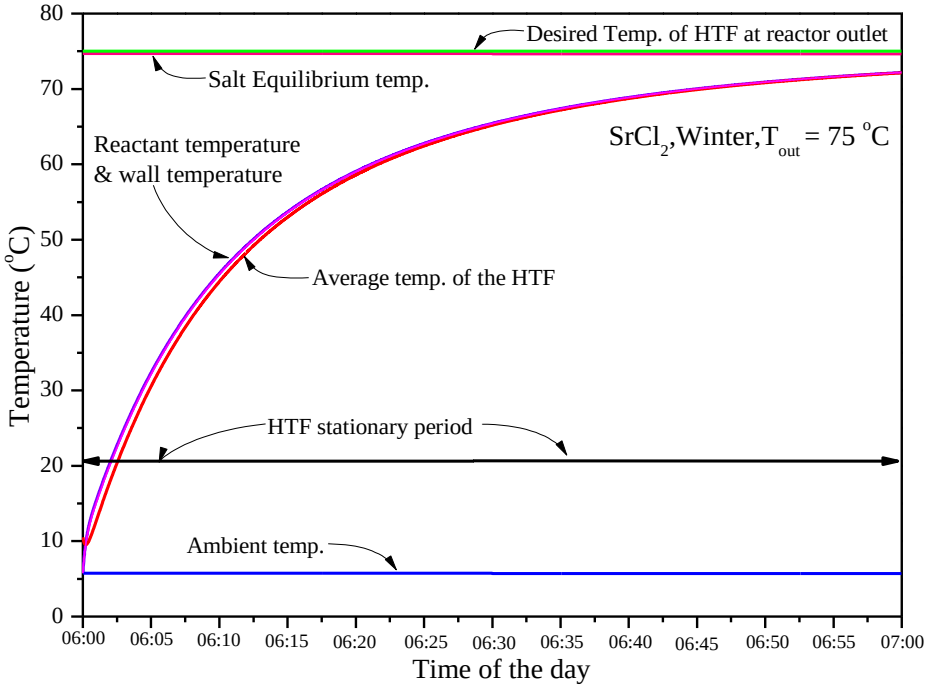

(a)

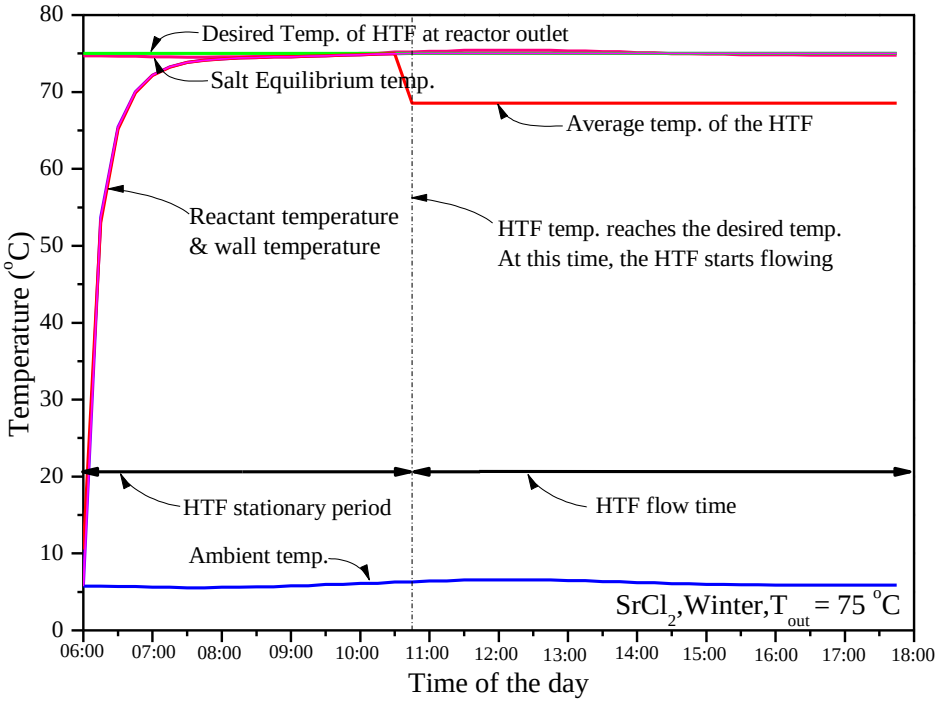

(b)

Fig. 5.20 *The temperature responses of each component when setting the desired temperature output at 75 °C in a $SrCl_2$-EG reactor containing 0.18kg of salt in a cloudy winter day at Newcastle upon Tyne; (a) at the first one hour of the reaction, (b) the entire day.*

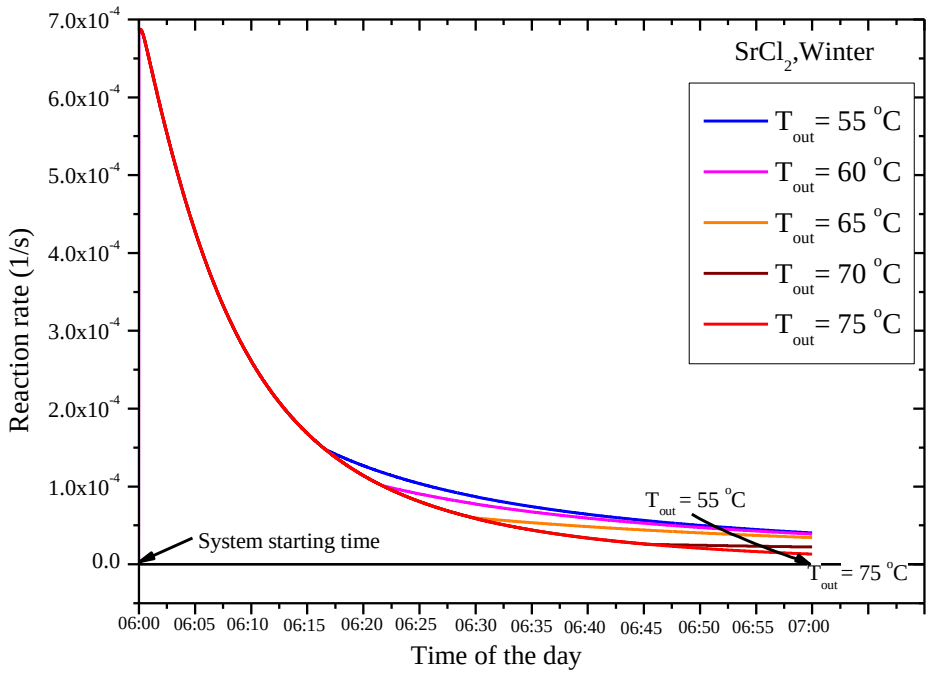

(a)

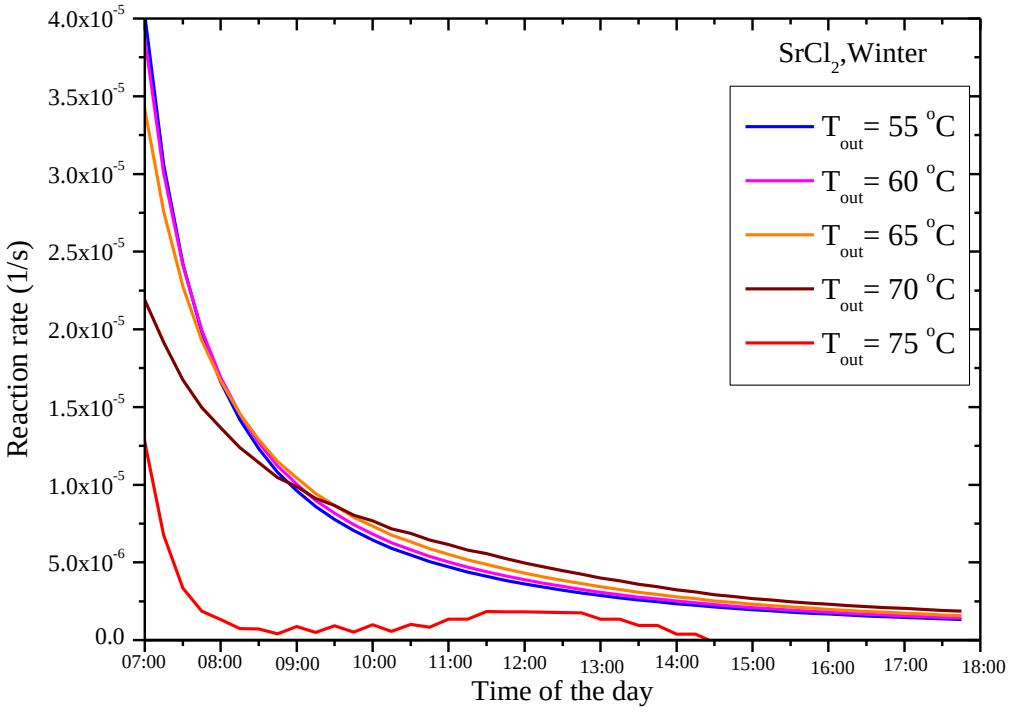

(b)

Fig. 5.21 *The reaction rate of the $SrCl_2$-EG reactor containing 0.18kg of salt in a cloudy winter day at Newcastle upon Tyne; (a) at the first one hour of the reaction, (b) from 07:00 to 18:00.*

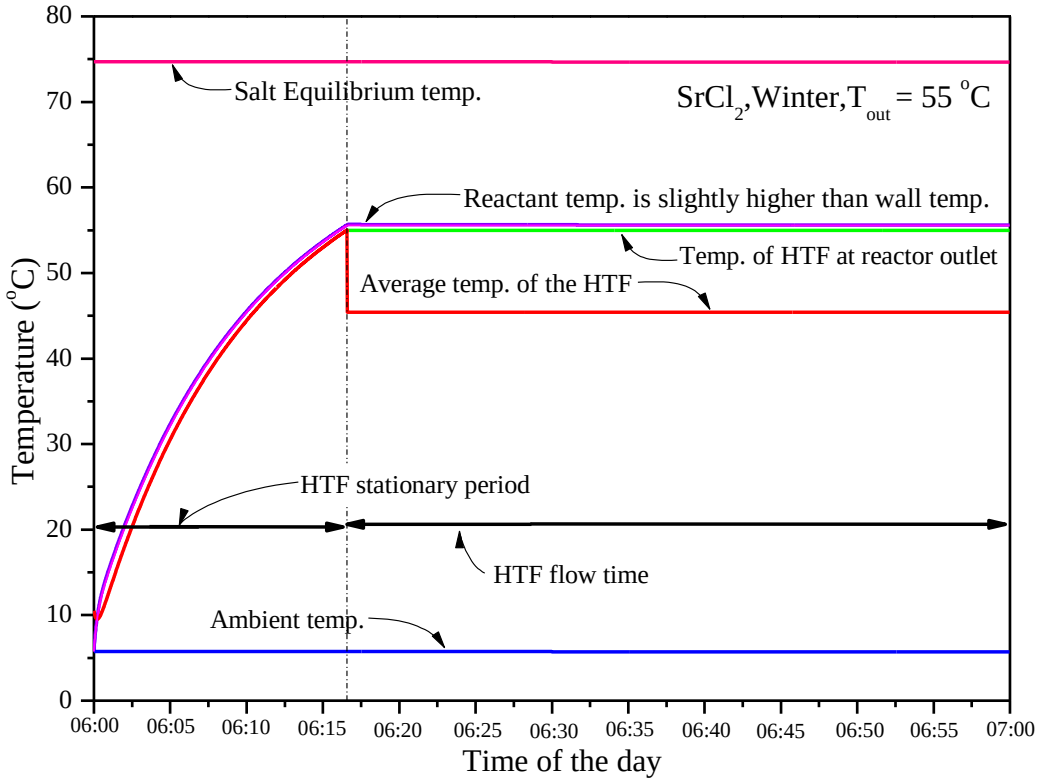

(a)

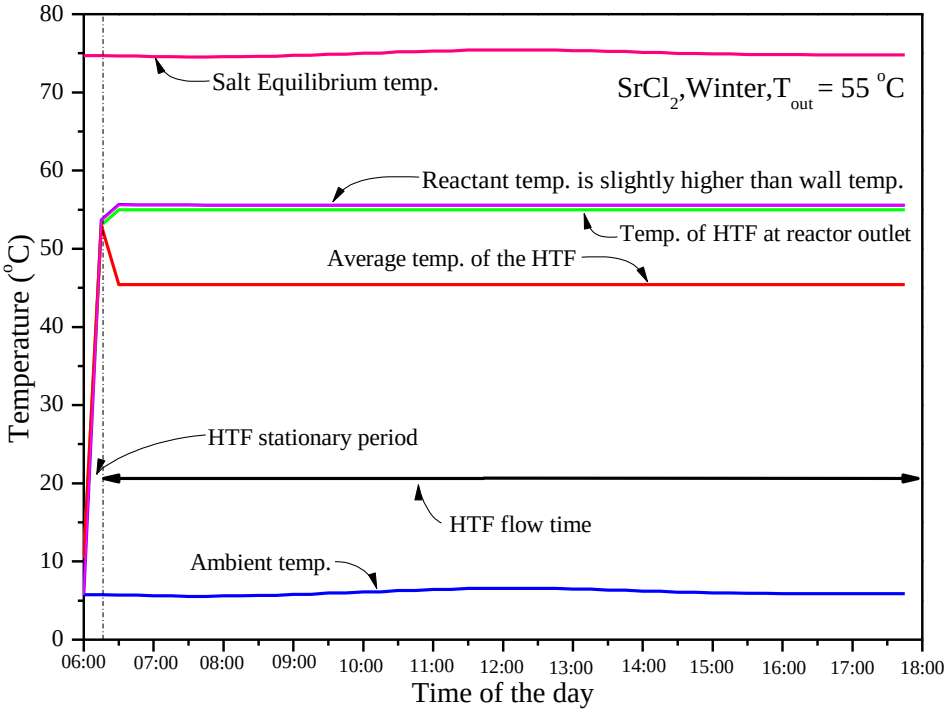

(b)

Fig. 5.22 *The temperature responses of each component when setting the desired temperature output at 55 °C in the $SrCl_2$-EG reactor containing 0.18kg of salt in a cloudy winter day at Newcastle upon Tyne; (a) at the first one hour of the reaction, (b) the entire day.*

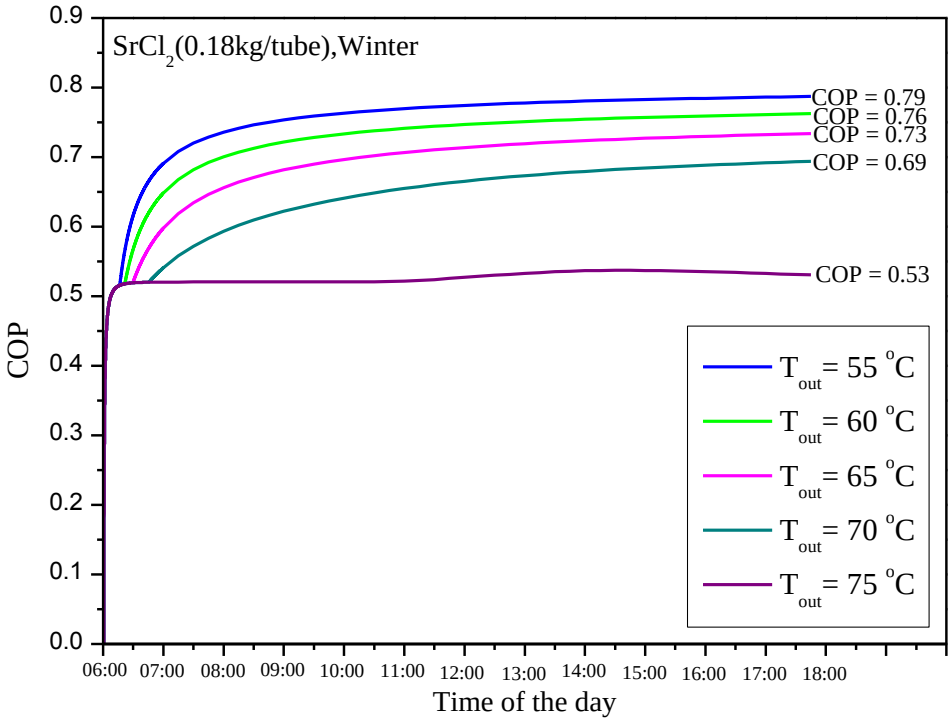

Fig. 5.23 *The COP of the $SrCl_2$-EG reactor containing 0.18kg of salt in a cloudy winter day at Newcastle upon Tyne when operated with different level of output temperature.*

As presented in Fig. 5.25 and Fig. 5.26 for the pressure drop and temperature drop, respectively, setting the desired output temperature at a lower level resulting in the larger pressure and temperature drops in the reactor resulting in faster reaction rate and at the end of the day, the degree of conversion of the adsorption process is higher as shown in Fig. 5.27. Therefore, at the initial global conversion of 0.1, the reacted part of the salt mass packed in the reactor is less than 90% according to the desired T_{out}. For example, when T_{out} = 60 °C, the final global conversion after 12-hour adsorption process is 0.88 which means only 78% of the total packed salt could be actively used as the energy storage material; the 22% of the packed salt mass is inactive and should not include in the detailed analysis.

The useful accumulative thermal energy output from one tube of the 0.18kg $SrCl_2$ reactor is presented in Fig. 5.28. Although there is the thermal production accumulated in the HTF from the starting of the adsorption process, the HTF mass cannot be obtained from that time until its temperature reaches the desired level then the entire stationary mass can be pump out very quickly before adjusting the mass flow rate according to the desired output temperature level. By doing so, the sudden accumulative HTF mass outputs happen at the first moment when it reaches the T_{out} temperature level shown in Fig. 5.29.

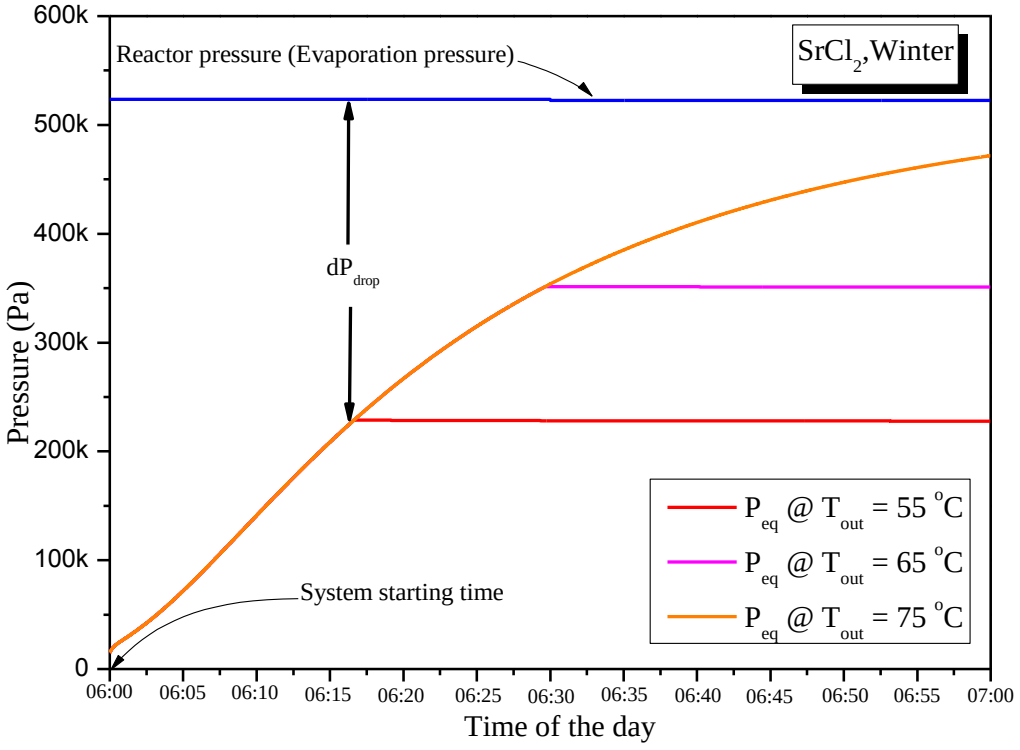

(a)

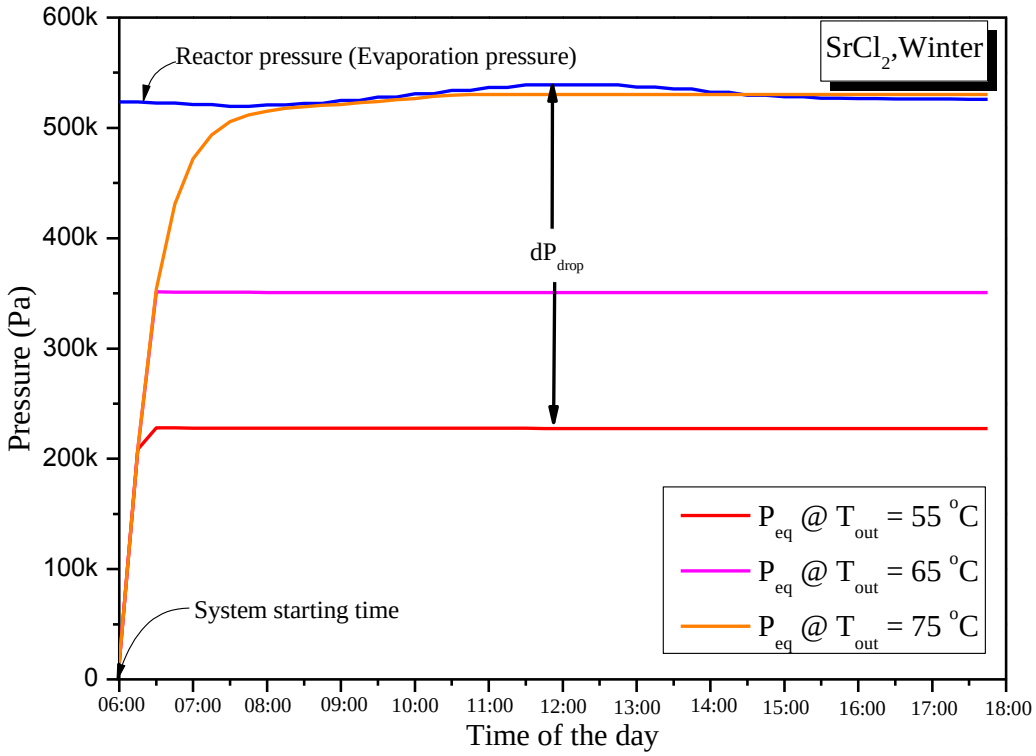

(b)

Fig. 5.24 *The reactor pressure and the salt equilibrium pressures of the $SrCl_2$-EG reactor containing 0.18kg of salt in a cloudy winter day at Newcastle upon Tyne when operated with different level of output temperature; (a) at the first one hour of the reaction, (b) the entire day.*

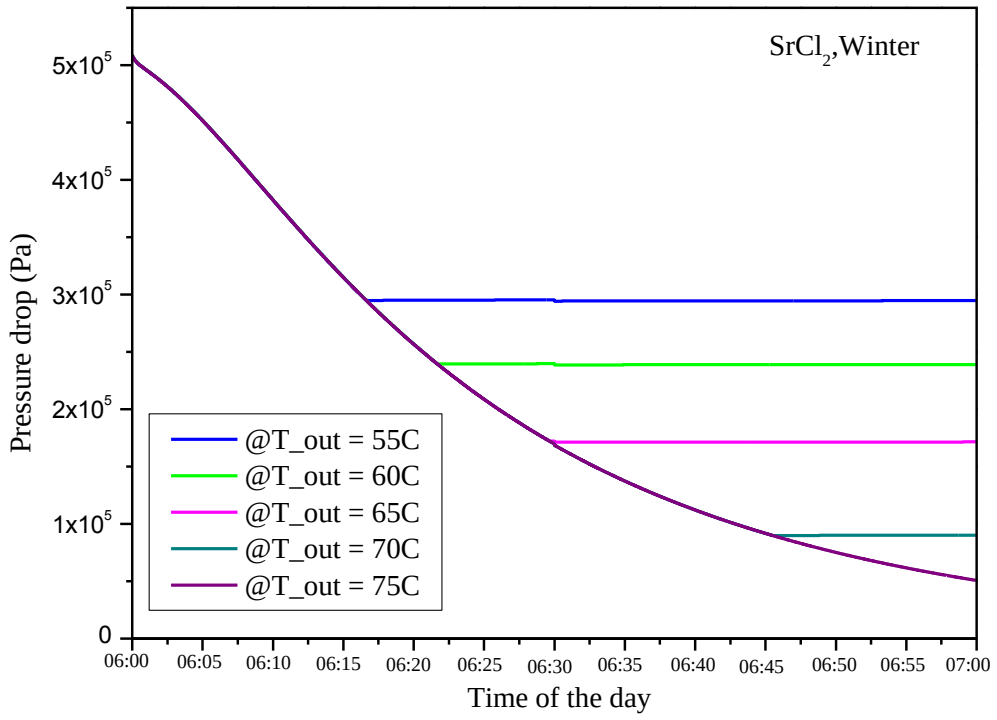

(a)

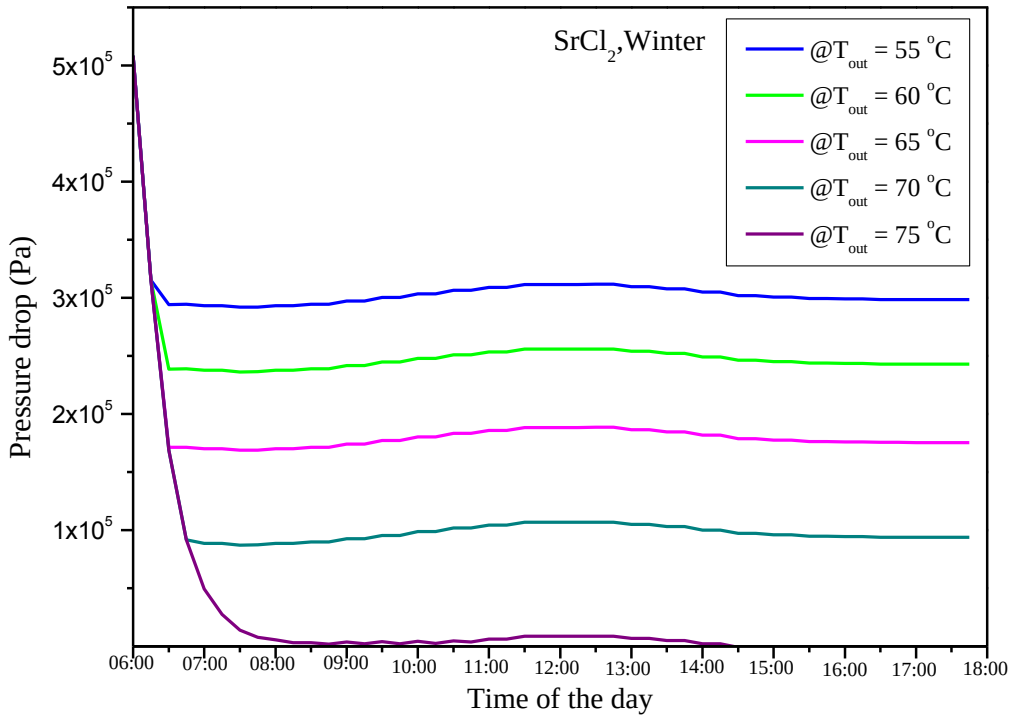

(b)

Fig. 5.25 *The pressure drops of the $SrCl_2$-EG reactor containing 0.18kg of salt in a cloudy winter day at Newcastle upon Tyne when operated with different level of output temperature; (a) at the first one hour of the reaction, (b) the entire day.*

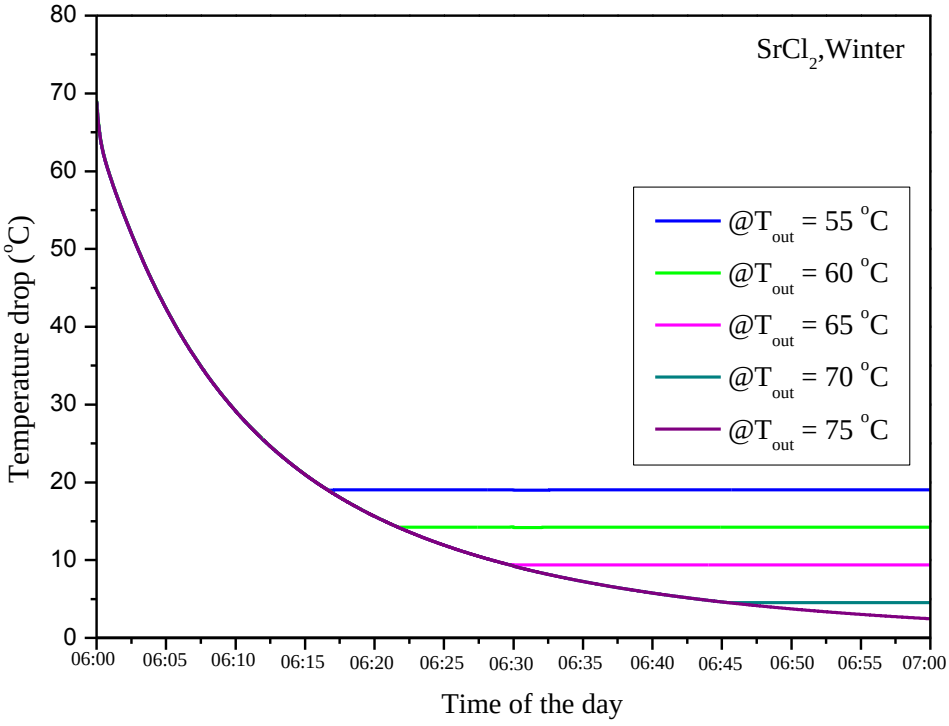

(a)

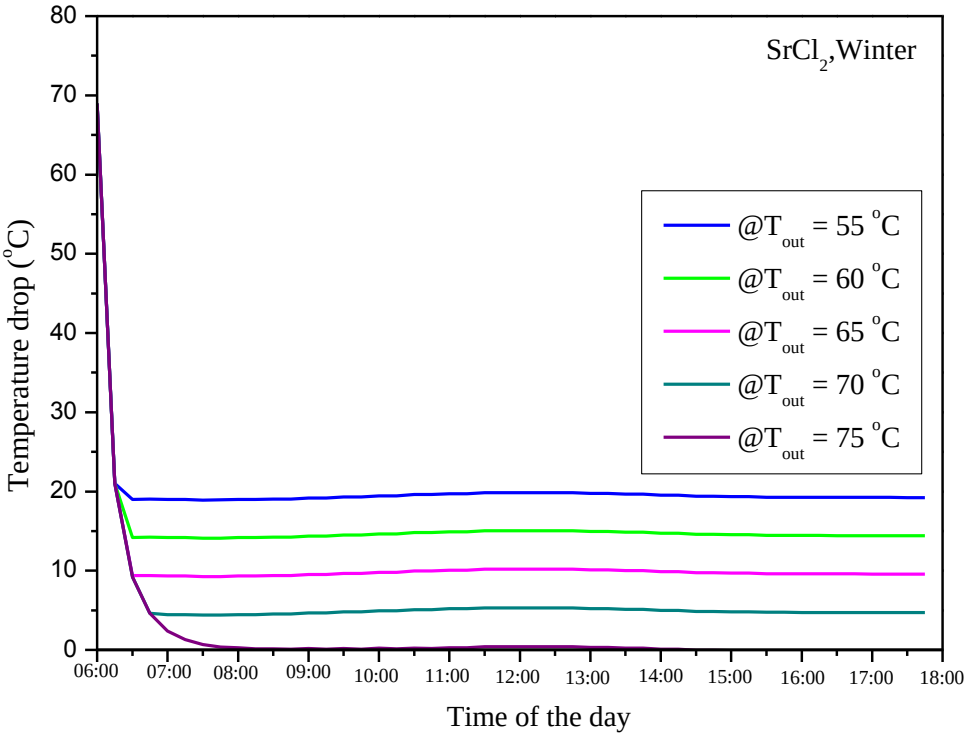

(b)

Fig. 5.26 *The temperature drops of the $SrCl_2$-EG reactor containing 0.18kg of salt in a cloudy winter day at Newcastle upon Tyne when operated with different level of output temperature; (a) at the first one hour of the reaction, (b) the entire day.*

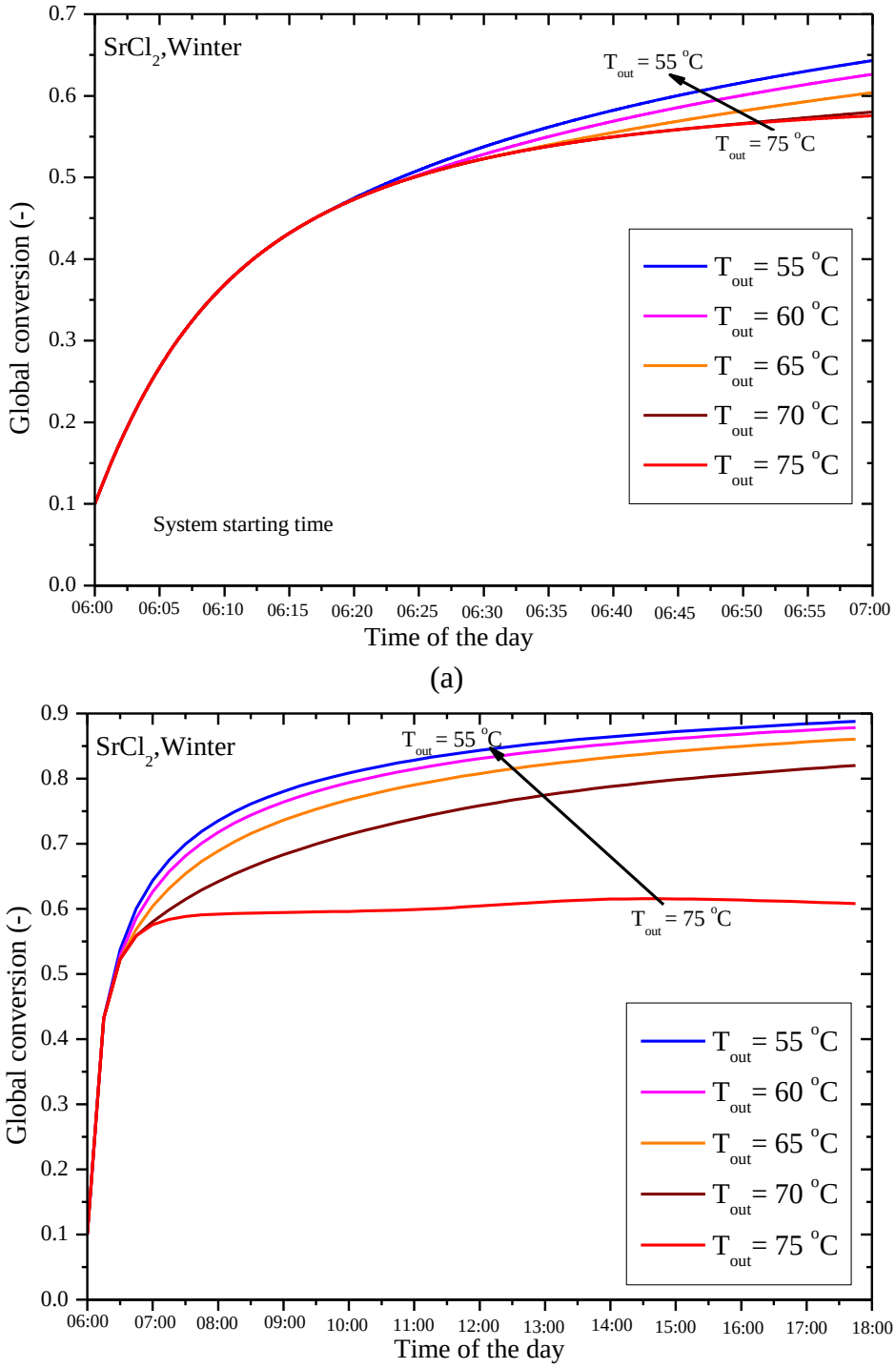

Fig. 5.27 *The adsorption global conversion of the $SrCl_2$-EG reactor containing 0.18kg of salt in a cloudy winter day at Newcastle upon Tyne when operated with different level of output temperature; (a) at the first one hour of the reaction, (b) the entire day.*

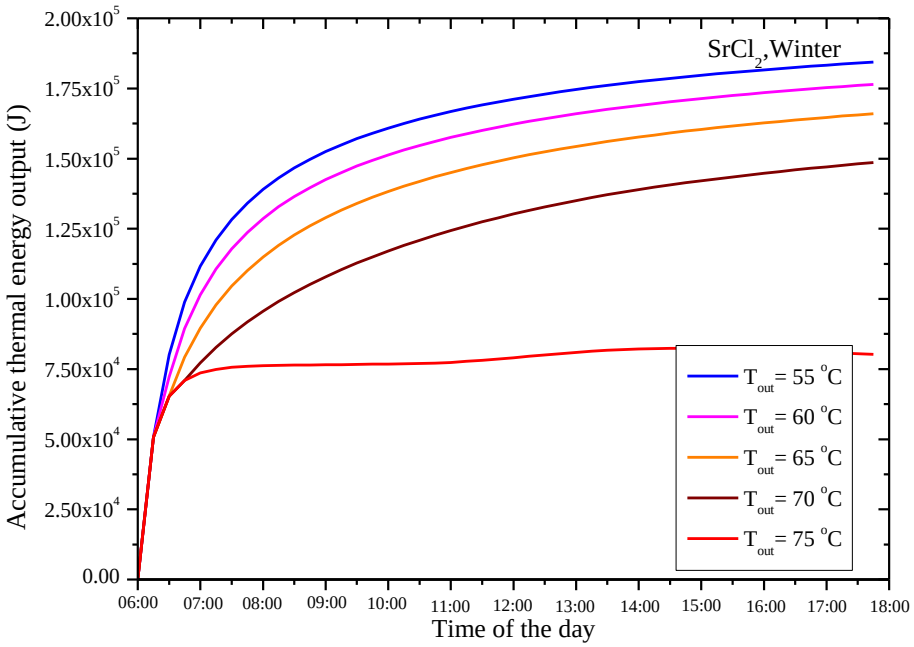

Fig. 5.28 *The accumulative useful thermal energy output of the $SrCl_2$-EG reactor containing 0.18kg of salt in a cloudy winter day at Newcastle upon Tyne when operated with different level of output temperature.*

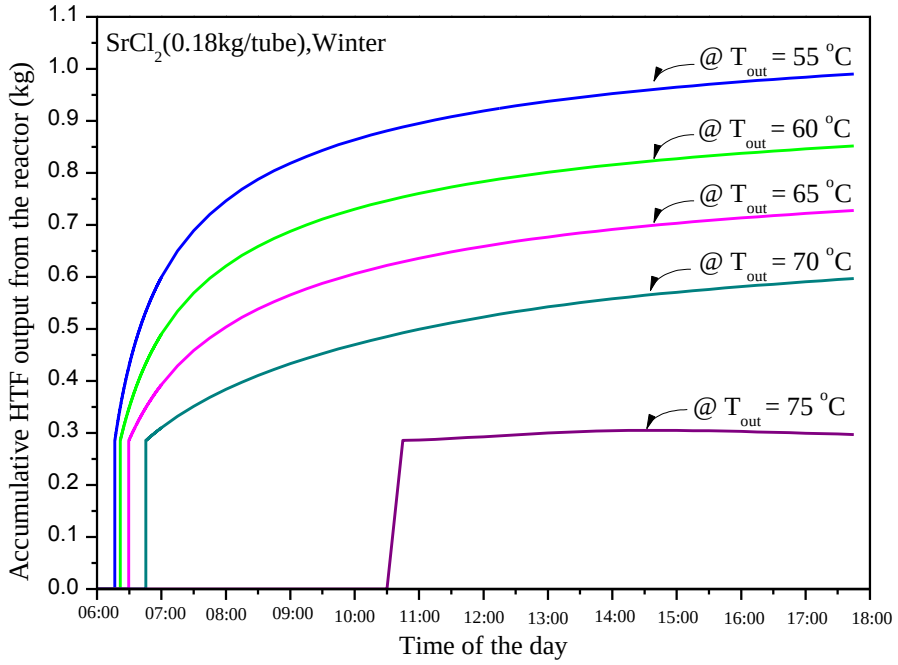

Fig. 5.29 *The accumulative HTF mass output from the $SrCl_2$-EG reactor containing 0.18kg of salt in a cloudy winter day at Newcastle upon Tyne when operated with different level of output temperature.*

5.4.3 The overall performance of the water-jacket reactor using $SrCl_2$ as a reactive adsorbent

Considering the desorption results at the final time by varying different parameters in three different seasons, the results of the summer, spring and autumn sunny days using 30 m^2 of PV/T installation area with $SrCl_2$-EG adsorbent are presented in Table 5.4, Table 5.5 and Table 5.6 respectively. Statistical data of Newcastle weather suggests that there are only around 9 sunny days per month in the summer, and 7-10 sunny days per month in spring and autumn; for the rest of the time, there would be barely recoverable solar energy. Therefore, this thesis assumed that there was only 9-day-per-month availability of solar energy in three seasons (from March to October). Consequently, the yearly performance for the charging period during three seasons can be concluded in Table 5.7.

The results suggest that if there is no compressor to assist the desorption, the higher the HTF output temperature from the PV/T (T_{PVT}), the more thermal energy stored in the thermochemical storage system. Moreover, depending on the ambient temperature, if the T_{PVT} is too low with insufficient help of the compressor, there may not be thermal energy stored in the storage as seen in the case of CR = 1 in summer presented in Table 5.4. If the compressor is used, the higher the CR, the more thermal energy stored in the thermochemical storage system regardless of the T_{PVT}. However, at each CR, there will be an optimum T_{PVT} that provide maximum thermal energy stored which was discussed in Chapter 4.

Based on the 12.3 GJ of heating demand in a typical household in Newcastle, without the facilitation of the compressor, the thermochemical sorption energy storage may not be able to store sufficient energy for the 100% solar fraction of the mentioned demand. With the compressor assisted thermochemical sorption energy storage, the integrated system can supply 100% solar fraction for the winter heating demands, including the domestic hot water and the space heating demands when the CR of at least 12 is used with the HTF temperature of 85 ^oC or with the CR of at least 16 when the HTF temperature is at 90 ^oC. Although there may be many possible ways to supply the heating demand with 100% solar fraction, the case with the lowest CR with the lowest T_{PVT} is preferred because the electrical energy consumption of the compressor is going to be lower with the case of lower CR and the life cycle of the PV cell is going to be longer with the case of lower $T_{PVT.}$

Future work should be studied in detail with the optimum parameters on each operating day. In this thesis, the conclusion is based on the operational conditions which are used as fixed parameters throughout the year. Therefore, future work may provide the optimum operating

point on each day which is promising in giving better performance than the study in this thesis. In the end, even though the results in this thesis are not from the mentioned improved study, they still show the potential of using the integrated system of the PV/T with the thermochemical energy storage with the assistance of the compressor to supply 100% solar fraction of the heating demands.

When the discharging performance is considered, it will be the sensible heat consumed by the thermal mass of the reactor in winter, leading to energy loss in the energy-releasing time and the discharging efficiency is presented in Table 5.8. The results showed as expected that when the temperature output is high, the discharging efficiency is low. Moreover, As the charging performance in Table 5.7 suggested that by using the CR of at least 12 with the HTF temperature of 85 ^{o}C, 100% solar fraction can be achieved. However, with the discharging performance taken into account, only 70% solar fraction can be obtained due to the mentioned sensible thermal mass of the reactor and, more importantly, part of the reactive salt does not adsorb the ammonia gas to the fully adsorbed state (only around 0.9 of global conversion can be achieved) because of the sorption saturation characteristic. Nevertheless, as mentioned before, trying to operate the integrated system at optimum points in every operation day may be possible to provide 100% solar fraction for the heating demand in Newcastle upon Tyne.

5.5 Summary

In this chapter, the kinetic performances of the compressor-assisted thermochemical energy storage were analysed by using the water-jacket type reactor. The desorption and adsorption kinetic reaction rates' equations from Huang *et al.* (2004) were used and validated against the experimental data from Yuan *et al.* (2018) to obtain the kinetic parameters which are the Arrhenius term, the reaction pseudo-order and the activation energy. The validated desorption model of the reactor was used to simulate the desorption process during charging seasons (spring, summer and autumn) with the starting reaction time at the sunset until the next morning by using different compression ratio (from CR = 1 to 16).

The results show that NH_3 tends to be desorbed at a slightly higher percentage when operating at low compression ratio because of high operating temperature. However, significant increasing of storable thermal energy could be achieved when high compression ratio was applied. For example, only 10.27 kWh/day of a summer sunny day could be stored when no compressor assistance, compared to the storable thermal energy of 72.39 kWh/day when CR = 16 if the PV/T is operated at its optimum temperature at each CR. Operating the storage system

at high CR also promotes high storage efficiency because of its lower operating temperature, leading to low thermal mass consumption and heat loss of the reactor. For example, 94.30% of charging efficiency could be obtained when CR =16 compared to only 77.80% when no compressor is used. For the adsorption process in the discharging period in winter, the results suggest that operating the adsorption process at its lowest temperature is preferred for the high-efficiency system. However, for the DHW application, 60 ^{o}C should be maintained to avoid bacteria growth. In this case, 76.24% of discharging efficiency could be achieved when 60 ^{o}C of HTF was output from the reactor.

Combining the full cycle analysis of the integrated system with the kinetic performances taking into account, $SrCl_2$ reactor could support 73.87% of a typical domestic household annual thermal energy demands when the compression ratio of 16 is applied. It means that the solar fraction of only 0.7387 was achieved, lower than expected in the previous chapter because of the fact that the reactive salt could not fully react at a limited time of daily operation. Moreover, the thermal mass of the reactor was taken into account in this chapter. Nevertheless, 0.7387 solar fraction is still a promising positive start for this new integrated system and performance is believed to be improved in future work.

Table 5.4 *The performance of the $SrCl_2$-EG reactor containing 0.18kg of salt in a tube integrated with the 30 m^2 PV/T installation area in summer*

Season	T_{PVT} (^oC)	Total HTF from the PV/T (kg/day)	CR (-)	Q_{in} (kJ/tube)	Q_{stored} (kJ/tube)	HTF used (kg/tube)	Salt needed (kg/day)	Reacted salt (%)	Q_{stored} (MJ/day)	Q_{stored} (kWh/day)	$\eta_{storage,\ charging}$ (-)
Summer	95	943.91	1	353.26	274.07	9.53	17.84	92.16	27.16	7.54	0.7758
			4	326.68	280.89	1.92	88.45	94.46	138.03	38.34	0.8598
			8	308.05	277.56	1.35	125.84	93.34	194.05	53.90	0.9010
			12	297.82	275.53	1.15	148.25	92.66	226.92	63.03	0.9252
			16	290.81	274.03	1.03	164.42	92.15	250.31	69.53	0.9423
	90	1050.6	1	354.64	275.29	22.24	8.50	92.58	13.00	3.61	0.7763
			4	324.50	279.04	2.17	87.01	93.84	134.89	37.47	0.8599
			8	307.92	277.48	1.49	127.27	93.31	196.20	54.50	0.9012
			12	297.70	275.49	1.25	151.77	92.64	232.28	64.52	0.9254
			16	290.52	273.86	1.12	169.56	92.09	257.98	71.66	0.9426
	85	1153.1	1	37.66*	0	0.24*	0	0	0	0	0
			4	325.24	279.67	2.53	81.87	94.05	127.20	35.33	0.8599
			8	307.79	277.40	1.65	125.63	93.28	193.60	53.78	0.9012
			12	297.43	275.30	1.36	152.12	92.58	232.67	64.63	0.9256
			16	290.37	273.80	1.21	171.23	92.07	260.46	72.35	0.9429

Season	T_{PVT} (°C)	Total HTF from the PV/T (kg/day)	CR (-)	Q_{in} (kJ/tube)	Q_{stored} (kJ/tube)	HTF used (kg/tube)	Salt needed (kg/day)	Reacted salt (%)	Q_{stored} (MJ/day)	Q_{stored} (kWh/day)	$\eta_{storage,\ charging}$ (-)
Summer @ optimal T_{PVT}	100.00	820.36	1	360.21	280.23	6.22	23.74	94.24	36.96	10.27	0.7780
	95.76	926.53	4	326.01	280.31	1.88	88.66	94.27	138.07	38.35	0.8598
	91.51	1,019.43	8	307.70	277.27	1.44	127.36	93.24	196.18	54.50	0.9011
	88.68	1,077.60	12	297.39	275.22	1.27	152.23	92.55	232.76	64.66	0.9255
	84.44	1,164.89	16	289.99	273.46	1.22	171.53	91.96	260.59	72.39	0.9430

** The sensible heat transfers into the reactor. No reaction because of the salt equilibrium temperature is higher than the HTF temperature*

Table 5.5 *The performance of the $SrCl_2$-EG reactor containing 0.18kg of salt in a tube integrated with the 30 m^2 PV/T installation area in spring*

Season	T_{PVT} (°C)	Total HTF from the PV/T (kg/day)	CR (-)	Q_{in} (kJ/tube)	Q_{stored} (kJ/tube)	HTF used (kg/tube)	Salt needed (kg/day)	Reacted salt (%)	Q_{stored} (MJ/day)	Q_{stored} (kWh/day)	$\eta_{storage,\ charging}$ (-)
Spring	95	540.96	1	362.18	281.84	6.023	16.17	94.78	25.31	7.03	0.7782
			4	333.22	285.38	1.76	55.26	95.97	87.61	24.34	0.8564
			8	315.81	282.82	1.29	75.73	95.11	118.99	33.05	0.8955
			12	306.14	281.12	1.11	87.94	94.54	137.34	38.15	0.9183
			16	299.53	279.87	1.01	96.71	94.12	150.37	41.77	0.9344
	90	608.66	1	363.35	282.84	9.32	11.76	95.12	18.48	5.13	0.7784

Season	T_{PVT} (°C)	Total HTF from the PV/T (kg/day)	CR (-)	Q_{in} (kJ/tube)	Q_{stored} (kJ/tube)	HTF used (kg/tube)	Salt needed (kg/day)	Reacted salt (%)	Q_{stored} (MJ/day)	Q_{stored} (kWh/day)	$\eta_{storage,\ charging}$ (-)
			4	333.26	285.41	1.98	55.28	95.98	87.65	24.35	0.8564
			8	315.68	282.75	1.41	77.98	95.08	122.49	34.02	0.8957
			12	306.03	281.09	1.20	91.48	94.53	142.86	39.68	0.9185
			16	299.28	279.74	1.08	101.24	94.07	157.34	43.71	0.9347
	85	676.97	1	364.90	284.14	20.47	5.95	95.55	9.40	2.61	0.7787
			4	331.61	284.07	2.25	54.16	95.54	85.48	23.75	0.8567
			8	315.62	282.72	1.55	78.66	95.08	123.55	34.32	0.8958
			12	305.83	280.98	1.30	93.48	94.49	145.93	40.54	0.9187
			16	299.14	279.694	1.17	104.13	94.06	161.80	44.95	0.9350
Spring @ optimal T_{PVT}	100.00	468.24	1	368.97	287.43	4.57	18.43	96.66	29.43	8.18	0.7790
	92.49	575.22	4	332.92	285.13	1.86	55.56	95.89	88.01	24.45	0.8565
	84.98	677.26	8	315.40	282.53	1.55	78.73	95.01	123.57	34.33	0.8958
	74.46	848.29	12	305.38	280.68	1.60	95.26	94.39	148.54	41.26	0.9191
	60.94	1,193.30	16	298.22	279.13	1.92	111.58	93.87	173.04	48.07	0.9360

Table 5.6 *The performance of the $SrCl_2$-EG reactor containing 0.18kg of salt in a tube integrated with the 30 m^2 PV/T installation area in autumn*

Season	T_{PVT} (^oC)	Total HTF from the PV/T (kg/day)	CR (-)	Q_{in} (kJ/tube)	Q_{stored} (kJ/tube)	HTF used (kg/tube)	Salt needed (kg/day)	Reacted salt (%)	Q_{stored} (MJ/day)	Q_{stored} (kWh/day)	$\eta_{storage,\ charging}$ (-)
Autumn	95	613.56	1	371.21	290.12	10.69	10.33	97.56	16.66	4.63	0.7816
			4	331.47	285.97	1.96	56.22	96.17	89.32	24.81	0.8627
			8	314.26	283.97	1.39	79.74	95.49	125.79	34.94	0.9036
			12	304.47	282.40	1.18	93.82	94.97	147.20	40.89	0.9275
			16	297.76	281.21	1.06	103.96	94.57	162.41	45.11	0.9444
	90	691.67	1	358.99	280.18	24.98	4.98	94.22	7.76	2.15	0.7805
			4	331.55	286.03	2.24	55.49	96.19	88.17	24.491	0.8627
			8	314.16	283.92	1.52	81.62	95.48	128.74	35.76	0.9037
			12	304.28	282.30	1.28	97.27	94.93	152.56	42.38	0.9277
			16	297.55	281.11	1.15	108.52	94.53	169.47	47.08	0.9448
	85	767.90	1	37.37*	0	0.24*	0	0	0	0	0
			4	330.19	284.95	2.60	53.15	95.83	84.14	23.37	0.8630
			8	314.06	283.86	1.70	81.43	95.46	128.42	35.67	0.9039
			12	304.19	282.28	1.40	98.51	94.93	154.49	42.91	0.9280
			16	297.33	281.00	1.25	110.84	94.50	173.03	48.06	0.9451

Season	T_{PVT} (°C)	Total HTF from the PV/T (kg/day)	CR (-)	Q_{in} (kJ/tube)	Q_{stored} (kJ/tube)	HTF used (kg/tube)	Salt needed (kg/day)	Reacted salt (%)	Q_{stored} (MJ/day)	Q_{stored} (kWh/day)	$\eta_{storage,\ charging}$ (-)
Autumn @ optimal T_{PVT}	100.00	524.33	1	364.13	284.62	6.46	14.60	95.72	23.09	6.41	0.7816
	94.30	624.96	4	331.52	286.00	2.00	56.26	96.18	89.39	24.83	0.8627
	88.61	712.66	8	313.93	283.73	1.57	81.79	95.42	128.93	35.81	0.9038
	82.91	801.42	12	303.92	282.06	1.46	98.76	94.85	154.76	42.99	0.9281
	60.12	1,438.71	16	296.40	280.44	2.21	117.33	94.31	182.79	50.78	0.9461

** The sensible heat transfers into the reactor. No reaction because of the salt equilibrium temperature is higher than the HTF temperature*

Table 5.7 *The annual performance of the $SrCl_2$-EG reactor (Adsorbent density = 450 kg/m3) at charging period (spring, summer and autumn)*

Winter heating demand	T_{PVT} (°C)	CR (-)	Q_{stored} (GJ)	Q_{stored} (MWh)	Salt needed (kg)	Desorbed salt (%)	Adsorbent mass required (kg)	Adsorbent volume (m^3)	Energy density (kWh/m^3)	$\eta_{storage,\ charging}$ (-)	Solar fraction @ charging (-)
12.3 GJ or 3.416 MWh	95	1	1.6221	0.4505	1,036.62	95.17	1,382.16	3.07	146.66	0.7789	0.1319
		4	7.2617	2.0172	4,602.06	95.67	6,136.08	13.64	147.93	0.8596	0.5904
		8	10.1020	2.8059	6,462.81	94.81	8,617.08	19.15	146.53	0.8999	0.8213
		12	11.7671	3.2686	7,576.02	94.23	10,101.36	22.45	145.61	0.9235	0.9567
		16	12.9506	3.5973	8,377.65	93.80	11,170.20	24.82	144.92	0.9401	1.0529

Winter heating demand	T_{PVT} (^oC)	CR (-)	Q_{stored} (GJ)	Q_{stored} (MWh)	Salt needed (kg)	Desorbed salt (%)	Adsorbent mass required (kg)	Adsorbent volume (m^3)	Energy density (kWh/m^3)	$\eta_{storage, charging}$ (-)	Solar fraction @ charging (-)
	90	1	0.9425	0.2615	604.98	94.15	806.64	1.79	145.91	0.7787	0.0766
		4	7.1752	1.9932	4,556.97	95.52	6,075.96	13.50	147.62	0.8596	0.5834
		8	10.3148	2.8651	6,600.06	94.79	8,800.08	19.56	146.51	0.9001	0.8386
		12	12.1574	3.3770	7,828.11	94.21	10,437.48	23.19	145.60	0.9237	0.9884
		16	13.4675	3.7412	8,715.60	93.75	11,620.8	25.82	144.87	0.9405	1.0949
	85	1	0.2538	0.0705	160.65	35.83	214.20	0.48	148.05	0.2920	0.0206
		4	6.8693	1.9082	4,371.03	95.28	5,828.04	12.95	147.34	0.8599	0.5585
		8	10.2880	2.8578	6,583.77	94.77	8,778.36	19.51	146.50	0.9002	0.8364
		12	12.2994	3.4165	7,921.89	94.18	10,562.52	23.47	145.55	0.9239	1.0000
		16	13.7287	3.8136	8,886.33	93.73	11,848.44	26.33	144.84	0.9408	1.1162
	At optimum temperature of each season and CR	1	2.0834	0.5787	1,319.25	95.40	1,759.00	3.91	148.05	0.7795	0.1694
		4	7.2750	2.0207	4,614.98	95.25	6,153.30	13.67	147.79	0.8597	0.5915
		8	10.3488	2.8747	6,626.50	94.34	8,835.34	19.63	146.41	0.9003	0.8414
		12	12.3788	3.4386	7,978.70	93.71	10,638.26	23.64	145.45	0.9243	1.0064
		16	14.2979	3.9717	9,268.05	93.18	12,357.40	27.46	144.63	0.9418	1.1624

Table 5.8 *The annual performance of the $SrCl_2$-EG reactor at the discharging period (winter) with the initial global conversion of 0.1 and the full cycle performance*

@ Charging period			@ Discharging period				Full cycle performance				
T_{PVT} (^oC)	CR (-)	Q_{stored} (MWh)	T_{out} (^oC)	Adsorbed salt* (%)	$\eta_{storage,discharging}$ (-)	Q_{out} (MWh)	Storage volume (m^3)	Reactive salt** (% mass)	$\eta_{storage,total}$ (%)	Solar fraction (%)	Energy density (kWh/m^3)
95	1	0.4505	60	86.49%	0.7624	0.2823	3.07	77.84%	59.38%	8.26%	91.91
			65	86.49%	0.7624	1.2533	3.07	76.08%	57.16%	7.77%	86.47
			70	84.54%	0.7338	1.1791	3.07	72.03%	54.06%	6.96%	77.42
	4	2.0172	60	80.03%	0.6940	1.0557	13.64	77.84%	65.54%	36.68%	91.91
			65	86.49%	0.7624	1.7600	13.64	76.08%	63.08%	34.51%	86.47
			70	84.54%	0.7338	1.6559	13.64	72.03%	59.66%	30.90%	77.42
	8	2.8059	60	80.03%	0.6940	1.4825	19.15	77.84%	68.61%	51.51%	91.91
			65	86.49%	0.7624	2.0632	19.15	76.08%	66.04%	48.46%	86.47
			70	84.54%	0.7338	1.9411	19.15	72.03%	62.46%	43.39%	77.42
	12	3.2686	60	80.03%	0.6940	1.7379	22.45	77.84%	70.41%	60.39%	91.91
			65	86.49%	0.7624	2.2815	22.45	76.08%	67.77%	56.81%	86.47
			70	84.54%	0.7338	2.1465	22.45	72.03%	64.09%	50.86%	77.42

@ Charging period			@ Discharging period				Full cycle performance				
T_{PVT} (^oC)	CR (-)	Q_{stored} (MWh)	T_{out} (^oC)	Adsorbed salt* (%)	$\eta_{storage,discharging}$ (-)	Q_{out} (MWh)	Storage volume (m^3)	Reactive salt** (% mass)	$\eta_{storage,total}$ (%)	Solar fraction (%)	Energy density (kWh/m^3)
	16	3.5973	60	80.03%	0.6940	1.9217	24.82	77.84%	71.67%	66.78%	91.91
			65	86.49%	0.7624	0.1648	24.82	76.08%	68.99%	62.82%	86.47
			70	84.54%	0.7338	0.1550	24.82	72.03%	65.25%	56.25%	77.42
90	1	0.2615	60	80.03%	0.6940	0.1388	1.79	77.84%	59.36%	4.82%	91.91
			65	86.49%	0.7624	1.2410	1.79	76.08%	57.14%	4.54%	86.47
			70	84.54%	0.7338	1.1676	1.79	72.03%	54.04%	4.06%	77.42
	4	1.9932	60	80.03%	0.6940	1.0453	13.50	77.84%	65.54%	36.32%	91.91
			65	86.49%	0.7624	1.7974	13.50	76.08%	63.08%	34.17%	86.47
			70	84.54%	0.7338	1.6910	13.50	72.03%	59.66%	30.59%	77.42
	8	2.8651	60	80.03%	0.6940	1.5140	19.56	77.84%	68.62%	52.61%	91.91
			65	86.49%	0.7624	2.1318	19.56	76.08%	66.05%	49.49%	86.47
			70	84.54%	0.7338	2.0057	19.56	72.03%	62.47%	44.31%	77.42
	12	3.3770	60	80.03%	0.6940	1.7957	23.19	77.84%	70.42%	62.40%	91.91

@ Charging period			@ Discharging period				Full cycle performance				
T_{PVT} (^oC)	CR (-)	Q_{stored} (MWh)	T_{out} (^oC)	Adsorbed salt* (%)	$\eta_{storage,discharging}$ (-)	Q_{out} (MWh)	Storage volume (m^3)	Reactive salt** (% mass)	$\eta_{storage,total}$ (%)	Solar fraction (%)	Energy density (kWh/m^3)
			65	86.49%	0.7624	2.3735	23.19	76.08%	67.78%	58.70%	86.47
			70	84.54%	0.7338	2.2330	23.19	72.03%	64.10%	52.56%	77.42
	16	3.7412	60	80.03%	0.6940	1.9993	25.82	77.84%	71.70%	69.47%	91.91
			65	86.49%	0.7623	0.0438	25.82	76.08%	69.01%	65.36%	86.47
			70	84.54%	0.7338	0.0412	25.82	72.03%	65.27%	58.51%	77.42
85	1	0.0705	60	80.03%	0.6940	0.0369	0.476	77.84%	22.26%	1.28%	91.91
			65	86.49%	0.7624	1.1904	0.476	76.08%	21.43%	1.20%	86.47
			70	84.54%	0.7338	1.1199	0.476	72.03%	20.27%	1.08%	77.42
	4	1.9082	60	80.03%	0.6940	1.0027	12.9512	77.84%	65.56%	34.84%	91.91
			65	86.49%	0.7624	1.7930	12.9512	76.08%	63.10%	32.78%	86.47
			70	84.54%	0.7338	1.6868	12.9512	72.03%	59.68%	29.35%	77.42
	8	2.8578	60	80.03%	0.6940	1.5102	19.5075	77.84%	68.63%	52.48%	91.91
			65	86.49%	0.7624	2.1574	19.5075	76.08%	66.06%	49.37%	86.47

@ Charging period			@ Discharging period				Full cycle performance				
T_{PVT} (^oC)	CR (-)	Q_{stored} (MWh)	T_{out} (^oC)	Adsorbed salt* (%)	$\eta_{storage,discharging}$ (-)	Q_{out} (MWh)	Storage volume (m^3)	Reactive salt** (% mass)	$\eta_{storage,total}$ (%)	Solar fraction (%)	Energy density (kWh/m^3)
			70	84.54%	0.7338	2.0297	19.5075	72.03%	62.47%	44.20%	77.42
	12	3.4165	60	80.03%	0.6940	1.8172	23.4723	77.84%	70.44%	63.14%	91.91
			65	86.49%	0.7624	2.4200	23.47227	76.08%	67.80%	59.41%	86.47
			70	84.54%	0.7338	2.2768	23.47227	72.03%	64.12%	53.19%	77.42
	16	3.8136	60	80.03%	0.6940	2.0384	26.33	77.84%	71.72%	70.83%	91.91
			65	86.49%	0.7624	1.2533		76.08%	69.04%	66.64%	86.47
			70	84.54%	0.7338	1.1791		72.03%	65.29%	59.66%	77.42
Optimums	1	0.5787	60	86.49%	0.7624	0.3593	3.91	77.84%	59.43%	10.52%	91.91
			65	84.54%	0.7338	0.3380		76.08%	57.20%	9.89%	86.47
			70	80.03%	0.6940	0.3026		72.03%	54.10%	8.86%	77.42
	4	2.0207	60	86.49%	0.7624	1.2568	13.67	77.84%	65.54%	36.78%	91.91
			65	84.54%	0.7338	1.1824		76.08%	63.08%	34.61%	86.47
			70	80.03%	0.6940	1.0586		72.03%	59.66%	30.98%	77.42

@ Charging period			@ Discharging period				Full cycle performance				
T_{PVT} (^oC)	CR (-)	Q_{stored} (MWh)	T_{out} (^oC)	Adsorbed salt* (%)	$\eta_{storage,discharging}$ (-)	Q_{out} (MWh)	Storage volume (m^3)	Reactive salt** (% mass)	$\eta_{storage,total}$ (%)	Solar fraction (%)	Energy density (kWh/m^3)
	8	2.8747	60	86.49%	0.7624	1.8046	19.63	77.84%	68.64%	52.82%	91.91
			65	84.54%	0.7338	1.6978		76.08%	66.07%	49.69%	86.47
			70	80.03%	0.6940	1.5200		72.03%	62.48%	44.49%	77.42
	12	3.4386	60	86.49%	0.7624	2.1729	23.64	77.84%	70.47%	63.60%	91.91
			65	84.54%	0.7338	2.0442		76.08%	67.83%	59.83%	86.47
			70	80.03%	0.6940	1.8302		72.03%	64.15%	53.57%	77.42
	16	3.9717	60	86.49%	0.7624	2.5240	27.46	77.84%	71.80%	**73.87%**	91.91
			65	84.54%	0.7338	2.3746		76.08%	69.11%	**69.50%**	86.47
			70	80.03%	0.6940	2.1260		72.03%	65.36%	**62.22%**	77.42

* Calculated based on the 90% desorbed part of the salt mass in the reactor (Initial global conversion of 0.1)

** Calculated based on the total content of salt mass in the reactor

(This page intentionally left blank)

Chapter 6: Conclusions and discussions

The thesis starts with the introduction with the main purpose is to emphasise that fossil fuels, the main sources of primary energy in the world, are causing global warming with several negative consequences. Solar energy has long been being attracted by researchers to utilise it for replacing the fossil fuels due to its high potential of energy input to the earth surface. However, solar energy shares an extremely low amount in the world energy consumption because of its daily and seasonal intermittent property, especially in high latitude regions, regardless of its potential. It leads to the motivation of this thesis to study the feasibility of increasing the solar fraction in a typical household in a high latitude region, using Newcastle upon Type as a case study. A typical household in the UK consumes mainly the thermal energy for domestic hot water and space heating; therefore, chapter 2 of this thesis focuses on reviewing technologies to annually contribute the heating demands in a typical UK household.

The literature review chapter (chapter 2) reveals that the Photovoltaic/thermal (PV/T) collector is a promising solar conversion technology for a residential sector because of its flexibility to produce both electrical and thermal energy simultaneously, resulting in high total conversion efficiency. Because of the seasonal variation of the solar energy, long-term thermal energy storage is required (4-6 months storage) to move the excessive solar energy (high solar energy input with low energy demand) in summer to use in high thermal energy demand time in winter when there is very limited solar energy. The literature reviews showed that thermochemical sorption energy storage is a promising long-term thermal energy storage due to its high energy density, a minimal loss for long-term storage, environmentally friendly storage materials and availability of materials to work with the temperature range from the PV/T technology. Although there are a number of researches in both mention technologies, chapter 2 found that the integration of these two technologies is rarely researched which leads to the study of the solar conversion technologies, the thermochemical sorption energy storage and the novel study of the integration between the two technologies with the detail methods and performances summarised in the following sections.

6.1 The PV, PV/T and solar thermal collectors' summary

This thesis numerically demonstrated the feasibility of the hybrid solar photovoltaic-thermal collector for domestic hot water application and the integration with thermochemical sorption system for seasonal energy storage. Instead of using the simplified model of electrical

power generation in majority of research works on the PV/T collectors, a detailed model based on the one-diode model and the modified equations of R_{SH} and R_S were developed to couple with a CFD model for performance prediction of both thermal power and electrical power generation under various operating conditions.

The model validation suggests that the modified equations of R_{SH} and R_S proposed in this work as a function of irradiance and cell's temperature can improve the simulation accuracy under a wider range of operating conditions, especially for the cases with high PV cell temperature, compared to that resulted from assuming constant internal series resistances. The average error of the electrical power outputs at MPP can be considerably decreased from 3.57% to 0.85% for Siemens SM46 PV module operating at 60 °C, from 2.40% to 0.83% for Solarex MSX-60 module operating at 75 °C. In the meantime, the average error of the PV cell's temperature can be also improved to 0.63%.

Two types of PV/T collectors, with and without air gap, were simulated to see their performances under the high-latitude weather conditions, while the mass flow rate of the water loop was controlled and adjusted to obtain the hot water that leaves the PV/T collector at the targeted temperatures (from 60 to 100 °C) for specific applications. In Newcastle upon Tyne, to achieve the targeted heat output temperature of 60 °C in a sunny summer day based on 1 m^2 PV/T panel, the PV/T-AG collector has to operate at the HTF mass flow rate of lower than 0.175 kg/min and produces 68.18 litre/day/m^2 hot water with a thermal efficiency of around 47%, while the electrical efficiency is 12.03%, which is 0.94% lower than the PV panel. In contrast, the PV/T-no-AG collector produces heat output at no higher than about 43 °C under the same conditions.

Both thermal efficiency and electrical efficiency of the PV/T-AG collector is increased when it operates with lower outlet HTF temperature, because of less heat loss caused by the smaller temperature difference between the PV/T temperature and the ambient air and the positive effect of lower PV cell temperature on the electrical efficiency. The PV/T-AG can produce hot water at 100 °C in sunny summer days with lower total efficiency (44.68%) resulting from the high temperature of the panel leading to high heat loss and low electrical efficiency (9.88%). The comparative results suggest that the air-gap layer has a significant effect to prevent massive heat loss especially in cold climate region where the ambient temperature is low almost all year round.

The application case studies demonstrated that (1) an installation of 7.76 m^2 air-gap PV/T collector can satisfy hot water demand (at 60 °C) of an ordinary single household in the city of Newcastle upon Tyne from March to October; (2) integrated with an installation of 26 m^2 air-gap PV/T collector, the thermochemical sorption system using the working pair of $SrCl_2$-NH_3 can seasonally store and shift the heat load to cover the hot water demand from November to February. Such an integrated system can fully satisfy the hot water demand all year round and half of the annual electricity consumption for a single household. By taking the longevity of the collector into account, further studies on the life cycle analysis for high temperatures operation should be conducted.

6.2 The summary of the Integration of the PV/T collector and the thermochemical energy storage

The PVT with air-gap type was used to generate thermal energy that was seasonally stored in the charging stage to use in winter by using the compressor assisted thermochemical storage. The compressor is electrically supplied by the PVT electrical output or optional import electricity from the grid. The integrated system was studied to be able to contribute heating demand for a typical household in a cold climate region using Newcastle upon Tyne, the UK as a case study. The HTF produced from the PVT was managed in two different schematics to supply the DHW demand in the charging stage. The overall performances of several reactive salts were assessed to determine the most promising reactive salt for the storage system suitable for the PVT thermal qualities.

According to the DHW and SPH temperature constraints, a chosen reactive salts should be able to provide HTF with the temperature of at least 60 ^oC in discharging stage and the desorption temperature in the charging stage should not exceed 100 ^oC to avoid boiling pressure in the PVT system resulting in $CaCl_2$(8/4), NaI(4.5/0), $BaBr_2$(8/4), $SrCl_2$(8/1) and $CaCl_2$(4/2) is viable when no compressor assistance. If the compressor is used at the CR of 16, $SrBr_2$(8/2), $MnCl_2$(6/2) and $CaBr_2$(6/2) can be included in the viable salts list as the compressor assists the salt equilibrium temperatures to be lower than 100 ^oC.

By studying the CR from 1 to 16, with the HTF schematic #1 (HTF from the PVT is sufficiently stored for the DHW before running the excessive amount to the reactor) and the HTF schematic #2 (the entire HTF from the PVT is directly fed to the reactor and the HTF output from the reactor is used to support the DHW), the results show that when low CR is used (~1-9), the HTF schematic #2 provides more net useful energy as well as the storable thermal

energy in the system than the HTF schematic #1. When high CR is used (~9-16), the HTF schematic #1 slightly delivers more net useful energy than the HTF schematic #2; however, the HTF schematic #2 still contribute more storable thermal energy leading to more contribution on the winter solar fraction for the annual performance. As the main aim of this study is to move abundant solar energy in summer to winter, the HTF schematic #2 is preferable regardless of the CR.

Operating the system at higher CR resulting in lower optimum HTF temperature (supplied from the PVT) which may lead to a positive effect on PV-cells life cycle. The optimum HTF temperature varies depending on the weather conditions which the results show that summer has the highest optimum HTF temperature following by autumn and spring respectively. For example, when $SrCl_2$(8/1) is used and CR of 8 is applied, the optimum HTF temperature for maximizing the net useful energy in Newcastle upon Tyne in Summer, Autumn and spring are 86.09, 76.58 and 69.33 ^oC respectively.

When the winter heating demands of a typical household in Newcastle upon Tyne is considered (12.32 GJ), the minimum CR required to supply the winter heating demand with 100% solar fraction for NaI(4.5/0), $CaCl_2$(8/4), $SrCl_2$(8/1) and $BaBr_2$(8/4) are 8.17, 9.44, 11.35 and 14.99 respectively with the electricity supply for the compressor can be covered by the PVT itself except for the $BaBr_2$(8/4) that grid electricity is required to sufficiently assist the 100% solar fraction. Although NaI(4.5/0) has the most preferable optimum working condition (the lowest HTF temperature and CR) which means easy to find the compatible compressor in the market and potentially longer PV-cell life, its raw material cost is much more expensive than $CaCl_2$(8/4) and $SrCl_2$(8/1); moreover, because of its lower energy density, more material and larger storage volume are required resulting in uneconomical material to deploy.

Therefore, the most promising reactive salts to deploy for the integration between PVT and thermochemical seasonal storage are $CaCl_2$(8/4) and $SrCl_2$(8/1). If storage volume in a household is limited, $SrCl_2$(8/1) may be preferable with its required storage material volume of 21.91 m^3 with 87.61% storage efficiency compared to 28.52 m^2 with 82.29% efficiency of $CaCl_2$(8/4). If the CR of a compressor is limited and the budget is more concerned, $CaCl_2$(8/4) is admirable with its minimum CR for 100% solar fraction of 9.44 compared with 11.35 for $SrCl_2$(8/1) and the material price of $CaCl_2$(8/4) is around 6 times less than $SrCl_2$(8/1). The two competitive salts $CaCl_2$(8/4) and $SrCl_2$(8/1) meet the requirement to produce the winter temperature of the HTF at 66.54 and 74.33 ^oC respectively, more than 60 ^oC for heating applications. If the compressor is able to work at CR of 16, the installed PVT area can be

reduced to meet the 100% winter fraction, however, the grid electricity may be required in the charging stage as less PVT area produces less electricity to supply the compressor.

6.3 Summary of the kinetic performances of the $SrCl_2$ water-jacket reactor

The water-jacket reactor models were developed by using $SrCl_2$-EG as the composite adsorbent. The adsorption and desorption kinetic equations from Huang *et al.* (2004) were used in the models. Validations were performed by using the experiments from Yuan *et al.* (2018) with the salt:EG mass ratio of 2:1 and the composite adsorbent density of 300 kg/m^3. The validations suggested that the desorption reaction parameters should have the Arrhenius number of 0.009, the exponential term of 3.06 and the activation energy of 1,421 J/mol and the desorption reaction parameters with the Arrhenius number of 0.125, the exponential term of 1.52 and the activation energy of 14,000 J/mol should be used.

The validated models were used to simulate the reaction kinetic behaviours of the reactor when integrated with the PV/T collector in the charging stage (spring, summer and autumn) using the desorption model and in the discharging stage (winter) using the adsorption model. The desorption process (charging stage) was simulated with the compressor assistance with the compression ratio (CR) ranges from 1 to 16 (CR = 1 means no compressor being used). All the simulation cases were done with the temperature equilibrium drop of 5 ^oC to maintain the reaction. The desorption processes started after sunset of every simulated day to make sure that the HTF from the PV/T was completely collected and stored in the storage hot water tank and to get the advantage of low ambient temperature for the desorption.

The results showed that with higher CRs, the desorption could be activated earlier with faster initial reaction rates. For example, at CR = 8 to 16, the desorption started at less than half a minute after running a 90 ^oC HTF into the reactor while it took more than two minutes in the case of no compressor (CR=1). The desorption rate could go as high as -1.0e-3 when CR = 16 and the rate was less than -1.0e-4 when CR=1 for the first 5 minutes. After 5 minutes, using higher CRs tends to have slower desorption rates; however, due to faster initial rates, the amount of reacted adsorbent is higher (lower global conversion) for the first 1.5 hours. After 1.5 hours of desorption time, the reaction rate incrementally slowed down and did not make considerable changes in global conversion for the cases of the compressor assistance (CR>1). The results suggested that the compressor improves the desorption rate, especially in the first few minutes.

Considering the coefficient of performance (COP) of the desorption at different CRs, with higher CRs, the higher COP was achieved. As the compressor helps to reduce the equilibrium

operating pressure in the reactor, the reactor temperature could be maintained at lower temperatures than the no-compressor case; therefore, the input HTF can be utilised to a greater degree. When the compressor was operated at CR = 16, 12, 8 and 4, the COP of 0.94, 0.93, 0.90 and 0.86 could be achieved respectively, compared to the COP of only 0.78 when the compressor was not used. In summary, the compressor facilitates the desorption processes at lower operating temperatures, leading to the higher COP of the reactor.

For the adsorption process (energy discharging stage) in winter, the compressor is not preferred following the objective of this thesis that the energy discharging stage in winter should be operated without additional energy input. With the initial global conversion of 0.1, the thermal energy releasing from the reactor was carried out by the HTF with the controlled mass flow rate to adjust its output temperature from the reactor. The output temperature ranges from 55 ^{o}C to 75 ^{o}C was performed to explore the performances. The adsorption was set to be stared at 6 AM in the winter morning day expecting that it could generate DHW and SPH heat before a household's members wake up around 7:30 to 8:00 AM. The results showed as expected that if a lower output temperature was targeted, the reactor could output the HTF earlier than when a higher output temperature was set. For example, if output temperature (T_{out}) was set at 55 ^{o}C, the reactor took about 15 minutes to heat up its thermal mass until the HTF reached $T_{out,}$ compared to around 45 minutes in case of T_{out} = 75 ^{o}C.

Considering the reaction rate of the adsorption process, the rate during the thermal mass heat-up period is independent of the T_{out}. After the reactor temperature reached $T_{out,}$ the reaction rate slightly decreased which is the effect of the adjusted mass flow rate to maintain the output temperature at a specific value. With an ambient temperature in winter, the reactor has a related equilibrium temperature (T_{eq}) which is a threshold temperature for the adsorption. In the studied case of Newcastle upon Tyne with the ambient temperature in a winter cloudy day of around 5 ^{o}C to 7 ^{o}C, T_{eq} is about 75 ^{o}C when $SrCl_2$-EG is used as the composite adsorbent. The reactor cannot produce T_{out} that is higher than T_{eq}. With higher T_{out}, the COP is lower as the reaction heat is lost in a greater amount for the thermal mass. For example, when T_{out} was set at 75 ^{o}C, the COP was 0.53 compared to the COP of 0.79 when T_{out} was 55 ^{o}C. In the case of a UK household, the temperature of the DHW is required to keep at higher than 60 ^{o}C, the COP of 0.76 can be achieved from the water-jacket reactor. Moreover, the lower the T_{out} the greater the temperature drop, resulting in higher power output. Therefore, setting the T_{out} as low as possible is preferred for better performances of the reactor, however, with the requirement of the downstream applications taken into consideration.

For the annual performances of the reactor, based on the 12.3 GJ of heating demand in a typical household in Newcastle and the PV/T installation area of 30 m^2, although the charging stage results showed that by using the CR of at least 12 with the HTF temperature of 85 ^oC, 100% solar fraction can be achieved. However, with the discharging performance taken into account, only 70% solar fraction can be obtained due to the sensible thermal mass of the reactor and, more importantly, part of the reactive salt does not adsorb the ammonia gas to the fully adsorbed state (only around 0.9 of global conversion can be achieved) because the reaction rate when the global conversion approaches one is very slow.

6.4 Research contributions

The feasibility study for seasonally storing solar energy for a typical UK's household was revealed. This thesis for the first time contributes the knowledge of how to increase the solar fraction for the annual heating demands of a household located in high latitude regions via the integration of the conversion and storage technologies; the solar photovoltaic/thermal (PV/T) collector integrated with the compressor-assisted thermochemical sorption energy storage (CATSES). The optimal operational points for the PV/T to work with the CATSES were studied along with the criteria of the reactive salt selection to choose the suitable reactive salt to work in high latitude regions. The thesis used Newcastle upon Tyne in the UK, the city in a high latitude region, as a case study and the preliminary results show that there is potential to increase the solar fraction for the energy demand in a residential sector which may promote the bright sustainable energy future for a residential sector.

6.5 Recommendations for future works

Referring back to the solar energy conversion technologies, the monocrystalline silicon PV cell was analysed this thesis because of its availability in the commercial market. However, there are several other types of PV cells which are interesting to be studied such as the perovskite solar cell which is currently focused by researchers. There are very limited (or actually has not been seen from any published article by the author yet) researches in the field that used the perovskite solar cell as a component of the PV/T; thus, it would be a valuable information for the future PV/T technologies to be analysed with different kinds of PV cells.

Considering the composite adsorbent density, this thesis analysed the reactor containing $SrCl_2$-EG of the mass ratio of 4:1 and density of 450 kg/m^3 based on the ability of the author to manually pack the composite adsorbent as shown in Appendix D. However, with proper compressing machine, the adsorbent material can be compressed with a higher density.

Therefore, future works related to finding the optimum packing parameters that work well in different applications may be useful.

Because of the time limitation of the PhD study, in this thesis, there are only eight days of a year were studied and used as representatives of different weather conditions in different seasons of the year. Only sunny and cloudy days were included in the study; therefore, other weather conditions on the days with high intermittency may be further studied to explore a more reliable annual performance. Future work should be studied in detail with the optimum parameters on each operating day so that the optimum operational point on each day will be obtained which is promising in giving the better performance than the study in this thesis as the energy production on other days are going to be included. In the end, even though the results in this thesis are not from the mentioned improved study, they still show the potential of using the integrated system of the PV/T with the thermochemical energy storage with the assistance of the compressor to supply a high solar fraction of the heating demands in a UK typical household.

About the reactor design, this thesis used the water-jacket reactor to see the kinetic performances of the integrated system; however, the finned-tube reactor is suggested to be future work to explore the influence of the reactor design on the storage performance. The finned-tube reactor is expected to have higher heat transfer performances which may lead to a more interesting storage system which is going to influence researchers to pay attention to the long-term solar energy storage for a sustainable world.

Appendix A: Modelling of the PV, PV/T and thermal collector in ANSYS

A.1 Modelling of the PV/T panels in ANSYS Fluent

A.1.1 PV/T panel Geometry Model

Photovoltaic thermal collector (PV/T) can be modelled in ANSYS DesignModeller. The geometries of the PV/T model without airgap (PV/T-no-AG) and the PV/T model with airgap (PV/T-AG) are shown in Fig. A.1, and Fig. A.2 respectively. All models' dimensions are shown in Table A.1. The models mentioned above are cut along the x-axis at the centre of the full models (z=0, on the X-Y plane) and set the boundary at z=0 to be symmetry. The absorber and the fluid tube of the full PVT model are shown in Fig. A.3. At z=49.3 mm, parallel to the X-Y plane, the models were cut along the x-axis and the boundary is set to be periodic as they are the midpoint between two fluid tubes of the full model which the tube geometries are repeated along the z-axis.

Lower airflow is neglected in both PV/T models because the insulator is attached between the absorber and the environment in real PVTs blocking heat to flow between the lower surface of the absorber and environment. Therefore, the lower surface of the absorber can be set as an adiabatic wall in Fluent.

In order to reduce the computational time, ground and sky will not be geometrically modelled but will be treated as source terms in ANSYS FLUENT by the UDFs (user-defined functions) of a source term in the unit of Watt per cubic metre as a function of glass temperatures, sky temperatures, and glass cover material properties according to the volume of surface cell elements participating in radiation.

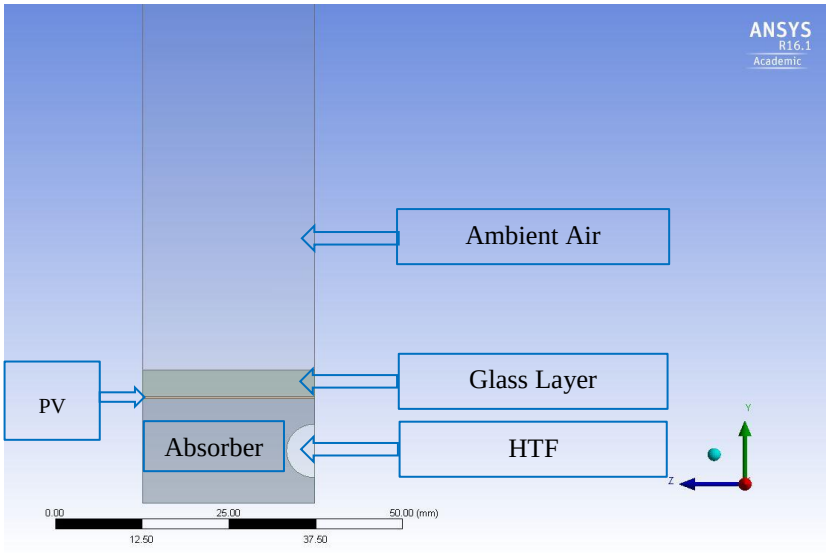

(a)

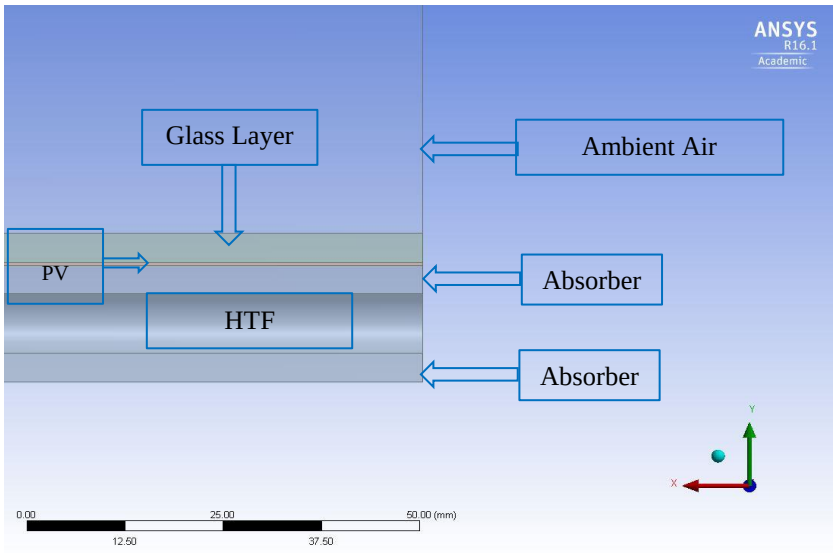

(b)

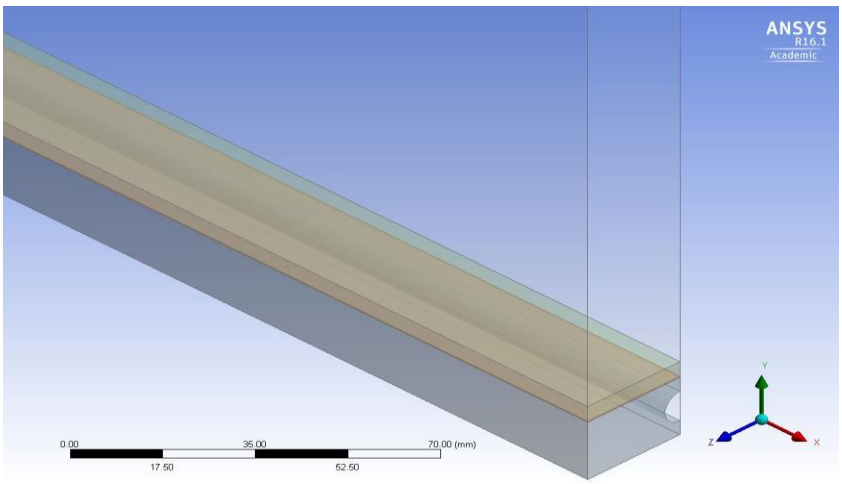

(c)

Fig. A.1 *The PV/T-no-AG model in ANSYS DesignModellor: (a) Cross-sectional view, (b) Longitudinal view, (c) Isometric view*

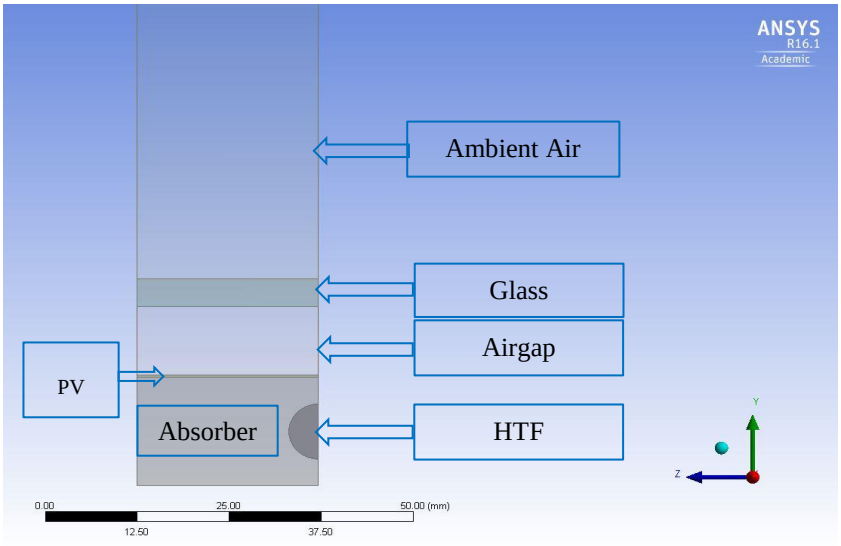

(a)

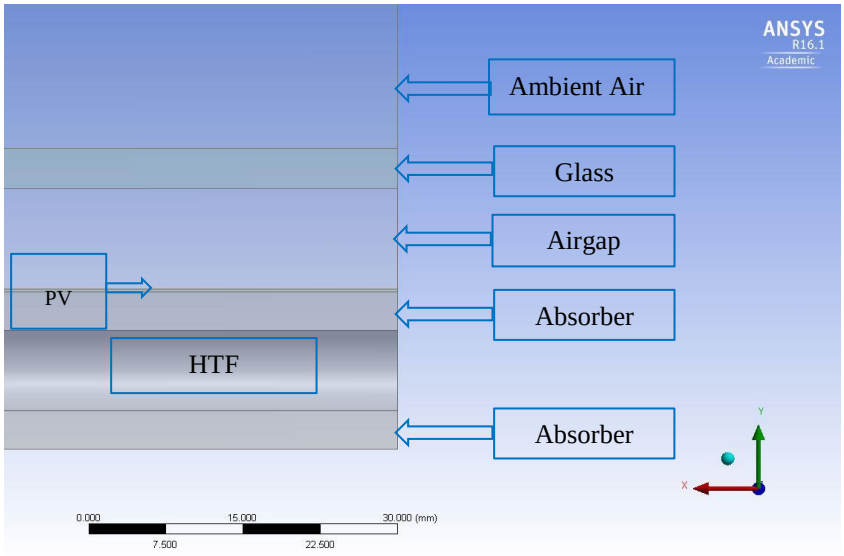

(b)

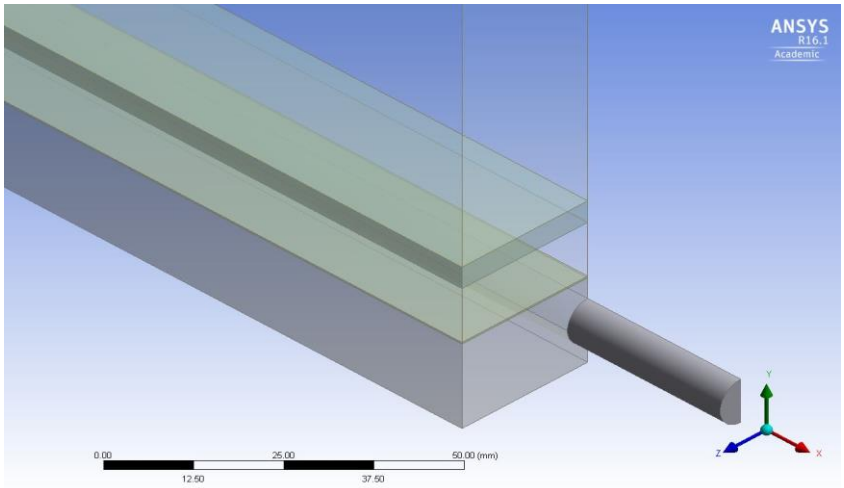

(c)

Fig. A.2 *PV/T-AG model with a fluid tube with airgap in ANSYS DesignModellor: (a) Cross-sectional view, (b) Longitudinal view, (c) Isometric view*

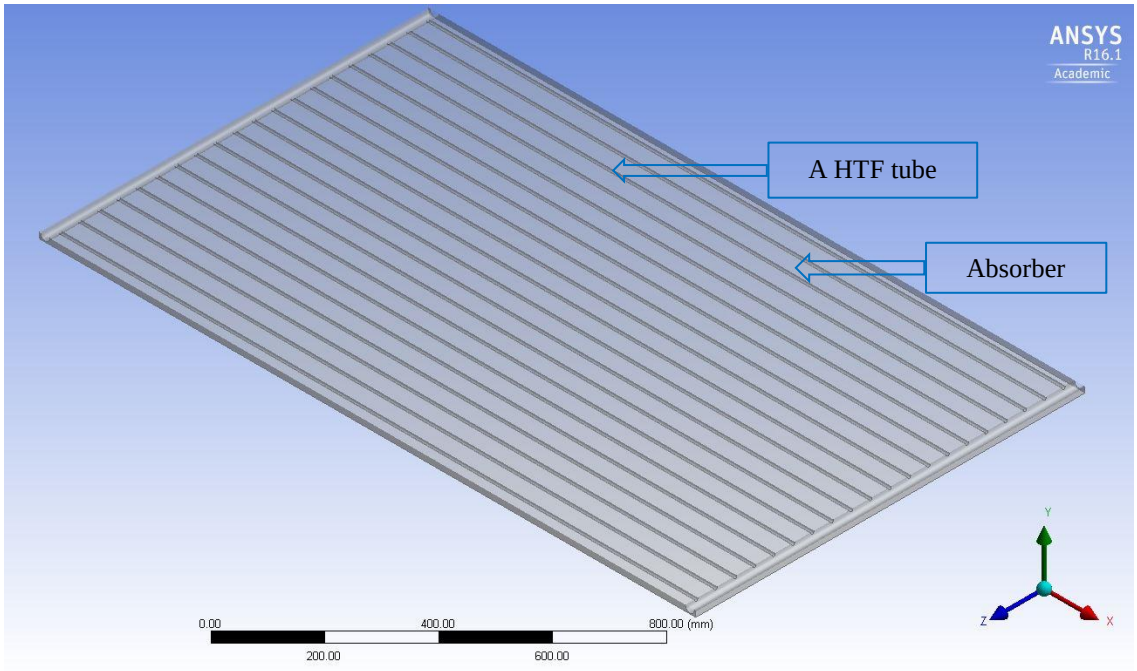

Fig. A.3 *The absorber and the fluid tube section of the full PV/T model in DesignModeller*

Table A.1 *PV/T Models' Dimensions*

	PV/T-no-AG	**PV/T-AG**
Ambient air thickness or Upper air thickness (Y-axis)	300 mm	300 mm
Lower air thickness (Y-axis)	-	-
Glass thickness (Y-axis)	4 mm	4 mm
Air-gap thickness (Y-axis)	-	10 mm
PV layer thickness (Y-axis)	0.3 mm	0.3 mm
Absorber thickness (Y-axis)	15.7 mm	15.7 mm
Fluid tubes' diameter	8 mm	8 mm
All components' length (X-axis)	1830 mm	1830 mm
Cut models' width (Z-axis)	24.65 mm using symmetry analysis	24.65 mm using symmetry analysis
Full model width (Z-axis)	986 mm	986 mm
The length between 2 fluid tubes	49.3 mm	49.3 mm

A.1.2 PV/T models' meshing

After geometry modelling, meshing is done by using ANSYS Meshing to construct small elements in order to computationally solve flow and energy equations for the PV/T models. Three important mesh qualities which are skewness, aspect ratio and orthogonal quality are monitored to be in reasonable ranges to produce good quality meshes for ANSYS Fluent to solve the flow and energy equations accurately.

Skewness is the mesh quality that indicates the perfectness of each cell in terms of the angles. If all angles in one cell are equal, the skewness will be zero which is the best possible quality meshed cell. Skewness quality ranges from zero which is the best to one which is the worst and the qualities of the value between them are present in Table A.2 (ANSYS, 2013). Poor meshed cells can lead to inaccurate or divergent solutions.

Table A.2 *Skewness values relating to the meshed cells' qualities* (ANSYS, 2013)

Skewness	**Quality of meshed cell**
0.98-1	Unacceptable
0.9 – 0.98	Bad
0.75 – 0.9	Poor
0.5 – 0.75	Fair
0.25 – 0.5	Good
>0 – 0.25	Excellent
0	Equilateral

Orthogonal quality spans from one to zero. Unlike skewness, orthogonal quality of one is the best-meshed cell quality and zero is the worst. Orthogonal quality tells whether the surface vector of each cell's face is well aligned with the distant vector from the cell's centroid to the adjacent cell's centroid or not. (ANSYS, 2013) suggests that orthogonal quality should not less than 0.001 and the range is shown in Table A.3.

Table A.3 *Orthogonal quality relating to the meshed cells' qualities* (ANSYS, 2013)

Skewness	**Quality of meshed cell**
0-0.001	Unacceptable
0.001-0.15	Bad
0.15-0.20	Acceptable
0.20-0.70	Good
0.70-0.95	Very good
0.95-1.00	Excellent

Aspect ratio expresses the balance of a cell's sides; for example, in case of the rectangle, it can be calculated from dividing the longer length with the shorter length of the rectangle's sides. It should not exceed 100 to make a good overall mesh quality for most cases. However,

in some specific cases when the exact one direction of the flow field is known, the cells' length along the flow direction can be much longer than the cells' length perpendicular to the flow direction because of the fact that variables' gradients along the flow direction are much less than the perpendicular direction. In those cases, the aspect ratio of more than 100 is acceptable.

By using the mesh qualities described above as a reference, the geometry models of the PV/T-no-AG and the PV/T-AG are meshed by using ANSYS meshing. Isometric views of the meshed PV/T-no-AG and the PV/T-AG with their mesh qualities are represented in Fig. A.4 and Fig. A.5 respectively. For each model, the number of the element were firstly obtained by coarse meshing then finer meshes were done until the mesh independent solutions were achieved. In this thesis, the number of elements for each model is the number that the solutions were mesh-independent.

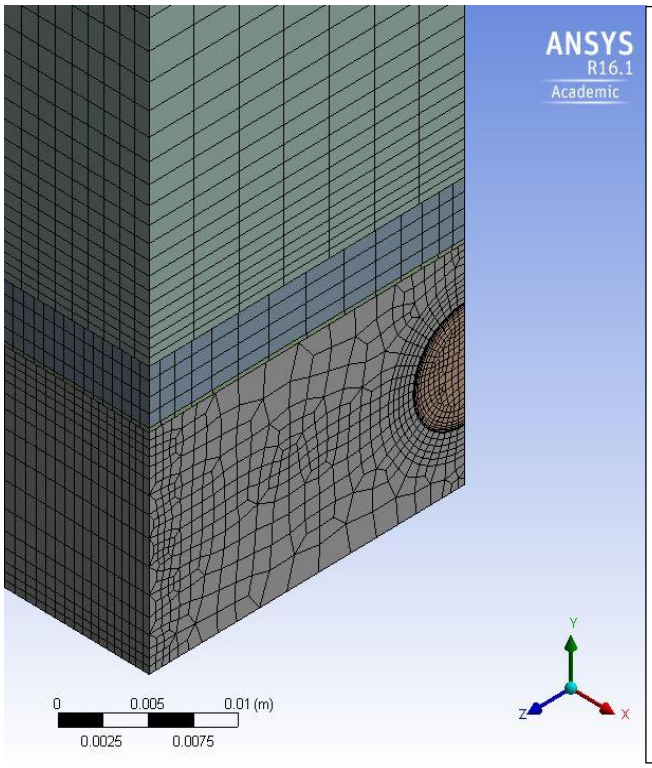

Mesh Properties

Nodes:	365,100
Elements:	312,500
Skewness:	
Min:	1.3057e-10
Max:	0.66777
Average:	8.6865e-2
Standard Deviation:	0.13099
Orthogonal Quality	
Min:	0.54267
Max:	1
Average:	0.98096
Standard Deviation:	4.786e-2
Aspect Ratio	
Min:	1.0064
Max:	501.78
Average:	17.521
Standard Deviation:	38.055

Fig. A.4 *The Isometric views of the meshed PV/T-no-AG model along with mesh qualities*

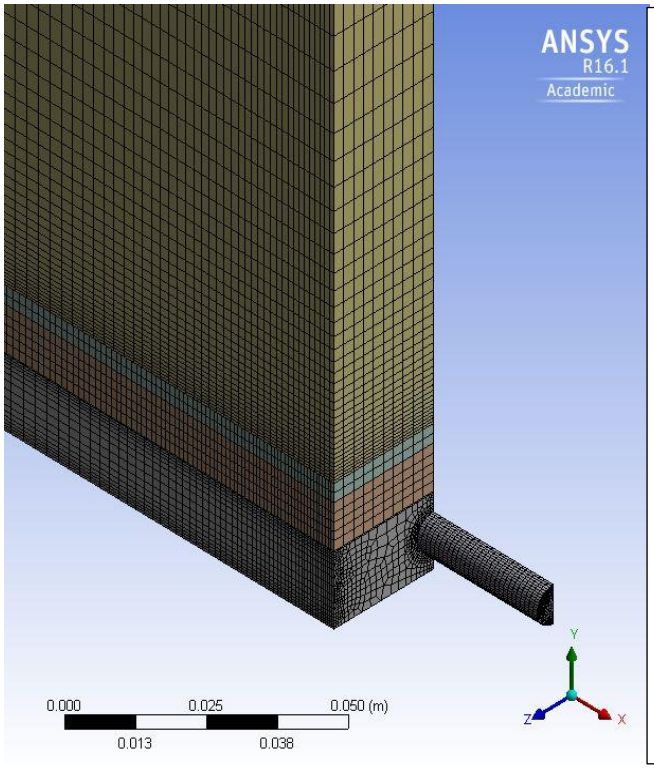

Mesh Properties

Nodes:	398,516
Elements:	339,434
Skewness:	
Min:	1.3057e-10
Max:	0.67027
Average:	7.3301e-2
Standard Deviation:	0.12447
Orthogonal Quality	
Min:	0.53955
Max:	1
Average:	0.9838
Standard Deviation:	4.5832e-2
Aspect Ratio	
Min:	1.0108
Max:	497.61
Average:	16
Standard Deviation:	36

Fig. A.5 *The Isometric views of the meshed PV/T-AG model with along with mesh qualities*

A.1.3 PV/T model setup in Fluent

Meshed models are loaded into ANSYS Fluent in order to solve flow, energy, and other necessary equations to represent the real physical heat and flow fields' solutions. The procedure of setting physics in ANSYS Fluent is described as the following;

1. In "General Setup", check meshes to be sure that each inputted mesh is compatible in Fluent. Solver type and velocity formulation are kept being pressure-based and absolute as default values respectively. Solver time is changed from steady to transient as physical conditions change in accordance with the time of the day. Gravitational effect is included in the problem by selecting the gravity box then set it to be 9.81 $\mathrm{m/s^2}$ in the direction that is consistent with the geometry (or mesh) model coordinates. In this thesis, all models are built that the gravity is in the negative y-direction; therefore, -9.81 $\mathrm{m/s^2}$ is set as shown in Fig. A.6.
2. In models setup, by default, inviscid flow with continuity and momentum equations will be solved. In order to get heat transfer solutions, the energy model is selected as shown in Fig. A.7 that energy is on. Accurate solutions of heat transfer effects and flow fields will not be obtained in the inviscid model; therefore, turbulent flow by using SST k-omega (2 equations) model is chosen along with the viscous heating option to get

more accurate solutions especially in viscous heating cases such as the heat transfer between solid and fluid zones. Low-Re Corrections is selected in the cases of low Reynold number flow and the rest of settings are left as default values as shown in Fig. A.7.

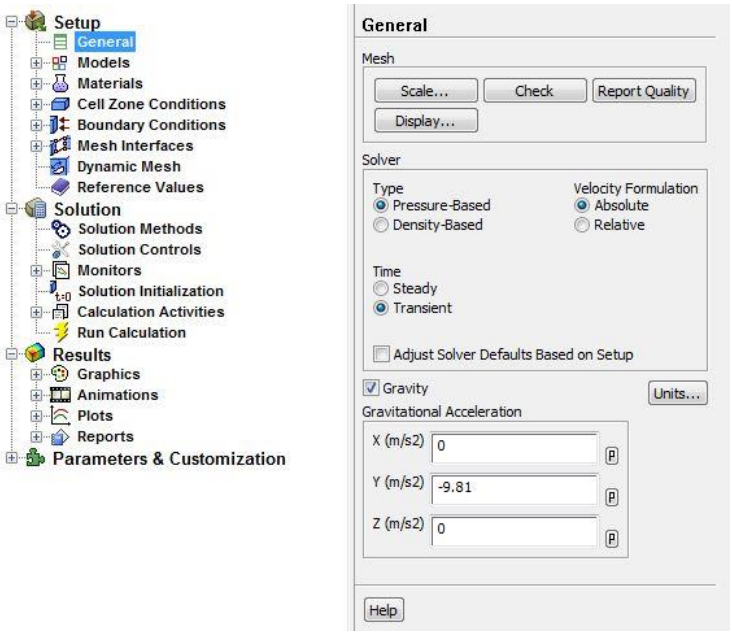

Fig. A.6 *General setup of physical models in ANSYS Fluent*

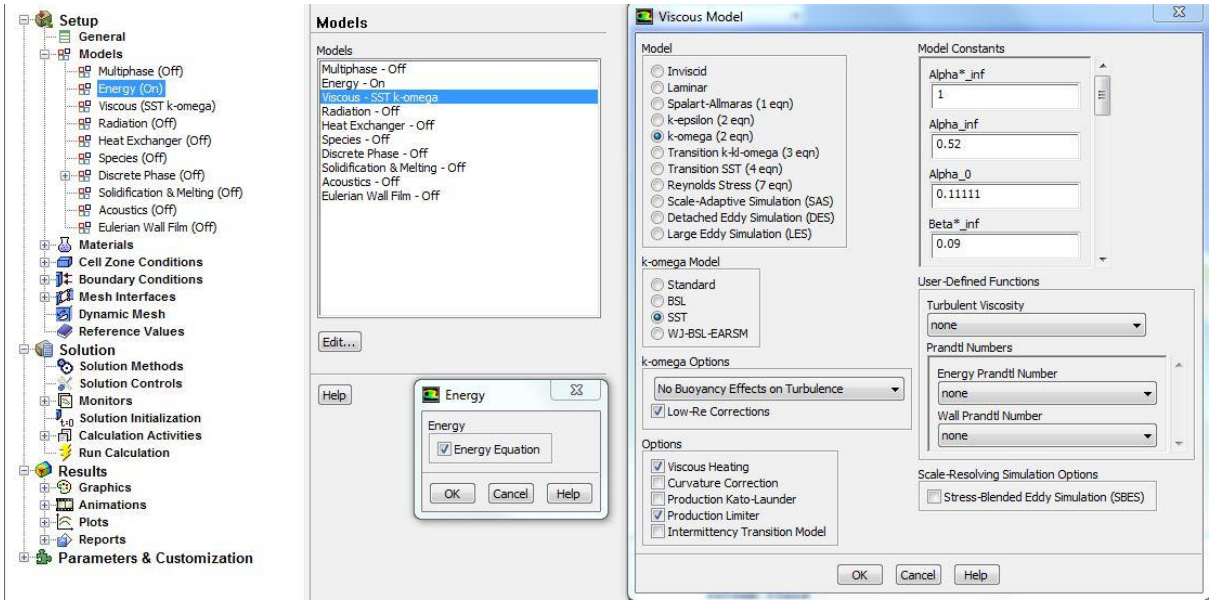

Fig. A.7 *Mathematical models setup of physical models in ANSYS Fluent*

3. For the material setup, the air in fluid materials and aluminium in solid materials are given as defaults. Aluminium is used as absorber material in the PVT layer. Water-liquid, PV cell material, and glass are added in the Change/Create button as shown in Fig. A.8 with the properties shown in Table A.4. The other way of adding materials is

by clicking one of the existing materials then select the available material which is needed in the fluent database.

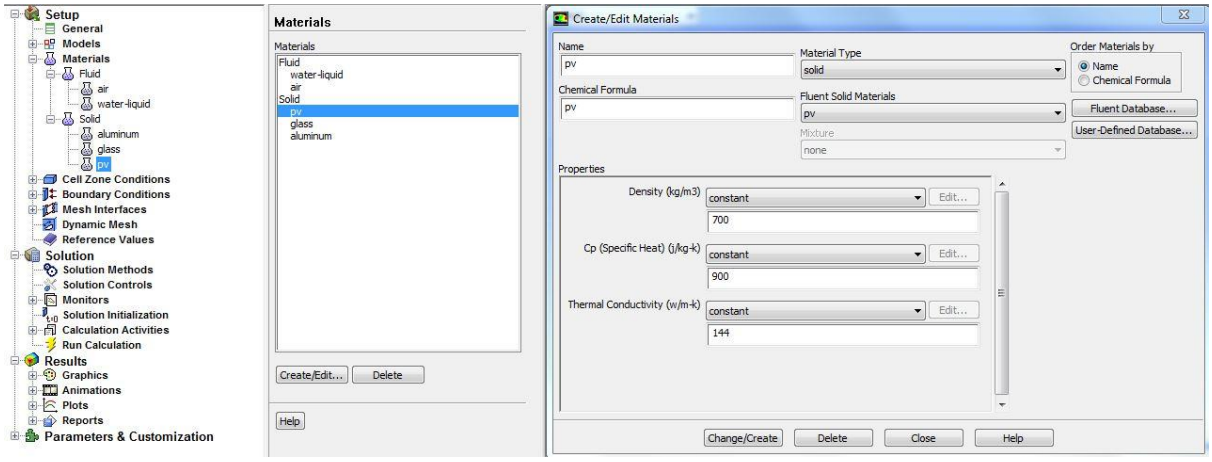

Fig. A.8 *Materials setup in ANSYS Fluent*

Table A.4 *Materials' properties for the Photovoltaic-Thermal (PVT) simulation*

Materials	**Density (ρ)** $(\boldsymbol{kg/m^3})$	**Specific heat (C_p)** $(\boldsymbol{J/kg \cdot K})$	**Thermal conductivity (k)** $(\boldsymbol{W/m \cdot K})$
Water-liquid	998.2	4182	0.6
PV	700	900	144
Glass	2200	670	0.9

4. After adding materials which are needed for solution solving, the materials will be available to be applied in "Cell Zone Conditions" setup. "Single phase flow" in Fluent is treated as only one domain in all zones in the model with two types of cell zone, solid and fluid. In PVT models, cell zone types should be set in the process of geometries modelling in DesignModeller and all zones and boundaries should be named in meshing process before loading to Fluent to be convenient to recognize and to correctly set parameters and boundary conditions.

   There are six main cell zones in the PVT model which are absorber (solid), air gap (fluid), ambient air (fluid), energy carrier fluid (fluid), glass (solid), and PV layer (solid). With the computational issue of reverse flow back into the tube from the energy carrier fluid outlet, it produces incorrect values of temperature output for some initial iterations before the solutions converse. This issue may lead to divergent solutions or incorrectly measure the temperature output of the energy carrier fluid at the outlet if the reverse flow happens. Therefore, extended fluid zone, which is the same fluid as used for the energy carrier fluid, is added into the model so that the real outlet of the model, the reverse backflow will not reach in. The reverse flow usually disappears when solutions converse. However, if the outlet temperature is being monitored along

the iteration process, the extended zone must be added to avoid incorrect controlled mass flow-modification.

By default, all fluid zones are set to be air and all solid zones are set to be aluminium in Fluent. Therefore, zones which are not the default materials must be changed to the corresponding materials. Fluent treats cell zones as groups of cells called "cell treads" with individual IDs that can be used in user-defined functions (UDF).

5. Radiation can be included in the PVT model by activating Radiation in model's setup; however, dealing with the radiation model is computationally time-consumed and complicated. Therefore, in this thesis, User-defined function (UDF) will be written in C language before interpreted via Define – User-Defined toolbar then attached them into appropriate cell zones as source terms.

   Several UDF can be interpreted and attached in on cell zone as shown in Fig. A.9. The UDF code for running a PV/T model with an air gap is present in Appendix F. However, in order to reduce the human error of inputting information in each time-step, MATLAB is used to arrange information and write UDF files output. In the glass cell zone, three energy sources are attached which are the heat generation from absorbed irradiance in the glass layer, radiation between glass and sky, and radiation between glass and ground. In the PV cell zone, two energy sources are attached which are the heat generation from absorbed irradiance in the PV layer, and the negative heat source that absorbed energy is converted to electricity. Radiation between glass and PV layers can be neglected as the temperatures between glass and PV layer is almost equal.

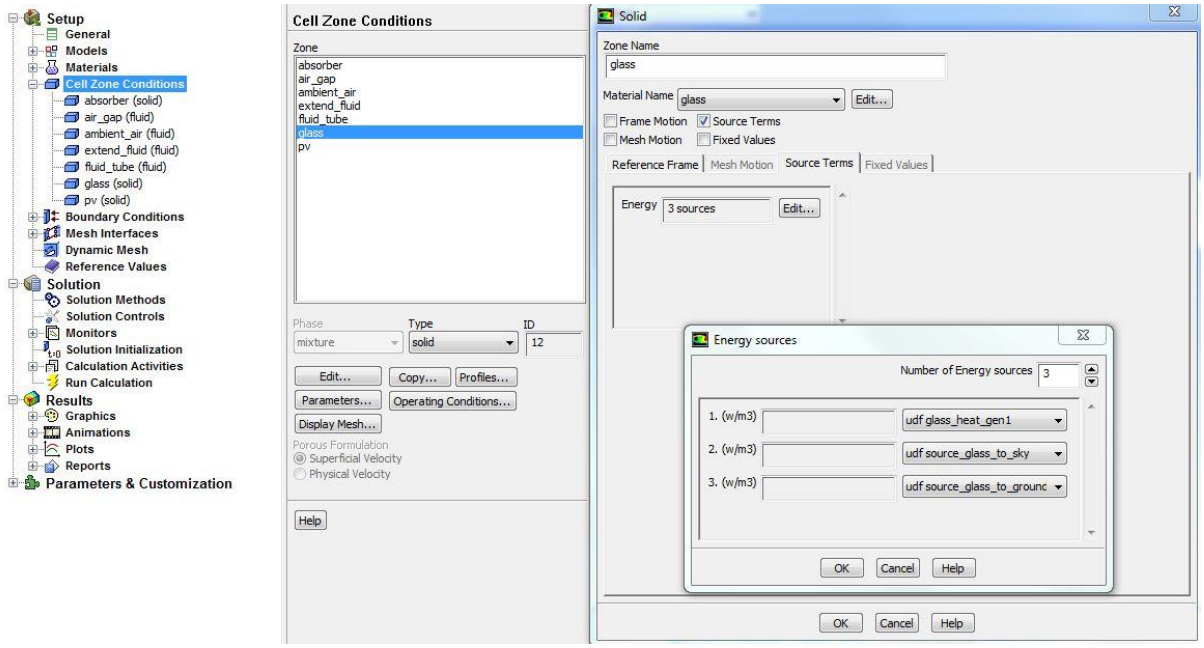

Fig. A.9 *Cell Zone Conditions setup in ANSYS Fluent*

6. After applying materials and energy sources in cell zone conditions setup, boundary conditions will be set and user-defined functions are attached as shown in Fig. A.10 for the PV/T-AG simulation. By naming all faces of the model, the boundary condition setup is more convenient. The face names which are related to fluent boundary types will be automatically set the types in accordance with the names and others will be set as an adiabatic wall. Contact regions between two zones are required to be changed to interface boundary type if they are not named to be the interface.

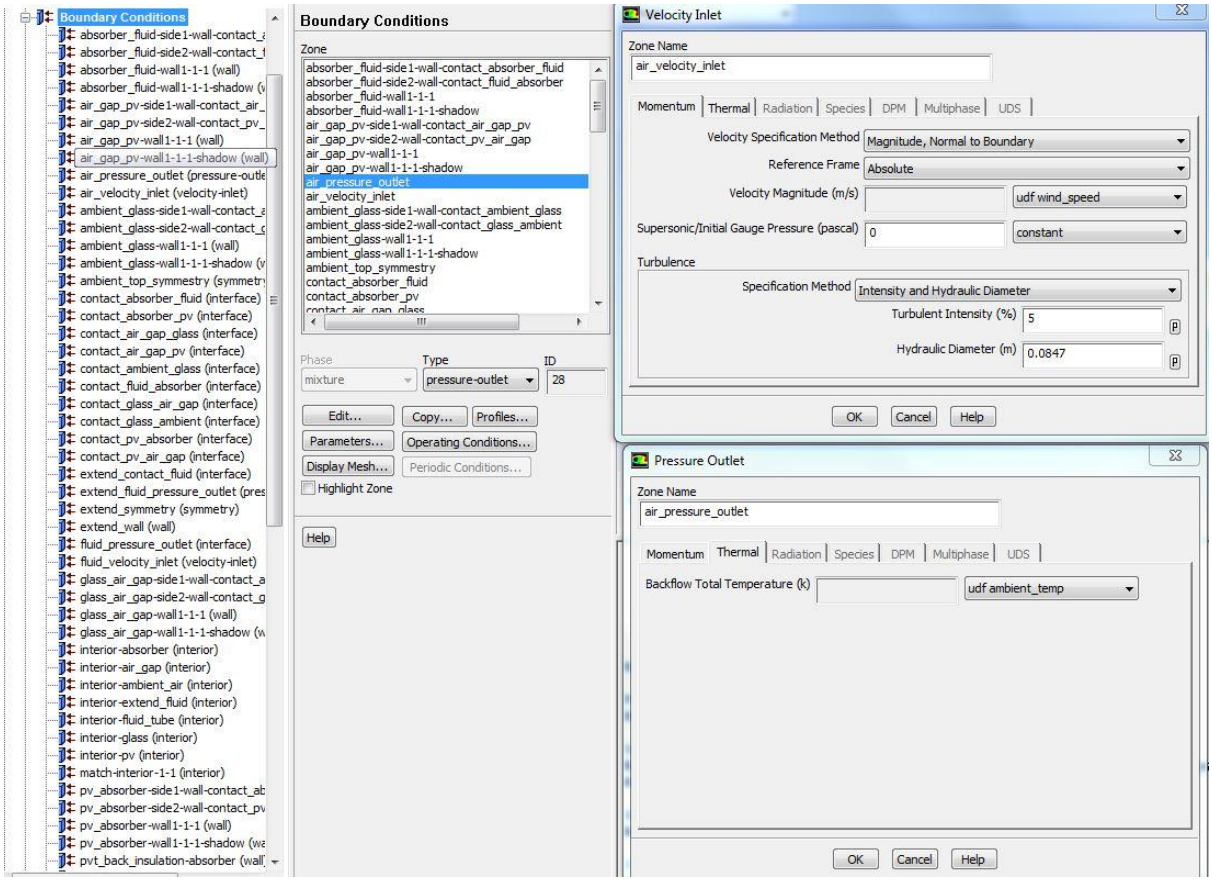

Fig. A.10 *Fluent boundary conditions setup windows of PVT with air-gap model*

Note that fluid tube is extended out for 30 millimetres to prevent incorrect outlet values' monitoring in cases of backflow computational solutions which may occur during iterations that bring in ambient conditions into account although those values usually get into the model for just one cell layer which does not represent the real overall values. The extended fluid zone is needed to be separated from the main fluid zone to remain the outlet boundary face for the outlet monitoring purpose. Therefore, the outlet face of the main fluid and the inlet face of the extended fluid were set to "interface type" boundary which make them available in the Mesh Interfaces setup to be matched. Moreover, in Fluent, in order to get the heat transfer between two contact boundaries (conduction and convection heat transfers), the contact boundaries must be set as "coupled wall". Therefore, boundaries have to be set as an interface to make them available in Mesh Interfaces setup.

7. Mesh Interfaces setup is the step to set all contact boundaries together with appropriate interface types in order to obtain accurate solutions. All interface boundaries which are set in the previous step are set as the types described in Table A.5.

Table A.5 *Fluent boundary conditions setup types and values of PVT with air-gap model*

Model's face name	Boundary Type	Boundary value
air_pressure_outlet	Pressure outlet	Back Pressure : 0 (Pa,gauge) Hydraulic Diameter : 0.0847 (m) Back Temperature : UDF-ambient temperature (K)
air_velocity_inlet	Velocity inlet	Velocity Magnitude : UDF-wind speed (m/s) Turbulent Intensity : 5% Hydraulic Diameter : 0.0847 (m) Inlet Temperature : UDF-ambient temperature (K)
ambient_top_symmetry	Symmetry	Assume the velocity far field where the flow near the model does not affect the far-field flow
symmetry - absorber	Symmetry	The symmetry plane where the model was cut into half and assume the same solution to the other half to reduce computational time.
symmetry - air_gap	Symmetry	
symmetry - ambient_air	Symmetry	
symmetry - fluid_tube	Symmetry	
symmetry - glass	Symmetry	
symmetry - pv	Symmetry	
pvt_side - absorber	Interface - Periodic	The periodic plane has to be set to interface boundary type then periodic boundary condition can be set in Mesh Interfaces setup.
pvt_side - air_gap	Interface - Periodic	
pvt_side - ambient_air	Interface - Periodic	
pvt_side - glass	Interface - Periodic	
pvt_side - pv	Interface - Periodic	
fluid_velocity_inlet	Velocity inlet	Velocity Magnitude : UDF-fluid_inlet_velocity (m/s) Turbulent Intensity : 5% Hydraulic Diameter : 0.008 (m) Inlet Temperature : UDF-fluid_inlet_temp (K)
fluid_pressure_outlet	Interface - Matching	Matching interface with extended_fluid_inlet
extended_fluid_inlet	Interface - Matching	Matching interface with fluid_pressure_outlet
Extended_fluid_ pressure_outlet	Pressure outlet	Back Pressure : 0 (Pa,gauge) Hydraulic Diameter : 0.008 (m) Back Temperature :UDF-ambient temperature (K)
contact_absorber_fluid	Interface - Coupled Wall	Coupled wall with contact_fluid_absorber
contact_fluid_absorber	Interface - Coupled Wall	Coupled wall with contact_absorber_fluid
contact_absorber_pv	Interface - Coupled Wall	Coupled wall with contact_pv_absorber
contact_pv_absorber	Interface - Coupled Wall	Coupled wall with contact_absorber_pv
contact_air_gap_glass	Interface - Coupled Wall	Coupled wall with contact_glass_air_gap
contact_glass_air_gap	Interface - Coupled Wall	Coupled wall with contact_air_gap_glass
contact_glass_ambient	Interface - Coupled Wall	Coupled wall with contact_ambient_glass
contact_ambient_glass	Interface - Coupled Wall	Coupled wall with contact_glass_ambient
contact_pv_air_gap	Interface - Coupled Wall	Coupled wall with contact_air_gap_pv
contact_air_gap_pv	Interface - Coupled Wall	Coupled wall with contact_pv_air_gap
All other boundaries	Adiabatic wall	- Assume that the heat losses through those boundaries are negligible due to the very small surface areas compared to other surfaces. - Bottom of the absorber is also set to an adiabatic wall because of the fact that the insulation is installed in the real model. Therefore, heat loss through this surface is neglected.

A.1.4 PV/T solution setup in Fluent

The first solution setup to consider is "Solution Methods". Due to the robustness of the "SIMPLE" method of the Pressure-Velocity Coupling Scheme, it is mostly used in this thesis. For Spatial Discretization, the second-order discretization provides more accurate solutions; therefore, in this thesis, the second order is preferred except when the convergence is hardly reached, the first order will be used as it is likely to give converged solution than he second-order discretization. Transient Formulation is set to First Order Implicit because it provides the availability of adaptive time-step size which is preferred in this thesis as adaptive time-step can be used with user-defined functions (UDF) to adjust the time-step size according to solar irradiance. For example, when there is no solar irradiance, only one time-step will be computationally calculated as an initial condition for the next time-step when solar radiation is available. In this fashion, MATLAB coding can be written to adjust the time-step size automatically corresponding to the irradiance of any day of a year which solar radiation does not start at the same time before adding the time-step function to a UDF file for Fluent. As a result, computational time dramatically reduces. Solution Methods are illustrated in Table A.6 where the green colour marked the preferred method.

Solution Controls are the under-relaxation factors which is used to control the solution variables for the next iteration from current conditions. Default values of the under-relaxation factors are set as optimum values for most of the non-combustion computational cases. Small values usually lead to more stable computation but slower in time to reach convergent solutions. For PVT model in this thesis, all default values are used as shown in Table A.7.

In order to know that the solutions are converged, residuals of all variables are monitored along with at least one of the variables to illustrate that the value really converges to a single value with minimal change. By default, residuals of continuity, x-velocity, y-velocity, z-velocity, Turbulent Kinetic Energy, and Turbulent Kinetic Energy Dissipation Rate equations are set to 0.001 where the residual of the energy equation is set to 1e-6. That means that if the solutions of those equations change with the values of less than the residuals, converged solutions are obtained. However, in this thesis, because of the nature of flow conditions which are low Reynold numbers, by monitoring individual values of solutions, residuals of all equation should be set as the values in Table A.8 to really get converged solutions.

Table A.6 *Fluent Solution Methods setup*

		Solution Methods				
Pressure-Velocity Coupling	**Scheme**	SIMPLE	SIMPLEC	PISO	Coupled	
Spatial Discretization	**Gradient**	Green-Gauss Cell Based	Green-Gauss Node Based	Least Squares Cell Based		
	Pressure	Second Order	Standard	PRESTO!	Linear	Body Force Weighted
	Momentum	First Order Upwind	Second Order Upwind	Power Law	QUICK	Third-Order MUSCL
	Turbulent Kinetic Energy	First Order Upwind	Second Order Upwind	Power Law	QUICK	Third-Order MUSCL
	Specific Dissipation Rate	First Order Upwind	Second Order Upwind	Power Law	QUICK	Third-Order MUSCL
	Energy	First Order Upwind	Second Order Upwind	Power Law	QUICK	Third-Order MUSCL
Transient Formulation		First Order Implicit	Second Order Implicit	Bounded Second-Order Implicit		
Note: The green labels are the methods used in this thesis						

Table A.7 *The under-relaxation factors in solution controls in Fluent being used in most PVT cases in this thesis*

	Under Relaxation Factors
Pressure	0.3
Density	1
Body Forces	1
Momentum	0.7
Turbulent Kinetic Energy	0.8
Specific Dissipation Rate	0.8
Turbulent Viscosity	1
Energy	1

Solutions initialization have to be done before starting calculation to apply initial values of all variables in all cells of models. Hybrid Initialization is preferred because it treats the initial values corresponding to physical models. Unlike Standard initialization that applies one single value for flow and energy variables to all cells.

Lastly, the calculation can be run in “Run Calculation”. Time-step is set to adaptive with the setting of 86,400 seconds (one day) ending time and the UDF-time_step is attached. The number of time steps and time step sizes are controlled by the UDF-time_step. Maximum iteration per time step is set to be 150. Normally, not more than 100 iterations of calculations will provide converged solutions.

Results of solutions can be set as preferred. In this thesis, PVT model solutions are reported as export-files which can be done in surface and volume monitors. Fluid temperature output, fluid velocity output, and PV electrical power output are monitored and reported by using user-defined functions (UDFs) then stored in the user-defined memories (UFMs) to be called in surface and volume monitors.

Table A.8 *Residual Monitors of equations solved in PVT models*

Equations	Residuals
continuity	3e-4
x-velocity	1e-4
y-velocity	1e-4
z-velocity	1e-4
Turbulent Kinetic Energy	1e-4
Turbulent Kinetic Energy Dissipation Rate	1e-4
Energy	1e-8

A.2 Modelling of the PV panel and the thermal collector in ANSYS Fluent

The modelling detail of the PV panel is similar to the PV/T models. The PV panel model in ANSYS DesignModellor in cross-sectional view, longitudinal view and isometric view are presented in Fig. A.11 and all dimensions are stated in Table A.9. The thermal collector model in ANSYS DesignModellor in cross-sectional view, longitudinal view and isometric view are presented in Fig. A.12 and all dimensions are stated in Table A.10.

The meshing procedure and meshes quality of the PV panel and thermal collector are performed by using the recommendation guidelines in Table A.2 and Table A.3. The mesh qualities of the PV model and the thermal collector model are shown in Fig. A.13 and Fig. A.14 respectively.

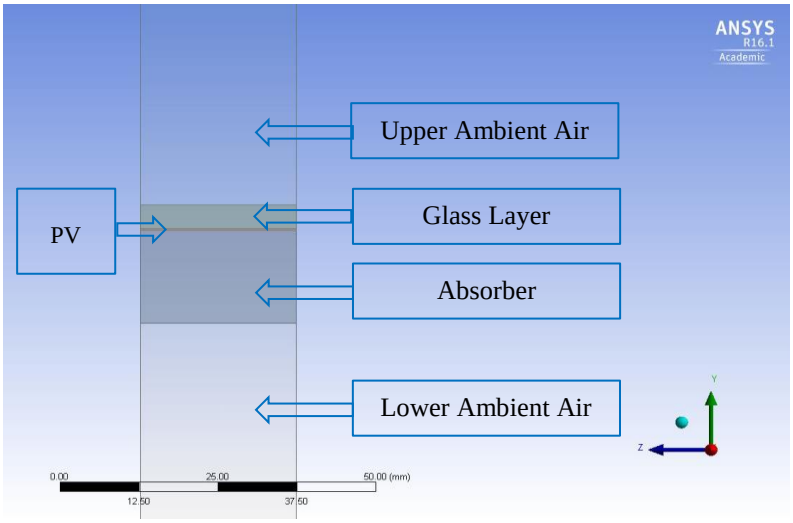

(a)

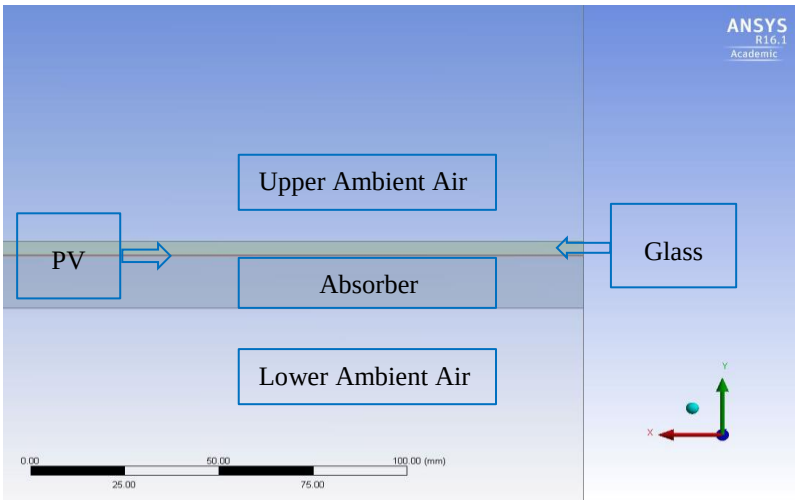

(b)

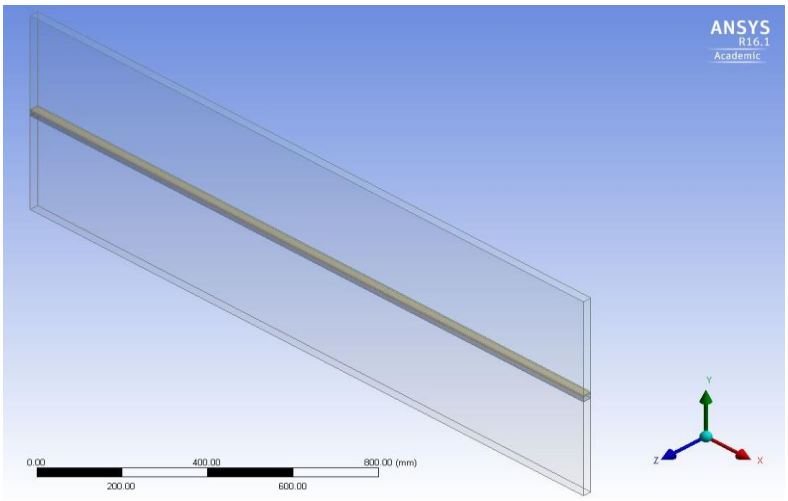

(c)

Fig. A.11 *PV panel model in ANSYS DesignModellor: (a) Cross-sectional view, (b) Longitudinal view, (c) Isometric view*

Table A.9 *PV Panel Models' Dimensions*

Parameters	**PV only**
Ambient air thickness or Upper air thickness (Y-axis)	300 mm
Lower air thickness (Y-axis)	300 mm
Glass thickness (Y-axis)	4 mm
PV layer thickness (Y-axis)	0.3 mm
backsheet thickness (Y-axis)	15.7 mm
All components' length (X-axis)	1830 mm
Cut models' width (Z-axis)	24.65 mm using symmetry analysis
Full model width (Z-axis)	986 mm

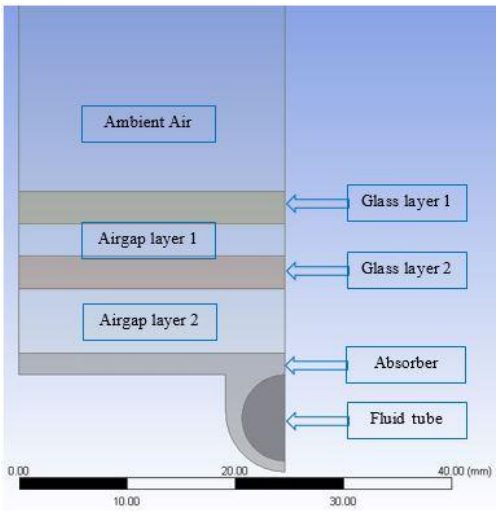

(a)

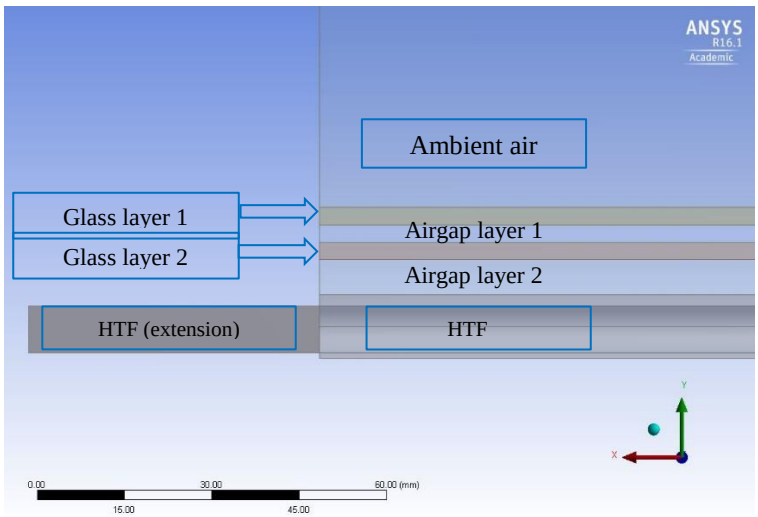

(b)

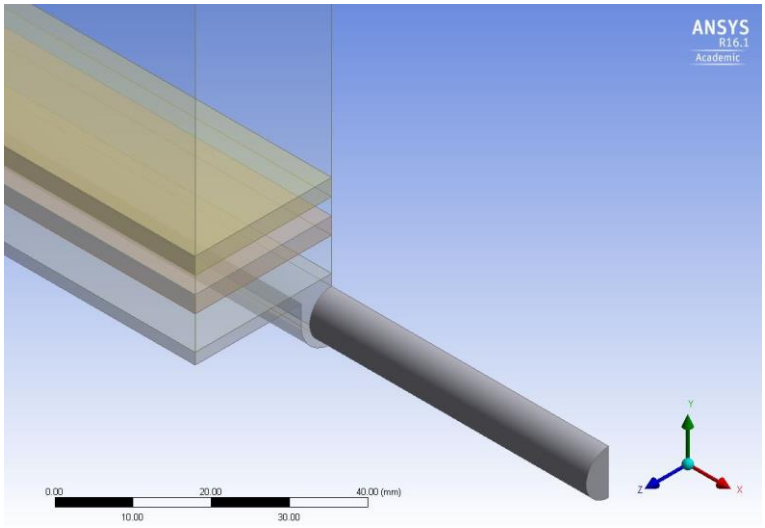

(c)

Fig. A.12 *Thermal collector model in ANSYS DesignModellor: (a) Cross-sectional View, (b) Longitudinal View, (c) Isometric View*

Table A.10 *Thermal collector Model's Dimensions*

Thermal collector	
Ambient air thickness or Upper air thickness (Y-axis)	300 mm
Lower air thickness (Y-axis)	-
Glass thickness (Y-axis)	3/3 mm (1^{st} layer/ 2^{nd} layer)
Air-gap thickness (Y-axis)	3/6 mm (1^{st} layer/ 2^{nd} layer)
PV layer thickness (Y-axis)	-
Absorber thickness (Y-axis)	15.7 mm
Fluid tubes' diameter	8 mm
All components' length (X-axis)	1830 mm
Cut models' width (Z-axis)	24.65 mm using symmetry analysis
Full model width (Z-axis)	986 mm
The length between 2 fluid tubes	49.3 mm

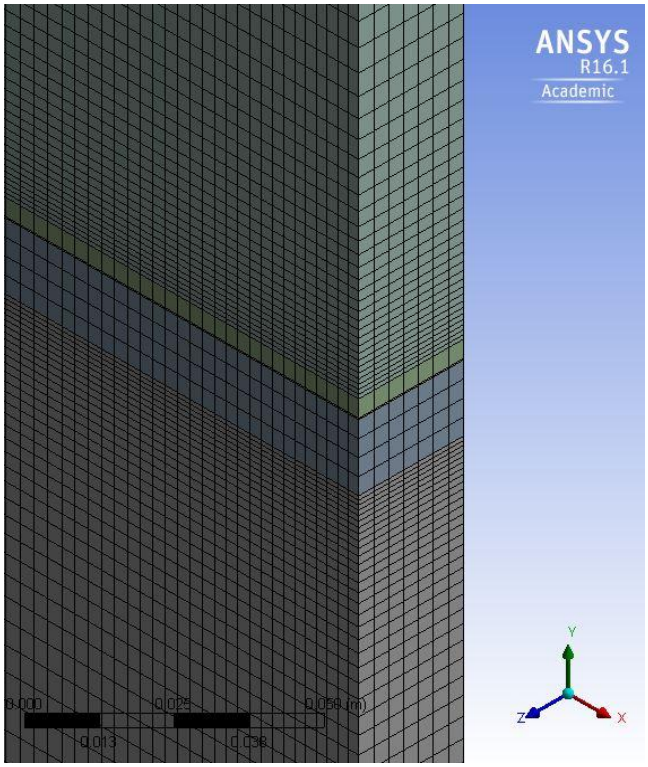

Mesh Properties

Nodes: 269,696
Elements: 224,700
Skewness:
Min: 1.3057e-10
Max: 4.9178e-2
Average: 3.2136e-4
Standard Deviation: 3.0112e-3
Orthogonal Quality
Min: 0.99738
Max: 1
Average: 0.99999
Standard Deviation: 8.2916e-5
Aspect Ratio
Min: 1.0175
Max: 40.85
Average: 3.4205
Standard Deviation: 2.5876

Fig. A.13 *The Isometric views of the meshed PV model with mesh qualities*

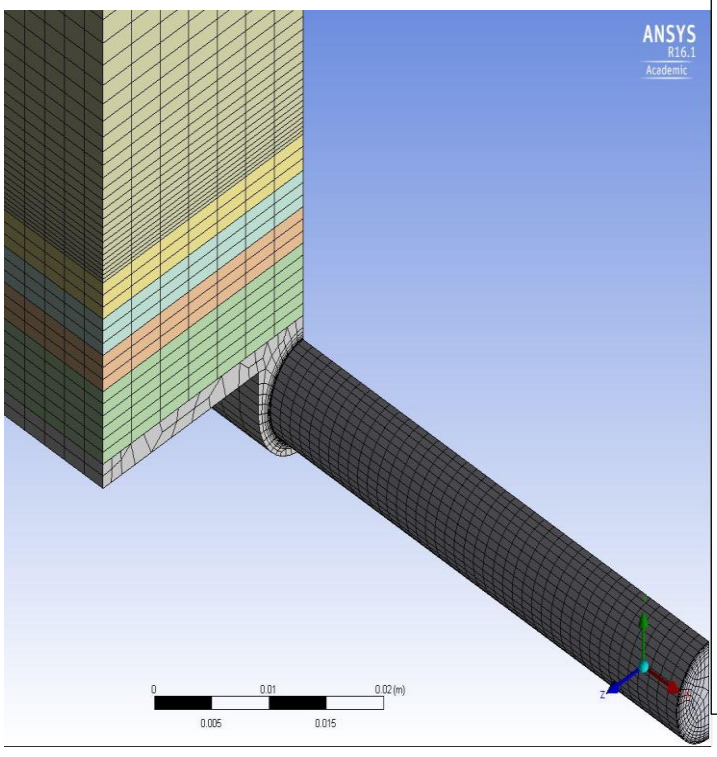

Mesh Properties

Nodes: 462,920
Elements: 401,752
Skewness:
Min: 1.3057e-10
Max: 0.7358
Average: 0.1107
Standard Deviation: 0.1342
Orthogonal Quality
Min: 0.526
Max: 1
Average: 0.97117
Standard Deviation: 8.2916e-5
Aspect Ratio
Min: 1.0266
Max: 739.93
Average: 17.367
Standard Deviation: 45.135

Fig. A.14 *The Isometric views of the meshed thermal collector model with mesh qualities*

Appendix B: Modelling of electrical energy production for PV panel in MATLAB Simulink

MATLAB Simulink can be used to model a PV module as the main system with input conditions and PV input parameters as shown in Fig. B.1. The PV module contains sub-systems of the photocurrent, the diode current and the shunt current which are illustrated in Fig. B.2, Fig. B.3, and Fig. B.4 respectively. The subsystems of the cell's reverse saturation current and the cell's saturation current are shown in Fig. B.5 and the cell's reverse saturation current and the cell's saturation current components are illustrated in Fig. B.6 and Fig. B.7 respectively.

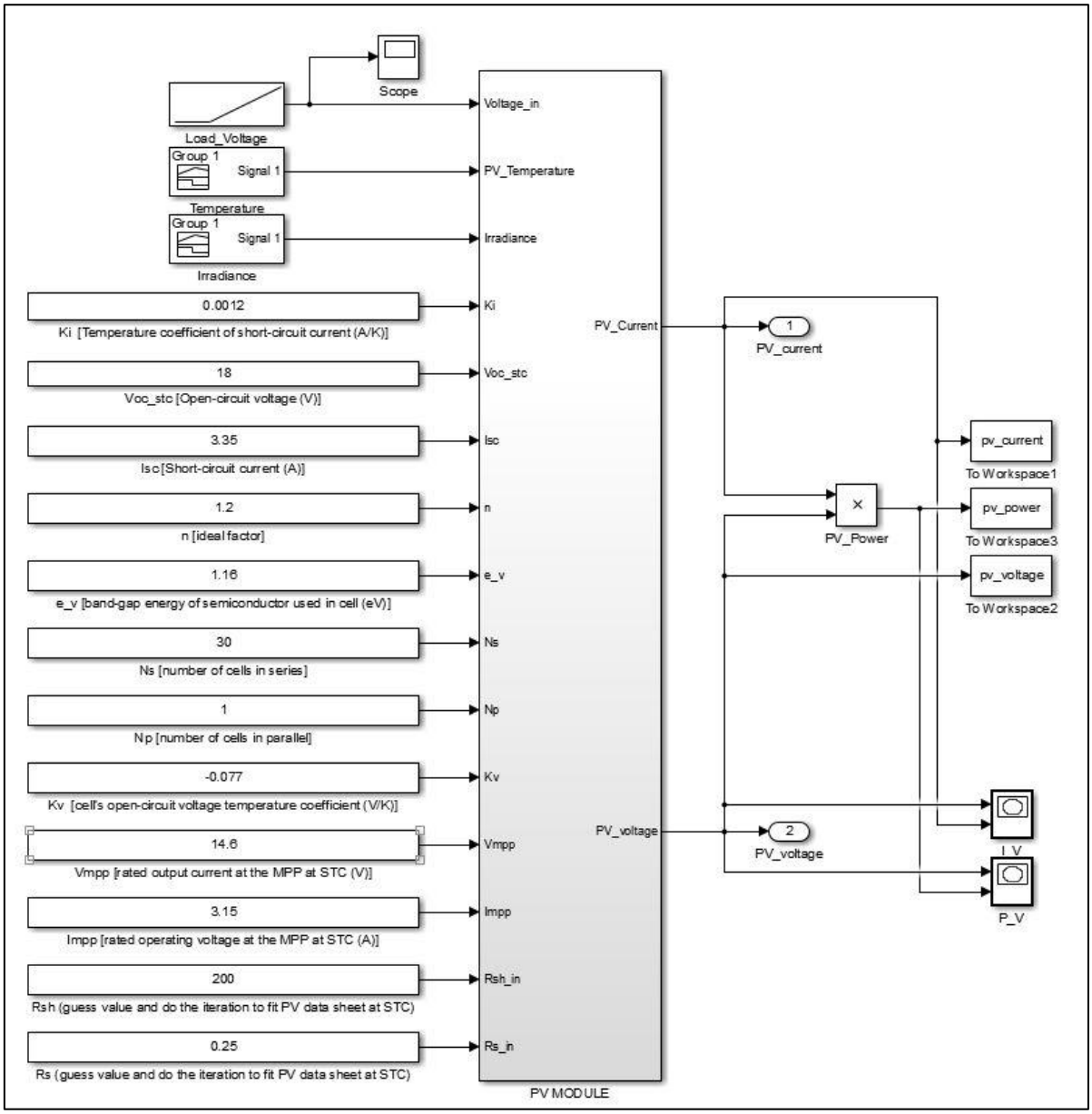

Fig. B.1 *MATLAB Simulink of a PV module*

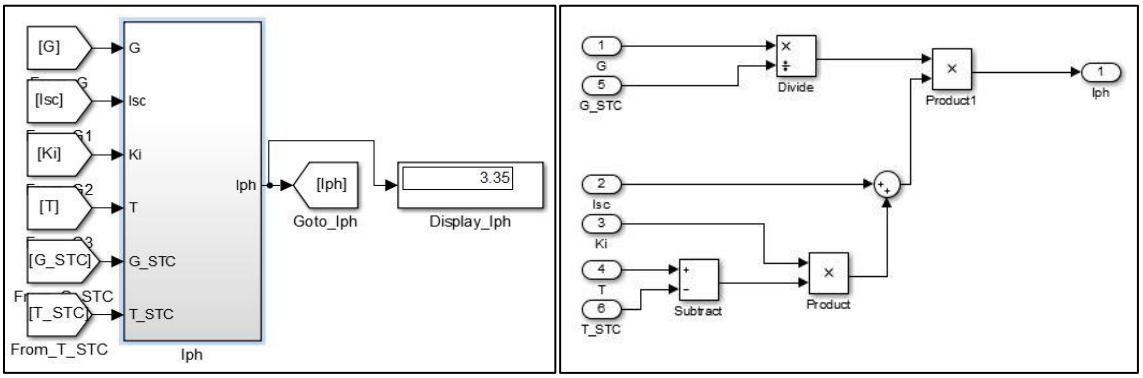

Fig. B.2 *Subsystem of Photocurrent (left) and its components (right)*

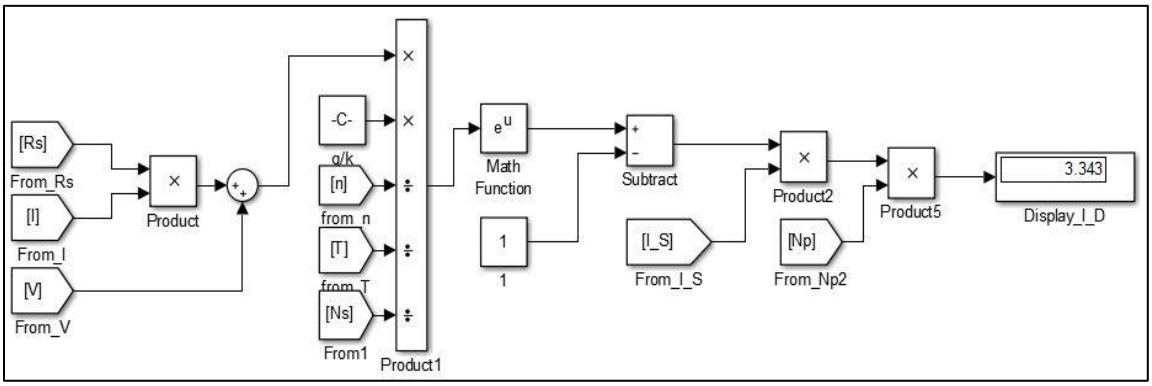

Fig. B.3 *The Diode current subsystem components*

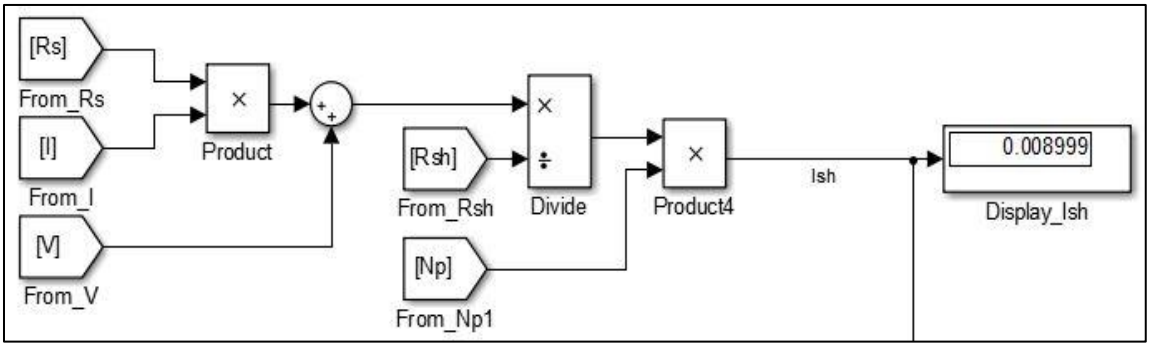

Fig. B.4 *The shunt current subsystem components*

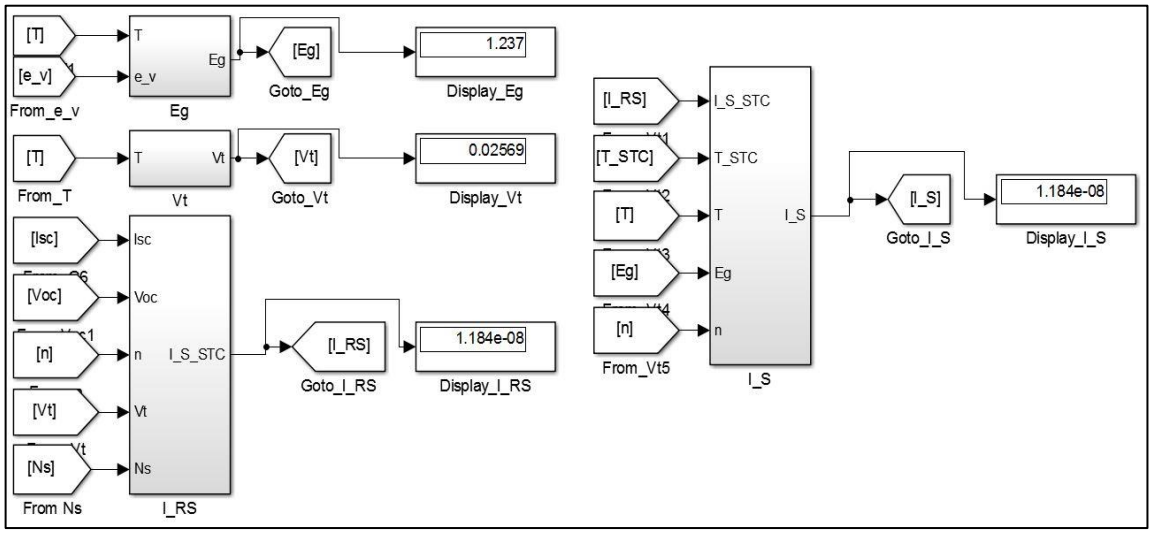

Fig. B.5 *Subsystems of cell's reverse saturation current and cell's saturation current*

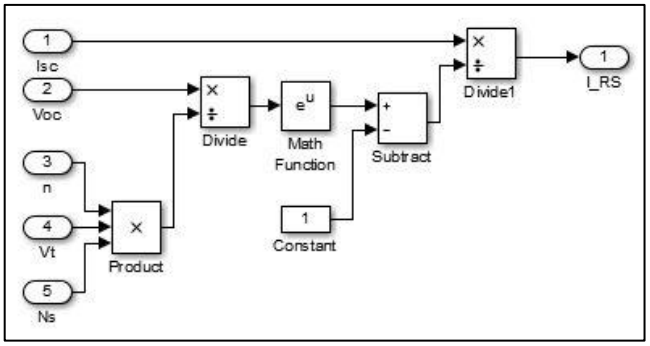

Fig. B.6 *The cell's reverse saturation current components*

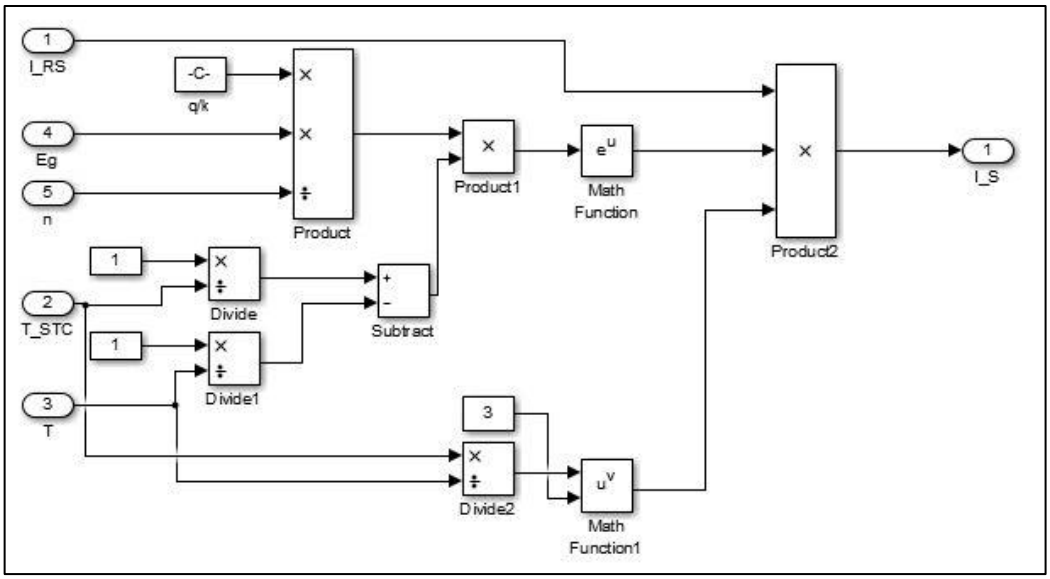

Fig. B.7 *The cell's saturation current components*

(This page intentionally left blank)

Appendix C: The datasheets of the Siemens SM46 PV and Solarex MSX60 PV modules

C.1 Siemens SM46 PV module

Siemens Solar Panels direct from Bullnet

HOME PRODUCTS APPLICATIONS ABOUT PV SEARCH LINKS VIEW CART

BULLNET SUPPLIERS OF Siemens Solar Panels

SM46 Siemens Solar module details and specifications.

Intelligent module design
30 PowerMax® solar cells form the heart of the module. These cells make optimum use of the module surface area. Thanks to their square shape, they are highly efficient and still provide the maximum power possible even under low light level conditions. The specially hardened front glass has excellent light transmitting properties and protects the module against most adverse environmental conditions such as hail or ice. The solar cells are laminated in EVA (ethylene-vinyl acetate) between a multilayer rear film and the front glass. This permanently laminated assembly protects the cells against moisture and ensures electrical insulation. A torsion-resistant module frame made of anodized aluminum guarantees particularly high mechanical strength.


SM46

The SM46 datasheet is also available in the Adobe Acrobat (.PDF) format.

Electrical Parameters [1]			**SM46**
			12V
Maximum power rating	Pmax	[Watts]	46
Minimum power rating	Pmin	[Watts]	41
Rated current	Imp	[Amps]	3.15
Rated voltage	Vmp	[Volts]	14.6
Short circuit current	Isc	[Amps]	3.35
Open circuit voltage	Voc	[Volts]	18
Thermal Parameters			
Nominal operating cell temperature[2]		[°C]	45
Change of Isc with temperature, α			+1.2mA/°C (+0.04%/°K)
Change of Voc with temperature, β			-0.058 Volts/°C (-0.34%/°K)
Qualification Test Parameters[3]			
Temperature cycling range		[°C]	

Humidity, freeze, damp heat condition	[% RH]	-40 to +85 85
Maximum system voltage	[Volts]	1000 per ISPRA (EC), 600 per UL 1703
Wind loading or surface pressure	[N/m²] (PSF)	2400 (50)
Maximum distortion[4]	[degrees]	1.2
Hailstone impact withstand (diameter @ velocity)	[mm @ m/s] (in @ MPH)	25 @ 23 (1.0 @ 52)
Physical Parameters		
Number of series cells		30
Length	[mm] (in)	1083 (42.7)
Width	[mm] (in)	329 (13.0)
Depth	[mm] (in)	34 (1.3)
Weight	[kg] (lbs)	4.6 (10.2)
Warranty[5]		
Power >= 90% of minimum power	[Years]	10
Power >= 80% of minimum power	[Years]	25

1 Determined under standard test conditions (STC): Irradiance = 1000w/m² cell temperature = 25 °C; solar spectral irradiance per ASTM E892 (Air Mass = 1.5).

2 Determined under nominal operating conditions (NOC): Irradiance = 800 w/m² ambient temperature = 20 °C; wind speed = 1m/s.

3 Qualification Tests performed as per CEC 503 Test Specification, to ensure durability and performance in outdoor conditions.

4 Diagonal lifting of module corner with three corners fixed.

5 To original consumer purchaser. See full Limited Warranty for all conditions.

C.2 Solarex MSX60 PV module

MSX-60 and MSX-64 Photovoltaic Modules

25 ANNIVERSARY 1973-1998

SOLAREX

The MSX-64 and -60 are among the most powerful of Solarex's Megamodule™ series, a product line which is the culmination of nearly three decades of extensive research in polycrystalline silicon photovoltaics. With over 3 amperes of current at peak power, these modules offer the most cost-effective package in the industry, and charge batteries efficiently in virtually any climate.

These modules may be used in single-module arrays or deployed in multiple-module arrays, wired in series/parallel combinations as required to meet current and voltage requirements. They are engineered under Solarex's IntegraSystem™ system integration concept, which ensures full compatibility with other Solarex subsystems and components (support hardware, regulators, etc.) and easy system assembly. As single-module arrays, they may be mounted on a variety of surfaces using optional kits or by means of user-fabricated support hardware. Solarex also offers hardware for supporting multiple-module arrays.

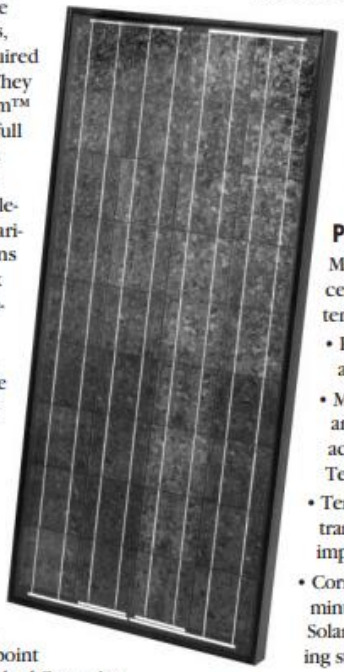

These modules are well-suited for virtually all applications where photovoltaics are a feasible energy source, including telecommunications systems, pumping and irrigation, cathodic protection, remote villages and clinics, and aids to navigation.

Individually Tested, Labeled and Warranted

As part of the final inspection procedure, every MSX module is tested in a solar simulator and labeled with its actual output—voltage, current, and power at maximum power point (P_{max})—at Standard Test Conditions and Standard Operating Conditions. Furthermore, the MSX-64 and -60 are covered by our industry-leading limited warranty, which guarantees:

- that no module will generate less than its guaranteed minimum P_{max} when purchased;
- at least 80% of the guaranteed minimum P_{max} for twenty years.

Contact Solarex's Marketing Department for full terms and limitations of this unparalleled warranty.

Reliable and Versatile

The Megamodule series has proved its reliability at thousands of installations in every climate on Earth. Among the features that contribute to its versatility:

Dual Voltage Capability

These modules consist of 36 polycrystalline silicon solar cells electrically configured as two series strings of 18 cells each. The strings terminate in the junction box on the module back. Shipped in 12V configuration, modules may easily be switched to 6V configuration in the field by moving leads in the junction box. This design also allows installation of bypass diodes on 18-cell strings, which can improve reliability and performance in systems with nominal voltage 24V and above.

High-Capacity Multifunction Junction Box

The size of the junction box (25 cubic inches, 411cc) and its six-terminal connection block allow most system array connections to be made right in the J-box. The box also can accommodate bypass or blocking diodes or a small regulator, which can save the expense and labor of additional boxes. The box is raintight (IP54 rated) and accepts 1/2" nominal or PG13.5 conduit or cable fittings. The standard terminals accept wire as large as AWG #10 (6mm^2); an optional terminal block accepts wire up to AWG #4 (25mm^2).

Proven Materials and Construction

Megamodule materials reflect Solarex's quarter-century of experience with solar modules and systems installed in virtually every climate on Earth.

- Polycrystalline silicon solar cells: efficient, attractive, stable.
- Modules are rugged and weatherproof: cell strings are laminated between sheets of ethylene vinyl acetate (EVA) and tempered glass with a durable Tedlar backsheet.
- Tempered glass superstrate is highly light-transmissive (low iron content), stable, and impact-resistant.
- Corrosion-resistant, bronze-anodized extruded aluminum frame is strong, attractive, compatible with Solarex mounting hardware and most other mounting structures.

Options

- Blocking and bypass diodes
- Solarstate™ charge regulator
- Protective aluminum backplate

More than 20 years ago, Solarex made the first polycrystalline silicon solar cell, advancing photovoltaics beyond the first-generation monocrystalline technology developed for electronics. Developed specifically for photovoltaics, polycrystalline silicon is used in Solarex's Mega™ series to provide a wide range of attractive, efficient modules. They require substantially less energy to manufacture and generate substantially more energy per rated watt than other crystalline silicon modules.

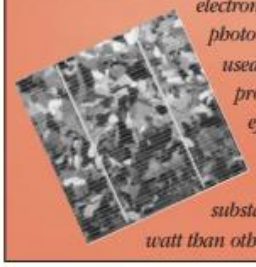

MSX-60 and -64 modules are listed by Underwriter's Laboratories for electrical and fire safety (Class C fire rating), certified by TUV Rheinland as Class II equipment, and approved by Factory Mutual Research for application in NEC Class 1, Division 2, Group C & D hazardous locations.

Quality Certified

These modules are manufactured in our ISO 9001-certified factories to demanding specifications, and comply with IEC 1215, IEEE 1262 and CEC 503 test requirements, including:

- repetitive cycling between -40°C and 85°C at 85% relative humidity;
- simulated impact of one-inch (25mm) hail at terminal velocity;
- 2700 VDC frame/cell string isolation test;
- a "damp heat" test, consisting of 1000 hours of exposure to 85°C and 85% relative humidity;
- a "hot-spot" test, which determines a module's ability to tolerate localized shadowing (which can cause reverse-biased operation and localized heating);
- simulated wind loading of 125 mph (200 kph).

Mechanical Characteristics

Weight: 15.9 pounds (7.2 kg)

Dimensions: Dimensions in brackets are in millimeters
Unbracketed dimensions are in inches
Overall tolerances ±1/8" (3mm)

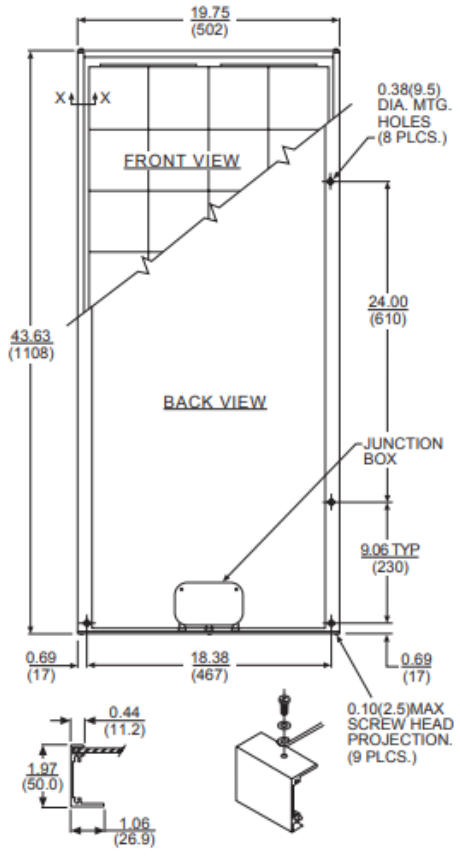

SECTION X–X GROUNDING DETAIL

	MSX-64	MSX-60
Maximum power (P_{max})	64W	60W
Voltage @ P_{max} (V_{mp})	17.5V	17.1V
Current @ P_{max} (I_{mp})	3.66A	3.5A
Guaranteed minimum P_{max}	62W	58W
Short-circuit current (I_{sc})	4.0A	3.8A
Open-circuit voltage (V_{oc})	21.3V	21.1V
Temperature coefficient of open-circuit voltage	.....–(80±10)mV/°C	
Temperature coefficient of short-circuit current	....(0.065±0.015)%/°C ..	
Temperature coefficient of power	.....–(0.5±0.05)%/°C ...	
NOCT[2]	..... 47±2°C	

NOTES:

(1) These modules are tested, labeled and shipped in 12V configuration. These data represent the performance of typical 12V modules as measured at their output terminals, and do not include the effect of such additional equipment as diodes and cabling. The data are based on measurements made in a solar simulator at Standard Test Conditions (STC), which are:

- illumination of 1 kW/m^2 (1 sun) at spectral distribution of AM 1.5;
- cell temperature of 25°C or as otherwise specified (on curves).

Operating characteristics in sunlight may differ slightly. To determine the characteristics of modules in 6V configuration, divide the 12V voltage characteristics by 2 and multiply current characteristics by 2. Power values are unchanged.

(2) Under most climatic conditions, the cells in a module operate hotter than the ambient temperature. NOCT (Nominal Operating Cell Temperature) is an indicator of this temperature differential, and is the cell temperature under Standard Operating Conditions: ambient temperature of 20°C, solar irradiation of 0.8 kW/m^2, and wind speed of 1 m/s.

MSX-60 I-V Characteristics

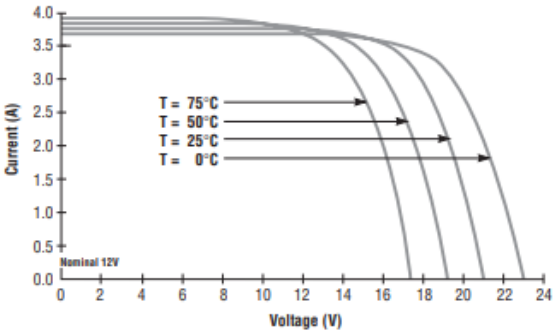

MSX-64 I-V Characteristics

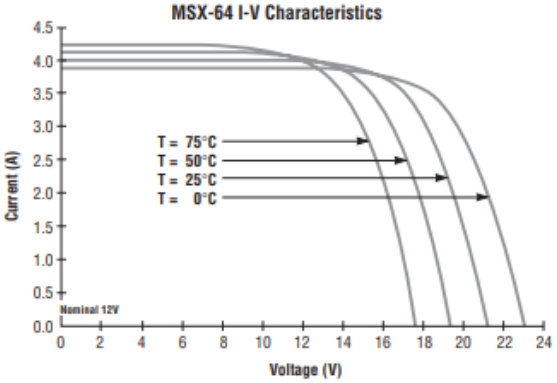

Download MSX-60 I-V XLS

Download MSX-64 I-V XLS

Download CAD

Appendix D: Composite adsorbent preparation and finned-tube reactor preparation

The reactant contains two components which are reactive salt and expanded graphite (EG). Graphite can be expanded to get a suitable porous structure by heating up to the temperatures higher than 600 ^{o}C (Han *et al.*, 1998). To be specific, Oliveira and Wang (2007) suggest that performing the heat treatment of graphite using 10 minutes with 700 ^{o}C provides exceptional apparent density for impregnated adsorbent at the minimal time of heating treatment. Therefore, in the experiments in this thesis, graphite is weighted to 30 g and put into the stainless-steel pot as shown in Fig. D.1 then heated to 700 ^{o}C for 10 minutes.

There are two reactors in the experiments; one reactor was prepared with Strontium-Chloride ($SrCl_2$) as the reactive salt and the other one is with Manganese-Chloride ($MnCl_2$). The adsorbent used in the reactors was prepared by impregnating reactive salts into the expanded graphite to obtain the desired densities for each reactor. The mass fraction of EG and salt, calculated from Eq.(E.13), of 1/3 is suitable to obtain a relatively high thermal conductivity while the ammonia mass diffusivity is acceptable for maintaining satisfactory reaction rates. Each reactor contains 10 finned-tubes and each tube has the inner diameter of 8mm with 2mm thickness and its length is 50cm. Eight fins, with the thickness of 1mm and the distance of 10mm from the outer tube walls, were welded to the outer surface of each tube to create gaps between fins for improving the heat transfer rate to/from the adsorbent. Ten tubes were packed into each reactor as shown in Fig. D.2. To protect the deposition of the adsorbent, a mesh with a diameter of 37.4 mm was used to support the adsorbent while allowing gas to pass through to the adsorbent. The available volume between the outer surface of a tube and the inner surface of a mesh is 0.48 dm^3.

$$f_{EG} = \frac{m_{EG}}{m_{salt}} \tag{D.1}$$

Fig. D.1 *The graphite before weighting and a pot to be used to expand the graphite*

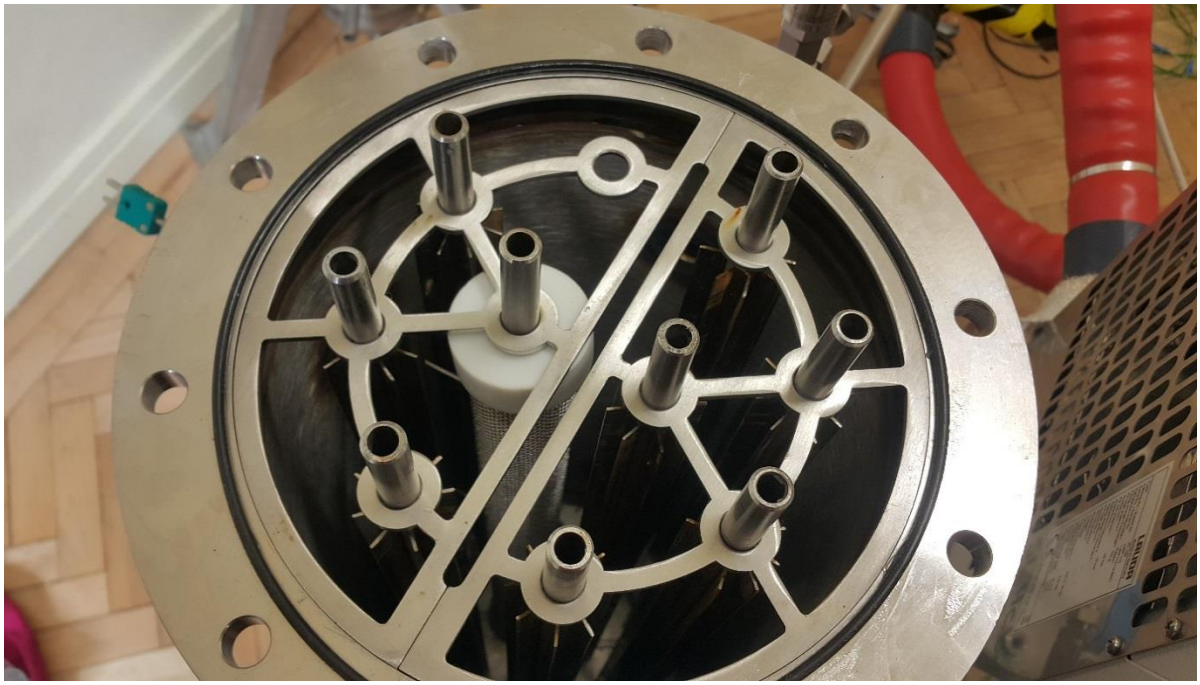

Fig. D.2 *The reactor with finned tubes inside*

The strontium-chloride reactor was designed with the reactant density of 450 kg/m^3 with f_{EG} equals 1/3 in the volume of 0.48 dm^3. To achieve the reactant density of 450 kg/m^3, 60g of EG and 180g of pure $SrCl_2$ are required per fin-tube. However, the available form of $SrCl_2$ is $SrCl_2 \cdot 6H_2O$ with the molar mass of 266.62 g/mol as shown in Fig. ***D.3***(a). Therefore, to get 180g of pure $SrCl_2$ (the molar mass is 158.53 g/mol), 302.73g of $SrCl_2 \cdot 6H_2O$ was used.

For the manganese-chloride reactor, the density of the reactant was determined to match the number of the reactive ammonia mole from the strontium-chloride reactor. Considering the 180g of $SrCl_2$ per tube which is 1.13543 mole, according to the ability of $SrCl_2$ to react with 7 moles of ammonia per salt mole, there are 7.948 moles of ammonia that can react with 1.13543 moles of $SrCl_2$. In accordance with the $MnCl_2$ that can react with 4 moles of ammonia per salt mole, 7.948-mole of ammonia from $SrCl_2$ requires 1.987 moles of $MnCl_2$ per tube. The commercially available form of $MnCl_2$ is dehydrate-97% $MnCl_2$ (the molar mass is 125.844 g/mol) as shown in Fig. D.3(b), therefore, 257.786 g of dehydrate-97% $MnCl_2$ (250.05 g of pure $MnCl_2$) is required per tube. To obtain the f_{EG} of 1/3 for the $MnCl_2$ adsorbent, 83.35 g of EG is needed resulting in 333.40 g of $MnCl_2$-EG adsorbent. By packing the $MnCl_2$-EG adsorbent into a fin-tube with the volume of 0.48 dm^3, the $MnCl_2$-EG adsorbent density is approximately 695 kg/m^3.

To ensure that each fin-tube contains the proper amount of adsorbent, 10 sets of $SrCl_2$-EG and 10 sets of $MnCl_2$-EG were prepared separately. To impregnate a portion of reactive salts to the EG, it was dissolved with water before adding the EG to the solution. A portion of salts was weighted to the right amount then put in a tray containing approximately 1 litre of water to make a solution. By doing so, the salt-solution can be absorbed by the EG evenly with careful stirring as shown in Fig. D.4. The measurement of each portion of reactive salts along with the fin-tubes and mesh weights are presented in Table D.1.

(a) (b)

Fig. D.3 *(a) The Strontium Chloride Hexahydrate ($SrCl_2 \cdot 6H_2O$), (b) The Manganese Chloride dehydrate (97% $MnCl_2$)*

Fig. D.4 *The mixture between Strontium Chloride Hexahydrate, water and EG*

After that, the mixture was dried by heating in a furnace. The mixture was heated to the temperature of 120 ^{o}C in the furnace for 3-4 hours then stirred every 2-hour until there is a small amount of water content in the adsorbent which was indicated by the weight of the adsorbent. To remove the last portion of moisture in the mixture (adsorbent), the temperature of the furnace was set to 150 ^{o}C for the last heating cycle for 2-3 hours. Crystallization usually occurs when leaving the mixture more than 3-4 hours without stirring in the first heating cycle (as shown in Fig. D.5). If there is a little of salt-crystals, it was mashed then mixed back to the mixture before putting back to the furnace at the same temperature.

Approximately, 8 hours of 120 ^{o}C and 2-3 hours of 150 ^{o}C was required to make the dried-adsorbent which was kept in the zip-lock to isolate it from absorbing moisture from the surrounding. After drying, one portion of the reactant has a volume of approximately 1.5 dm^2 which is ready to be compressed to the finned-tubes with the compression ratio of 3.13 into a finned-tube with the volume of 0.48 dm^2. The compression process is shown in Fig. D.6.

Fig. D.5 *Examples of salts' crystallization*

Table D.1 *Composite adsorbent weight*

Salt name	Lot number	Salt weight (g)	EG weight (g)	Fin-tube weight (g)	Mesh weight (g)	Total Weight (g)
$SrCl_2$	1	180.00	60.00	627.43	268.75	1136.18
	2	180.00	60.00	629.00	265.00	1134.00
	3	180.00	60.00	627.43	268.75	1136.18
	4	180.00	60.00	631.00	267.00	1138.00
	5	180.00	60.00	639.00	266.00	1145.00
	6	180.00	60.00	626.00	270.00	1136.00
	7	180.00	60.00	633.00	277.00	1150.00
	8	180.00	60.00	634.55	273.42	1147.97
	9	180.00	60.00	635.70	269.28	1144.98
	10	180.00	60.00	624.92	264.32	1129.24
$MnCl_2$	1	258.13	84.14	630.08	268.60	1240.95
	2	258.82	84.58	637.79	263.44	1244.63
	3	258.54	84.00	638.34	274.74	1255.62
	4	258.40	84.48	635.92	268.46	1247.26
	5	258.76	84.56	637.48	268.16	1248.96
	6	258.62	84.64	617.00	263.18	1223.44
	7	262.86	84.85	626.90	267.52	1242.13
	8	262.86	84.85	620.92	276.34	1244.97
	9	258.06	95.72	629.92	268.88	1252.58
	10	258.14	90.72	635.58	267.56	1252.00

Fig. D.6 *The compression process of adsorbent into the gap between a fin-tube and a mesh*

After compressing every portion of adsorbent into fin-tubes, they were put into the oven at 150 ^{o}C for 2days as shown in Fig. D.7 to completely remove the moisture absorbed during the compression process. Ten tubes were put into ten holes at the bottom of a reactor which are the flow channel for the HTF as illustrated in Fig. D.8. A single hole is for the ammonia gas flow into the reactor and three other holes are for thermocouples to measure the temperature of the mesh outer surface at different positions as shown in Fig. D.9. Those measure temperatures were used to represent the adsorbent temperature at different locations.

Fig. D.7 *The heating process of packed fin-tubes before assembling to reactors*

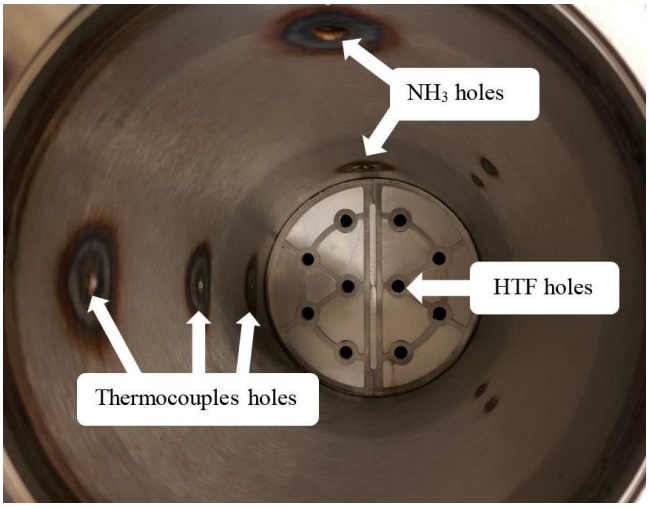

Fig. D.8 *Different channels inside a reactor*

Fig. D.9 *The contact surface between thermocouples and the mesh containing adsorbent inside*

After inserting all adsorbent in the reactors, they were covered with white lids and aligned with the alignment plates (as shown in Fig. D.10). The reactors were sealed with the rubber O-ring with grease (as shown in Fig. D.11) to prevent gas leakage. Two reactors were connected with the condenser/evaporator before pressurising nitrogen gas (as shown in Fig. D.12) for the natural gas test to ensure that there is no leakage in the system. Subsequently, three heating/cooling machines were connected to each component, i.e., two reactors and one condenser/evaporator (as shown in Fig. D.13) to control the designed conditions for experimental investigations.

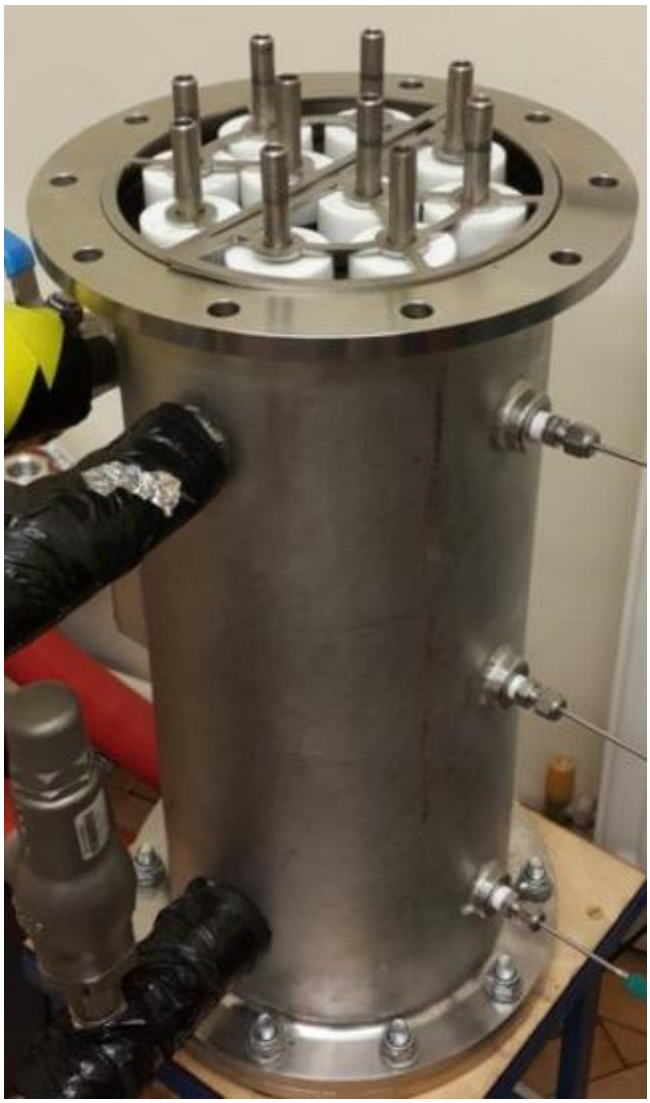

Fig. D.10 *A reactor filled with 10 tubes of adsorbent*

Fig. D.11 *A reactor top cover with the O-ring*

Fig. D.12 *Nitrogen gas pressuring process for the system's natural gas test*

(a)

(b)

Fig. D.13 *The overall system connection (a) horizontal view (b) vertical view*

Appendix E: Modelling of the water-jacket reactor in MATLAB Simulink

According to the mathematical analysis of the heat transfer and reaction kinetic of reactants in Chapter 5, as the global kinetic analysis was used, all of the governing equations are one-dimensional transient behaviour. The variables mentioned in Table 5.3 were treated as constant blocks with information linked to equations that require those constant values as shown as an example in Fig. E.1.

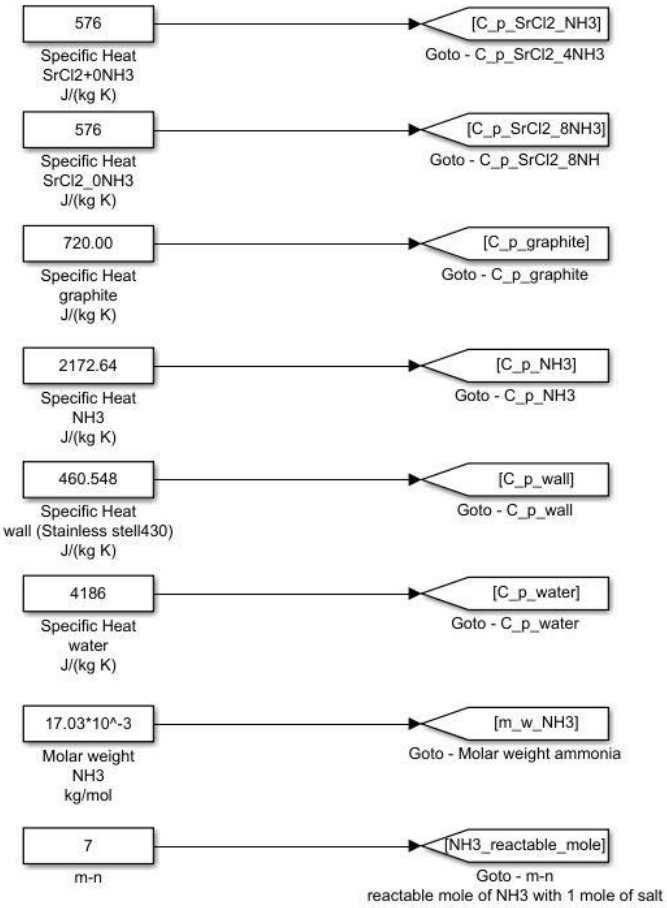

Fig. E.1 *An example of reactor models' constants treated in MATLAB Simulink*

The known parameters and reactant dimensions were input and stored in each individual reactor model and were used in other derived parameters in the models. The cross-sectional areas of each reactor layer were calculated from Eq. (E.1) for the ammonia gas channel, Eq. (E.2) for the reactant layer, Eq. (E.3) for the wall layer and Eq. (E.4) for the HTF layer. Eq. (E.1) to Eq. (E.4) were modelled in MATLAB Simulink as shown in Fig. E.2.

$$A_{NH3-CS} = \pi r_{NH3}^2 \quad \text{(E.1)}$$

where r_{NH3} is the radius of the gas channel (m)

$$A_{R-CS} = \pi(r_{NH3} + thk_R)^2 - A_{NH3-CS} \quad \text{(E.2)}$$

where thk_R is the thickness of the reactant layer (m)

$$A_{W-CS} = \pi(r_{NH3} + thk_R + thk_W)^2 - (A_{NH3-CS} + A_{R-CS}) \quad \text{(E.3)}$$

where thk_W is the thickness of the wall layer (m)

$$A_{HTF-CS} = \pi(r_{NH3} + thk_R + thk_W + thk_{HTF})^2 - (A_{NH3-CS} + A_{R-CS} + A_{W-CS}) \quad \text{(E.4)}$$

where thk_{HTF} is the thickness of the HTF layer (m)

By obtaining the preferable amount of contents in the adsorbent, i.e. salt and graphite, and the suitable density, the reactor's length can be calculated from Eq. (E.5) with components derived from Eq. (E.6) to Eq. (E.8). In MATLAB Simulink, Eq. (E.5) to Eq. (E.8) were modelled as shown in Fig. E.3(a) to Fig. E.3(d) respectively.

$$L_R = \frac{V_b}{A_{R-CS}} \quad \text{(E.5)}$$

where L_R is the reactor's length (m)

V_b is the buck (or adsorbent) volume calculated from Eq. (E.6) (m^3)

A_{R-CS} is the cross-sectional area of the reactant layer (m^2)

$$V_b = \frac{m_b}{\rho_b} \quad \text{(E.6)}$$

where m_b is the buck (or adsorbent) mass calculated from Eq. (E.7) (kg)

ρ_b is the buck (or adsorbent) density (kg/m^3)

$$m_b = m_s + m_{EG} \quad \text{(E.7)}$$

where m_s is the reactive salt mass (kg)

m_{EG} is the expanded graphite mass calculated from Eq. (E.8) (kg)

$$m_{EG} = f_{EG} \cdot m_s \quad \text{(E.8)}$$

(a)

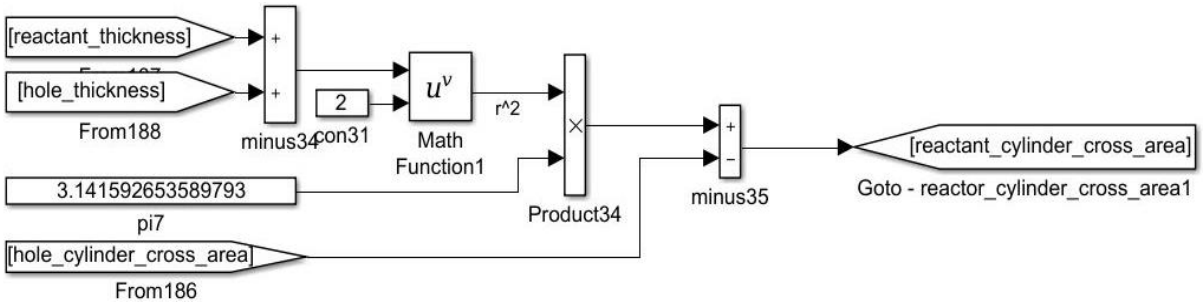

(b)

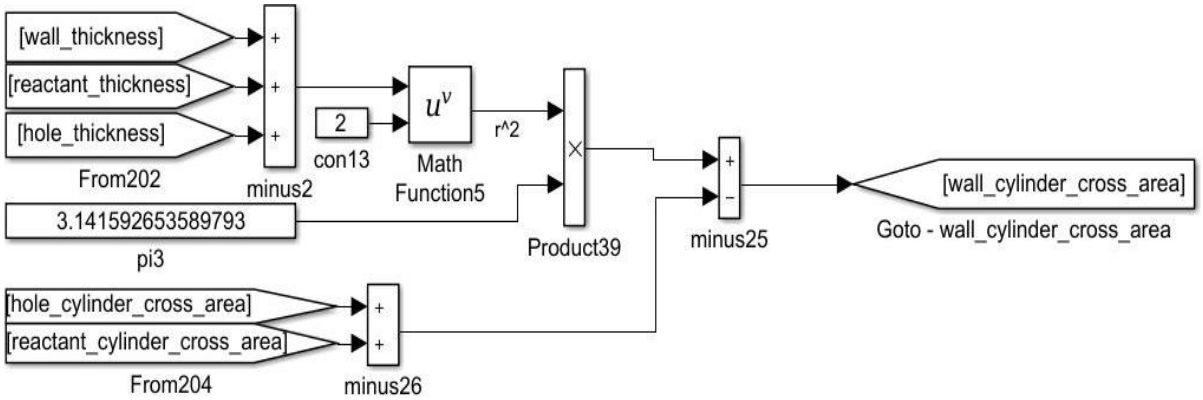

(c)

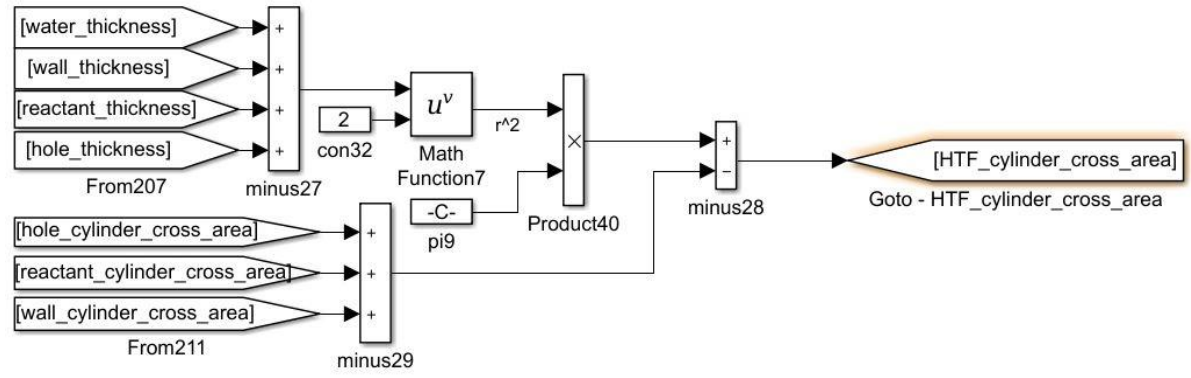

(d)

Fig. E.2 *The cross-sectional area calculation of each reactor layers modelled in MATLAB Simulink: (a) ammonia gas channel, (b) reactant layer, (c) wall layer and (d) HTF layer*

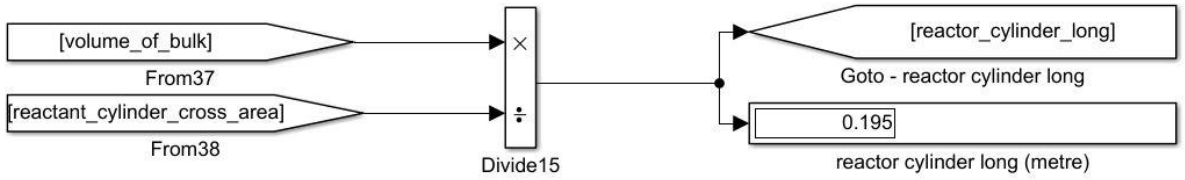

(a)

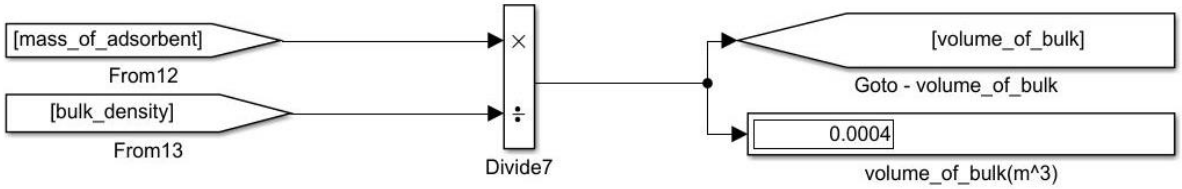

(b)

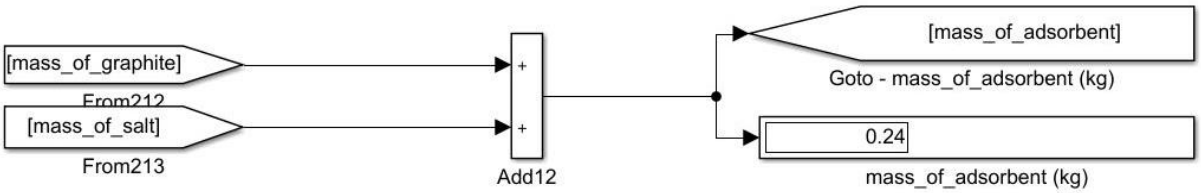

(c)

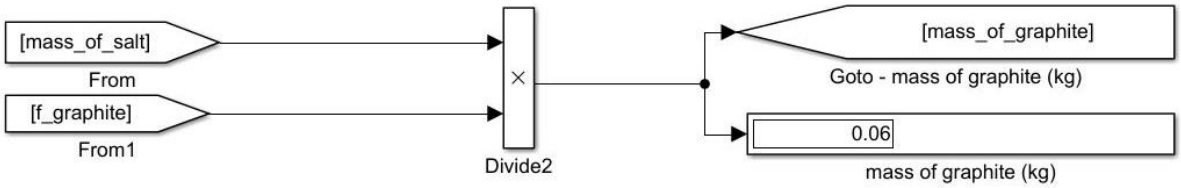

(d)

Fig. E.3 *MATLAB Simulink models of (a) reactor's length, (b) buck volume, (c) buck mass and (d) expanded graphite mass*

After every dimension of the reactor was obtained, the mass of the wall (m_W) and HTF (m_{HTF}) layers in the reactor can be derived from Eq. (E.9) and Eq. (E.10) respectively. The MATLAB Simulink models for Eq. (E.9) and Eq. (E.10) are presented in Fig. E.4(a) and Fig. E.4 (b) respectively.

$$m_W = \rho_W \cdot A_{W-CS} \cdot L_R \quad \text{(E.9)}$$

$$m_{HTF} = \rho_{water} \cdot A_{HTF-CS} \cdot L_R \quad \text{(E.10)}$$

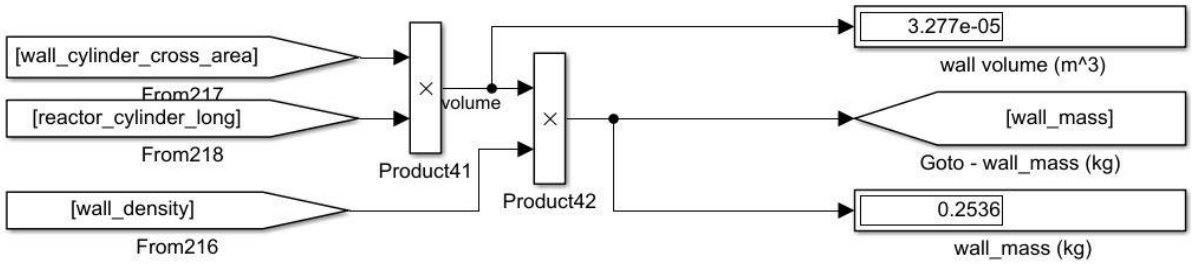

(a)

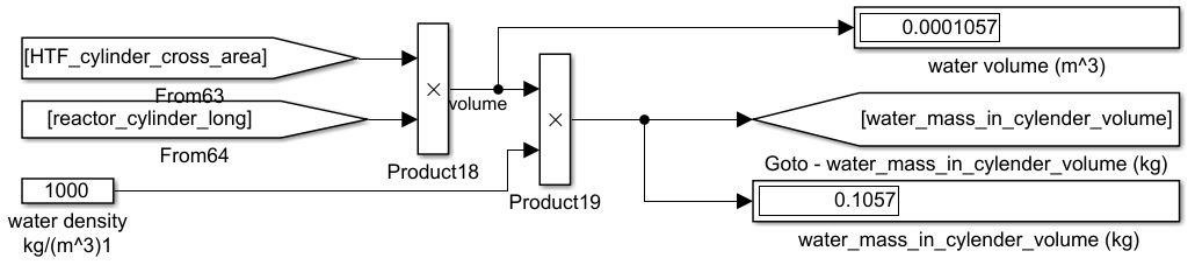

(b)

Fig. E.4 *MATLAB Simulink models of (a) the reactor's wall mass and (b) the HTF mass in the reactor*

To analyse the heat transfer between layers, contact areas between adsorbent-wall and wall-HTF were determined by Eq. (E.11) and Eq. (E.12) respectively. The MATLAB Simulink models for Eq. (E.11) and Eq. (E.12) are presented in Fig. E.5(a) and Fig. E.5 (b) respectively.

$$A_{R-W} = 2 \cdot \pi \cdot (r_{NH3} + thk_R) \cdot L_R \quad \text{(E.11)}$$

$$A_{W-HTF} = 2 \cdot \pi \cdot (r_{NH3} + thk_R + thk_W) \cdot L_R \quad \text{(E.12)}$$

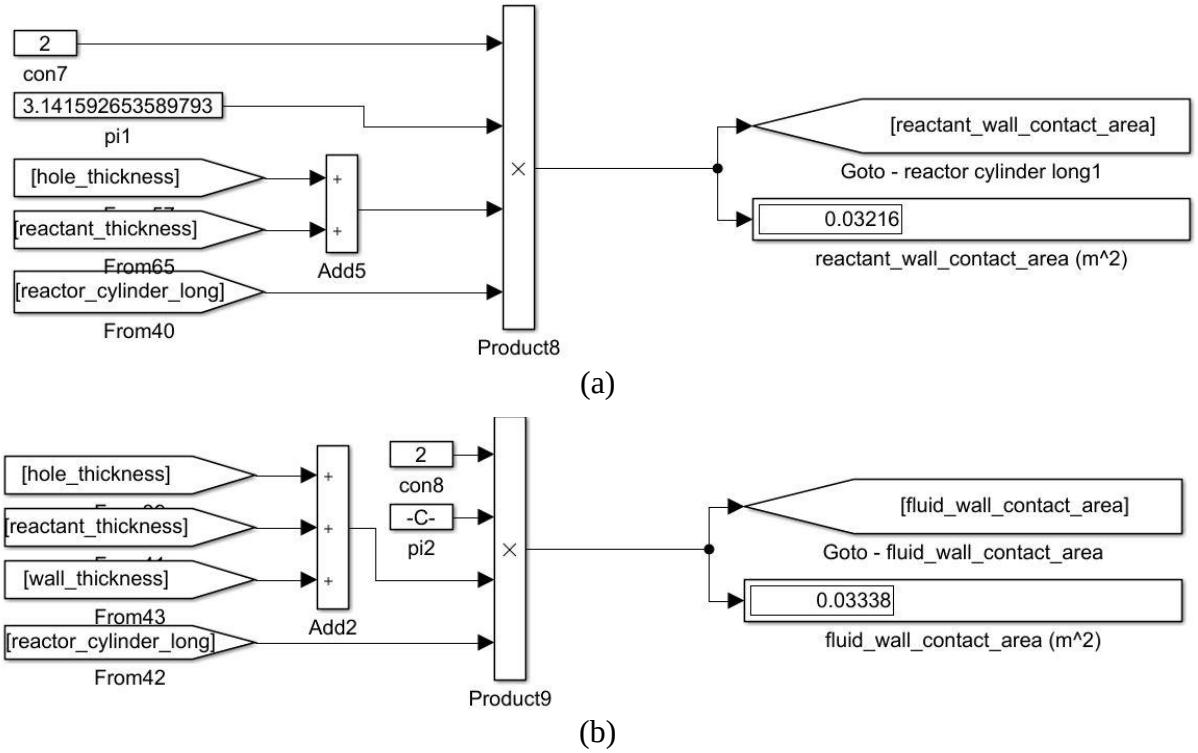

Fig. E.5 *MATLAB Simulink models of (a) the contact area between the reactant and the wall and (b) the contact area between the wall and the HTF in the reactor*

Porosity: Eq. (5.13)

To improve the heat conductivity in the reactant, expanded graphite is used as a porous material to impregnate the reactive salt and the density of the combined material called the composite material density ρ_b, affects the performance of the reaction. The porosity of the reactant in Eq. (5.13) can be modelled in MATLAB Simulink as shown in Fig. E.6.

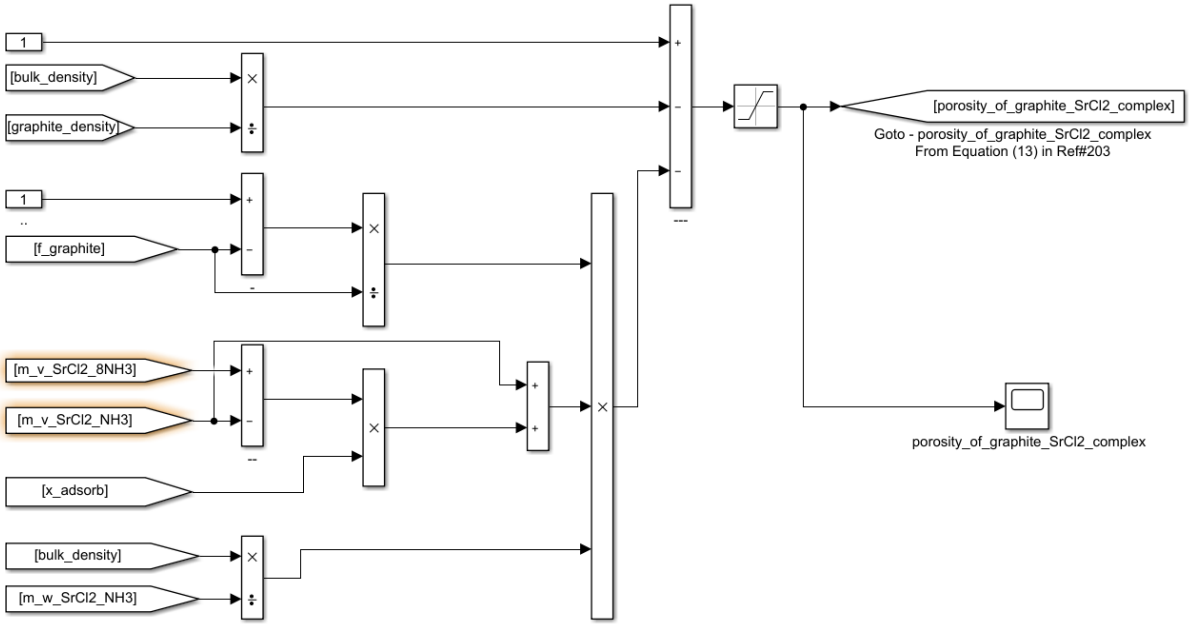

Fig. E.6 *The porosity of the reactant modelled in MATLAB Simulink*

Specific heat capacity: Eq. (5.12)

By knowing the porosity of the reactant which is a function of the degree of conversion of the reactive salt, the specific heat capacity of the reactant can be modelled as presented in Fig. E.7.

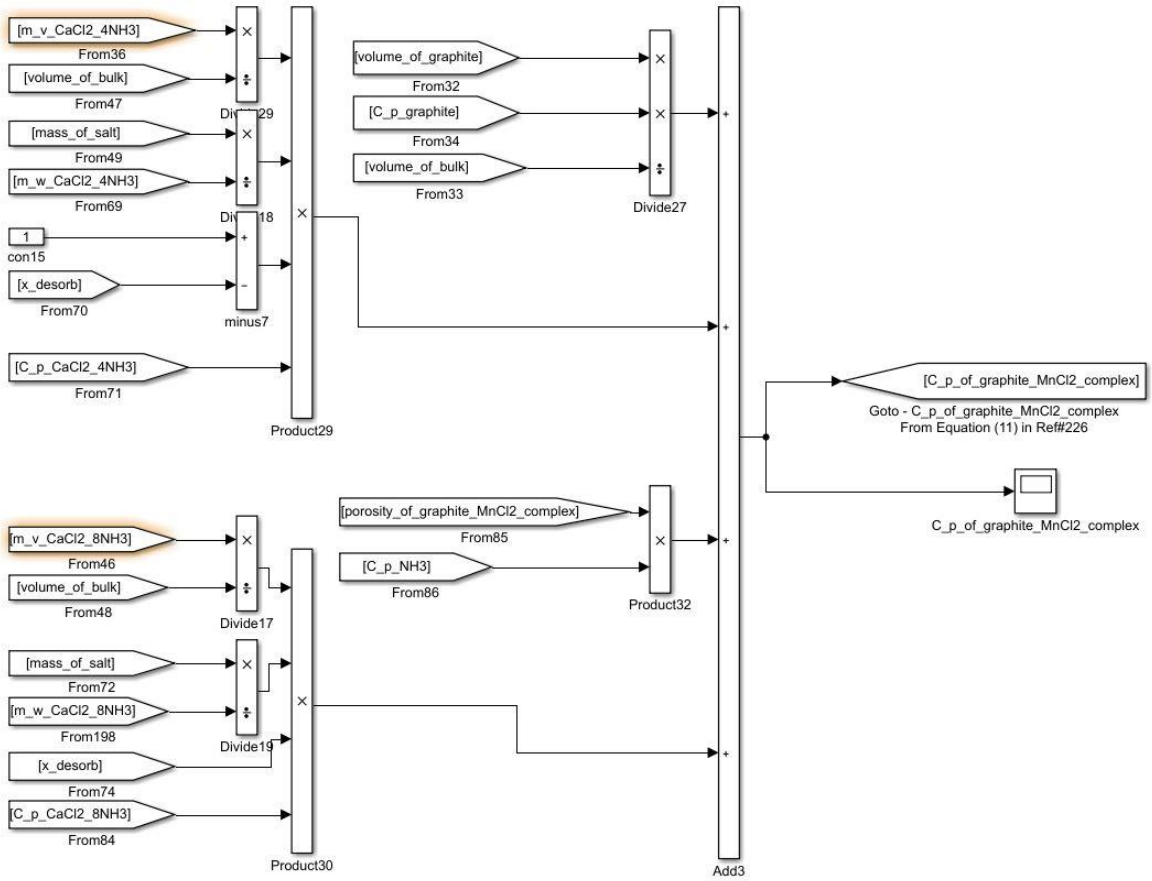

Fig. E.7 *The specific heat capacity of the reactant modelled in MATLAB Simulink*

Thermal conductivity (λ_r)

- For $SrCl_2$ model (Huang *et al.*, 2004): adsorption 19.1 W/(m· K), desorption 13.7 W/(m· K)

- For $MnCl_2$ model can be derived from (Han *et al.*, 2000) as Eq. (E.13)

The thermal conductivity of the reactant is not constant and can be experimentally obtained. The thermal conductivity of the $MnCl_2$ model is a function of the degree of conversion and can be derived from the experimental results from Han *et al.* (2000) as Eq. (E.13) which can be model in MATLAB as shown in Fig. E.8.

$$\lambda_r = 2.1417 \cdot x + 9.2 \qquad \text{(E.13)}$$

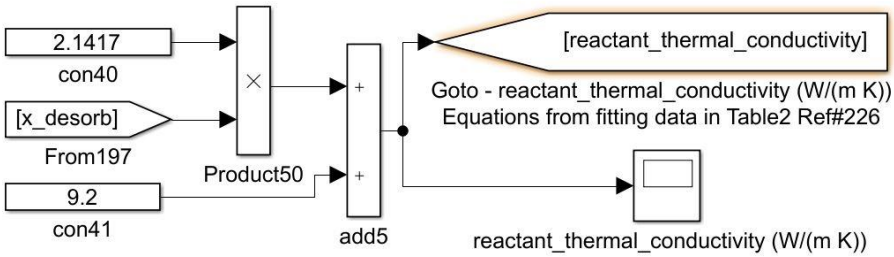

Fig. E.8 *The reactant thermal conductivity as a function of the degree of conversion modelled in MATLAB Simulink*

Overall heat exchanger coefficients (UA)

$(UA)_{fw}$ *:* Eq. (5.10)

$(UA)_{wr}$ *:* Eq. (5.11)

By knowing the convective heat transfer coefficient between the HTF and the wall (h_{fw}) and the heat transfer coefficient between the wall and the reactant (h_{wr}) in Table 5.3, the contact area between the HTF and the wall (A_{fw}), the wall thickness (δ_w) and the reactant thickness (δ_r), and the thermal conductivity of the wall (λ_w) and the reactant (λ_r), the overall heat exchange coefficient between the HTF and the wall $(UA)_{fw}$ and the overall heat exchange coefficient between the wall and the reactant $(UA)_{wr}$ can be obtained by applying Eq. (5.10) and Eq. (5.11) in MATLAB Simulink as shown in Fig. E.9 and Fig. E.10, respectively.

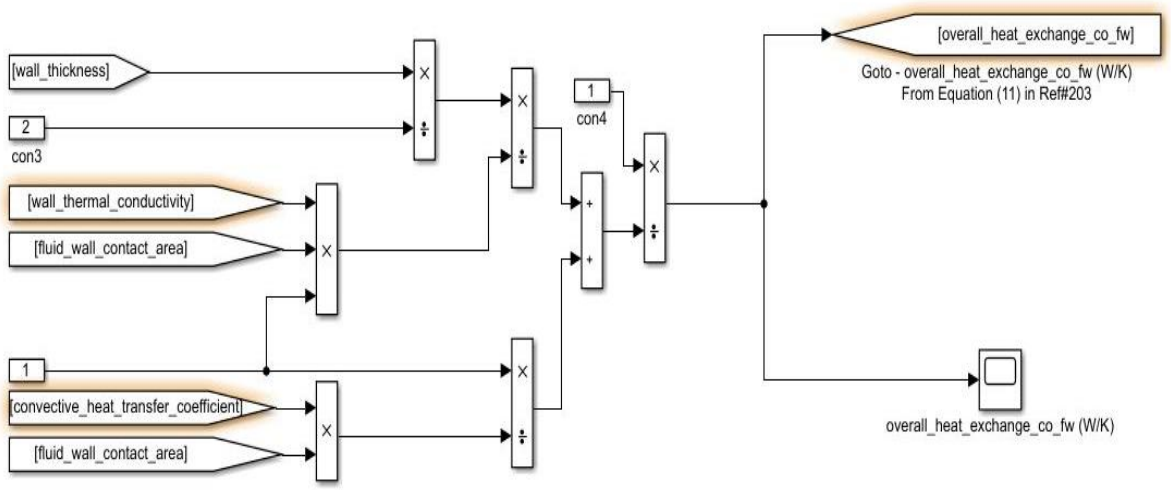

Fig. E.9 *MATLAB Simulink calculation of the overall heat exchange coefficient between the HTF and the wall* $(UA)_{fw}$

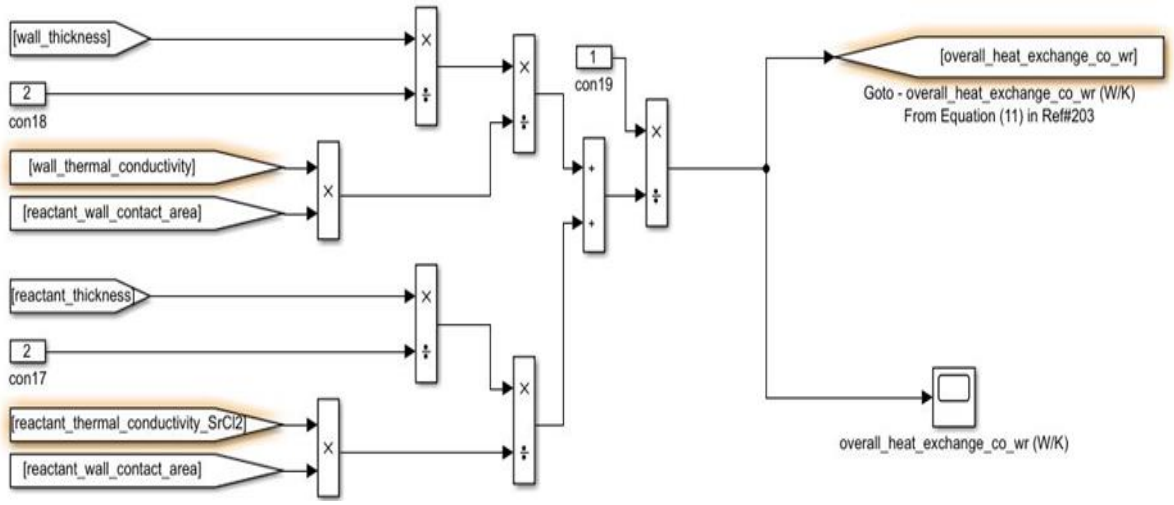

Fig. E.10 *MATLAB Simulink calculation of the overall heat exchange coefficient between the wall and the reactant* $(UA)_{wr}$

To perform the heat transfer analysis in all layers of the reactor, the reaction rate is required. The reaction rate is dependent on the operating pressure and salt equilibrium pressure. When the valve between the condenser and reactor is opened, condensation pressure will dominate the pressure in the reactor; therefore, the operating pressure (P_c), is equal to the condensation pressure. The condensation pressure in the condenser can be calculated in the MATLAB Simulink by using the ambient temperature as shown in Fig. E.11. All constants used in Fig. E.11 are from the linear correlation between temperature and pressure of the ammonia liquid/gas saturation line.

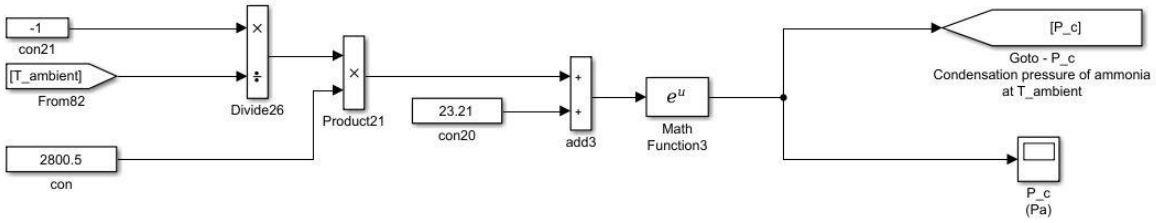

Fig. E.11 *The calculation of the condensation pressure to be used as the operating pressure in the reactor*

The salt equilibrium pressure can be achieved by recalling Eq. (4.2). However, the temperature in each layer is coupled with each other. Therefore, the numerical calculation is simultaneously performed to iteratively solve the salt equivalent pressure as shown in Fig. E.12 which has to be coupled with the reaction rate (modelled in Fig. E.13), the reactant temperature T_r (modelled in Fig. E.14), the wall temperature (modelled in Fig. E.15), and the HTF temperature (modelled in Fig. E.16).

$$\ln\left(P_{eq}\right) = -\frac{\Delta H}{RT} + \frac{\Delta S}{R} \tag{4.2}$$

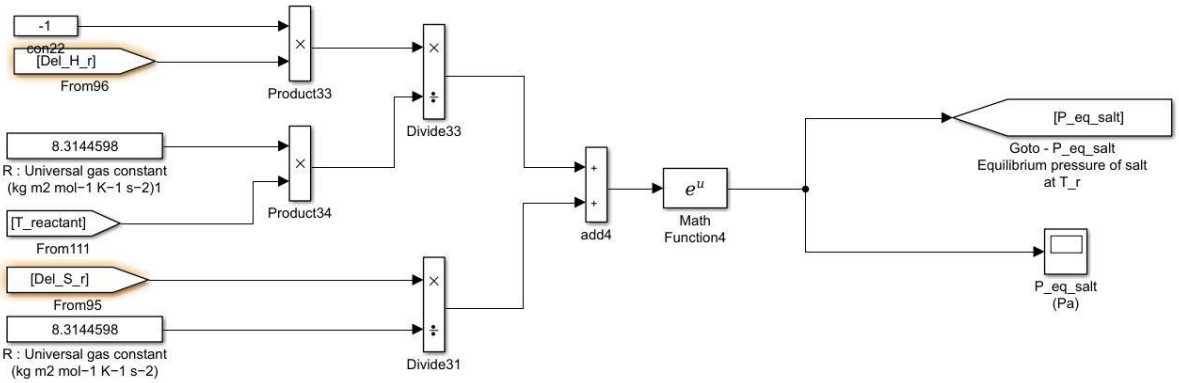

Fig. E.12 *MATLAB Simulink model to calculate the salt equilibrium pressure*

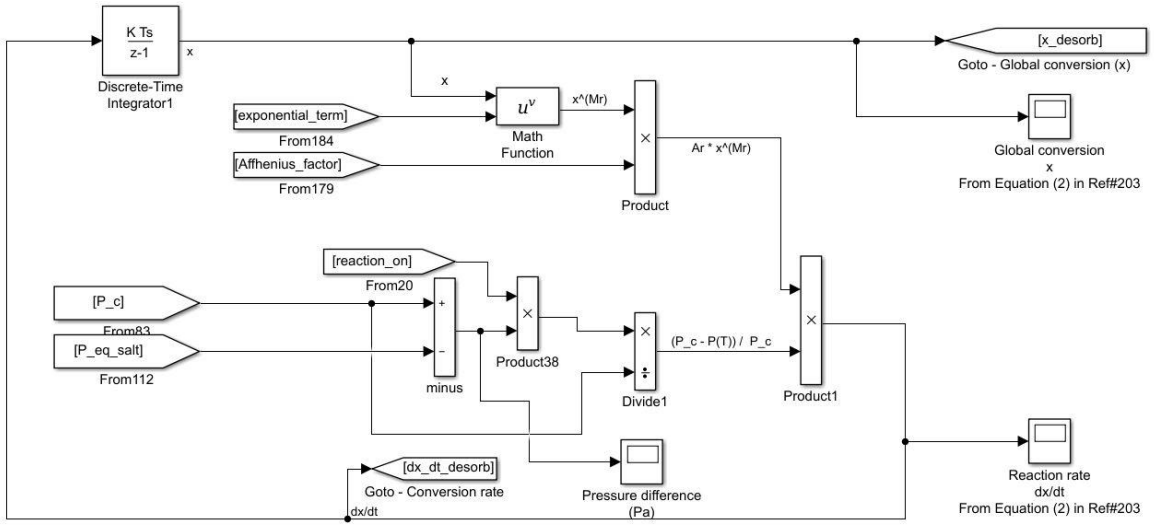

Fig. E.13 *MATLAB Simulink model to calculate the reaction rate and the degree of conversion*

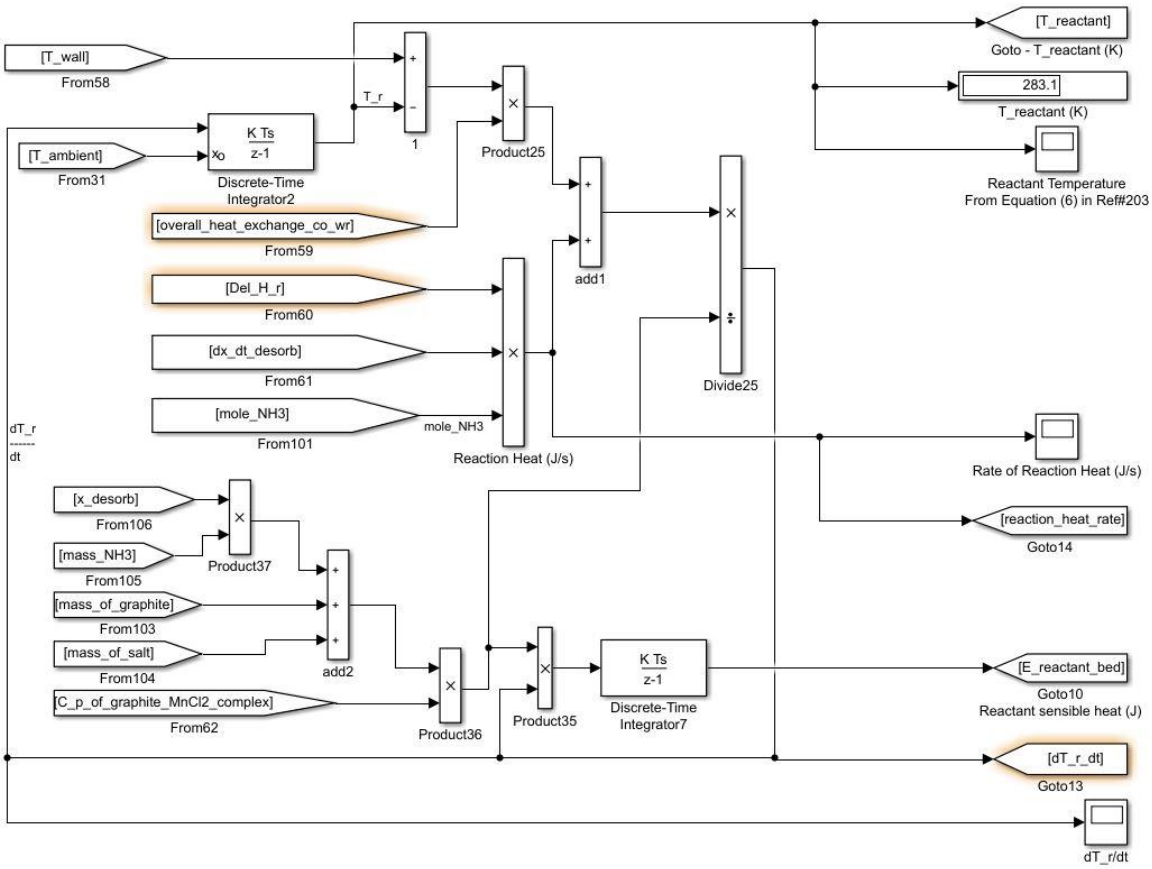

Fig. E.14 *MATLAB Simulink model to calculate the reactant temperature*

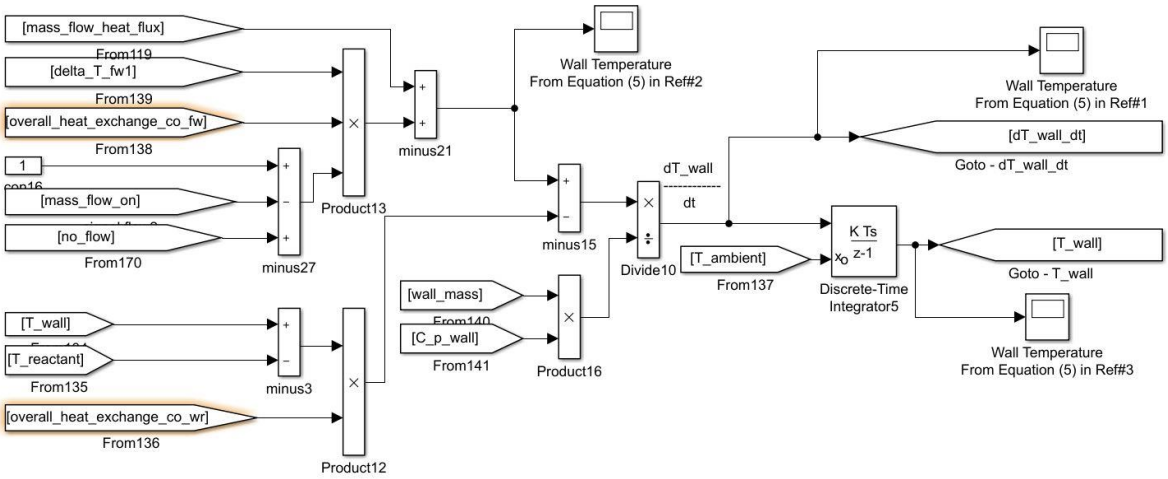

Fig. E.15 *MATLAB Simulink model to calculate the wall temperature*

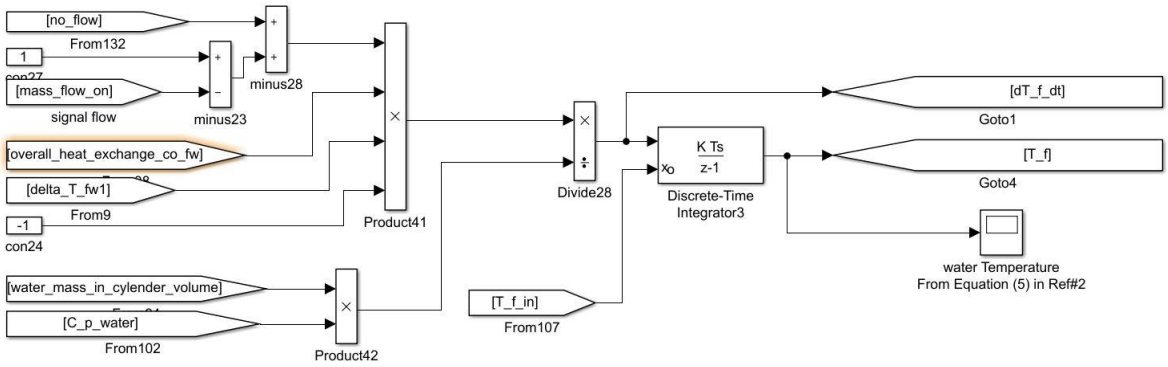

Fig. E.16 *MATLAB Simulink model to calculate the HTF temperature*

The temperature difference between the HTF and the wall (Eq. (5.6)) can be obtained from the heat exchanger logarithmic mean temperature which can be modelled in Fig. E.17.

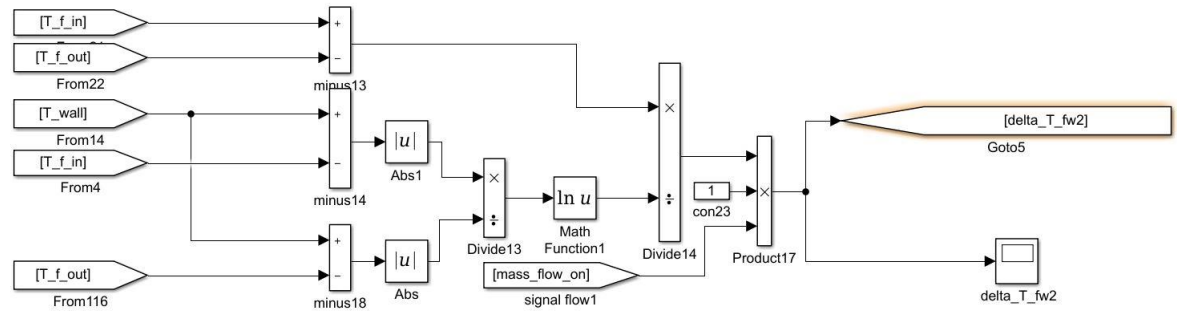

Fig. E.17 *MATLAB Simulink model to calculate the logarithmic mean temperature difference between the HTF and the wall*

Appendix F: Examples of the User Defined Function (UDF)

Example of the User Defined Function (UDF) for treating heat sources, electrical production, radiation between material layers, and transient boundary conditions

[Using the weather data on 2011/07/08 of Da-Yeh University in Taiwan in (Tsai & Tsai, 2012)]

```
/*****************************************************************************
UDF for calculating transient radiation absorbed by PVT
"[2011/07/08 of Da-Yeh University in Taiwan]"
*****************************************************************************/

#include "udf.h"
#include "unsteady.h"

#define N_PV 7000.0000
#define pv_thck 3.000000e-04
#define gl_thck 4.000000e-03
/*Define real volume of the PV (not just a part on the simulation model*/
#define pv_volume_real 1.068921e-04
#define glass_volume_real 1.425228e-03
#define Target_Temperature 3.331500e+02

/*****************Time Step Size*****************************/
DEFINE_DELTAT(time_step, domain)
{
  real time=RP_Get_Real("flow-time");
  real time_step;

  if(time<28500.0000 && time>=0.0000)

      time_step = 28500.0000;

  else if(time<57600.0000 && time>=28500.0000)

  {
      time_step = 300.0000;
  }

  else if(time>=57600.0000)

  {
      time_step = 28800.0000;
  }

   printf("TIME_STEP_SIZE= %f seconds",time_step);
```

```
    return time_step;
}

/*****************Electrical Power Generation*****************************/
/*Coefficient for P_max fitting from Temperature and Irradiance variations */
#define p00 6.613000e+02
#define p10 -1.080000e+01
#define p01 5.843000e-01
#define p20 6.982000e-02
#define p11 -4.560000e-03
#define p02 3.155000e-04
#define p30 -2.245000e-04
#define p21 1.871000e-05
#define p12 2.593000e-07
#define p03 -6.927000e-07
#define p40 3.597000e-07
#define p31 -3.874000e-08
#define p22 -2.331000e-09
#define p13 5.745000e-10
#define p04 5.717000e-10
#define p50 -2.299000e-10
#define p41 2.927000e-11
#define p32 2.442000e-12
#define p23 9.227000e-14
#define p14 -3.113000e-13
#define p05 -1.719000e-13

real source;
/*For PV*/
real avg_source=0;
real tot_vol=0;
real n=0;

/*For Glass to Sky*/
real avg_source_sky=0;
real tot_vol_glass=0;
real n_glass=0;

/*For Glass to Ground*/
real avg_source_grd=0;

DEFINE_SOURCE(source_pv2_elec_power_gen,c,t,dS,eqn)
{    real time=RP_Get_Real("flow-time");
     C_T(c,t);
     C_VOLUME(c,t);

     if(time<=300.0000 && time>0.0000)
       {
       source                                                                    =(-
1/pv_thck)*(p00+p10*C_T(c,t)+p01*0.0000+p20*C_T(c,t)*C_T(c,t)+p11*C_T(c,t)*0.0000+
p02*0.0000*0.0000+p30*C_T(c,t)*C_T(c,t)*C_T(c,t)+p21*C_T(c,t)*C_T(c,t)*0.0000+p12*
```

```
C_T(c,t)*0.0000*0.0000+p03*0.0000*0.0000*0.0000+p40*C_T(c,t)*C_T(c,t)*C_T(c,t)*C_
T(c,t)+p31*C_T(c,t)*C_T(c,t)*C_T(c,t)*0.0000+p22*C_T(c,t)*C_T(c,t)*0.0000*0.0000+p13
*C_T(c,t)*0.0000*0.0000*0.0000+p04*0.0000*0.0000*0.0000*0.0000+p50*C_T(c,t)*C_T(c
,t)*C_T(c,t)*C_T(c,t)*C_T(c,t)+p41*C_T(c,t)*C_T(c,t)*C_T(c,t)*C_T(c,t)*0.0000+p32*C_
T(c,t)*C_T(c,t)*C_T(c,t)*0.0000*0.0000+p23*C_T(c,t)*C_T(c,t)*0.0000*0.0000*0.0000+p1
4*C_T(c,t)*0.0000*0.0000*0.0000*0.0000+p05*0.0000*0.0000*0.0000*0.0000*0.0000);
          dS[eqn]=(-
1/pv_thck)*(p10+2*p20*C_T(c,t)+p11*0.0000+3*p30*C_T(c,t)*C_T(c,t)+2*p21*C_T(c,t)*
0.0000+p12*0.0000*0.0000+4*p40*C_T(c,t)*C_T(c,t)*C_T(c,t)+3*p31*C_T(c,t)*C_T(c,t)*
0.0000+2*p22*C_T(c,t)*0.0000*0.0000+p13*0.0000*0.0000*0.0000+5*p50*C_T(c,t)*C_T(
c,t)*C_T(c,t)*C_T(c,t)+4*p41*C_T(c,t)*C_T(c,t)*C_T(c,t)*0.0000+3*p32*C_T(c,t)*C_T(c,t
)*0.0000*0.0000+2*p23*C_T(c,t)*0.0000*0.0000*0.0000+p14*0.0000*0.0000*0.0000*0.00
00);
          }
         else if(time<=600.0000 && time>300.0000)

     until the last time step of 86400 seconds (one day)
     ********** time step in this UDF is 300 seconds (5 minutes)***********


         else if(time<=86400.0000 && time>86100.0000)
           {
           source                                                                    =(-
1/pv_thck)*(p00+p10*C_T(c,t)+p01*0.0000+p20*C_T(c,t)*C_T(c,t)+p11*C_T(c,t)*0.0000+
p02*0.0000*0.0000+p30*C_T(c,t)*C_T(c,t)*C_T(c,t)+p21*C_T(c,t)*C_T(c,t)*0.0000+p12*
C_T(c,t)*0.0000*0.0000+p03*0.0000*0.0000*0.0000+p40*C_T(c,t)*C_T(c,t)*C_T(c,t)*C_
T(c,t)+p31*C_T(c,t)*C_T(c,t)*C_T(c,t)*0.0000+p22*C_T(c,t)*C_T(c,t)*0.0000*0.0000+p13
*C_T(c,t)*0.0000*0.0000*0.0000+p04*0.0000*0.0000*0.0000*0.0000+p50*C_T(c,t)*C_T(c
,t)*C_T(c,t)*C_T(c,t)*C_T(c,t)+p41*C_T(c,t)*C_T(c,t)*C_T(c,t)*C_T(c,t)*0.0000+p32*C_
T(c,t)*C_T(c,t)*C_T(c,t)*0.0000*0.0000+p23*C_T(c,t)*C_T(c,t)*0.0000*0.0000*0.0000+p1
4*C_T(c,t)*0.0000*0.0000*0.0000*0.0000+p05*0.0000*0.0000*0.0000*0.0000*0.0000);
           dS[eqn]=(-
1/pv_thck)*(p10+2*p20*C_T(c,t)+p11*0.0000+3*p30*C_T(c,t)*C_T(c,t)+2*p21*C_T(c,t)*
0.0000+p12*0.0000*0.0000+4*p40*C_T(c,t)*C_T(c,t)*C_T(c,t)+3*p31*C_T(c,t)*C_T(c,t)*
0.0000+2*p22*C_T(c,t)*0.0000*0.0000+p13*0.0000*0.0000*0.0000+5*p50*C_T(c,t)*C_T(
c,t)*C_T(c,t)*C_T(c,t)+4*p41*C_T(c,t)*C_T(c,t)*C_T(c,t)*0.0000+3*p32*C_T(c,t)*C_T(c,t
)*0.0000*0.0000+2*p23*C_T(c,t)*0.0000*0.0000*0.0000+p14*0.0000*0.0000*0.0000*0.00
00);
           }
         tot_vol=tot_vol+C_VOLUME(c,t);
         avg_source=avg_source+source*C_VOLUME(c,t);
         n=n+1;
         if(n==N_PV)
           {
            avg_source=avg_source/tot_vol;
            /*Store averaged source based on real PV volume at each cell (positive is elec
production but thermal deduction)*/
            begin_c_loop(c,t)
               {
               C_UDMI(c,t,0)=-avg_source*pv_volume_real;
               }
```

```
        end_c_loop(c,t)
        n=0;
        tot_vol=0;
        avg_source=0;
       }

return source;
}


/******************Glass to Sky Radiation*****************************/
#define Zigma 5.670367e-08
#define glass_emis 8.800000e-01
DEFINE_SOURCE(source_glass_to_sky,c,t,dS,eqn)
{   real time=RP_Get_Real("flow-time");
    C_T(c,t);
    C_VOLUME(c,t);

    if(time<=300.0000 && time>0.0000)
      {
      source                          =(1/gl_thck)*glass_emis*Zigma*(9857600427.1605-
C_T(c,t)*C_T(c,t)*C_T(c,t)*C_T(c,t));
       dS[eqn]=(-4/gl_thck)*glass_emis*Zigma*(C_T(c,t)*C_T(c,t)*C_T(c,t));
       }
    else if(time<=600.0000 && time>300.0000)

until the last time step of 86400 seconds (one day)
********** time step in this UDF is 300 seconds (5 minutes)***********

   tot_vol_glass=tot_vol_glass+C_VOLUME(c,t);
   avg_source_sky=avg_source_sky+source*C_VOLUME(c,t);
   n_glass=n_glass+1;
   if(n_glass>=14999)
     {
   avg_source_sky=avg_source_sky/tot_vol_glass;
   n_glass=0;
   tot_vol_glass=0;
   avg_source_sky=0;
     }

return source;
}


/******************Glass to ground Radiation*****************************/
#define Zigma 5.670367e-08
#define glass_emis 8.800000e-01
DEFINE_SOURCE(source_glass_to_ground,c,t,dS,eqn)
{   real time=RP_Get_Real("flow-time");
    C_T(c,t);
    C_VOLUME(c,t);
```

```
        if(time<=300.0000 && time>0.0000)
          {
          source                              =(1/gl_thck)*glass_emis*Zigma*(7902040563.7635-
C_T(c,t)*C_T(c,t)*C_T(c,t)*C_T(c,t));
          dS[eqn]=(-4/gl_thck)*glass_emis*Zigma*(C_T(c,t)*C_T(c,t)*C_T(c,t));
          }
        else if(time<=600.0000 && time>300.0000)

    until the last time step of 86400 seconds (one day)
    ********** time step in this UDF is 300 seconds (5 minutes)***********

       tot_vol_glass=tot_vol_glass+C_VOLUME(c,t);
       avg_source_grd=avg_source_grd+source*C_VOLUME(c,t);
       n_glass=n_glass+1;
       if(n_glass>=14999)
         {
       avg_source_grd=avg_source_grd/tot_vol_glass;
       n_glass=0;
       tot_vol_glass=0;
       avg_source_grd=0;
         }

    return source;
    }



    /******************ambient temp************************************/
    DEFINE_PROFILE(ambient_temp, thread, position)
    {   face_t f;

       begin_f_loop(f, thread)
       {   real time=RP_Get_Real("flow-time");
            if(time<=300.0000 && time>0.0000)
           F_PROFILE(f, thread, position)=300.1500;
            else if(time<=600.0000 && time>300.0000)

    until the last time step of 86400 seconds (one day)
    ********** time step in this UDF is 300 seconds (5 minutes)***********

       }
       end_f_loop(f,thread)
    }



    /********************Fluid inlet temp************************************/
    DEFINE_PROFILE(fluid_inlet_temp, thread, position)
    {   face_t f;
```

```
   begin_f_loop(f, thread)
   {
      F_PROFILE(f, thread, position)=300.1500;
   }
   end_f_loop(f,thread)
}



/***************wind speed************************************/
DEFINE_PROFILE(wind_speed, thread, position)
{  face_t f;

   begin_f_loop(f, thread)
   {   real time=RP_Get_Real("flow-time");
         if(time<=300.0000 && time>0.0000)
        F_PROFILE(f, thread, position)=2.0000;
         else if(time<=600.0000 && time>300.0000)
           F_PROFILE(f, thread, position)=2.0000;

until the last time step of 86400 seconds (one day)
********** time step in this UDF is 300 seconds (5 minutes)***********

   }
   end_f_loop(f,thread)
}



/********************glass heat absorption**********************/
DEFINE_PROFILE(glass_heat_gen1, thread, position)
{  cell_t c;
   begin_c_loop(c, thread)
   {   real time=RP_Get_Real("flow-time");
         if(time<=300.0000 && time>0.0000)
        F_PROFILE(c, thread, position)=0.0000;
         else if(time<=600.0000 && time>300.0000)
           F_PROFILE(c, thread, position)=0.0000;

until the last time step of 86400 seconds (one day)
********** time step in this UDF is 300 seconds (5 minutes)***********

   }
   end_c_loop(c,thread)
}



/**********************pv heat absorption*************************/
DEFINE_PROFILE(pv_heat_gen1, thread, position)
{  cell_t c;
   begin_c_loop(c, thread)
   {   real time=RP_Get_Real("flow-time");
```

```
          if(time<=300.0000 && time>0.0000)
         F_PROFILE(c, thread, position)=0.0000;
          else if(time<=600.0000 && time>300.0000)
            F_PROFILE(c, thread, position)=0.0000;

          until the last time step of 86400 seconds (one day)
********** time step in this UDF is 300 seconds (5 minutes)***********

    }
    end_c_loop(c,thread)
}


/**************DEFINE_EXECUTE_AT_END*************************/
DEFINE_EXECUTE_AT_END(execute_at_end)
{
Domain *d;
int id;
Thread *t;
cell_t c;
real time;
real m=0;
real EX_tot_vol=0;
real EX_avg_T_PV=0;
real EX_avg_PV_source=0;
int id3;
Thread *t3;
face_t f3;
d=Get_Domain(1);
time=RP_Get_Real("flow-time");
id=10.0000; /*PV cell thread ID*/
t=Lookup_Thread(d,id);

   begin_c_loop(c,t)
      {
       EX_tot_vol=EX_tot_vol+C_VOLUME(c,t);
       EX_avg_T_PV=EX_avg_T_PV+C_T(c,t)*C_VOLUME(c,t);
       EX_avg_PV_source=EX_avg_PV_source+C_UDMI(c,t,0)*C_VOLUME(c,t);
       m=m+1;
      }
   end_c_loop(c,t)
   EX_avg_T_PV=EX_avg_T_PV/EX_tot_vol;
   EX_avg_PV_source=EX_avg_PV_source/EX_tot_vol;
   /*----------for clearing velocity value at each time step----------    */
   id3=35.0000; /*Fluid velocity inlet face thread ID*/
   t3=Lookup_Thread(d,id3);

          begin_f_loop(f3,t3)
            {
             F_UDMI(f3,t3,2)=0;
            }
```

```
            end_f_loop(f3,t3)
   /*---------------------------------------------------------------    */
printf(" *****EX_avg_T_PV = %f Kelvin !!
",EX_avg_T_PV );
printf(" *****EX_Pv_electricity_source= %f W !!
",EX_avg_PV_source);
printf(" *****First Iteration if 0 = %f m/s !!\n",F_UDMI(10,t3,2));
}


/*************DEFINE_ADJUST(mass_flow_adjust)************************/
DEFINE_ADJUST(mass_flow_adjust,d2)
{
/*  ----------Define variables-------------------------------------     */
Domain *d2;
int id2;
Thread *t2;
face_t f;
real AD_tot_area=0;
real AD_tot_area3=0;
real AD_avg_T_Fluid=0;
real AD_avg_U_Fluid_in=0;
real A1[ND_ND];
real A3[ND_ND];
real current_time;
real previous_time;
real increment;
/*  ---------------------------------------------------------------    */
/*  ----------Point to the calculated zone(s)----------      */
d2=Get_Domain(1);
id2=29.0000; /*Fluid pressure outlet face thread ID*/
t2=Lookup_Thread(d2,id2);
/*  ---------------------------------------------------------------    */
/*  ----------Loop for Temperature (Area-weighted average)----------      */
       begin_f_loop(f,t2)
       {
         F_AREA(A1,f,t2);
         AD_tot_area=AD_tot_area+NV_MAG(A1);
         AD_avg_T_Fluid=AD_avg_T_Fluid+F_T(f,t2)*NV_MAG(A1);
       }
       end_f_loop(f,t2)

       AD_avg_T_Fluid=AD_avg_T_Fluid/AD_tot_area;

printf(" *****AD_avg_Temperature_Fluid_Out= %f Kelvin !!\n",AD_avg_T_Fluid);

/*  ---------------------------------------------------------------    */
/*  -------Condition for Fluid Output Temperature is less than target Temperature------     */
       if(AD_avg_T_Fluid<333.1500)
       {
        int id3;
```

```
        Thread *t3;
        face_t f3;
        id3=35.0000; /*Fluid velocity inlet face thread ID*/
        t3=Lookup_Thread(d2,id3);

            begin_f_loop(f3,t3)
              {
    /*  ------------------First Iteration at Current Time-step----------      */
                  current_time=CURRENT_TIME;
                  previous_time=PREVIOUS_TIME;
                if(F_UDMI(10,t3,2)==0)
                 {
                  F_U(f3,t3)=F_UDMI(f3,t3,1);
                  F_UDMI(f3,t3,1)=F_U(f3,t3);
                  F_UDMI(f3,t3,2)=1;
                 }
    /*  ------------------Later Iteration at Current Time-step----------      */
                else if(F_UDMI(10,t3,2)==2)
                 {
                  F_U(f3,t3)=0.0010;
                  F_UDMI(f3,t3,1)=F_U(f3,t3);
                  F_UDMI(f3,t3,2)=2;
                 }
                else
                 {
                    if(F_UDMI(10,t3,1)<=0.001)
                    {
                      F_U(f3,t3)=0.001;
                      F_UDMI(f3,t3,2)=2;
                    }
                    else
                    {
                      F_U(f3,t3)=F_UDMI(f3,t3,1)-0.0001;
                      F_UDMI(f3,t3,2)=3;
                    }
                  F_UDMI(f3,t3,1)=F_U(f3,t3);
                 }
              }
            end_f_loop(f3,t3)
    printf(" *****Velocity in at next Iteration(T<333.1500)= %f m/s !!\n",F_U(10,t3));
    printf(" *****F_UDMI(f3,t3,2)=%f [Clear with Execute at end =0 ; Set V=0.005m/s at
first iteration =1 ; Reduce V until V=0m/s then set to 0.001m/s =2 ; else Still reducing fluid
velocity to get target Temperature  !!\n",F_UDMI(10,t3,2));

        }
    /*  ---------------------------------------------------------------    */
    /*  ------Condition for Fluid Output Temperature reaches the target Temperature-------     */
        else if(AD_avg_T_Fluid>=333.1500)
        {
         int id3;
         Thread *t3;
```

```
        face_t f3;
        id3=35.0000; /*Fluid velocity inlet face thread ID*/
        t3=Lookup_Thread(d2,id3);

           begin_f_loop(f3,t3)
           {
/*  ------------------First Iteration at Current Time-step----------      */
              if(F_UDMI(10,t3,2)==0)
              {
                 F_U(f3,t3)=0.0050;
                 F_UDMI(f3,t3,1)=F_U(f3,t3);
                 F_UDMI(10,t3,2)=1;
              }
/*  ------------------Later Iteration at Current Time-step----------      */
              else
              {
                F_U(f3,t3)=F_UDMI(f3,t3,1)+0.0001;
                F_UDMI(f3,t3,1)=F_U(f3,t3);
                F_UDMI(f3,t3,2)=3;
              }
           }
           end_f_loop(f3,t3)

printf(" *****Velocity in at next Iteration(T>=333.1500)= %f m/s !!\n",F_UDMI(1,t3,1));
printf(" *****First Iteration if 0      [%f]  !!\n",F_UDMI(10,t3,2));

      }
/*  ----------------------------------------------------------------    */

}
/***************FINISHED DEFINE_ADJUST(mass_flow_adjust)****************/


/****************DEFINE_PROFILE(velocity_inlet_adjust)******************** /
DEFINE_PROFILE(fluid_inlet_velocity, thread, position)
{
face_t f;

   begin_f_loop(f, thread)
   {
              if(F_UDMI(10,thread,2)==0)
              {
                 F_PROFILE(f, thread, position)=0.005;
               }
              else
              {
                 F_PROFILE(f, thread, position)=F_UDMI(f,thread,1);
               }
   }
   end_f_loop(f, thread)
}
```

References

Aberg, E., Adib, R., Appavou, F., Brown, A., et al. (2018) *RENEWABLES 2018 GLOBAL STATUS REPORT*. [Online]. Available from: doi:978-3-9818911-3-3.

Adelard, L., Pignolet-Tardan, F., Mara, T., Lauret, P., et al. (1998) Sky temperature modelisation and applications in building simulation. *Renewable Energy*. 15 (1–4), 418–430.

Akinyele, D.O. & Rayudu, R.K. (2014) Review of energy storage technologies for sustainable power networks. *Sustainable Energy Technologies and Assessments*. [Online] 8, 74–91. Available from: doi:10.1016/j.seta.2014.07.004.

Al-Waeli, A.H.A., Sopian, K., Chaichan, M.T., Kazem, H.A., et al. (2017a) An experimental investigation of SiC nanofluid as a base-fluid for a photovoltaic thermal PV/T system. *Energy Conversion And Management*. [Online] 142, 547–558. Available from: doi:10.1016/j.enconman.2017.03.076.

Al-Waeli, A.H.A., Sopian, K., Chaichan, M.T., Kazem, H.A., et al. (2017b) Evaluation of the nanofluid and nano-PCM based photovoltaic thermal (PVT) system: An experimental study. *Energy Conversion And Management*. [Online] 151, 693–708. Available from: doi:10.1016/j.enconman.2017.09.032.

Al-Waeli, A.H.A., Sopian, K., Kazem, H.A. & Chaichan, M.T. (2017c) Photovoltaic/Thermal (PV/T) systems: Status and future prospects. *Renewable and Sustainable Energy Reviews*. [Online] 77, 109–130. Available from: doi:10.1016/j.rser.2017.03.126.

Ali, D.M. (2011) Energy Capacity and Economic Viability Assessment of the Renewable Hydrogen Energy Storage as a Balancing Mechanism in addressing the Electric System Integration Issues Inherent with Variable Renewable Energy Resources. *IET Conference on Reliability of Transmission and Distribution Networks (RTDN 2011)*. [Online] 1–7. Available from: doi:10.1049/cp.2011.0523.

AltaDevices (2017) *Why Use Gallium Arsenide Solar Cells? - Alta Devices*. [Online]. 2017. Available from: https://www.altadevices.com/use-gallium-arsenide-solar-cells/ [Accessed: 17 July 2019].

Amori, K.E. & Taqi Al-Najjar, H.M. (2012) Analysis of thermal and electrical performance of a hybrid (PV/T) air based solar collector for Iraq. *Applied Energy*. [Online] 98, 384–395. Available from: doi:10.1016/j.apenergy.2012.03.061.

Anglin, R. V (2010) *Promoting Sustainable Local and Community Economic Development*.

Anon (2019a) *Gaas Gallium Arsenide Solar Cell With Up To 30% Conversion Efficiency - Buy Gaas,Gaas Solar Cell,Solar Cell Product on Alibaba.com*. [Online]. 2019. Alibaba.com. Available from: https://www.alibaba.com/product-detail/GaAs-Gallium-Arsenide-Solar-Cell-with_62230272381.html?spm=a2700.7724857.normalList.21.364751a9HIiaZd [Accessed: 17 August 2019].

Anon (2019b) *Gaas Gallium Arsenide Solar Cell With Up To 30% Conversion Efficiency - Buy Gaas,Gaas Solar Cell,Solar Cell Product on Alibaba.com*. 2019. Alibaba.com.

Anon (2015) *Solar Energy Calculator Sizing Guide*. [Online]. Available from: http://www.pvfitcalculator.energysavingtrust.org.uk/Documents/150224_SolarEnergy_C

alculator_Sizing_Guide_v1.pdf.

ANSYS Fluent (2013) *ANSYS Fluent Theory Guide Release 15.0*. Southpointe 275, Technology Drive, Canonsburg, PA 15317.

ANSYS, I. (2013) ANSYS Meshing User's Guide. In: *ANSYS Meshing User's Guide*. Canonsburg, PA, ANSYS, Inc. p. 492.

Aste, N., Leonforte, F. & Del Pero, C. (2015) Design, modeling and performance monitoring of a photovoltaic-thermal (PVT) water collector. *Solar Energy*. [Online] 112, 85–99. Available from: doi:10.1016/j.solener.2014.11.025.

Avasthi, P. & Balakrishnan, V. (2019) Tuning the Wettability of Vertically Aligned CNT–TiO 2 Hybrid Electrodes for Enhanced Supercapacitor Performance. *Advanced Materials Interfaces*. [Online] 6 (6). Available from: doi:10.1002/admi.201801842.

Ayompe, L.M., Duffy, A., Mc Keever, M., Conlon, M., et al. (2011) Comparative field performance study of flat plate and heat pipe evacuated tube collectors (ETCs) for domestic water heating systems in a temperate climate. *Energy*. [Online] Available from: doi:10.1016/j.energy.2011.03.034.

Azoumah, Y., Neveu, P. & Mazet, N. (2007) Optimal design of thermochemical reactors based on constructal approach. *AIChE Journal*. [Online] Available from: doi:10.1002/aic.11152.

Babu, C. & Ponnambalam, P. (2017) The role of thermoelectric generators in the hybrid PV/T systems: A review. *Energy Conversion And Management*. [Online] 151, 368–385. Available from: doi:10.1016/j.enconman.2017.08.060.

Baggs, S.A. (1983) Remote prediction of ground temperature in Australian soils and mapping its distribution. *Solar Energy*. [Online] 30(4), 351–366. Available from: doi:10.1016/0038-092x(83)90189-5info:doi/10.1016/0038-092X(83)90189-5.

Bahaidarah, H.M.S., Baloch, A.A.B. & Gandhidasan, P. (2016) Uniform cooling of photovoltaic panels: A review. *Renewable and Sustainable Energy Reviews*. [Online] 57, 1520–1544. Available from: doi:10.1016/j.rser.2015.12.064.

Bakos, G.C., Ioannidis, I., Tsagas, N.F. & Seftelis, I. (2001) Design, optimisation and conversion-efficiency determination of a line-focus parabolic-trough solar-collector (PTC). *Applied Energy*. [Online] 68 (1), 43–50. Available from: doi:10.1016/S0306-2619(00)00034-9.

Bao, H., Ma, Z. & Roskilly, A.P. (2017) An optimised chemisorption cycle for power generation using low grade heat. *Applied Energy*. [Online] Available from: doi:10.1016/j.apenergy.2016.06.080.

Bao, H., Ma, Z. & Roskilly, A.P. (2016) Integrated chemisorption cycles for ultra-low grade heat recovery and thermo-electric energy storage and exploitation. *Applied Energy*. [Online] 164, 228–236. Available from: doi:10.1016/j.apenergy.2015.11.052.

Bao, H., Wang, Y. & Roskilly, A.P. (2014) Modelling of a chemisorption refrigeration and power cogeneration system. *Applied Energy*. [Online] 119, 351–362. Available from: doi:10.1016/j.apenergy.2014.01.012.

Bao, H.S., Oliveira, R.G., Wang, R.Z. & Wang, L.W. (2010) Choice of low temperature salt for a resorption refrigerator. *Industrial and Engineering Chemistry Research*. [Online] 49, 4897–4903. Available from: doi:10.1021/ie901575k.

Bell, I.H., Wronski, J., Quoilin, S. & Lemort, V. (2014) Pure and pseudo-pure fluid thermophysical property evaluation and the open-source thermophysical property library coolprop. *Industrial and Engineering Chemistry Research*. [Online] 53, 2498–2508. Available from: doi:10.1021/ie4033999.

Bell Telephone, L. (2000) Bell telephone system technical publications - v.2271-2300 1954. *Bell telephone system technical publications*.

Bendor, R., Anacleto, J., Facey, D., Fels, S., et al. (2015) Sustainability in an imaginary world. *Interactions*. [Online] 22 (5), 54–57. Available from: doi:10.1145/2801039.

van Den Berg, M., Hof, A., van Vliet, J. & van Vuuren, D. (2015) Impact of the choice of emission metric on greenhouse gas abatement and costs. *Environmental Research Letters*. [Online] 10 (2). Available from: doi:10.1088/1748-9326/10/2/024001.

Bianchini, A., Gambuti, M., Pellegrini, M. & Saccani, C. (2016) Performance analysis and economic assessment of different photovoltaic technologies based on experimental measurements. *Renewable Energy*. [Online] 85, 1–11. Available from: doi:10.1016/j.renene.2015.06.017.

Bluesun (2019) *300w 350w Amorphous Silicon Solar Panel For Roof Solar Panel System - Buy Roof Solar Panel System,Amorphous Silicon Solar Panel System,Grid-tie Solar Power System Product on Alibaba.com*. [Online]. 2019. Alibaba.com. Available from: https://www.alibaba.com/product-detail/300w-350w-amorphous-silicon-solar-panel_62054215509.html?spm=a2700.7724838.2017115.32.30d274edlRks3X&s=p [Accessed: 18 August 2019].

Bolund, B., Bernhoff, H. & Leijon, M. (2007) Flywheel energy and power storage systems. *Renewable and Sustainable Energy Reviews*. [Online] 11, 235–258. Available from: doi:10.1016/j.rser.2005.01.004.

Brian Wang (2019) *First Commercial Perovskite Solar Late in 2019 and the Road to Moving the Energy Needle – NextBigFuture.com*. [Online]. 2019. Next big future. Available from: https://www.nextbigfuture.com/2019/02/first-commercial-perovskite-solar-late-in-2019-and-the-road-to-moving-the-energy-needle.html [Accessed: 18 August 2019].

Buck, A. (1981) New equations for computing vapor pressure and enhancement factor Arden Buck (ed.). *Journal of Applied Meteorology, Boston*. 20 (12), 1527–1532.

Carrero, C., Amador, J. & Arnaltes, S. (2007) A single procedure for helping PV designers to select silicon PV modules and evaluate the loss resistances. *Renewable Energy*. [Online] 32 (15), 2579–2589. Available from: doi:10.1016/j.renene.2007.01.001.

Chen, J., Yang, D., Song, D., Jiang, J., et al. (2015) Recent progress in enhancing solar-to-hydrogen efficiency. *Journal of Power Sources*. [Online] 280, 649–666. Available from: doi:10.1016/j.jpowsour.2015.01.073.

Chin, V.J., Salam, Z. & Ishaque, K. (2016) An accurate modelling of the two-diode model of PV module using a hybrid solution based on differential evolution. *Energy Conversion And Management*. [Online] 124, 42–50. Available from: doi:10.1016/j.enconman.2016.06.076.

Chow, T. (2007) Photovoltaic-Thermal Collector System for Domestic Application T Chow (ed.). *Journal of Solar Energy Engineering (Transactions of the ASME)*. [Online] 129 (2), 205–209. Available from: doi:10.1115/1.2711474.

Chow, T.T. (2010) A review on photovoltaic/thermal hybrid solar technology. *Applied Energy*. [Online] 87 (2), 365–379. Available from: doi:10.1016/j.apenergy.2009.06.037.

Chow, T.T., Chan, A.L.S., Fong, K.F., Lin, Z., et al. (2009a) Annual performance of building-integrated photovoltaic/water-heating system for warm climate application. *Applied Energy*. [Online] 86 (5), 689–696. Available from: doi:10.1016/j.apenergy.2008.09.014.

Chow, T.T., Pei, G., Fong, K.F., Lin, Z., et al. (2009b) Energy and exergy analysis of photovoltaic–thermal collector with and without glass cover. *Applied Energy*. [Online] 86 (3), 310–316. Available from: doi:10.1016/j.apenergy.2008.04.016.

Chu, S. & Majumdar, A. (2012) Opportunities and challenges for a sustainable energy future. *Nature*. [Online]. Available from: doi:10.1038/nature11475.

Connolly, J.P., Mencaraglia, D., Renard, C. & Bouchier, D. (2013) *Designing III-V Multijunction Solar Cells on Silicon*. [Online] Available from: doi:10.4229/28thEUPVSEC2013-1AV.1.24.

Converse, A. (2012) Seasonal Energy Storage in a Renewable Energy System. *Proceedings Of The Ieee*. [Online] 100 (2), 401–409. Available from: doi:10.1109/JPROC.2011.2105231.

Czanderna, A.W. & Pern, F.J. (1996) Encapsulation of PV modules using ethylene vinyl acetate copolymer as a pottant: A critical review. *Solar Energy Materials and Solar Cells*. [Online] Available from: doi:10.1016/0927-0248(95)00150-6.

Daghigh, R., Ruslan, M.H., Zaharim, A. & Sopian, K. (2011) Effect of packing factor on the performance of PV/T water heater. In: *International Conference on ENERGY & ENVIRONMENT, 6th*. 2011 Citeseer. pp. 304–309.

Daneshazarian, R., Cuce, E., Cuce, P.M. & Sher, F. (2018) Concentrating photovoltaic thermal (CPVT) collectors and systems: Theory, performance assessment and applications. *Renewable and Sustainable Energy Reviews*. [Online] 81, 473–492. Available from: doi:10.1016/j.rser.2017.08.013.

Energy and Industrial Strategy Department for Business (ed.) (2018) *Energy Trends: Gas*. [Online]. Available from: https://www.gov.uk/government/statistics/gas-section-4-energy-trends.

Department of Energy and Climate Change, D. (2015) *UK ENERGY IN BRIEF 2015*.

Dodds, P.E., Staffell, I., Hawkes, A.D., Li, F., et al. (2015a) Hydrogen and fuel cell technologies for heating: A review. *International Journal of Hydrogen Energy*. [Online] 40, 2065–2083. Available from: doi:10.1016/j.ijhydene.2014.11.059.

Dodds, P.E., Staffell, I., Hawkes, A.D., Li, F., et al. (2015b) Hydrogen and fuel cell technologies for heating: A review. *International Journal of Hydrogen Energy*. [Online] 40, 2065–2083. Available from: doi:10.1016/j.ijhydene.2014.11.059.

Doetsch, C. & Burfeind, J. (2016) Vanadium Redox Flow Batteries. In: *Storing Energy: With Special Reference to Renewable Energy Sources*. [Online]. Elsevier Inc. pp. 227–246. Available from: doi:10.1016/B978-0-12-803440-8.00012-9.

Drück, H., Fischer, S. & Müller-Steinhagen, H. (2007) Solar keymark testing of solar thermal products. In: *ISES Solar World Congress 2007, ISES 2007*. [Online]. 2007 pp. 2094–2099. Available from: doi:10.1007/978-3-540-75997-3_425.

Dubey, S. & Tiwari, G.N. (2009) Analysis of PV/T flat plate water collectors connected in

series. *Solar Energy*. [Online] 83 (9), 1485–1498. Available from: doi:10.1016/j.solener.2009.04.002.

Duffie, J.A. & Beckman, W.A. (2013) *Solar Engineering of Thermal Processes: Fourth Edition*. [Online]. Available from: doi:10.1002/9781118671603.

Dupeyrat, P., Ménézo, C., Rommel, M. & Henning, H.-M. (2011) Efficient single glazed flat plate photovoltaic–thermal hybrid collector for domestic hot water system. *Solar Energy*. [Online] 85 (7), 1457–1468. Available from: doi:10.1016/j.solener.2011.04.002.

Dutour, S., Mazet, N., Joly, J.L. & Platel, V. (2005) Modeling of heat and mass transfer coupling with gas-solid reaction in a sorption heat pump cooled by a two-phase closed thermosyphon. *Chemical Engineering Science*. [Online] Available from: doi:10.1016/j.ces.2005.02.046.

Eberle, U., Felderhoff, M. & Schüth, F. (2009) Chemical and physical solutions for hydrogen storage. *Angewandte Chemie - International Edition*. [Online] 48, 6608–6630. Available from: doi:10.1002/anie.200806293.

Ehrhart, B. & Gill, D. (2013) Evaluation of Annual Efficiencies of High Temperature Central Receiver Concentrated Solar Power Plants with Thermal Energy Storage. *Energy Procedia*. [Online] 49, 752–761. Available from: doi:10.1016/j.egypro.2014.03.081.

Elmegaard, B., Ommen, T.S., Markussen, M. & Iversen, J. (2016) Integration of space heating and hot water supply in low temperature district heating. *Energy and Buildings*. [Online] 124, 255–264. Available from: doi:10.1016/j.enbuild.2015.09.003.

Eltawil, M.A. & Zhao, Z. (2010) Grid-connected photovoltaic power systems: Technical and potential problems-A review. *Renewable and Sustainable Energy Reviews*. [Online] 14, 112–129. Available from: doi:10.1016/j.rser.2009.07.015.

energysavingtrust.org.uk (2018) *Heating and hot water*. [Online]. 2018. Available from: http://www.energysavingtrust.org.uk/home-energy-efficiency/heating-and-hot-water.

Eperon, G., Burlakov, V., Docampo, P., Goriely, A., et al. (2014) Morphological Control for High Performance, Solution-Processed Planar Heterojunction Perovskite Solar Cells. *Advanced Functional Materials*. [Online] 24 (1), 151–157. Available from: doi:10.1002/adfm.201302090.

Escobar, B., Hernandez, J., Barbosa, R. & Verde-Gomez, Y. (2013) Analytical model as a tool for the sizing of a hydrogen production system based on renewable energy: The Mexican Caribbean as a case of study. *International Journal Of Hydrogen Energy*. [Online] 38, 12562–12569. Available from: doi:10.1016/j.ijhydene.2012.11.018.

Evans, D.L. (1981) Simplified method for predicting PV array output. *Solar Energy*. 27 (6), 555–560.

Faizal, M., Saidur, R., Mekhilef, S. & Alim, M.A. (2013) Energy, economic and environmental analysis of metal oxides nanofluid for flat-plate solar collector. *Energy Conversion and Management*. [Online] 76, 162–168. Available from: doi:10.1016/j.enconman.2013.07.038.

Feng, G., Liu, S., Huang, K., Pan, Y., et al. (2015) Simulation for a New Type of Photovoltaic (PV) Fresh Air and Domestic Hot Water System. *Procedia Engineering*. [Online] 121, 1428–1434. Available from: doi:10.1016/j.proeng.2015.09.055.

Fernandez, A.I., Martinez, M., Segarra, M., Martorell, I., et al. (2010) Selection of materials

with potential in sensible thermal energy storage. *Solar Energy Materials And Solar Cells*. [Online] 94 (10), 1723–1729. Available from: doi:10.1016/j.solmat.2010.05.035.

Ferrucci, F., Stitou, D., Ortega, P. & Lucas, F. (2018) Mechanical compressor-driven thermochemical storage for cooling applications in tropical insular regions. Concept and efficiency analysis. *Applied Energy*. [Online] 219, 240–255. Available from: doi:10.1016/j.apenergy.2018.03.049.

Fischer, S. & Drück, H. (2014) Standards and certification schemes for solar thermal collectors, stores and systems - An overview about the latest developments. In: *Energy Procedia*. [Online]. 2014 Elsevier Ltd. pp. 2867–2871. Available from: doi:10.1016/j.egypro.2014.10.320.

Freeman, J., Hellgardt, K. & Markides, C.N. (2015) An assessment of solar-powered organic Rankine cycle systems for combined heating and power in UK domestic applications. *Applied Energy*. [Online] 138, 605–620. Available from: doi:10.1016/j.apenergy.2014.10.035 [Accessed: 21 June 2019].

Fuso Nerini, F., Tomei, J., To, L.S., Bisaga, I., et al. (2018) Mapping synergies and trade-offs between energy and the Sustainable Development Goals. *Nature Energy*. [Online] Available from: doi:10.1038/s41560-017-0036-5.

Gall, S., Becker, C., Conrad, E., Dogan, P., et al. (2009) Polycrystalline silicon thin-film solar cells on glass. *Solar Energy Materials and Solar Cells*. [Online] 93, 1004–1008. Available from: doi:10.1016/j.solmat.2008.11.029.

Gao, Y., Zhang, Q., Fan, R., Lin, X., et al. (2013) Effects of thermal mass and flow rate on forced-circulation solar hot-water system: Comparison of water-in-glass and U-pipe evacuated-tube solar collectors. *Solar Energy*. [Online] 98, 290–301. Available from: doi:10.1016/j.solener.2013.10.014.

Gargoom, A., Abu Mohammad Osman Haruni, M.E., Haque, M. & Negnevitsky, M. (2010) *Hybrid stand-alone power systems with hydrogen energy storage for isolated communities*. [Online]. pp.1–6. Available from: doi:10.1109/TDC.2010.5484293.

Gaur, A., Ménézo, C. & Giroux--Julien, S. (2017) Numerical studies on thermal and electrical performance of a fully wetted absorber PVT collector with PCM as a storage medium. *Renewable Energy*. [Online] 109, 168–187. Available from: doi:10.1016/j.renene.2017.01.062.

González, A., Goikolea, E., Barrena, J.A. & Mysyk, R. (2016) Review on supercapacitors: Technologies and materials. *Renewable and Sustainable Energy Reviews*. [Online] (58), 1189–1206. Available from: doi:10.1016/j.rser.2015.12.249.

Guney, M.S. & Tepe, Y. (2017) Classification and assessment of energy storage systems. *Renewable and Sustainable Energy Reviews*. [Online] 75, 1187–1197. Available from: doi:10.1016/j.rser.2016.11.102.

Haase, F., Hollemann, C., Schäfer, S., Merkle, A., et al. (2018) Laser contact openings for local poly-Si-metal contacts enabling 26.1%-efficient POLO-IBC solar cells. *Solar Energy Materials and Solar Cells*. [Online] 186, 184–193. Available from: doi:10.1016/j.solmat.2018.06.020.

Haim, C., Ilan, L., Ori, K., Ruediger, L., et al. (2010) *HIGH EFFICIENCY, LOW COST PARABOLIC DISH SYSTEM FOR COGENERATION OF ELECTRICITY AND HEAT*. In: [Online]. 2010 p. 175. Available from: doi:10.1063/1.3509183.

Hammarberg, E. & Roos, A. (2003) Antireflection treatment of low-emitting glazings for energy efficient windows with high visible transmittance. *Thin Solid Films*. [Online] Available from: doi:10.1016/S0040-6090(03)00986-6.

Han, J.H., Cho, K.W., Lee, K.H. & Kim, H. (1998) Porous graphite matrix for chemical heat pumps. *Carbon*. [Online] 36 (12), 1801–1810. Available from: doi:10.1016/S0008-6223(98)00150-X.

Han, J.H., Lee, K.-H., Kim, D.H. & Kim, H. (2000) Transformation analysis of thermochemical reactor based on thermophysical properties of graphite-MnCl 2 complex. *Industrial and Engineering Chemistry Research*. [Online] 39, 4127–4139. Available from: doi:10.1021/ie9904394.

Han, X., Zhao, G., Xu, C., Ju, X., et al. (2017) Parametric analysis of a hybrid solar concentrating photovoltaic/concentrating solar power (CPV/CSP) system. *Applied Energy*. [Online] 189, 520–533. Available from: doi:10.1016/j.apenergy.2016.12.049.

Hassani, S., Saidur, R., Mekhilef, S. & Taylor, R.A. (2016) Environmental and exergy benefit of nanofluid-based hybrid PV/T systems. *Energy Conversion And Management*. [Online] 123, 431–444. Available from: doi:10.1016/j.enconman.2016.06.061.

Hazami, M., Mehdaoui, F., Naili, N., Noro, M., et al. (2017) Energetic, exergetic and economic analysis of an innovative Solar CombiSystem (SCS) producing thermal and electric energies: Application in residential and tertiary households. *Energy Conversion And Management*. [Online] 140, 36–50. Available from: doi:10.1016/j.enconman.2017.02.040.

Hazami, M., Riahi, A., Mehdaoui, F., Nouicer, O., et al. (2016) Energetic and exergetic performances analysis of a PV/T (photovoltaic thermal) solar system tested and simulated under to Tunisian (North Africa) climatic conditions. *Energy*. [Online] 107, 78–94. Available from: doi:10.1016/j.energy.2016.03.134.

He, W., Chow, T.-T., Ji, J., Lu, J., et al. (2006) Hybrid photovoltaic and thermal solar-collector designed for natural circulation of water. *Applied Energy*. [Online] 83 (3), 199–210. Available from: doi:10.1016/j.apenergy.2005.02.007.

Herrando, M., Markides, C.N. & Hellgardt, K. (2014) A UK-based assessment of hybrid PV and solar-thermal systems for domestic heating and power: System performance. *Applied Energy*. [Online] 122, 288–309. Available from: doi:10.1016/j.apenergy.2014.01.061.

Herrando, M., Ramos, A., Freeman, J., Zabalza, I., et al. (2018) Technoeconomic modelling and optimisation of solar combined heat and power systems based on flat-box PVT collectors for domestic applications. *Energy Conversion And Management*. [Online] 175, 67–85. Available from: doi:10.1016/j.enconman.2018.07.045.

Hosseinzadeh, M., Salari, A., Sardarabadi, M. & Passandideh-Fard, M. (2018) Optimization and parametric analysis of a nanofluid based photovoltaic thermal system: 3D numerical model with experimental validation. *Energy Conversion And Management*. [Online] 160, 93–108. Available from: doi:10.1016/j.enconman.2018.01.006.

Huang, H.-J., Wu, G.-B., Yang, J., Dai, Y.-C., et al. (2004) Modeling of gas–solid chemisorption in chemical heat pumps. *Separation and Purification Technology*. [Online] 34 (1), 191–200. Available from: doi:10.1016/S1383-5866(03)00192-8.

Hubbard, H.M. (1989) Photovoltaics today and tomorrow. *Science*. 244 (4902), 297.

Huide, F., Xuxin, Z., Lei, M., Tao, Z., et al. (2017) A comparative study on three types of solar utilization technologies for buildings: Photovoltaic, solar thermal and hybrid photovoltaic/thermal systems. *Energy Conversion and Management*. [Online] Available from: doi:10.1016/j.enconman.2017.02.059.

Huld, T., Muller, R. & Gambardella, A. (2012) A new solar radiation database for estimating PV performance in Europe and Africa. *Solar Energy*. [Online] 86 (6), 1803–1815. Available from: doi:10.1016/j.solener.2012.03.006.

Hussein, H.M.S. (2007) Theoretical and experimental investigation of wickless heat pipes flat plate solar collector with cross flow heat exchanger. *Energy Conversion And Management*. [Online] 48 (4), 1266–1272. Available from: doi:10.1016/j.enconman.2006.09.021.

Ibrahim, A., Fudholi, A., Sopian, K., Othman, M.Y., et al. (2014) Efficiencies and improvement potential of building integrated photovoltaic thermal (BIPVT) system. *Energy Conversion And Management*. [Online] 77 (C), 527–534. Available from: doi:10.1016/j.enconman.2013.10.033.

Ibrahim, H., Ilinca, A. & Perron, J. (2008) Energy storage systems-Characteristics and comparisons. *Renewable and Sustainable Energy Reviews*. [Online] 12, 1221–1250. Available from: doi:10.1016/j.rser.2007.01.023.

IEA (2018a) *World Energy Outlook 2018*. [Online]. Available from: doi:10.1787/weo-2018-en.

IEA (2018b) *World Energy Outlook 2018*. [Online]. Available from: doi:10.1787/weo-2018-en.

Al Imam, M.F.I., Beg, R.A., Rahman, M.S. & Khan, M.Z.H. (2016) Performance of PVT solar collector with compound parabolic concentrator and phase change materials. *Energy and Buildings*. [Online] 113, 139–144. Available from: doi:10.1016/j.enbuild.2015.12.038.

Iqbal, M. & Iqbal, M. (1983) Chapter 3 – THE SOLAR CONSTANT AND ITS SPECTRAL DISTRIBUTION. In: *An Introduction to Solar Radiation*. [Online]. pp. 43–58. Available from: doi:10.1016/B978-0-12-373750-2.50008-2.

J.P. Zimmermann, M. Evans, J. Griggs, N. King, et al. (2012) Household Electricity Survey: A study of domestic electrical product usage. *Intertek*.

Jamar, A., Majid, Z.A.A., Azmi, W.H., Norhafana, M., et al. (2016) A review of water heating system for solar energy applications. *International Communications in Heat and Mass Transfer*. [Online]. Available from: doi:10.1016/j.icheatmasstransfer.2016.05.028.

Jänes, A., Kurig, H. & Lust, E. (2007) Characterisation of activated nanoporous carbon for supercapacitor electrode materials. *Carbon*. [Online] 45, 1226–1233. Available from: doi:10.1016/j.carbon.2007.01.024.

Jazayeri, M., Uysal, S. & Jazayeri, K. (2013) *A simple MATLAB/Simulink simulation for PV modules based on one-diode model*. [Online]. pp.44–50. Available from: doi:10.1109/HONET.2013.6729755.

Jiang, L. & Roskilly, A.P. (2019) Thermal conductivity, permeability and reaction characteristic enhancement of ammonia solid sorbents: A review. *International Journal of Heat and Mass Transfer*. [Online]. Available from: doi:10.1016/j.ijheatmasstransfer.2018.11.029.

Jiang, L., Wang, R., Lu, Y., Paul Roskilly, A., et al. (2017) Investigation on novel modular

sorption thermal cell with improved energy charging and discharging performance. *Energy Conversion and Management*. [Online] 148, 110–119. Available from: doi:10.1016/j.enconman.2017.05.067.

Jidong, W., Zhiqing, S., Yue, Z. & Jiaqiang, D. (2012) *Optimal dispatching model of Smart Home Energy Management System*. [Online]. pp.1–5. Available from: doi:10.1109/ISGT-Asia.2012.6303266.

Johnston, D. & Siddall, M. (2016) The building fabric thermal performance of passivhaus dwellings-Does it do what it says on the tin? *Sustainability (Switzerland)*. [Online] Available from: doi:10.3390/su8010097.

Jorgensen, G.J., Terwilliger, K.M., DelCueto, J.A., Glick, S.H., et al. (2006) Moisture transport, adhesion, and corrosion protection of PV module packaging materials. *Solar Energy Materials and Solar Cells*. [Online] Available from: doi:10.1016/j.solmat.2006.04.003.

Jouhara, H., Milko, J., Danielewicz, J., Sayegh, M.A., et al. (2016) The performance of a novel flat heat pipe based thermal and PV/T (photovoltaic and thermal systems) solar collector that can be used as an energy-active building envelope material. *Energy*. [Online] 108 (C), 148–154. Available from: doi:10.1016/j.energy.2015.07.063.

Kaiyan, H., Hongfei, Z. & Tao, T. (2011) A novel multiple curved surfaces compound concentrator. *Solar Energy*. [Online] 85, 523–529. Available from: doi:10.1016/j.solener.2010.12.019.

Kalogirou, S. (2003) The potential of solar industrial process heat applications. *Applied Energy*. [Online] 76 (4), 337–361. Available from: doi:10.1016/S0306-2619(02)00176-9.

Kalogirou, S.A. (2004) Solar thermal collectors and applications. *Progress in Energy and Combustion Science*. [Online] 30, 231–295. Available from: doi:10.1016/j.pecs.2004.02.001.

Kalogirou, S.A. & Tripanagnostopoulos, Y. (2006) Hybrid PV/T solar systems for domestic hot water and electricity production. *Energy Conversion And Management*. [Online] 47 (18–19), 3368–3382. Available from: doi:10.1016/j.enconman.2006.01.012.

Kane, T., Firth, S.K. & Lomas, K.J. (2015) How are UK homes heated? A city-wide, socio-technical survey and implications for energy modelling. *Energy and Buildings*. [Online] Available from: doi:10.1016/j.enbuild.2014.10.011.

Kang, S., Yoo, S., Lee, J., Boo, B., et al. (2012) Experimental investigations for recycling of silicon and glass from waste photovoltaic modules. *Renewable Energy*. [Online] Available from: doi:10.1016/j.renene.2012.04.030.

Kayes, B.M., Nie, H., Twist, R., Spruytte, S.G., et al. (2011) 27.6% Conversion efficiency, a new record for single-junction solar cells under 1 sun illumination. In: *Conference Record of the IEEE Photovoltaic Specialists Conference*. [Online]. 2011 p. Available from: doi:10.1109/PVSC.2011.6185831.

Kesmez, Ö., Erdem Çamurlu, H., Burunkaya, E. & Arpaç, E. (2009) Sol-gel preparation and characterization of anti-reflective and self-cleaning SiO2-TiO2 double-layer nanometric films. *Solar Energy Materials and Solar Cells*. [Online] Available from: doi:10.1016/j.solmat.2009.06.022.

Kim, S.T., Ryu, J. & Kato, Y. (2013) Optimization of magnesium hydroxide composite material mixed with expanded graphite and calcium chloride for chemical heat pumps. In: *Applied*

Thermal Engineering. [Online]. 2013 pp. 485–490. Available from: doi:10.1016/j.applthermaleng.2012.07.005.

King, R.R., Law, D.C., Edmondson, K.M., Fetzer, C.M., et al. (2007) 40% efficient metamorphic GaInPGaInAsGe multijunction solar cells. *Applied Physics Letters*. [Online] 90. Available from: doi:10.1063/1.2734507.

Kumar, L., Hasanuzzaman, M. & Rahim, N.A.A. (2019) Global advancement of solar thermal energy technologies for industrial process heat and its future prospects: A review. *Energy Conversion and Management*. [Online] 195, 885–908. Available from: doi:10.1016/j.enconman.2019.05.081.

Lämmle, M., Oliva, A., Hermann, M., Kramer, K., et al. (2017) PVT collector technologies in solar thermal systems: A systematic assessment of electrical and thermal yields with the novel characteristic temperature approach. *Solar Energy*. [Online] 155, 867–879. Available from: doi:10.1016/j.solener.2017.07.015.

Lee, B., Liu, J.Z., Sun, B., Shen, C.Y., et al. (2008) Thermally conductive and electrically insulating EVA composite encapsulant for solar photovoltaic (PV) cell. *Express Polymer Letters*. [Online] Available from: doi:10.3144/expresspolymlett.2008.42.

Lee, S.C., Kim, S.J. & Kim, S. (2011) Demand Side Management With Air Conditioner Loads Based on the Queuing System Model. *IEEE Transactions on Power Systems*. [Online] 26 (2), 661–668. Available from: doi:10.1109/TPWRS.2010.2066583.

Lewis, N. (2016) Research opportunities to advance solar energy utilization. *Science*. [Online] 351 (6271). Available from: doi:10.1126/science.aad1920.

Li, T., Wang, R. & Kiplagat, J. (2013) A Target-Oriented Solid-Gas Thermochemical Sorption Heat Transformer for Integrated Energy Storage and Energy Upgrade. *Aiche Journal*. [Online] 59 (4), 1334–1347. Available from: doi:10.1002/aic.13899.

Li, T.X., Wu, S., Yan, T., Xu, J.X., et al. (2016) A novel solid-gas thermochemical multilevel sorption thermal battery for cascaded solar thermal energy storage. *Applied Energy*. [Online] 161, 1–10. Available from: doi:10.1016/j.apenergy.2015.09.084.

Li, W. & Hao, Y. (2017) Explore the performance limit of a solar PV – thermochemical power generation system. *Applied Energy*. [Online] 206, 843–850. Available from: doi:10.1016/j.apenergy.2017.08.172.

Lin, H., Chen, W. & Hong, F. (2013) Improvement of polycrystalline silicon wafer solar cell efficiency by forming nanoscale pyramids on wafer surface using a self-mask etching technique. *Journal Of Vacuum Science & Technology B*. [Online] 31 (3). Available from: doi:10.1116/1.4795862.

Lindberg, K.B. & Doorman, G. (2013) Hourly load modelling of non-residential building stock. *PowerTech (POWERTECH)*. [Online]. pp.1–6. Available from: doi:10.1109/PTC.2013.6652495.

Liu, C., Yu, Z., Neff, D., Zhamu, A., et al. (2010a) Graphene-based supercapacitor with an ultrahigh energy density. *Nano Letters*. [Online] 10, 4863–4868. Available from: doi:10.1021/nl102661q.

Liu, C., Yu, Z., Neff, D., Zhamu, A., et al. (2010b) Graphene-based supercapacitor with an ultrahigh energy density. *Nano Letters*. [Online] 10, 4863–4868. Available from: doi:10.1021/nl102661q.

Louwen, A., Van Sark, W., Schropp, R. & Faaij, A. (2016) A cost roadmap for silicon heterojunction solar cells. *Solar Energy Materials and Solar Cells*. [Online] Available from: doi:10.1016/j.solmat.2015.12.026.

Lund, P.D., Lindgren, J., Mikkola, J. & Salpakari, J. (2015) Review of energy system flexibility measures to enable high levels of variable renewable electricity. *Renewable and Sustainable Energy Reviews*. [Online] 45, 785–807. Available from: doi:10.1016/j.rser.2015.01.057.

Luo, X., Wang, J., Dooner, M. & Clarke, J. (2015) Overview of current development in electrical energy storage technologies and the application potential in power system operation. *Applied Energy*. [Online] 137, 511–536. Available from: doi:10.1016/j.apenergy.2014.09.081.

Lyakh, M.Y., Rabinovich, O.S., Vasiliev, L.L. & Tsitovich, A.P. (2013) Improving the Performance of an Adsorption Heat Converter in Condensation and Evaporation of the Adsorbate in Sorbent Pores. *Journal of Engineering Physics and Thermophysics*. 86 (6), 1185–1198.

Ma, Z., Bao, H. & Roskilly, A.P. (2018) Feasibility study of seasonal solar thermal energy storage in domestic dwellings in the UK. *Solar Energy*. [Online] 162, 489–499. Available from: doi:10.1016/j.solener.2018.01.013.

Ma, Z., Bao, H. & Roskilly, A.P. (2019) Seasonal solar thermal energy storage using thermochemical sorption in domestic dwellings in the UK. *Energy*. [Online] 166, 213–222. Available from: doi:10.1016/j.energy.2018.10.066.

Madduri, A., Loeder, D., Beutler, N., He, M., et al. (2012) Concentrated evacuated tubes for solar-thermal energy generation using stirling engine. In: *2012 IEEE Energytech, Energytech 2012*. [Online]. 2012 p. Available from: doi:10.1109/EnergyTech.2012.6304625.

Mahlia, T.M.I., Saktisahdan, T.J., Jannifar, A., Hasan, M.H., et al. (2014) A review of available methods and development on energy storage; Technology update. *Renewable and Sustainable Energy Reviews*. [Online] (33), 532–545. Available from: doi:10.1016/j.rser.2014.01.068.

Mahmood, A., Ullah, M.N., Razzaq, S., Basit, A., et al. (2014) A New Scheme for Demand Side Management in Future Smart Grid Networks. *Procedia Computer Science*. [Online] 32, 477–484. Available from: doi:10.1016/j.procs.2014.05.450.

Masuko, K., Shigematsu, M., Hashiguchi, T., Fujishima, D., et al. (2014) Achievement of more than 25% conversion efficiency with crystalline silicon heterojunction solar cell. *IEEE Journal of Photovoltaics*. [Online] 4, 1433–1435. Available from: doi:10.1109/JPHOTOV.2014.2352151.

Mazet, N., Amouroux, M. & Spinner, B. (1991) Analysis and experimental study of the transformation of a non-isothermal solid/gas reacting medium. *Chemical Engineering Communications*. [Online] Available from: doi:10.1080/00986449108911585.

Mazloomi, K., Sulaiman, N. & Moayedi, H. (2012) Electrical Efficiency of Electrolytic Hydrogen Production. *Int. J. Electrochem. Sci.*7 pp.3314–3326.

Mehta, J.R. & Rane, M. V. (2013) Liquid desiccant based solar air conditioning system with novel evacuated lube collector as regenerator. *Procedia Engineering*. [Online] 51, 688–693. Available from: doi:10.1016/j.proeng.2013.01.098.

Meteonorm (2017) *Meteonorm database*. [Online]. 2017. Available from: https://meteonorm.com/en/ [Accessed: 15 October 2019].

Mishra, A., Shukla, A. & Sharma, A. (2015) Latent heat storage through phase change materials. *Resonance*. [Online] 20 (6), 532–541. Available from: doi:10.1007/s12045-015-0212-5.

Mofidi, S.A.H. & Udell, K.S. (2017) Study of Heat and Mass Transfer in $MgCl_2/NH_3$ Thermochemical Batteries. *Journal of Energy Resources Technology*. [Online] Available from: doi:10.1115/1.4035750.

Muhammad, M.J., Muhammad, I.A., Che Sidik, N.A. & Muhammad Yazid, M.N.A.W. (2016) Thermal performance enhancement of flat-plate and evacuated tube solar collectors using nanofluid: A review. *International Communications in Heat and Mass Transfer*. [Online] 76, 6–15. Available from: doi:10.1016/j.icheatmasstransfer.2016.05.009.

Muratori, M. (2018) Impact of uncoordinated plug-in electric vehicle charging on residential power demand. *Nature Energy*. [Online] 3, 193–201. Available from: doi:10.1038/s41560-017-0074-z.

Nasrin, R., Hasanuzzaman, M. & Rahim, N.A. (2018) Effect of high irradiation and cooling on power, energy and performance of a PVT system. *Renewable Energy*. [Online] 166, 552–569. Available from: doi:10.1016/j.renene.2017.10.004.

Nejat, P., Jomehzadeh, F., Taheri, M.M., Gohari, M., et al. (2015) A global review of energy consumption, CO2 emissions and policy in the residential sector (with an overview of the top ten CO2 emitting countries). *Renewable and Sustainable Energy Reviews*. [Online] Available from: doi:10.1016/j.rser.2014.11.066.

nelsonmandelabay.gov.za (n.d.) *About Photovoltaic (PV)*. [Online]. Available from: http://www.nelsonmandelabay.gov.za/Residents.aspx?pageID=289 [Accessed: 19 April 2019].

Neveu, P. & Castaing-Lavignottes, J. (1997) Development of a Numerical Sizing Tool for a Solid-Gas Thermochemical Transformer--I. Impact of the Microscopic Process on the Dynamic Behaviour of a Solid-Gas Reactor P. *Applied Thermal Engineering*. [Online] Available from: doi:10.1016/S1359-4311(96)00065-8.

Nostell, P., Roos, A. & Karlsson, B. (1999) Optical and mechanical properties of sol-gel antireflective films for solar energy applications. *Thin Solid Films*. [Online] Available from: doi:10.1016/S0040-6090(99)00257-6.

NREL (2019) *Best Research-Cell Efficiencies*. [Online]. Available from: https://www.nrel.gov/pv/cell-efficiency.html.

Oliveira, R.G. & Wang, R.Z. (2007) A consolidated calcium chloride-expanded graphite compound for use in sorption refrigeration systems. *Carbon*. [Online] 45 (2), 390–396. Available from: doi:10.1016/j.carbon.2006.09.007.

Othman, M., Ibrahim, A., Jin, G., Ruslan, M., et al. (2013) Photovoltaic-thermal (PV/T) technology - The future energy technology. *Renewable Energy*. [Online] 49, 171–174. Available from: doi:10.1016/j.renene.2012.01.038.

Othman, M.Y., Hamid, S.A., Tabook, M.A.S., Sopian, K., et al. (2016) Performance analysis of PV/T Combi with water and air heating system: An experimental study. *Renewable Energy*. [Online] 86, 716–722. Available from: doi:10.1016/j.renene.2015.08.061.

Ould Amrouche, S., Rekioua, D., Rekioua, T. & Bacha, S. (2016) Overview of energy storage in renewable energy systems. *International Journal of Hydrogen Energy*. [Online] 41, 20914–20927. Available from: doi:10.1016/j.ijhydene.2016.06.243.

van der Pal, M., de Boer, R., Wemmers, A., Smeding, S.F., et al. (2013) *Experimental results and model calculations of a hybrid adsorption-compression heat pump based on a roots compressor and silica gel-water sorption*.

Pandey, K.M. & Chaurasiya, R. (2017) A review on analysis and development of solar flat plate collector. *Renewable and Sustainable Energy Reviews*. [Online] 67, 641–650. Available from: doi:10.1016/j.rser.2016.09.078.

Paquette, B., Boucherif, A., Aimez, V. & Arès, R. (2016) Novel multijunction solar cell design for low cost, high concentration systems. *Progress in Photovoltaics: Research and Applications*. [Online] 24, 150–158. Available from: doi:10.1002/pip.2646.

Pardo García, N., Zubi, G., Pasaoglu, G. & Dufo-López, R. (2017) Photovoltaic thermal hybrid solar collector and district heating configurations for a Central European multi-family house. *Energy Conversion And Management*. [Online] 148, 915–924. Available from: doi:10.1016/j.enconman.2017.05.065.

Parida, B., Iniyan, S. & Goic, R. (2011) A review of solar photovoltaic technologies. *Renewable and Sustainable Energy Reviews*. [Online] 15, 1625–1636. Available from: doi:10.1016/j.rser.2010.11.032.

Park, S., Baik, S.J., Im, J., Fang, L., et al. (2011) Towards a high efficiency amorphous silicon solar cell using molybdenum oxide as a window layer instead of conventional p-type amorphous silicon carbide. *Applied Physics Letters*. [Online] 99 (6). Available from: doi:10.1063/1.3624591.

Pathak, M., Pearce, J. & Harrison, S.J. (2012) Effects on amorphous silicon photovoltaic performance from high-temperature annealing pulses in photovoltaic thermal hybrid devices. *Solar Energy Materials And Solar Cells*. [Online] 100, 199–203. Available from: doi:10.1016/j.solmat.2012.01.015.

Peighambardoust, S.J., Rowshanzamir, S. & Amjadi, M. (2010) Review of the proton exchange membranes for fuel cell applications. *International Journal of Hydrogen Energy*. [Online] 35, 9349–9384. Available from: doi:10.1016/j.ijhydene.2010.05.017.

Le Pierrès, N., Driss, S. & Nathalie, M. (2008) Design of a thermochemical process for deep freezing using solar low-grade heat. *Chemical Engineering and Processing: Process Intensification*. [Online] Available from: doi:10.1016/j.cep.2007.01.011.

Le Pierrès, N., Mazet, N. & Stitou, D. (2007) Modelling and performances of a deep-freezing process using low-grade solar heat. *Energy*. [Online] Available from: doi:10.1016/j.energy.2006.02.009.

Pinel, P., Cruickshank, C.A., Beausoleil-Morrison, I. & Wills, A. (2011) A review of available methods for seasonal storage of solar thermal energy in residential applications. *Renewable and Sustainable Energy Reviews*. [Online] 15, 3341–3359. Available from: doi:10.1016/j.rser.2011.04.013.

Popiel, C.O., Wojtkowiak, J. & Biernacka, B. (2001) Measurements of temperature distribution in ground. *Experimental Thermal And Fluid Science*. 25 (5), 301–309.

Qiu, S., Ruth, M. & Ghosh, S. (2015) Evacuated tube collectors: A notable driver behind the

solar water heater industry in China. *Renewable and Sustainable Energy Reviews*. [Online]. Available from: doi:10.1016/j.rser.2015.03.067.

Qiu, Z., Zhao, X., Li, P., Zhang, X., et al. (2015) Theoretical investigation of the energy performance of a novel MPCM (Microencapsulated Phase Change Material) slurry based PV/T module. *Energy*. [Online] 87 (C), 686–698. Available from: doi:10.1016/j.energy.2015.05.040.

Ramírez-Mendiola, J.L., Grünewald, P. & Eyre, N. (2017) The diversity of residential electricity demand – A comparative analysis of metered and simulated data. *Energy & Buildings*. [Online] 151 (C), 121–131. Available from: doi:10.1016/j.enbuild.2017.06.006.

Ramos, A., Chatzopoulou, M.A., Guarracino, I., Freeman, J., et al. (2017) Hybrid photovoltaic-thermal solar systems for combined heating, cooling and power provision in the urban environment. *Energy Conversion And Management*. [Online] 150 (C), 838–850. Available from: doi:10.1016/j.enconman.2017.03.024.

Rejeb, O., Dhaou, H. & Jemni, A. (2015) A numerical investigation of a photovoltaic thermal (PV/T) collector. *Renewable Energy*. [Online] 77, 43–50. Available from: doi:10.1016/j.renene.2014.12.012.

Rosa-Clot, M., Rosa-Clot, P., Tina, G.M. & Ventura, C. (2016) Experimental photovoltaic-thermal Power Plants based on TESPI panel. *Solar Energy*. [Online] 133, 305–314. Available from: doi:10.1016/j.solener.2016.03.024.

Sabiha, M.A., Saidur, R., Mekhilef, S. & Mahian, O. (2015) Progress and latest developments of evacuated tube solar collectors. *Renewable and Sustainable Energy Reviews*. [Online] 51, 1038–1054. Available from: doi:10.1016/j.rser.2015.07.016.

Saygin, H., Nowzari, R., Mirzaei, N. & Aldabbagh, L.B.Y. (2017) Performance evaluation of a modified PV/T solar collector: A case study in design and analysis of experiment. *Solar Energy*. [Online] 141, 210–221. Available from: doi:10.1016/j.solener.2016.11.048.

Shahin, M.S., Orhan, M.F. & Uygul, F. (2016) Thermodynamic analysis of parabolic trough and heliostat field solar collectors integrated with a Rankine cycle for cogeneration of electricity and heat. *Solar Energy*. [Online] Available from: doi:10.1016/j.solener.2016.06.057.

Shanmugam, S., Veerappan, A. & Eswaramoorthy, M. (2014) An Experimental Evaluation of Energy and Exergy Efficiency of a Solar Parabolic Dish Thermoelectric Power Generator. *Energy Sources Part A-Recovery Utilization And Environmental Effects*. [Online] 36 (17), 1865–1870. Available from: doi:10.1080/15567036.2011.578110.

Sharaf, O.Z. & Orhan, M.F. (2015) Concentrated photovoltaic thermal (CPVT) solar collector systems: Part I – Fundamentals, design considerations and current technologies. *Renewable and Sustainable Energy Reviews*. [Online] Available from: doi:10.1016/j.rser.2015.05.036.

Sherahilo, T. (2018) *Perovskite world record | Oxford PV*. [Online]. 2018. Available from: https://www.oxfordpv.com/news/oxford-pv-perovskite-solar-cell-achieves-28-efficiency [Accessed: 17 July 2019].

Shukla, R., Sumathy, K., Erickson, P. & Gong, J. (2013) Recent advances in the solar water heating systems: A review. *Renewable and Sustainable Energy Reviews*. [Online]. Available from: doi:10.1016/j.rser.2012.10.048.

Da Silva, R.M. & Fernandes, J. (2010) Hybrid photovoltaic/thermal (PV/T) solar systems simulation with Simulink/Matlab. *Solar Energy*. [Online] 84 (12), 1985–1996. Available from: doi:10.1016/j.solener.2010.10.004.

Skagestad, Bard and Mildenstein, P. (2002) *District Heating and Cooling Connection Handbook*. [Online]. Netherlands Agency for Energy and the Environment. Available from: http://dedc.dk/sites/default/files/programme_of_research_development_and_demonstration_on_district_heating_and_cooling.pdf.

Smith, C.J., Forster, P.M. & Crook, R. (2014) Global analysis of photovoltaic energy output enhanced by phase change material cooling. *Applied Energy*. [Online] 126 (C), 21–28. Available from: doi:10.1016/j.apenergy.2014.03.083.

Solar_home (2019) *Hefei Bluesun Solar Energy Tech. Co., Ltd. - Solar Panels, Solar System*. [Online]. 2019. Alibaba.com. Available from: https://bluesunsolar.en.alibaba.com/?spm=a2700.details.cordpanyb.1.1be73e7650jg6Y [Accessed: 17 August 2019].

Solar Keymark (2019) *THE Quality Label for Solar Thermal Products in Europe The Solar Keymark CEN Keymark Scheme*. [Online]. 2019. Available from: www.solarkeymark.org.

Soloveichik, G. (2014) Regenerative Fuel Cells for Energy Storage. *Proceedings Of The Ieee*. [Online] 102 (6), 964–975. Available from: doi:10.1109/JPROC.2014.2314955.

Su, B., Han, W., Qu, W., Liu, C., et al. (2018) A new hybrid photovoltaic/thermal and liquid desiccant system for trigeneration application. *Applied Energy*. [Online] 226, 808–818. Available from: doi:10.1016/j.apenergy.2018.06.034.

Su, D., Jia, Y., Huang, X., Alva, G., et al. (2016) Dynamic performance analysis of photovoltaic-thermal solar collector with dual channels for different fluids. *Energy Conversion And Management*. [Online] 120, 13–24. Available from: doi:10.1016/j.enconman.2016.04.095.

Šúri, M., Huld, T.A., Dunlop, E.D. & Ossenbrink, H.A. (2007) Potential of solar electricity generation in the European Union member states and candidate countries. *Solar Energy*. [Online] 81, 1295–1305. Available from: doi:10.1016/j.solener.2006.12.007.

Tang, R., Yang, Y. & Gao, W. (2011) Comparative studies on thermal performance of water-in-glass evacuated tube solar water heaters with different collector tilt-angles. *Solar Energy*. [Online] 85, 1381–1389. Available from: doi:10.1016/j.solener.2011.03.019.

Thinsurat, K., Bao, H., Ma, Z. & Roskilly, A.P. (2019) Performance study of solar photovoltaic-thermal collector for domestic hot water use and thermochemical sorption seasonal storage. *Energy Conversion and Management*. [Online] 180, 1068–1084. Available from: doi:10.1016/J.ENCONMAN.2018.11.049 [Accessed: 20 December 2018].

Tilman, D., Cassman, K.G., Matson, P.A., Naylor, R., et al. (2002) Agricultural sustainability and intensive production practices. *Nature*. [Online] Available from: doi:10.1038/nature01014.

Tiwari, A. & Sodha, M.S. (2006) Performance evaluation of hybrid PV/thermal water/air heating system: A parametric study. *Renewable Energy*. [Online] 31 (15), 2460–2474. Available from: doi:10.1016/j.renene.2005.12.002.

Todorov, T.K., Bishop, D.M. & Lee, Y.S. (2018) Materials perspectives for next-generation

low-cost tandem solar cells. *Solar Energy Materials and Solar Cells*. [Online] Available from: doi:10.1016/j.solmat.2017.07.033.

Tomar, V., Tiwari, G.N. & Bhatti, T.S. (2017) Performance of different photovoltaic-thermal (PVT) configurations integrated on prototype test cells: An experimental approach. *Energy Conversion And Management*. [Online] 154, 394–419. Available from: doi:10.1016/j.enconman.2017.11.033.

Touafek, K., Haddadi, M. & Malek, A. (2013) Design and modeling of a photovoltaic thermal collector for domestic air heating and electricity production. *Energy and Buildings*. [Online] 59, 21–28. Available from: doi:10.1016/j.enbuild.2012.10.037.

Touafek, K., Khelifa, A. & Adouane, M. (2014) Theoretical and experimental study of sheet and tubes hybrid PVT collector. *Energy Conversion And Management*. [Online] 80, 71–77. Available from: doi:10.1016/j.enconman.2014.01.021.

Tripanagnostopoulos, Y., Nousia, T., Souliotis, M. & Yianoulis, P. (2002) Hybrid photovoltaic/thermal solar systems. *Solar Energy*. [Online] 72 (3), 217–234. Available from: doi:10.1016/S0038-092X(01)00096-2.

Tripathi, R., Tiwari, G.N. & Al-Helal, I.M. (2016) Thermal modelling of N partially covered photovoltaic thermal (PVT) - Compound parabolic concentrator (CPC) collectors connected in series. *Solar Energy*. [Online] 123, 174–184. Available from: doi:10.1016/j.solener.2015.11.014.

Tsai, H.L.H.F. & Tsai, H.L.H.F. (2012) Implementation and verification of integrated thermal and electrical models for commercial PV modules. *Solar Energy*. [Online] 86 (1), 654–665. Available from: doi:10.1016/j.solener.2011.11.014.

Tyagi, V., Kaushik, S.C. & Tyagi, S. (2012) Advancement in solar photovoltaic/thermal (PV/T) hybrid collector technology. *Renew. Sust. Energ. Rev.* [Online]. 16 pp.1383–1398. Available from: doi:10.1016/j.rser.2011.12.013.

Tzivanidis, C., Bellos, E., Korres, D., Antonopoulos, K.A., et al. (2015) Thermal and optical efficiency investigation of a parabolic trough collector. *Case Studies in Thermal Engineering*. [Online] 6, 226–237. Available from: doi:10.1016/j.csite.2015.10.005.

UN (2017) *Sustainable development goals - United Nations*. [Online]. 2017. United Nations. Available from: doi:10.1016/j.eururo.2010.10.002.

Vats, K., Tomar, V. & Tiwari, G.N. (2012) Effect of packing factor on the performance of a building integrated semitransparent photovoltaic thermal (BISPVT) system with air duct. *Energy & Buildings*. [Online] 53, 159–165. Available from: doi:10.1016/j.enbuild.2012.07.004.

Wang, C., Zhang, P. & Wang, R.Z. (2010) Performance of solid–gas reaction heat transformer system with gas valve control. *Chemical Engineering Science*. [Online] 65 (10), 2910–2920. Available from: doi:10.1016/j.ces.2010.01.011.

Wang, L.W., Metcalf, S.J., Critoph, R.E., Thorpe, R., et al. (2011) Thermal conductivity and permeability of consolidated expanded natural graphite treated with sulphuric acid. *Carbon*. [Online] Available from: doi:10.1016/j.carbon.2011.06.093.

Wang, Z., Zhang, J., Wang, Z., Yang, W., et al. (2016) Experimental investigation of the performance of the novel HP-BIPV/T system for use in residential buildings. *Energy & Buildings*. [Online] 130, 295–308. Available from: doi:10.1016/j.enbuild.2016.08.060.

World Energy Council (2013a) Energy Resources: Solar. *World Energy Council 2013 World Energy Resources: Solar*. [Online] Available from: doi:https://www.worldenergy.org/wp-content/uploads/2013/10/WER_2013_8_Solar_revised.pdf.

World Energy Council (2013b) World Energy Resources: 2013 survey. *World Energy Council*. [Online]. Available from: doi:http://www.worldenergy.org/wp-content/uploads/2013/09/Complete_WER_2013_Survey.pdf.

Wronski, C.R., Pearce, J., Deng, J., Vlahos, V., et al. (2004) Intrinsic and light induced gap states in a-Si : H materials and solar cells - effects of microstructure. *Thin Solid Films*. [Online] 451–52, 470–475. Available from: doi:10.1016/j.tsf.2003.10.129.

Wu, S., Li, T.X., Yan, T. & Wang, R.Z. (2018) Experimental investigation on a thermochemical sorption refrigeration prototype using EG/SrCl2–NH3 working pair. *International Journal of Refrigeration*. [Online] 88, 8–15. Available from: doi:10.1016/j.ijrefrig.2017.11.030.

Xu, J., Wang, R.Z. & Li, Y. (2014) A review of available technologies for seasonal thermal energy storage. *Solar Energy*. [Online] 103, 610–638. Available from: doi:10.1016/j.solener.2013.06.006.

Xu, Z. & Kleinstreuer, C. (2014) Concentration photovoltaic-thermal energy co-generation system using nanofluids for cooling and heating. *Energy Conversion And Management*. [Online] 87, 504–512. Available from: doi:10.1016/j.enconman.2014.07.047.

Yan, T., Wang, R.Z., Li, T.X., Wang, L.W., et al. (2015) A review of promising candidate reactions for chemical heat storage. *Renewable and Sustainable Energy Reviews*. [Online] 43, 13–31. Available from: doi:10.1016/j.rser.2014.11.015.

Yang, Z., Zhang, J., Kintner-Meyer, M.C.W., Lu, X., et al. (2011) Electrochemical energy storage for green grid. *Chemical Reviews*. [Online] 111, 3577–3613. Available from: doi:10.1021/cr100290v.

Yangtze_Solar (2019) *Hot Sale Monocristalline Solar Panel Pv Module - Buy Monocristalline Solar Panel,Solar Panel,Pv Module Product on Alibaba.com*. [Online]. 2019. alibaba.com. Available from: https://www.alibaba.com/product-detail/Hot-sale-monocristalline-solar-panel-pv_60807121562.html?spm=a2700.7724838.2017115.11.29294b60elWhwq&s=p [Accessed: 17 August 2019].

Yazdanifard, F., Ameri, M. & Ebrahimnia-Bajestan, E. (2017) Performance of nanofluid-based photovoltaic/thermal systems: A review. *Renewable and Sustainable Energy Reviews*. [Online] 76, 323–352. Available from: doi:10.1016/j.rser.2017.03.025.

Yoshida, S. (2019) *Solar Frontier Achieves World Record Thin-Film Solar Cell Efficiency of 23.35%*. [Online]. 2019. Available from: http://www.solar-frontier.com/eng/news/2019/0117_press.html [Accessed: 17 July 2019].

YouGen (n.d.) *Heating and Hot Water - Energy Saving Information | Renewable Energy Made Easy*. [Online]. Available from: http://www.yougen.co.uk/energy-saving/Heating+Hot+Water/ [Accessed: 18 January 2019].

Yousefi, T., Shojaeizadeh, E., Veysi, F. & Zinadini, S. (2012) An experimental investigation on the effect of pH variation of MWCNT-H 2O nanofluid on the efficiency of a flat-plate solar collector. *Solar Energy*. [Online] 86, 771–779. Available from: doi:10.1016/j.solener.2011.12.003.

Yu, N., Wang, R.Z. & Wang, L.W. (2013) Sorption thermal storage for solar energy. *Progress in Energy and Combustion Science*. [Online] 39 (5), 489–514. Available from: doi:10.1016/j.pecs.2013.05.004.

Yu, Y.Q., Zhang, P., Wu, J.Y. & Wang, R.Z. (2008) Energy upgrading by solid-gas reaction heat transformer: A critical review. *Renewable and Sustainable Energy Reviews*. [Online] 12 (5), 1302–1324. Available from: doi:10.1016/j.rser.2007.01.010.

Yuan, Y., Bao, H., Lu, Y., Ma, Z., et al. (2018) Investigation of equilibrium and dynamic performance of SrCl2-expanded graphite composite in chemisorption refrigeration system. *Applied Thermal Engineering*. [Online] Available from: doi:10.1016/j.applthermaleng.2018.10.071.

Zamengo, M., Ryu, J. & Kato, Y. (2013) Magnesium hydroxide - Expanded graphite composite pellets for a packed bed reactor chemical heat pump. *Applied Thermal Engineering*. [Online] 61 (2), 853–858. Available from: doi:10.1016/j.applthermaleng.2013.04.045.

Zhai, H., Dai, Y.J., Wu, J.Y., Wang, R.Z., et al. (2010) Experimental investigation and analysis on a concentrating solar collector using linear Fresnel lens. *Energy Conversion And Management*. [Online] 51 (1), 48–55. Available from: doi:10.1016/j.enconman.2009.08.018.

Zhang, L.L. & Zhao, X.S. (2009) Carbon-based materials as supercapacitor electrodes. *Chemical Society Reviews*. [Online] 38, 2520–2531. Available from: doi:10.1039/b813846j.

Zhang, X., He, M. & Zhang, Y. (2012) A review of research on the Kalina cycle. *Renewable and Sustainable Energy Reviews*. [Online] 16, 5309–5318. Available from: doi:10.1016/j.rser.2012.05.040.

Zhang, X., Li, M., Shi, W., Wang, B., et al. (2014a) Experimental investigation on charging and discharging performance of absorption thermal energy storage system. *Energy Conversion and Management*. [Online] Available from: doi:10.1016/j.enconman.2014.05.100.

Zhang, X., Wu, Y., Skitmore, M. & Jiang, S. (2014b) Sustainable infrastructure projects in balancing urban-rural development: towards the goal of efficiency and equity. *Journal of Cleaner Production*. [Online] Available from: doi:10.1016/j.jclepro.2014.09.068.

Zhang, X., You, S., Ge, H., Gao, Y., et al. (2014c) Thermal performance of direct-flow coaxial evacuated-tube solar collectors with and without a heat shield. *Energy Conversion And Management*. [Online] 84, 80–87. Available from: doi:10.1016/j.enconman.2014.04.014.

Zhao, Y. (2008) *Photovoltaic cell radiating and combined heat and power system*.

Ziapour, B.M. & Khalili, M.B. (2016) PVT type of the two-phase loop mini tube thermosyphon solar water heater. *Energy Conversion And Management*. [Online] 129, 54–61. Available from: doi:10.1016/j.enconman.2016.10.004.

Ziapour, B.M., Palideh, V. & Baygan, M. (2014) Performance comparison of four passive types of photovoltaic–thermal systems. *Energy Conversion And Management*. [Online] 88, 732–738. Available from: doi:10.1016/j.enconman.2014.09.011.

Zondag, H., de Vries, D., van Helden, W., van Zolingen, R., et al. (2003) The yield of different combined PV-thermal collector designs. *Solar Energy*. [Online] 74, 253–269. Available from: doi:10.1016/S0038-092X(03)00121-X.